NATIONAL CENTRE FOR NUCLEAR RESEARCH

DOCTORAL THESIS

Vector-like fermions as candidates for New Physics

Author:
Daniele RIZZO

Supervisor:
dr. hab. Kamila KOWALSKA,
Prof. NCBJ

A thesis submitted in fulfillment of the requirements for the degree of Doctor of Philosophy

in the

Department BP2

June 9th, 2025

Declaration of Authorship

I, Daniele RIZZO, declare that this thesis titled, "Vector-like fermions as candidates for New Physics" and the work presented in it are my own. I confirm that:

- This work was done wholly or mainly while in candidature for a research degree at the National Centre for Nuclear Research.
- Where any part of this thesis has previously been submitted for a degree or any other qualification at the National Centre for Nuclear Research or any other institution, this has been clearly stated.
- Where I have consulted the published work of others, this is always clearly attributed.
- Where I have quoted from the work of others, the source is always given. With the exception of such quotations, this thesis is entirely my own work.
- I have acknowledged all main sources of help.
- Where the thesis is based on work done by myself jointly with others, I have made clear exactly what was done by others and what I have contributed myself.

Signed:

Date:

NATIONAL CENTRE FOR NUCLEAR RESEARCH

Abstract

Vector-like fermions as candidates for New Physics

Daniele RIZZO

The Standard Model of particle physics, while remarkably successful, leaves several fundamental questions unanswered. Issues such as the origin of fermion masses, the hierarchy problem, and the absence of viable dark matter candidates suggest the presence of new physics beyond the Standard Model. Among the many proposed extensions, models incorporating vector-like fermions offer a compelling avenue for exploration. Their non-chiral nature permits interactions with the Standard Model fields without introducing gauge anomalies, enabling flexible phenomenological implementations.

This thesis presents a comprehensive investigation of models featuring vector-like fermions from both phenomenological and theoretical perspectives. It begins with an analysis of a minimal extension of the Standard Model featuring additional scalars and vector-like fermions. This model offers a novel mechanism for the generation of Standard Model fermion masses, while also accommodating the observed anomaly in the muon's magnetic moment and remaining consistent with current collider constraints through dedicated parameter space scans. The work then transitions to a more theoretical investigation. First, it examines the renormalization group flow in a toy model of vector-like quarks and $SU(N_C)$ gluons, extended to include infinitely many flavors and colors. Using functional renormalization group techniques, the ultraviolet behavior of this model is studied non-perturbatively, and the existence of interacting fixed points is explored. The presence of such a fixed point – which may provide a UV completion – is a welcome feature, however, a scenario with an infinite number of fields is not realistic. Another theory that exhibits an ultraviolet fixed point is quantum gravity. The thesis investigates how quantum gravity effects–through the assumption of asymptotic safety–can impact the parameter space of beyond the Standard Model scenarios. Specifically, the idea that ultraviolet fixed points emerge from gravity-induced corrections is used to predict viable configurations of vector-like fermions and new gauge bosons, linking low-energy observables to Planck-scale physics.

Overall, the results underscore the versatility of vector-like fermions in beyond the Standard Model model building and highlight the complementary roles of phenomenological studies and non-perturbative methods in exploring physics beyond the Standard Model.

NATIONAL CENTRE FOR NUCLEAR RESEARCH

Streszczenie

Vector-like fermions as candidates for New Physics

Daniele RIZZO

Standard Model fizyki czstek, mimo swojej niezwykej skutecznoci, pozostawia wiele fundamentalnych pyta bez odpowiedzi. Problemy takie jak pochodzenie mas fermionów, problem hierarchii oraz brak odpowiednich kandydatów na ciemn materi sugeruj istnienie nowej fizyki poza Standard Model. Wród wielu proponowanych rozszerze, szczególnie interesujc ciek bada s modele zawierajce vector-like fermions. Ich nie-chiralna natura pozwala na oddziaywania z polami Standard Model bez wprowadzania anomalii cechowania, umoliwiajc elastyczne zastosowania fenomenologiczne.

Niniejsza rozprawa przedstawia kompleksowe badania vector-like fermions z perspektywy zarówno fenomenologicznej, jak i teoretycznej. Rozpoczyna si od analizy minimalnego rozszerzenia Standard Model, zawierajcego dodatkowe skalary oraz vector-like fermions. Przez przeszukiwanie przestrzeni parametrów i uwzgldnienie ogranicze eksperymentalnych wykazano, e model ten potrafi wyjani anomalny moment magnetyczny mionu, a take proponuje mechanizm generowania mas dla fermionów Standard Model. Nastpnie praca przechodzi do bardziej teoretycznego ujcia, badajc przepyw grupy renormalizacji w modelu zoonym z kwarków i gluonów, rozszerzonym o nieskoczenie wiele smaków i kolorów. Za pomoc techniki functional renormalization group analizowane jest zachowanie w ultrafioletowym zakresie energii, z naciskiem na istnienie punktów staych. W ostatnim etapie rozprawy przedstawiono, w jaki sposób efekty grawitacji kwantowej – poprzez zaoenie asymptotic safety – mog ogranicza przestrze parametrów modeli beyond the Standard Model. W szczególnoci pokazano, e przyjcie istnienia punktów staych w ultrafiolecie wynikajcych z poprawek indukowanych przez grawitacj pozwala przewidzie dopuszczalne konfiguracje vector-like fermions i nowych bozonów cechowania, wic obserwacje niskoenergetyczne z fizyk w skali Plancka.

Wyniki pracy podkrelaj uniwersalno vector-like fermions w budowaniu modeli beyond the Standard Model oraz ukazuj komplementarno podejcia fenomenologicznego i metod nieperturbacyjnych w badaniu nowej fizyki.

Contents

To Poland, and all it gave me.

1

Introduction

The Standard Model (SM) of particle physics stands as a cornerstone of modern theoretical physics, successfully accounting for a wide range of high-energy and low-energy phenomena. Nevertheless, it is widely regarded as an effective theory, valid only up to a certain energy scale. Several experimental facts and theoretical considerations point to the existence of new physics beyond the SM. Additionally, the SM fails to incorporate gravity and does not achieve unification of the fundamental forces.

Among the many proposed extensions of the SM, vector-like fermions (VLFs) offer a particularly appealing and minimal possibility. Unlike the chiral fermions of the SM, both left- and right-handed components of VLFs transform identically under the gauge group. This feature ensures automatic cancellation of gauge anomalies and allows the introduction of VLFs without disturbing the internal consistency of the theory. Their gauge-invariant Dirac mass terms enable them to be heavy without requiring electroweak symmetry breaking, making them ideal candidates for beyond the SM (BSM) physics. VLFs appear in a variety of theoretical frameworks, such as grand unified theories (GUTs), extra-dimensional models, and composite Higgs constructions. Their presence can modify electroweak precision observables, and leave detectable imprints at colliders. Moreover, they influence the renormalization group (RG) running of SM couplings and may contribute to electroweak vacuum stability or even provide hints toward resolving the naturalness problem.

The aim of this thesis is to explore the theoretical consistency and phenomenological implications of VLFs as extensions of the SM. The investigation proceeds from two complementary perspectives. On one hand, we study the low-energy phenomenology of VLF extensions of the SM, by scanning their parameter space and identifying viable benchmark points. On the other hand, we explore the high-energy behavior of these models by examining whether their RG flow is consistent with asymptotic safety (AS). This dual approach – combining bottom-up and top-down insights – allows us to develop a consistent picture of VLF-based BSM models and their physical implications.

In Chapter 2, the essential theoretical background underlying this thesis is presented. It begins with a concise overview of the SM, briefly reviewing particle content, the Higgs mechanism, and the distinction between chiral and vector-like fermions, with particular emphasis on gauge consistency and anomaly cancellation. The chapter then shifts focus toward the RG formalism, extensively discussing its crucial role in understanding the energy dependence of coupling constants, masses, and the general structure of quantum field theories. Concepts such as running couplings, perturbative expansions, and the emergence of fixed points – both perturbative and non-perturbative – are carefully introduced. Special attention is given to illustrating RG flows in simple yet instructive examples, highlighting phenomena like asymptotic freedom, triviality, and asymptotic safety. This comprehensive RG discussion provides the necessary foundation for the deeper explorations of non-perturbative dynamics and ultraviolet (UV) completions investigated in subsequent chapters.

Chapters 3-5 present original research performed during my doctoral studies, each exploring different facets of VLF phenomenology and their theoretical embeddings.

In Chapter 3, based on [1], the phenomenological implications of extending the SM with VLFs and additional scalar fields are thoroughly explored. This chapter particularly emphasizes the potential of VLFs to address several outstanding questions within particle physics, such as the anomalous magnetic moment of the muon and the hierarchical structure of fermion masses. Employing global analyses and collider studies, the research identifies viable benchmark scenarios consistent with current experimental constraints, highlighting the versatility and significance of VLF-based extensions in probing physics beyond the SM. Additionally, detailed constraints from flavor physics and scalar potential stability are meticulously incorporated into the analysis. These efforts culminate in concrete predictions that can be directly tested in ongoing and future collider experiments.

In Chapter 4, based on an ongoing project, the theoretical foundations of VLF extensions are rigorously examined through non-perturbative RG techniques. The investigation primarily focuses on the UV dynamics of gauge-Yukawa theories, exploring the existence and properties of UV fixed points within these models. By employing functional renormalization group (FRG) methods in the limit of large numbers of fermion flavors and gauge colors, the study identifies scenarios where asymptotic safety could be realized, potentially providing a UV-complete theoretical embedding for VLF models. The chapter thoroughly addresses the impact of including higher-dimensional, beyond-marginal operators, highlighting the intricate and non-trivial RG structure that emerges.

In Chapter 5, based on [2, 3], the interplay between asymptotically safe gravity and the phenomenology of VLF models is examined in detail. This chapter introduces a heuristic framework where quantum gravitational effects, characterized by trans-Planckian fixed points, impose stringent boundary conditions on gauge, Yukawa, and scalar couplings at the Planck scale. By applying this approach to minimal Z' extensions of the SM motivated by the now-resolved flavor anomalies, precise predictions for the couplings in the model are derived. The analysis robustly incorporates current experimental constraints from LHC searches, revealing substantial predictive power and highlighting scenarios that remain viable against stringent collider data. Additionally, the chapter critically evaluates the theoretical robustness of these predictions, particularly concerning higher-order corrections and uncertainties related to gravitational decoupling at the Planck scale, thereby demonstrating both the potential and the limitations inherent the heuristic approach to asymptotically safe quantum gravity as a guiding principle for BSM phenomenology.

Finally, chapter 6 summarizes the results and presents the conclusions.

2

Background

In what follows we will introduce the SM of particle physics and the RG, and review the properties that are relevant for the manuscript. This chapter must not be taken as exhaustive, but just as an introduction to the most basic formulation of the SM and a discussion on the main challenges the model faces and fails to solve. The reader who is interested in studying in more depth such topics, should refer to textbooks on quantum field theory (QFT) and the SM, *e.g.* [4, 5].

2.1 The Standard Model of Particle Physics

The SM stands as the most successful QFT constructed to date, accurately describing the electromagnetic, weak, and strong interactions among elementary particles. Its predictions span a vast range of energy scales and have been confirmed to remarkable precision by experimental data from collider experiments, precision electroweak tests, and flavor physics. Despite its success, the SM is widely regarded as an effective field theory (EFT) that needs to be completed in the UV, as it leaves several key questions unanswered - such as the nature of dark matter, the origin of neutrino masses, the matter-antimatter asymmetry of the Universe, and the mechanism behind electroweak symmetry breaking.

2.1.1 Particle content

The SM incorporates all experimentally verified fundamental interactions, excluding gravity, within a mathematically elegant and relatively simple theoretical framework. Its structure emerges naturally once we demand Lorentz invariance and impose local gauge symmetries. These internal symmetries form the gauge group

$$SU(3)_c \times SU(2)_L \times U(1)_Y,$$

representing color charge, weak isospin, and hypercharge, respectively. The particles, specifically fermions and the Higgs scalar, transform under distinct representations of these symmetry groups, as detailed in Table 2.1. Their mutual interactions are mediated by gauge bosons, arising inherently from the theory's invariance under the aforementioned gauge symmetries.

Field	Spin	$SU(3)_c$	$SU(2)_L$	Y	$Q = T_3 + Y$
$q = \begin{pmatrix} u_L \\ d_L \end{pmatrix}$	$1/2$	3	2	$1/6$	$\begin{pmatrix} +2/3 \\ -1/3 \end{pmatrix}$
u_R	$1/2$	3	1	$+2/3$	$+2/3$
d_R	$1/2$	3	1	$-1/3$	$-1/3$
$l = \begin{pmatrix} \nu_L \\ e_L \end{pmatrix}$	$1/2$	1	2	$-1/2$	$\begin{pmatrix} 0 \\ -1 \end{pmatrix}$
e_R	$1/2$	1	1	-1	-1
$\phi = \begin{pmatrix} \phi^+ \\ \phi^0 \end{pmatrix}$	0	1	2	$+1/2$	$\begin{pmatrix} +1 \\ 0 \end{pmatrix}$

TABLE 2.1: SM scalar and (Weyl) fermions and their representations under the gauge group of the SM.

The SM Lagrangian represents the most general renormalisable theory consistent with the gauge group $SU(3)_c \times SU(2)_L \times U(1)_Y$. In a concise form, the Lagrangian reads:

$$\begin{aligned}\mathcal{L}_{\text{SM}} = &- \frac{1}{4} G^a_{\mu\nu} G^{a\,\mu\nu} - \frac{1}{4} W^i_{\mu\nu} W^{i\,\mu\nu} - \frac{1}{4} B_{\mu\nu} B^{\mu\nu} \\ &+ (D_\mu \phi)^\dagger (D_\mu \phi) + \mu^2 \phi^\dagger \phi - \frac{\lambda}{2} (\phi^\dagger \phi)^2 \\ &+ i\, \overline{\psi}_i \not{D}\, \psi_i - \left(\overline{q}_i\, y_u^{ij}\, u_{jR}\, \widetilde{\phi} + \overline{q}_i\, y_d^{ij}\, d_{jR}\, \phi + \overline{l}_i\, y_l^{ij}\, e_{jR}\, \phi + \text{h.c.} \right),\end{aligned} \tag{2.1}$$

where we define $\not{D} = D_\mu \gamma^\mu$ and ψ_i are Dirac spinor corresponding to the Weyl spinors introduced in Table 2.1. The covariant derivative is expressed as:

$$D_\mu = \partial_\mu + i g_3\, G^a_\mu T^a + i g_2 W^i_\mu T^i + i g_Y\, B_\mu Y, \tag{2.2}$$

with gauge fields G^a_μ, W^i_μ, and B_μ corresponding to the strong and electroweak gauge symmetries. Indices a and i run over the adjoint representations of their respective gauge groups, with $T^a = \lambda^a/2$ for $SU(3)_c$ (using Gell-Mann matrices λ^a) and $T^i = \sigma^i/2$ for $SU(2)_L$ (using Pauli matrices σ^i). Hypercharge is indicated by Y. When acting upon fields invariant under certain groups, the associated generator vanishes. Field strengths are defined as:

$$B_{\mu\nu} = \partial_\mu B_\nu - \partial_\nu B_\mu, \tag{2.3}$$

$$W^i_{\mu\nu} = \partial_\mu W^i_\nu - \partial_\nu W^i_\mu - g_2\, \epsilon^{ijk}\, W^j_\mu W^k_\nu, \tag{2.4}$$

$$G^a_{\mu\nu} = \partial_\mu G^a_\nu - \partial_\nu G^a_\mu - g_3\, f^{abc}\, G^b_\mu G^c_\nu, \tag{2.5}$$

with structure constants ϵ^{ijk} and f^{abc} associated with $SU(2)$ and $SU(3)$ groups, respectively. While the strong interaction, carried by gluons, remains unaltered and retains its gauge symmetry, the electroweak interaction experiences a fundamental change due to spontaneous symmetry breaking. This breaking originates from the potential associated with the Higgs scalar field, often visualized as a "Mexican-hat" shaped potential, *cf.* figure 2.1. Specifically, the original electroweak gauge symmetry, $SU(2)_L \times U(1)_Y$, is spontaneously broken down to a residual symmetry group, $U(1)_{em}$, corresponding to electromagnetism.

This symmetry-breaking mechanism generates mass for the $W^\pm$ and Z gauge bosons [6–8], as the would-be Goldstone bosons produced by the symmetry breaking are absorbed by

these bosons – a property known as the Higgs mechanism. Consequently, the photon (γ), which corresponds to the unbroken $U(1)_{em}$, remains massless, while the $W^{\pm}$ and Z bosons gain significant masses. This mass acquisition explains why the weak interactions are inherently weaker than electromagnetic and strong interactions at low energies. The Higgs mechanism is going to be discussed in more details in section 2.1.3.
Moreover, spontaneous symmetry breaking is also responsible for generating fermion masses through their Yukawa couplings to the Higgs field. These Yukawa couplings, represented as 3×3 matrices in flavour space, are generally not diagonal, leading to flavour mixing among quarks and leptons. This flavour mixing manifests explicitly when transitioning from the gauge eigenbasis to the mass eigenbasis. In the quark sector, this is described by the Cabibbo-Kobayashi-Maskawa (CKM) matrix, while in the lepton sector, the analogous effect is encapsulated in the Pontecorvo-Maki-Nakagawa-Sakata (PMNS) matrix. Additionally, the conservation of baryon and lepton numbers emerges naturally as accidental symmetries within the structure of the SM Lagrangian [9]. These symmetries are not imposed explicitly in the Lagrangian but emerge due to the renormalizability and field content of the theory. As such, they are not expected to hold in a more fundamental theory, and indeed many extensions of the SM predict their violation, leading to phenomena such as proton decay or lepton-number violating processes like neutrinoless double beta decay.

2.1.2 Vector-like vs. chiral fermions

A key structural feature of the SM is its use of *chiral fermions* - fields whose left- and right-handed components transform differently under the gauge group. This chiral nature is responsible for many of the SM's distinctive properties, including the parity violation observed in weak interactions and the absence of explicit mass terms for fermions before electroweak symmetry breaking. In contrast, *vector-like fermions* have identical gauge transformation properties for both chiralities and thus allow for bare mass terms in the Lagrangian without violating gauge invariance. Understanding the distinction between these two types of fermions is essential when constructing theories beyond the SM.
To illustrate the difference, consider a free Dirac fermion in four dimensions, expressed in terms of its left- and right-handed Weyl components:

$$\mathcal{L}_D = i\,\psi_L^\dagger\,\bar{\sigma}^\mu\partial_\mu\psi_L + i\,\psi_R^\dagger\,\sigma^\mu\partial_\mu\psi_R - m\left(\psi_L^\dagger\psi_R + \psi_R^\dagger\psi_L\right), \tag{2.6}$$

where ψ_L and ψ_R are two-component left- and right-handed Weyl spinors, and m is a Dirac mass term coupling them. The kinetic terms are invariant under separate global $U(1)$ transformations acting on ψ_L and ψ_R:

$$\psi_L \to e^{i\theta_L}\psi_L, \qquad \psi_R \to e^{i\theta_R}\psi_R. \tag{2.7}$$

This symmetry can be decomposed into two independent transformations: a vector symmetry $U(1)_V$ and an axial symmetry $U(1)_A$, defined by

$$U(1)_V: \quad \psi_{L,R} \to e^{i\alpha}\psi_{L,R} \quad \Rightarrow \quad \Psi \to e^{i\alpha}\Psi, \tag{2.8}$$

$$U(1)_A: \quad \psi_L \to e^{i\beta}\psi_L, \quad \psi_R \to e^{-i\beta}\psi_R \quad \Rightarrow \quad \Psi \to e^{i\beta\gamma^5}\Psi, \tag{2.9}$$

where $\Psi = (\psi_L, \psi_R)^T$ is the four-component Dirac spinor and γ^5 is the usual chirality matrix.

According to Noether's theorem, every continuous global symmetry of the Lagrangian corresponds to a conserved current. In the case of fermionic field theories, global phase rotations give rise to vector and axial (chiral) symmetries, each associated with a distinct conserved quantity - provided the symmetry is respected by the full Lagrangian. For the Dirac fermion considered here, the conserved currents corresponding to the $U(1)_V$ and $U(1)_A$ symmetries are given by:

$$j_V^\mu = \bar{\Psi}\gamma^\mu\Psi, \qquad j_A^\mu = \bar{\Psi}\gamma^\mu\gamma^5\Psi. \tag{2.10}$$

Computing the divergences of these currents using the equations of motion yields:

$$\partial_\mu j_V^\mu = 0, \qquad \partial_\mu j_A^\mu = 2im\,\bar{\Psi}\gamma^5\Psi. \tag{2.11}$$

We see that the vector symmetry remains conserved even in the presence of the mass term, while the axial symmetry is explicitly broken by the fermion mass. This illustrates the essential distinction: the Dirac mass term preserves vector symmetries but violates axial (or chiral) ones.

This distinction becomes crucial in gauge theories. In a chiral gauge theory - like the SM - the left- and right-handed components of fermions transform under different gauge representations. Consequently, a mass term of the form $\overline{\psi}_L\psi_R$ is not gauge invariant and is therefore forbidden prior to spontaneous symmetry breaking. Fermion masses in the SM are generated dynamically via Yukawa interactions with the Higgs field, which restore gauge invariance after the Higgs acquires a vacuum expectation value (vev).

In contrast, VLFs have left- and right-handed components that transform identically under the gauge group. For example, a pair of Weyl spinors χ_L and χ_R both in the fundamental of $SU(3)_c$ and neutral under electroweak interactions can be combined into a Dirac fermion with a gauge-invariant mass term:

$$\mathcal{L}_{\text{mass}}^{\text{VLF}} \supset -M\,\chi_L^\dagger\,\chi_R. \tag{2.12}$$

No symmetry forbids this term, so VLFs can be naturally heavy, with masses even above the electroweak scale. This makes them excellent candidates for physics beyond the SM, appearing in theories such as:

- Extra-dimensional models (e.g., Kaluza-Klein fermions);
- Composite Higgs and partial compositeness scenarios;
- Grand Unified Theories with incomplete multiplets;
- Models with new vector-like quarks or leptons interacting with the Higgs.

2.1.3 The Higgs mechanism

As discussed in the previous section, the fermionic content of the SM is chiral, with left- and right-handed components transforming differently under the gauge group $SU(3)_c \times SU(2)_L \times U(1)_Y$. Consequently, gauge invariance forbids explicit mass terms of the form $m\overline{\psi}_L\psi_R$ in the Lagrangian. However, the observed elementary particles — both fermions and weak gauge bosons — are massive. Reconciling gauge invariance with the generation of particle masses requires a dynamical mechanism: the Higgs mechanism.

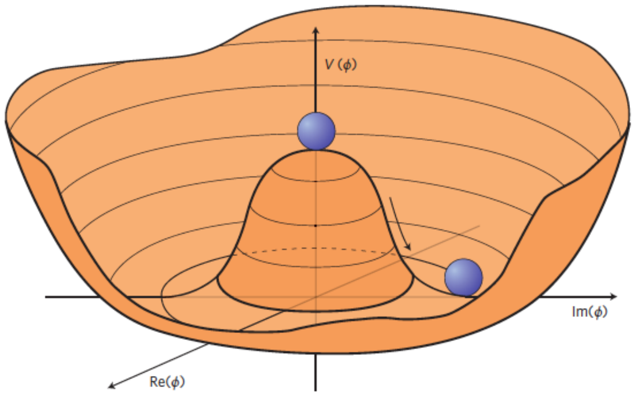

FIGURE 2.1: Illustration of the Higgs potential, equation 2.16. The minimum lies on a degenerate circle of vacua, leading to spontaneous symmetry breaking when a particular vacuum is selected. The figure is taken from [10].

Spontaneous symmetry breaking

The essential idea behind the Higgs mechanism is the phenomenon of spontaneous symmetry breaking. A continuous symmetry is said to be spontaneously broken when the ground state (vacuum) of the system does not respect the symmetry of the Lagrangian. In relativistic QFT, this implies the existence of massless scalar excitations — Goldstone bosons — as stated by Goldstone's theorem. In a gauge theory, however, these Goldstone bosons are "eaten" by the gauge bosons, giving them longitudinal degrees of freedom and hence mass, without explicitly breaking gauge invariance.
In the SM, this is achieved by introducing a scalar field — the Higgs doublet — which acquires a vev and spontaneously breaks the electroweak symmetry.

The Higgs sector

We consider a single complex scalar doublet field transforming under $SU(2)_L \times U(1)_Y$ as

$$\phi = \begin{pmatrix} \phi^+ \\ \phi^0 \end{pmatrix}, \qquad Y_\phi = +\frac{1}{2}. \tag{2.13}$$

The Higgs Lagrangian consists of a kinetic term and a scalar potential:

$$\mathcal{L}_{\text{Higgs}} = (D_\mu \phi)^\dagger (D^\mu \phi) - V(\phi), \tag{2.14}$$

where the covariant derivative is

$$D_\mu = \partial_\mu + i g_2 W_\mu^i \frac{\sigma^i}{2} + i g_Y B_\mu Y, \tag{2.15}$$

and the scalar potential takes the form of a Mexican hat, as shown in figure 2.1:

$$V(\phi) = -\mu^2 \phi^\dagger \phi + \lambda (\phi^\dagger \phi)^2, \qquad \mu^2, \lambda > 0. \tag{2.16}$$

This potential has a degenerate circle of minima, with nonzero vev:

$$\langle \phi \rangle = \frac{1}{\sqrt{2}} \begin{pmatrix} 0 \\ v \end{pmatrix}, \qquad v = \sqrt{\frac{\mu^2}{\lambda}}. \tag{2.17}$$

This choice breaks the gauge symmetry

$$SU(2)_L \times U(1)_Y \longrightarrow U(1)_{\text{em}},$$

where the unbroken generator corresponds to the electromagnetic charge $Q = T_3 + Y$. The three broken generators correspond to the would-be Goldstone bosons, which become the longitudinal components of the $W^\pm$ and Z bosons.

Mass generation for gauge bosons

Expanding around the vacuum in unitary gauge, the Higgs doublet is written as

$$\phi(x) = \frac{1}{\sqrt{2}} \begin{pmatrix} 0 \\ v + H(x) \end{pmatrix}, \tag{2.18}$$

where $H(x)$ is the physical Higgs field. Inserting this into the kinetic term, equation 2.1, and rotating from the unphysical basis (W^3, B) to the physical one (Z, A) yields the mass terms for the electroweak gauge bosons:

$$\mathcal{L}_{\text{mass}} = \frac{1}{2}\left(\frac{g_2 v}{2}\right)^2 W^+_\mu W^{-\mu} + \frac{1}{2}\left(\frac{v}{2}\sqrt{g_2^2 + g_Y^2}\right)^2 Z_\mu Z^\mu. \tag{2.19}$$

Thus, the masses of the weak bosons are

$$M_W = \frac{1}{2} g_2 v, \qquad M_Z = \frac{1}{2} v \sqrt{g_2^2 + g_Y^2}, \tag{2.20}$$

while the photon A_μ, corresponding to the unbroken $U(1)_{\text{em}}$, remains massless. The electroweak mixing angle θ_W is defined by

$$\sin\theta_W = \frac{g_Y}{\sqrt{g_2^2 + g_Y^2}}, \qquad e = g_2 \sin\theta_W = g_Y \cos\theta_W. \tag{2.21}$$

Higgs interactions and mass

The scalar potential, expanded around the vev, yields:

$$V(H) = \lambda v^2 H^2 + \lambda v H^3 + \frac{\lambda}{4} H^4, \tag{2.22}$$

from which we identify the Higgs mass:

$$m_H^2 = 2\lambda v^2. \tag{2.23}$$

The trilinear and quartic Higgs self-couplings follow directly from the cubic and quartic terms.
In addition, the Higgs boson couples to the fermions via Yukawa interactions:

$$\mathcal{L}_{\text{Yuk}} \supset -y_f \bar{f}_L \phi f_R + \text{h.c.}, \tag{2.24}$$

which, after symmetry breaking, yield fermion masses:

$$m_f = \frac{y_f v}{\sqrt{2}}, \qquad \Rightarrow \qquad y_f = \frac{\sqrt{2} m_f}{v}. \tag{2.25}$$

These couplings are proportional to mass, explaining why the Higgs couples more strongly to heavy fermions (e.g., the top quark).

Radiative corrections and the fine-tuning problem

While the Higgs mechanism elegantly explains the origin of electroweak symmetry breaking and the mass generation for elementary particles, it also introduces one of the most perplexing theoretical issues in the SM: the sensitivity of the Higgs mass to quantum corrections. In particular, the mass parameter μ^2 in the Higgs potential receives large radiative corrections from loop diagrams involving virtual particles, such as top quarks, gauge bosons, and the Higgs boson itself. These corrections are quadratically divergent in the UV:

$$\delta\mu^2 \sim \frac{\Lambda^2}{16\pi^2}, \tag{2.26}$$

where Λ is the cutoff scale at which new physics is expected to appear.

If the SM is valid all the way up to the Planck scale ($\Lambda \sim 10^{19}$ GeV), then the bare value of μ^2 must be finely tuned to cancel the enormous loop corrections and yield the observed Higgs mass at the electroweak scale ($m_H \sim 125$ GeV). This extreme sensitivity is known as the *hierarchy problem*, and it suggests that the SM is incomplete.

Various BSM scenarios have been proposed to address this problem, including low-scale supersymmetry, composite Higgs models, and theories with extra spatial dimensions. Each introduces new dynamics or symmetries that soften the quadratic divergences and stabilize the Higgs mass without fine-tuning. Although no such new physics has been confirmed so far, the issue of Higgs mass naturalness remains a strong theoretical motivation for exploring BSM physics.

Custodial symmetry and precision tests

A useful concept in analyzing the structure of the Higgs sector is custodial symmetry. In the limit $g_Y \to 0$, the Higgs potential and kinetic terms exhibit an approximate global $SU(2)_L \times SU(2)_R$ symmetry, spontaneously broken to the diagonal $SU(2)_V$. This symmetry ensures the tree-level relation:

$$\rho \equiv \frac{M_W^2}{M_Z^2 \cos^2\theta_W} = 1, \tag{2.27}$$

which agrees with experimental observations at the per-mille level. Any extension of the SM that introduces custodial symmetry breaking effects must be carefully constrained to maintain consistency with electroweak precision tests.

Phenomenological implications

The properties of the Higgs boson directly impact a wide range of observables accessible at particle colliders. Its couplings to fermions and gauge bosons are predicted by the SM and scale with particle masses, making precise measurements of Higgs production and decay rates a sensitive probe of new physics. Deviations from the SM expectations - for example, in Higgs signal strengths or branching ratios - can reveal the presence of higher-dimensional operators or loop effects from undiscovered particles.
The dominant Higgs production mechanism at the Large Hadron Collider (LHC) is gluon-gluon fusion, mediated by a top-quark loop, while the main decay channels include $H \to b\bar{b}$,

$H \to WW^*$, $H \to ZZ^*$, and $H \to \gamma\gamma$. These processes have been studied with increasing precision, and current measurements are in good agreement with SM predictions at the 10-20% level [11, 12].

Furthermore, the structure of the Higgs potential, specifically the Higgs self-coupling λ, is yet to be directly measured. Accessing this coupling requires observation of Higgs pair production, which is suppressed in the SM and remains a major experimental challenge. Any deviation in the Higgs self-interaction would provide crucial insight into the dynamics of electroweak symmetry breaking and could distinguish between competing scenarios, such as the SM, supersymmetric extensions, or composite Higgs models.

Finally, the Higgs plays an essential role in electroweak baryogenesis, vacuum stability, and naturalness arguments. Its mass and couplings determine whether the electroweak phase transition was first order - a necessary condition for baryogenesis - and whether the Higgs potential remains stable up to the Planck scale or becomes metastable. These considerations make the Higgs sector a central arena for testing the validity and limitations of the SM.

Summary

The Higgs mechanism is thus not merely a convenient tool for mass generation, but a central organizing principle of the SM. Its success rests on a subtle interplay of gauge invariance, spontaneous symmetry breaking, and renormalizability. The discovery of the Higgs boson at the LHC in 2012 with mass $m_H \approx 125\,\text{GeV}$ confirms the essential picture, but also opens several questions: the smallness of the Higgs mass compared to the Planck scale (hierarchy problem), the metastability of the electroweak vacuum, and the origin of the Yukawa structure. These open issues strongly suggest that the Higgs sector may be a portal to physics beyond the SM - a theme that will recur in subsequent chapters.

2.1.4 Anomalies and gauge consistency

The mathematical consistency of any quantum gauge theory hinges not only on renormalizability and unitarity, but also on the preservation of gauge invariance at the quantum level. In particular, the SM - as a chiral gauge theory - is potentially vulnerable to *anomalies*: quantum mechanical violations of classical symmetries. While some anomalies, such as global chiral anomalies in Quantum Chromodynamics (QCD), have meaningful physical implications, the presence of *gauge anomalies* renders a theory internally inconsistent by breaking gauge invariance, spoiling current conservation, and obstructing the cancellation of unphysical degrees of freedom. This makes anomaly cancellation a powerful constraint on the fermion content of the SM and any possible extension thereof.

Classical symmetries and quantum anomalies

At the classical level, continuous symmetries of the Lagrangian lead to conserved currents via Noether's theorem. However, this conservation law may fail in the quantum theory. An anomaly arises when the regularization and renormalization of loop diagrams introduce a non-zero divergence for this current. The prototypical case involves triangle diagrams where three gauge bosons couple to a fermion loop. If the symmetry being gauged is anomalous, the gauge variation of the effective action fails to vanish, destroying gauge invariance and invalidating the theory.

This phenomenon is illustrated in the Adler-Bell-Jackiw anomaly [13, 14], where the divergence of the axial current in quantum electrodynamics (QED) is:

$$\partial_\mu j_5^\mu = \frac{e^2}{16\pi^2} \epsilon^{\mu\nu\rho\sigma} F_{\mu\nu} F_{\rho\sigma}. \tag{2.28}$$

While this is acceptable for a global symmetry, it would be fatal for a gauged symmetry, such as the hypercharge or weak isospin symmetry in the SM.

Anomaly cancellation in the SM

Let us consider three gauge bosons $A_\mu^a, A_\nu^b, A_\rho^c$ coupling to a chiral fermion in some representation R of the gauge group. The amplitude for the triangle diagram involves the trace:

$$\mathcal{A}^{abc} \propto \mathrm{Tr}_R \left(\{T^a, T^b\} T^c \right), \tag{2.29}$$

where T^a are the generators of the gauge group in the representation R. For a vector-like theory, where left- and right-handed components transform identically, the contributions from left- and right-handed fermions cancel:

$$\mathcal{A}^{abc}_{\text{total}} = \mathcal{A}^{abc}_L - \mathcal{A}^{abc}_R = 0. \tag{2.30}$$

In chiral theories, however, these contributions do not cancel, and the resulting anomaly must vanish as a sum over all chiral fermions in the theory.
The possible triangle anomalies in the SM arise from gauge and mixed gauge-gravity diagrams:

- $[SU(3)_c]^2 \times U(1)_Y$
- $[SU(2)_L]^2 \times U(1)_Y$
- $[U(1)_Y]^3$
- $[\text{gravity}]^2 \times U(1)_Y$.

For consistency, the total contribution to each of these anomalies from all fermions must vanish.

To see how this works, consider the first anomaly in the list above, which involves two gluons and one hypercharge gauge boson, $[SU(3)_c]^2 \times U(1)_Y$. Only quark fields contribute here, as they are the only fermions carrying color. The relevant terms involve the left-handed quark doublet q_L, and the right-handed singlets u_R and d_R. Including color multiplicity, the anomaly coefficient is proportional to:

$$3 \left[2 \cdot \frac{1}{6} - \frac{2}{3} - \left(-\frac{1}{3} \right) \right] = 0, \tag{2.31}$$

where the factor of 3 accounts for the three colors. The contributions from up-type and down-type quarks cancel the doublet contribution, leading to a vanishing total.

Next, the $[SU(2)_L]^2 \times U(1)_Y$ anomaly receives contributions only from left-handed fermion doublets. In each generation, these include three copies of the quark doublet q_L, each with hypercharge $Y = 1/6$, and one lepton doublet l_L with $Y = -1/2$. The anomaly coefficient

Anomaly Type	Contributing Fermions	Cancels?	Remarks
$[SU(3)_c]^2 \times U(1)_Y$	q_L, u_R, d_R	Yes	Color triplet content balances
$[SU(2)_L]^2 \times U(1)_Y$	q_L, l_L	Yes	Quark vs lepton hypercharges
$[U(1)_Y]^3$	All fermions	Yes	Precise cancellation across sectors
$[U(1)_Y] \times \text{Gravity}^2$	All fermions	Yes	Sum of hypercharges vanishes

TABLE 2.2: Anomaly cancellation in one generation of SM fermions. Each anomaly listed is evaluated over all left- and right-handed Weyl fermions.

is:

$$3 \cdot \frac{1}{6} + 1 \cdot \left(-\frac{1}{2}\right) = 0, \tag{2.32}$$

again yielding cancellation.

The most subtle case involves the cubic hypercharge anomaly $[U(1)_Y]^3$, where all fermions contribute with their hypercharges cubed. The total anomaly coefficient, summing over one generation, is:

$$3\left[2 \cdot \left(\frac{1}{6}\right)^3 + \left(\frac{2}{3}\right)^3 + \left(-\frac{1}{3}\right)^3\right] + 2 \cdot \left(-\frac{1}{2}\right)^3 + (-1)^3 = 0. \tag{2.33}$$

The quark and lepton contributions exactly cancel, once again confirming anomaly freedom.

Another important consistency check is the mixed gauge-gravity anomaly, where two gravitons couple to a $U(1)_Y$ current. This anomaly is proportional to the sum of hypercharges of all fermions in a generation:

$$3 \cdot \left(2 \cdot \frac{1}{6} + \frac{2}{3} - \frac{1}{3}\right) + 2 \cdot \left(-\frac{1}{2}\right) - 1 = 0. \tag{2.34}$$

This condition ensures that coupling the SM to gravity does not violate gauge invariance at the quantum level.

The full set of anomaly cancellations in a single SM generation is summarized in Table 2.2. Taken together, these cancellations indicate that the SM fermion content is delicately arranged to ensure anomaly cancellation. This feature is not guaranteed in arbitrary chiral gauge theories and provides a strong constraint on any possible extension of the SM. In particular, the addition of new chiral fermions must respect these cancellation conditions. Thus, anomaly cancellation not only ensures the consistency of the SM but also shapes the structure of viable theories beyond it. It constrains charge assignments, fermion representations, and helps distinguish between allowed and inconsistent extensions, making it a foundational tool in model building.

Vector-like fermions and anomaly evasion

One natural way to avoid introducing anomalies is to add new fermions in vector-like pairs, since their left- and right-handed components contribute equally and oppositely to anomalies. VLFs provide a robust and anomaly-safe avenue for extending the SM. By construction, a vector-like fermion has left- and right-handed components transforming identically under the gauge group. As a result, their contributions to any potentially anomalous triangle diagram cancel identically:

$$\mathcal{A}_{\text{VLF}} = \text{Tr}_L(T^a T^b T^c) - \text{Tr}_R(T^a T^b T^c) = 0. \tag{2.35}$$

This cancellation occurs independently of the specific representation or hypercharge, provided that the left- and right-handed components are matched.

As mentioned previously, unlike chiral fermions, VLF can acquire gauge-invariant Dirac mass terms without requiring electroweak symmetry breaking. For instance, a pair of $SU(2)_L$ singlets with opposite hypercharge Y can be combined as in equation 2.12 with no involvement of the Higgs field. Because of this flexibility, VLFs are often invoked in BSM scenarios where new heavy fermions appear - such as in models with extended Higgs sectors, composite dynamics, extra dimensions, or partial compositeness.
Moreover, VLFs can couple to the Higgs boson through Yukawa-like terms, and participate in loop-induced processes such as Higgs production or decay, contributing observable signatures at colliders. Their gauge anomaly neutrality ensures that such extensions remain consistent even at the quantum level, without the need for delicate cancellations. This makes VLF especially appealing in phenomenological studies and model building.

Summary

Gauge and global anomalies represent essential consistency conditions for any QFT. Their cancellation is not optional, but a necessary requirement to preserve gauge invariance, unitarity, and the validity of the path integral formulation. The SM achieves anomaly cancellation in a highly non-trivial way, with each generation of fermions contributing precisely what is needed to ensure the vanishing of all gauge and mixed anomalies. This remarkable feature has implications beyond internal consistency: it constrains how we can extend the theory, which particles may be added, and which quantum numbers they may carry. VLF offer an elegant path to BSM physics that avoids the complications of anomaly cancellation, while global anomalies - such as the Witten anomaly in $SU(2)$ - impose more subtle, topological constraints. Furthermore, anomaly matching conditions and anomaly inflow arguments play a crucial role in understanding strongly coupled dynamics and UV completions. Taken together, anomalies form a powerful theoretical toolset. They illuminate the deep structure of QFT, link global and local symmetries, and tightly constrain the space of possible extensions to the SM.

2.1.5 Lepton Flavor Universality and anomalies in B decays

A key prediction of the SM is the universality of lepton couplings to gauge bosons. This principle, known as *Lepton Flavor Universality* (LFU), asserts that – apart from differences due to lepton masses – all charged leptons should interact identically with the weak and electromagnetic interactions. LFU can be tested in flavor physics by measuring ratios of decay rates involving different lepton flavors, especially in semileptonic B decays. Over the past decade, several such measurements have shown deviations from SM expectations, prompting significant interest in the possibility of new physics.

One of the most discussed LFU tests involves the neutral-current decays $b \to s\ell^+\ell^-$, where $\ell = e, \mu$. In the SM, the decay rates to electrons and muons are predicted to be nearly equal, up to tiny mass corrections. This can be tested by measuring the ratios:

$$R_K = \frac{\mathcal{B}(B^+ \to K^+\mu^+\mu^-)}{\mathcal{B}(B^+ \to K^+e^+e^-)}, \qquad R_{K^*} = \frac{\mathcal{B}(B^0 \to K^{*0}\mu^+\mu^-)}{\mathcal{B}(B^0 \to K^{*0}e^+e^-)}, \tag{2.36}$$

where $\mathcal{B}$ denotes the branching ratio. The SM predicts $R_K \approx R_{K^*} \approx 1$ with high precision in the low dilepton invariant mass region.
In 2014 and 2017, the LHCb Collaboration reported measurements indicating $R_K < 1$ and $R_{K^*} < 1$, with deviations from the SM at the level of 2.5σ–3.0σ [15, 16]. These anomalies sparked a wave of theoretical activity proposing new physics scenarios, including Z' bosons, leptoquarks, and effective operators violating LFU.

The situation changed significantly with LHCb's updated analysis in 2022, based on the full Run 1 and 2 datasets [17]. The revised measurements were:

$$R_K = 0.994^{+0.074}_{-0.063}, \qquad R_{K^*} = 0.927^{+0.093}_{-0.087}, \tag{2.37}$$

both consistent with the SM within 1σ uncertainties. These results have substantially weakened the earlier hints of LFU violation in $b \to s\ell^+\ell^-$ transitions. Global fits to EFT operators now find no significant preference for LFU-violating new physics in these modes [18, 19].

While earlier tensions in R_K and R_{K^*} played a central role in motivating new physics models, the most recent results suggest that these anomalies may have been statistical fluctuations or affected by underestimated hadronic uncertainties. Nevertheless, LFU remains a powerful probe of BSM physics, and upcoming measurements from LHCb's Run 3 and Belle II are expected to further clarify the situation.

2.1.6 The SM as an effective field theory

While the SM has proven extraordinarily successful in describing a wide range of particle interactions, it is widely regarded as an EFT: a low-energy approximation of a more complete theory valid at higher energy scales. This perspective is supported by both theoretical and phenomenological considerations, including the absence of gravitational interactions, the hierarchy problem, neutrino masses, and dark matter.
In EFT language, the SM captures the relevant degrees of freedom and symmetries up to a cutoff scale Λ, beyond which new physics is expected to emerge. Below that scale, any heavy particles or interactions can be "integrated out," and their effects encoded through higher-dimensional operators composed of SM fields. These operators are suppressed by powers of $1/\Lambda$, making their impact most noticeable in high-precision or high-energy experiments:

$$\mathcal{L}_{\text{eff}} = \mathcal{L}_{\text{SM}} + \sum_i \frac{C_i^{(5)}}{\Lambda}\mathcal{O}_i^{(5)} + \sum_i \frac{C_i^{(6)}}{\Lambda^2}\mathcal{O}_i^{(6)} + \cdots . \tag{2.38}$$

This extended Lagrangian is known as the *Standard Model Effective Field Theory* (SMEFT) [20, 21]. The first correction beyond the renormalizable SM terms appears at dimension five, with the unique *Weinberg operator*:

$$\mathcal{O}_5 = (\bar{l}_L^c \cdot \tilde{\phi})(\tilde{\phi}^T \cdot l_L), \tag{2.39}$$

which generates Majorana masses for neutrinos upon electroweak symmetry breaking. At dimension six, a much larger set of operators arises, many of which can contribute to Higgs couplings, electroweak observables, or flavor-changing processes.
Since the EFT formalism will be used in chapter 5, it is important to comment on how SMEFT offers a powerful and gauge-invariant way to:

- Parameterize generic deviations from SM predictions.
- Quantify the indirect impact of BSM physics without committing to a specific UV model.
- Connect observables across different energy regimes through renormalization group running and matching.

From a model-building perspective, the SMEFT acts as a common language: once a concrete BSM model is proposed (e.g., one with heavy VLF, extended Higgs sectors, or extra gauge bosons), it can be matched onto SMEFT operators. These in turn can be constrained by experimental data, particularly from precision tests and rare processes. Even in the absence of observed new particles, tight limits on the Wilson coefficients $C_i^{(d)}$ provide valuable information on the possible structure and energy scale of BSM physics.

In summary, viewing the SM as an EFT underscores its provisional status in the hierarchy of physical theories. It also motivates the use of EFT techniques, such as SMEFT, as a bridge between well-measured low-energy observables and speculative high-energy extensions of the SM.

2.2 Renormalization Group

The RG is a central framework in QFT that captures how the parameters of a theory – such as coupling constants, masses, and wavefunction normalizations – evolve with the energy scale at which physical processes are probed. This scale dependence arises because quantum fluctuations at different momentum scales contribute differently to physical observables, and regularization techniques (such as dimensional regularization) introduce an auxiliary energy scale μ to handle UV divergences. While physical observables must remain independent of μ, the individual terms in the Lagrangian typically acquire explicit μ-dependence after renormalization. This leads to the concept of running couplings, whose scale dependence is governed by differential equations called the renormalization group equations (RGEs). For a generic coupling $g(\mu)$, we define the β-function:

$$\mu \frac{dg}{d\mu} = \beta(g), \tag{2.40}$$

which encodes how g evolves under changes in the renormalization scale. The sign and magnitude of $\beta(g)$ determine whether the coupling grows, decreases, or flows toward a fixed value in the UV or infrared.
From a practical perspective, the RG allows for the resummation of logarithmic divergences in perturbative expansions and helps to improve the convergence of perturbation theory (PT) in processes involving widely separated energy scales. More fundamentally, it provides a window into the underlying structure of quantum field theories, exposing deep insights into universality, critical behavior, and the emergence of effective field theories at different scales.

To better understand how scale dependence enters physical predictions, it is useful to first review how perturbative calculations are organized in QFT. In particular, we are interested in how loop corrections modify bare parameters and how renormalization reabsorbs infinities into redefinitions of the couplings. This will allow us to identify the origin of the scale dependence and introduce the machinery required to compute β-functions.
After this general discussion, we will apply these ideas to a simple but illustrative case: a real scalar field theory with quartic self-interaction, commonly referred to as ϕ^4 theory. This model is perturbatively renormalizable in four spacetime dimensions and serves as a pedagogical example for studying the running of couplings. By computing the one-loop correction to the four-point function, we will extract the β-function for the quartic coupling λ, observe its logarithmic running, and highlight the appearance of a Landau pole – a hallmark of triviality in the UV.
Such behavior contrasts with other field theories, like non-Abelian gauge theories, where the β-function can be negative, leading to *asymptotic freedom*: the coupling vanishes logarithmically at high energies, allowing the theory to remain perturbative in the UV. These distinctions motivate a broader classification of RG behavior based on the structure of fixed points, which we will revisit in the context of non-perturbative RG flows later in this chapter and in more detail in Chapter 4.
In this way, the RG not only offers a computational tool for handling divergences, but also provides deep insight into the structure of QFTs across energy scales. It is a cornerstone in constructing effective field theories, understanding phase transitions, and exploring the viability of models as fundamental or effective descriptions of nature.

2.2.1 Perturbation Theory

The modern formulation of QFT is based on the path integral, in which physical observables are computed as weighted averages over all possible field configurations. For a scalar field theory, for instance, the generating functional is given by

$$Z[J] = \int \mathcal{D}\phi\, e^{i\int d^4x(\mathcal{L}[\phi]+J(x)\phi(x))}, \tag{2.41}$$

where $\mathcal{L}[\phi]$ is the Lagrangian density of the theory and $J(x)$ is an external source used to generate correlation functions. In principle, all correlation functions and scattering amplitudes can be derived from this functional by taking functional derivatives with respect to $J(x)$.
However, except for free (non-interacting) theories, the path integral cannot be computed exactly. To make progress, we typically split the Lagrangian into a solvable quadratic (free) part and a small interaction term:

$$\mathcal{L}[\phi] = \mathcal{L}_0[\phi] + \mathcal{L}_{\text{int}}[\phi], \tag{2.42}$$

and expand the path integral perturbatively as a series in the interaction Lagrangian:

$$Z[J] = \int \mathcal{D}\phi\, e^{iS_0[\phi]} \left(1 + i\int d^4x\, \mathcal{L}_{\text{int}} + \frac{(i)^2}{2!}\left(\int d^4x\, \mathcal{L}_{\text{int}}\right)^2 + \cdots\right) e^{i\int d^4x\, J(x)\phi(x)}, \tag{2.43}$$

where $S_0[\phi]$ is the action associated to the free Lagrangian, $\mathcal{L}_0[\phi]$. This is the essence of PT: an expansion in powers of the coupling constant(s), where each term corresponds to increasingly complex interactions.

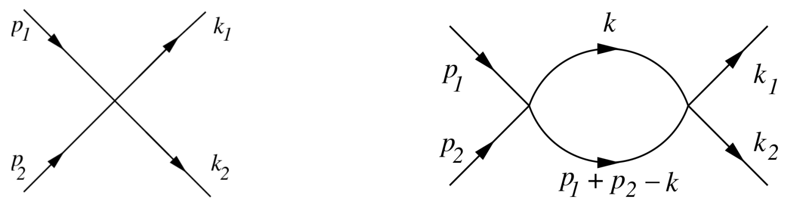

(A) Tree-level diagram (B) One-loop diagram

FIGURE 2.2: Examples of a tree-level diagram (a) and a one-loop correction (b) in a generic QFT. Loop diagrams account for quantum fluctuations and typically lead to divergent integrals.

Applying Wick's theorem to this expansion yields the Feynman rules of the theory, with each term corresponding to a specific Feynman diagram. These diagrams are a convenient way to organize the terms in the expansion and to compute physical quantities. The diagrams with no closed loops, known as *tree-level* diagrams, represent the leading-order contributions and correspond directly to classical processes, *cf.* Figure 2.2(a). Quantum effects enter through diagrams containing closed loops, which arise at higher orders in the expansion and encode the effects of virtual particles and quantum fluctuations, *cf.* Figure 2.2(b). These *loop diagrams* give rise to corrections to masses, couplings, and scattering amplitudes, and are responsible for phenomena such as running couplings and anomalous dimensions.

Loop integrals are often divergent and must be regularized and renormalized. In this process, infinities are absorbed into redefinitions of physical parameters, such as masses and coupling constants, resulting in finite, physically meaningful predictions. The appearance of divergences is not a flaw but a reflection of the scale-dependent nature of quantum field theories, which is precisely what the renormalization group formalism addresses.
Despite its predictive power, PT has fundamental limitations. It is fundamentally an expansion around the non-interacting theory and is valid only when the coupling constants are small. In many important physical contexts, however, this condition breaks down. For instance:

- In QCD, the strong coupling becomes large at low energies, rendering perturbative methods ineffective in the infrared.
- Critical phenomena near phase transitions involve divergent correlation lengths and require resummation or non-perturbative techniques.
- Certain UV completions of the Standard Model may feature non-trivial fixed points or strong dynamics that cannot be captured within a perturbative framework.

Moreover, PT often fails to capture non-analytic phenomena, such as confinement, instantons, or tunneling effects, which are inherently non-perturbative. These limitations motivate the search for alternative methods capable of probing the structure of quantum field theories beyond the perturbative regime. We will talk more in details about this in section 2.2.4.

In the next section, we illustrate how PT is used to compute scale dependence in a simple model – the ϕ^4 scalar theory – and derive the associated renormalization group equations. This concrete example sets the stage for a broader discussion on the energy dependence of couplings, and it later serves as a benchmark for comparing perturbative and non-perturbative approaches.

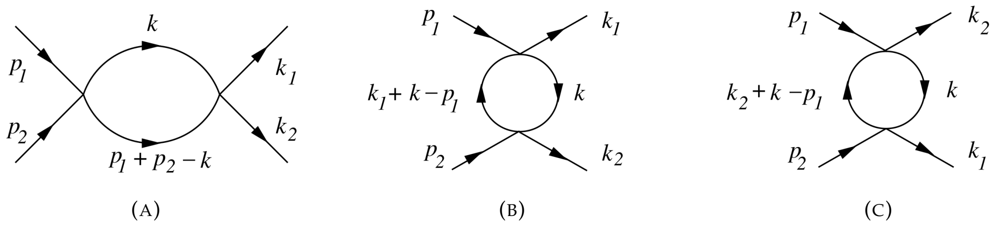

FIGURE 2.3: One-loop corrections to the four-point function in ϕ^4 theory. The three Feynman diagrams correspond to the s-, t-, and u-channel contributions, from left to right. Each diagram involves a loop with two internal propagators, representing the quantum corrections that contribute to the running of the quartic coupling λ.

2.2.2 An example: the scalar theory at 1-Loop

Having introduced the principles and limitations of PT, we now turn to a concrete example that illustrates how quantum corrections are computed and how they affect the scale dependence of physical parameters. A paradigmatic case is the real scalar field theory with a quartic self-interaction – often referred to as ϕ^4 theory – which provides a minimal yet instructive setup to explore renormalization and the RG equations in action.
We consider a real scalar field theory in four spacetime dimensions with the following Lagrangian:

$$\mathcal{L} = \frac{1}{2}(\partial_\mu \phi)^2 - \frac{1}{2}m^2\phi^2 - \frac{\lambda}{4!}\phi^4, \tag{2.44}$$

where λ is the dimensionless coupling constant. This theory is renormalizable and provides a simple context in which to understand scale dependence and running couplings.

The running of the coupling λ can be derived from the 1-loop corrections to the 4-point function. At one loop, three diagrams contribute - the s-, t-, and u-channel "fish" diagrams, as shown in figure 2.3.
Each diagram represents a one-loop correction with two internal propagators forming a loop and external legs connected according to the Mandelstam channels. All three diagrams yield the same divergence structure due to crossing symmetry.
Let us compute the amplitude of one of these diagrams (say, the s-channel) to extract the divergent part. The relevant expression in dimensional regularization (in $d = 4 - \varepsilon$) is:

$$\mathcal{A}_s^{(1)} = -i\frac{\lambda^2}{2}\int \frac{d^d k}{(2\pi)^d}\frac{1}{(k^2 - m^2)[(k+p)^2 - m^2]}, \tag{2.45}$$

where the factor of $1/2$ accounts for identical particles in the loop. This integral yields a logarithmic divergence in $d = 4$, and the divergent part evaluates to:

$$\mathcal{A}_s^{(1)}\Big|_{\text{div}} = -i\frac{\lambda^2}{32\pi^2}\left(\frac{2}{\varepsilon} + \text{finite}\right). \tag{2.46}$$

Including the t- and u-channel diagrams gives a total divergent contribution:

$$\mathcal{A}_{\text{total}}^{(1)} = -i\frac{3\lambda^2}{32\pi^2}\left(\frac{2}{\varepsilon} + \text{finite}\right). \tag{2.47}$$

To cancel the divergence, a counterterm $\delta\lambda$ is introduced in the renormalized Lagrangian:

$$\lambda_0 = \mu^{\varepsilon} \left(\lambda + \delta\lambda \right), \tag{2.48}$$

where μ is the renormalization scale introduced to keep λ dimensionless in $d \neq 4$. In the $\overline{\text{MS}}$ scheme, the counterterm absorbs only the pole part:

$$\delta\lambda = -\frac{3\lambda^2}{16\pi^2\varepsilon}. \tag{2.49}$$

The RGE for the running coupling follows from the requirement that the bare coupling λ_0 is independent of μ:

$$\mu\frac{d\lambda_0}{d\mu} = 0 \quad \Rightarrow \quad \mu\frac{d\lambda}{d\mu} = \beta(\lambda), \tag{2.50}$$

with

$$\beta(\lambda) = \mu\frac{d\lambda}{d\mu} = \frac{3\lambda^2}{16\pi^2} + \mathcal{O}(\lambda^3). \tag{2.51}$$

This positive β function implies that the quartic coupling λ increases with energy. Solving the RG equation yields

$$\lambda(\mu) = \frac{\lambda(\mu_0)}{1 - \frac{3\lambda(\mu_0)}{16\pi^2}\log\left(\frac{\mu}{\mu_0}\right)}, \tag{2.52}$$

where the boundary condition $\lambda(\mu_0)$ signifies that we must be provided – for example through an experiment – with the value of the coupling constant at the energy scale μ_0 to be able to predict its value at any energy scale. As the energy scale μ increases, the denominator eventually vanishes at a finite value:

$$\mu_{\text{LP}} \equiv \mu_0 \exp\left(\frac{16\pi^2}{3\lambda(\mu_0)}\right), \tag{2.53}$$

signaling a breakdown of the perturbative description - the so-called *Landau pole*. This phenomenon suggests that the theory becomes strongly coupled and non-predictive at high energies, unless new physics intervenes before reaching μ_{LP}. In fact, in the limit $\mu_{\text{LP}} \to \infty$, the only way to keep $\lambda(\mu)$ finite at all scales is to set $\lambda(\mu_0) \to 0$. This indicates that the interacting theory becomes trivial in the UV - a behavior known as triviality. For this reason, ϕ^4 theory in $d = 4$ is often regarded as an EFT valid only up to a finite cutoff.

2.2.3 Renormalization of the SM at 1-loop

The scale dependence of the SM coupling constants, governed by the renormalization group, is one of the central predictive tools of QFT. Unlike the scalar ϕ^4 theory, in which the coupling diverges in the UV, the SM contains gauge interactions with qualitatively different behavior. Let us recall that the gauge sector of the SM consists of three coupling constants: g_Y, g_2, and g_3, corresponding respectively to the gauge groups $U(1)_Y$, $SU(2)_L$, and $SU(3)_c$. The renormalization group equations for these couplings are:

$$\mu\frac{dg_i}{d\mu} = \beta_i(g_i) = \frac{b_i}{(4\pi)^2}g_i^3 + \mathcal{O}(g_i^5), \tag{2.54}$$

where the b_i are constants determined by the particle content of the theory and the group representations under which the fields transform. In the SM, the one-loop coefficients are

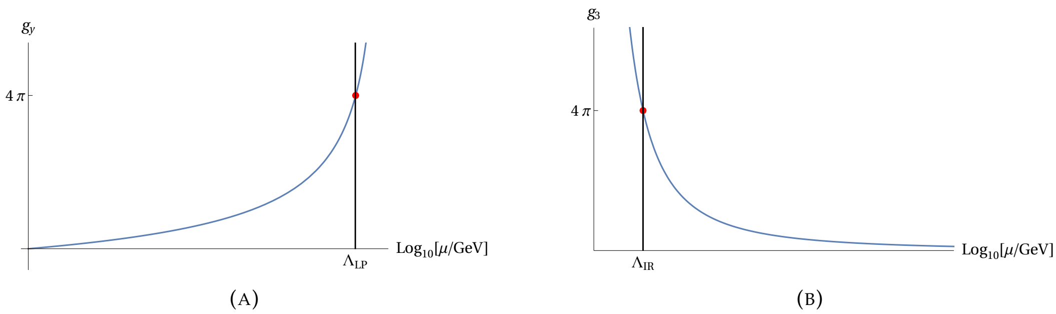

FIGURE 2.4: The asymptotic behavior of the hypercharge (on the left) and the color (on the right) gauge couplings of the SM. The hypercharge coupling goes to zero in the low energy limit, and has a Landau pole at high energy. The color gauge coupling has the opposite behavior: it goes to zero in the high energy limit, which is what is called *asymptotic freedom* and and grows large in the infrared. This strong coupling regime is associated with *confinement* and non-perturbative QCD dynamics.

given by:

$$b_Y = \frac{41}{6}, \qquad b_2 = -\frac{19}{6}, \qquad b_3 = -7. \tag{2.55}$$

The positive sign of b_Y indicates that the hypercharge coupling g_Y increases with energy - analogous to the Landau pole behavior seen in ϕ^4 theory. In contrast, the negative values of b_2 and b_3 imply that the $SU(2)_L$ and $SU(3)_c$ couplings decrease at high energies, a feature known as *asymptotic freedom*.

The running of these couplings can be plotted as a function of the energy scale μ, starting from their experimentally determined values at low energy (e.g. at the Z-boson mass scale, $\mu = M_Z$). At one-loop level, the solutions take the form:

$$\alpha_i^{-1}(\mu) = \alpha_i^{-1}(\mu_0) - \frac{b_i}{2\pi} \log\left(\frac{\mu}{\mu_0}\right), \tag{2.56}$$

with $\alpha_i = g_i^2/(4\pi)$. These expressions reveal that the couplings evolve logarithmically with energy. A schematic example of the running of g_Y and g_3 is shown in figure 2.4.

In what follows, we discuss three important consequences of SM renormalization group flow: asymptotic freedom in QCD, the possibility of gauge coupling unification, and the implications for Higgs vacuum stability.

Asymptotic freedom.

The phenomenon of asymptotic freedom is a defining feature of non-Abelian gauge theories, most notably QCD. It refers to the property that the gauge coupling becomes weaker at higher energies, implying that quarks and gluons interact more weakly when probed at short distances. This behavior was first discovered in 1973 by Gross and Wilczek [22] and Politzer [23], earning them the Nobel Prize in Physics in 2004.
Mathematically, asymptotic freedom arises from the structure of the one-loop β function in a non-Abelian Yang-Mills theory with n_f fermions:

$$\beta(g) = -\frac{g^3}{(4\pi)^2}\left(\frac{11}{3}C_2(G) - \frac{4}{3}T(R)n_f\right), \tag{2.57}$$

where $C_2(G)$ is the quadratic Casimir of the adjoint representation, $T(R)$ is the trace normalization of the fermion representation, and n_f is the number of active flavors at a given scale. For QCD, $C_2(G) = N = 3$, and $T(R) = 1/2$ for fundamental quarks, leading to

$$\beta_{g_3} = -\frac{g_3^3}{(4\pi)^2}\left(11 - \frac{2}{3}n_f\right). \tag{2.58}$$

As long as $n_f < 16.5$, the coefficient of the beta function remains positive, and the strong coupling g_3 decreases logarithmically with increasing energy - the hallmark of asymptotic freedom. This UV behavior justifies the use of PT at high energies, as is done in the analysis of hard scattering processes at colliders like the LHC. Conversely, in the infrared (low-energy) regime, the coupling grows large, and non-perturbative phenomena like confinement and chiral symmetry breaking dominate. Importantly, asymptotic freedom is not a generic feature of all gauge theories. Abelian gauge theories like QED, whose one-loop β function is positive, exhibit Landau pole behavior instead. The contrast between QED and QCD underscores the essential role of the non-Abelian gauge structure in enabling asymptotic freedom – a feature intimately tied to the self-interactions of the gauge bosons.

Gauge coupling unification.

A striking consequence of the renormalization group flow in the SM is the logarithmic running of the three gauge couplings associated with the $U(1)_Y$, $SU(2)_L$, and $SU(3)_c$ gauge groups. When extrapolated to high energies using the RGEs, these couplings approach one another, although they do not meet exactly at a single point. This near-convergence suggests the tantalizing possibility that the SM gauge interactions might be unified into a single gauge symmetry at very high energy - an idea that forms the foundation of *Grand Unified Theories*.

The basic premise of a GUT is that the three SM gauge groups are embedded into a larger simple group, such as $SU(5)$ [24], $SO(10)$ [25], or E_6 [26]. At some high unification scale μ_{GUT}, these groups break spontaneously to the SM gauge group. Above this scale, a single unified gauge coupling governs all gauge interactions, and the distinct SM couplings arise from symmetry breaking and threshold corrections at μ_{GUT}.
In the minimal (non-supersymmetric) SM, the couplings come close but fail to unify precisely when evolved using the one-loop RGEs. This mismatch can be attributed to the specific matter content of the SM, which determines the β function coefficients and hence the relative slopes of the running couplings. The discrepancy becomes apparent when plotting $g_Y(\mu)$, $g_2(\mu)$, and $g_3(\mu)$ as functions of $\log\mu$, as shown in figure 2.5: while they approach each other around 10^{14} GeV, they do not meet at a single point.
This near-miss motivates the extension of the SM to include additional matter content that modifies the RG running. A well-known example is the *Minimal Supersymmetric Standard Model* (MSSM), in which the presence of superpartners significantly alters the β function coefficients above the supersymmetry breaking scale. Remarkably, in the MSSM, the three gauge couplings do unify at a common scale $\mu_{\mathrm{GUT}} \sim 2\times10^{16}$ GeV, consistent with proton decay bounds and gauge-mediated neutrino mass generation [27, 28]. This observation is often cited as one of the key indirect motivations for low-energy supersymmetry.

Gauge unification is not merely aesthetically appealing; it offers predictive power. GUTs often relate fermion masses and mixing angles, explain charge quantization, and predict

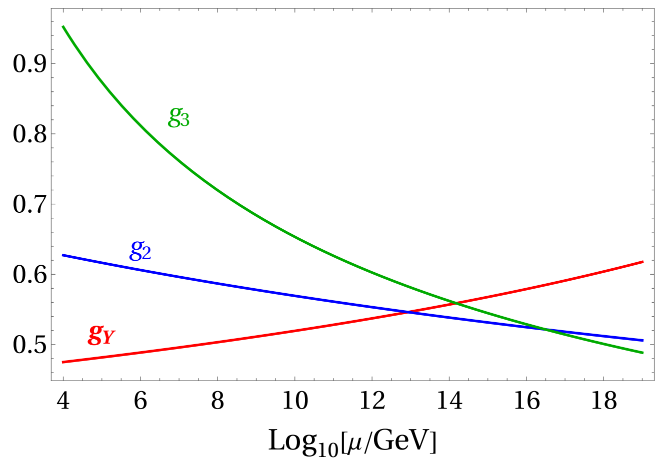

FIGURE 2.5: The running of the gauge couplings of the SM across many scales. Notice how at approximately $\sim 10^{14}$ GeV the three gauge couplings approach a common value, though they do not exactly unify.

baryon number violating processes such as proton decay. These features impose phenomenological constraints and connect high-scale physics to observable low-energy effects. Nonetheless, GUTs also face challenges. The precise value of the unification scale must be compatible with current limits on proton lifetime, and the breaking of the unified group must avoid problematic remnants like monopoles or excessive flavor violation. Moreover, threshold effects from unknown heavy states at the GUT scale can influence the apparent unification point, introducing model dependence into the interpretation of coupling unification.

In summary, the approximate convergence of the SM gauge couplings at high energies is a powerful hint toward unification and a guiding principle for model-building beyond the SM. Whether unification is realized in nature remains an open question, but the renormalization group flow offers a crucial window into this deep structural possibility.

Vacuum stability and the running Higgs quartic.

The renormalization group flow of the Higgs self-coupling λ plays a pivotal role in determining the fate of the electroweak vacuum at high energies. While the vev of the Higgs field sets the scale of electroweak symmetry breaking, the potential's shape at large field values is controlled by $\lambda(\mu)$, whose evolution is highly sensitive to both the top Yukawa coupling and the gauge sector. At tree level, the Higgs potential is given by

$$V(H) = -\mu^2 H^\dagger H + \lambda (H^\dagger H)^2, \tag{2.59}$$

with $\lambda > 0$ ensuring a stable vacuum at low energies. However, quantum corrections modify the effective potential at large field values, and the RG-improved potential can develop an instability if $\lambda(\mu)$ turns negative at some high scale $\mu > v$, where $v \simeq 246\,\mathrm{GeV}$ is the electroweak scale.

The one-loop β function for λ, includes contributions from self-interactions, gauge boson loops, and the top quark Yukawa coupling. The latter dominates due to the large value of y_t, and tends to drive λ downward:

$$\beta_\lambda^{(1)} = \frac{1}{(4\pi)^2}\left[24\lambda^2 - 6y_t^4 + \frac{3}{8}\left(2g_2^4 + (g_2^2+g_Y^2)^2\right) - 3\lambda\left(3g_2^2 + g_Y^2 - 4y_t^2\right)\right]. \tag{2.60}$$

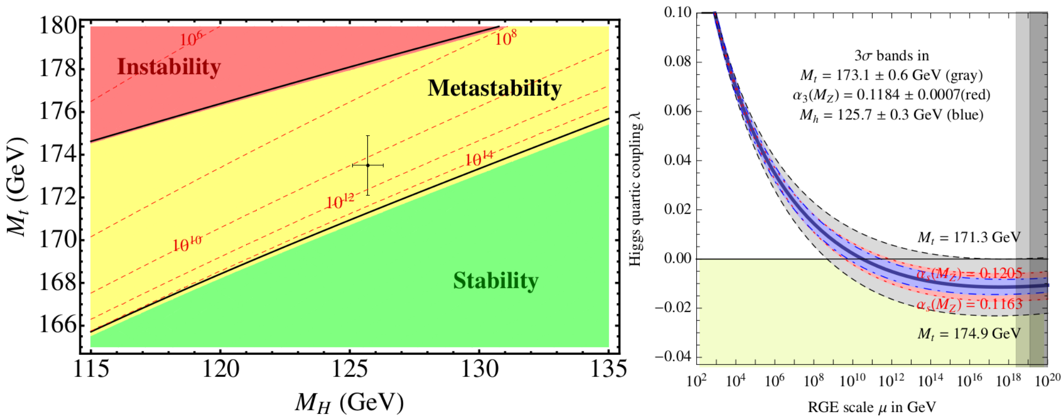

FIGURE 2.6: (Left) Stability phase diagram of the SM, derived from the running of the effective Higgs quartic coupling. The red region corresponds to an unstable vacuum, the yellow to a metastable one, and the green to absolute stability. The point with error bars represents the current experimental values of the top quark and Higgs boson masses. Red dashed contours indicate the energy scale (in GeV) at which the Higgs quartic coupling λ crosses zero. Figure adapted from Ref. [30]. (Right) Renormalization group evolution of the Higgs quartic coupling in the SM. The plot shows the scale dependence of λ based on current input parameters. Figure taken from Ref. [29].

Higher-loop corrections are also important and are known up to three loops in the $\overline{\text{MS}}$ scheme [29, 30].

Numerical studies incorporating the measured values of the Higgs mass $m_H \approx 125.1\,\text{GeV}$ [31] and the top mass $m_t \approx 173\,\text{GeV}$ show that $\lambda(\mu)$ decreases with energy and becomes negative at a scale around 10^{10}-10^{11} GeV, depending sensitively on m_t and α_s. This implies that the electroweak vacuum is not the global minimum of the effective potential, but rather a metastable local minimum. The stability of the Higgs potential is shown in figure 2.6.

In a metastable scenario, the lifetime of the vacuum is longer than the age of the Universe, and there is no immediate inconsistency with observations. The probability of quantum tunneling to the true vacuum is exponentially suppressed by the bounce action associated with the Higgs potential barrier. The current best-fit values place the SM in a narrow region of parameter space where vacuum decay is possible in principle, but extremely unlikely in practice. This result is highly nontrivial: the fact that the Higgs mass lies near the boundary between absolute stability and metastability may point toward some deeper principle or fine-tuning in the early Universe. Various BSM scenarios, including scalar extensions, supersymmetry, and seesaw models for neutrino masses, can shift the running of λ and restore vacuum stability.

The vacuum stability analysis highlights the extraordinary reach of the RG: it allows us to extrapolate from electroweak scale measurements to make meaningful statements about field configurations at energies near the Planck scale. Whether the SM remains consistent up to such scales or requires new physics for vacuum stability is still an open question - but one where RG methods provide the essential diagnostic.

Running of the Yukawa couplings

In addition to the gauge and scalar sectors, the SM contains Yukawa interactions that give rise to fermion masses after electroweak symmetry breaking. These couplings, which encode the interaction strength between fermions and the Higgs field, also evolve with energy scale under the renormalization group. Among them, the top quark Yukawa coupling y_t is the dominant one due to the large mass of the top quark, and it plays a central role in the renormalization group flow of the Higgs quartic coupling and the vacuum stability of the SM. At one-loop level, the renormalization group equation for the top Yukawa coupling is given by:

$$\beta_{y_t}^{(1)} = \mu \frac{dy_t}{d\mu} = \frac{y_t}{(4\pi)^2}\left(\frac{9}{2}y_t^2 - \frac{17}{12}g_Y^2 - \frac{9}{4}g_2^2 - 8g_3^2\right). \tag{2.61}$$

This equation reflects the competing effects of different interactions: the self-enhancing contribution from the Yukawa term y_t^3, and the screening effects from gauge boson loops.
Numerical integration of the RGE shows that, in the SM, the top Yukawa coupling decreases with energy and approaches zero asymptotically – a behavior reminiscent of asymptotic freedom. This occurs because the negative contributions from the gauge couplings dominate the running at high scales, particularly from QCD (the term proportional to g_3^2). Hence, the Yukawa sector is asymptotically free in the SM. This behavior has several consequences. First, it implies that the Yukawa interactions become negligible at very high energies, effectively decoupling from the dynamics. Second, it ensures that the theory remains perturbative up to the Planck scale in the Yukawa sector, as long as the initial value of y_t is not too large. This is consistent with the measured top quark mass, which places $y_t \sim 0.93$ at the electroweak scale.

In contrast to scalar ϕ^4 theory, which exhibits a Landau pole and becomes strongly coupled in the UV, the Yukawa sector of the SM remains well-behaved. This suggests that the fermionic sector, unlike the scalar one, does not require a UV completion from the perspective of perturbative consistency. The running of y_t is critical for determining the behavior of the Higgs quartic coupling $\lambda(\mu)$, especially because the y_t^4 term appears with a negative sign in β_λ, *cf.* equation 2.60, tending to drive λ toward negative values at high scales. This sensitivity makes precise determinations of the top mass, m_t, and the strong coupling constant, α_3, vital for vacuum stability analyses.

Although lighter fermion Yukawa couplings are much smaller and their contributions to RG flow are negligible in practice, they do run as well. For a general Dirac fermion with Yukawa coupling y_f, the one-loop β function is:

$$\beta_{y_f}^{(1)} = \mu \frac{dy_f}{d\mu} = \frac{y_f}{(4\pi)^2}\left(\frac{3}{2}y_f^2 - C_f\right), \tag{2.62}$$

where C_f is a positive coefficient that depends on the gauge quantum numbers of the fermion. As in the top quark case, this leads to a decrease of the Yukawa coupling at higher energies, though the effect is numerically negligible for the first and second generation fermions.
In extensions of the SM, such as supersymmetric models or theories with extended scalar sectors, the structure and running of Yukawa couplings can be drastically different, sometimes even playing a role in flavor symmetry breaking or radiative mass generation. However, even within the SM, the top Yukawa coupling stands out as a key parameter that bridges the electroweak and UV dynamics.

2.2.4 When perturbation theory fails

As discussed in Section 2.2.1, PT is a central computational tool in QFT, built upon expanding the path integral around a solvable free theory. This expansion yields a series of Feynman diagrams ordered by loop number, with tree-level diagrams corresponding to classical processes and loop diagrams encoding quantum corrections. The success of this method is evident in countless applications across particle physics, including the precision predictions of electroweak observables and high-energy collider processes within the SM. However, the utility of PT is fundamentally limited to regimes where the expansion parameter – the coupling constant – remains small. In Section 2.2.2, we illustrated how even a simple theory such as ϕ^4 scalar field theory reveals the shortcomings of PT in the UV: the one-loop beta function for the quartic coupling is positive, leading to a Landau pole at a finite scale. This signals a breakdown of the theory and suggests that ϕ^4 theory must be treated as an effective theory, valid only below some physical cutoff. Similar concerns arise in the SM, as discussed in Section 2.2.3, where the hypercharge coupling g_Y exhibits a Landau pole, and the Higgs quartic coupling λ may run negative at high energies, jeopardizing vacuum stability.

These examples already hint at the intrinsic limits of perturbative reasoning. In QCD, for instance, the strong coupling g_3 becomes large in the infrared – a fact reflected in its negative beta function and the phenomenon of asymptotic freedom. While this behavior justifies PT at high energies, it renders it ineffective at low energies, where confinement, chiral symmetry breaking, and hadron formation dominate. These are quintessentially non-perturbative effects that cannot be accessed by any finite-order expansion. Moreover, PT systematically misses non-analytic phenomena such as instantons, solitons, and tunneling transitions. These contribute to amplitudes with weights like e^{-1/g^2}, which vanish in the perturbative limit and are thus invisible to the series expansion. They play an essential role in contexts ranging from anomaly matching and symmetry breaking to the baryon asymmetry of the Universe. As such, a complete understanding of QFT – especially in strongly coupled regimes or at high scales – demands tools that go beyond PT.

Several non-perturbative approaches have been developed to fill this gap. Lattice field theory, for example, provides a rigorous formulation of QFT in Euclidean space and allows for ab initio numerical simulations, though it faces limitations in treating real-time dynamics, chiral fermions, or gauge-fixed frameworks. Schwinger-Dyson equations offer a continuum approach based on exact integral relations among Green's functions, but rely on truncation schemes that are difficult to systematically improve.
A particularly powerful and flexible method is the FRG, which generalizes the ideas introduced in Section 2.2 and reformulates the RG flow in terms of an exact functional differential equation. Unlike traditional perturbative approaches, the FRG tracks the evolution of the effective action itself across momentum scales and does not assume small couplings. This makes it ideally suited for exploring non-perturbative phenomena, characterizing fixed points, and constructing UV completions of quantum field theories.

In Chapter 4, we will employ the FRG to study the high-energy behavior of gauge-Yukawa theories with VLF, including the existence of non-trivial fixed points that render these models asymptotically safe. Before delving into those applications, we now provide a dedicated introduction to the FRG formalism, outlining its conceptual basis and its relevance to modern QFT.

2.2.5 Functional Renormalization Group

As highlighted in the previous discussion, perturbative techniques are limited in their ability to capture strongly coupled phenomena or resum contributions beyond finite-loop order. To overcome these limitations, non-perturbative frameworks are required. One of the most versatile among them is the FRG, which extends the Wilsonian renormalization group to the level of the quantum effective action [32, 33].

At the heart of the FRG is the concept of the *Effective Average Action* (EAA), denoted $\Gamma_k[\phi]$, which describes the dynamics of quantum fields as a function of a sliding infrared (IR) scale k. As k decreases from some UV scale toward zero, quantum fluctuations are integrated out progressively. This construction provides an interpolation between the bare (classical) action S at high energies and the full quantum effective action $\Gamma[\phi]$ at low energies:

$$\lim_{k\to\infty}\Gamma_k[\phi] = S[\phi], \qquad \lim_{k\to 0}\Gamma_k[\phi] = \Gamma[\phi]. \tag{2.63}$$

To achieve this scale separation, one modifies the standard path integral by introducing a regulator function $R_k(p^2)$ that suppresses the contribution of low-momentum modes below the scale k. The modified partition function becomes:

$$Z_k[J] = \int \mathcal{D}\varphi\, e^{-S[\varphi]-\Delta S_k[\varphi]+\int d^dx\, J\varphi}, \tag{2.64}$$

where the regulator term $\Delta S_k[\varphi]$ takes the form:

$$\Delta S_k[\varphi] = \frac{1}{2}\int d^dx\, \varphi(x) R_k(-\partial^2)\varphi(x). \tag{2.65}$$

The regulator function R_k effectively provides a momentum-dependent mass to the fluctuations, ensuring that the flow is infrared finite. From $Z_k[J]$, the EAA is defined through a modified Legendre transform:

$$\Gamma_k[\phi] = \sup_J \left(\int d^dx\, J(x)\phi(x) - W_k[J]\right) - \Delta S_k[\phi], \tag{2.66}$$

where $W_k[J] = \log Z_k[J]$ is the generating functional of connected Green's functions, and $\phi = \langle\varphi\rangle$ denotes the classical field expectation value.
A key strength of the FRG approach is that it admits an exact functional differential equation describing the scale dependence of the EAA, the so-called Wetterich equation [32]:

$$\partial_t\Gamma_k[\phi] = \frac{1}{2}\mathrm{Tr}\left[\left(\Gamma_k^{(2)}[\phi] + R_k\right)^{-1}\partial_t R_k\right], \tag{2.67}$$

where $t = \log(k/k_0)$, and $\Gamma_k^{(2)}[\phi]$ denotes the second functional derivative of the EAA with respect to the fields:

$$\Gamma_k^{(2)}[\phi](x,y) = \frac{\delta^2\Gamma_k[\phi]}{\delta\phi(x)\delta\phi(y)}. \tag{2.68}$$

The flow equation (2.67) encodes all quantum corrections in a compact, one-loop exact form. This structure facilitates non-perturbative approximation schemes since all contributions from quantum fluctuations are manifestly organized by the scale parameter k. Crucially, despite its one-loop appearance, Eq. (2.67) is exact, incorporating all loops and interactions through the functional dependence of $\Gamma_k^{(2)}$.

Although the Wetterich equation is exact, solving it exactly is generally infeasible due to its infinite-dimensional nature. Practical implementations typically rely on systematic truncation schemes, which reduce the infinite space of possible actions to a finite-dimensional subspace. Common truncation methods include the derivative expansion, vertex expansion, and background field expansions. The derivative expansion, for instance, involves expanding Γ_k in terms of derivatives of the fields and truncating the expansion at a certain order. Vertex expansions, on the other hand, truncate the hierarchy of equations for correlation functions at a certain number of external legs. These methods have proven highly effective in various physical contexts.

One significant advantage of the EAA framework is its natural connection with perturbation theory. Consider the perturbative expansion of the EAA around a classical background ϕ:

$$\Gamma_k[\phi] = S[\phi] + \frac{1}{2}\mathrm{Tr}\log\left(\frac{\delta^2 S[\phi]}{\delta\phi\delta\phi} + R_k\right) + \dots \tag{2.69}$$

This expression resembles the standard one-loop effective action but now explicitly incorporates the regulator term R_k. Thus, perturbation theory emerges naturally when the scale-dependent functional integral is expanded around a saddle point.
Expanding further, one obtains a systematic loop expansion:

$$\Gamma_k[\phi] = S[\phi] + \frac{1}{2}\mathrm{Tr}\log\left(S^{(2)}[\phi] + R_k\right) - \frac{1}{12}\mathrm{Tr}\left[\left(S^{(2)}[\phi] + R_k\right)^{-1} S^{(3)}[\phi]\right]^2 + \dots \tag{2.70}$$

where the regulator R_k ensures that all integrals are IR-finite. Higher-loop corrections can be generated systematically, but the FRG also provides access to resummed or strongly coupled regimes that go beyond perturbative expansions.

As we will see in Chapter 4, the FRG plays a central role in studying QFTs with many couplings, fixed-point structures, and asymptotic safety scenarios. Its ability to bridge perturbative and non-perturbative physics makes it an essential tool in modern QFT.

2.3 The need for physics beyond the SM

Despite its remarkable predictive power and experimental success, the SM is widely regarded as an effective low-energy theory, valid only up to some high-energy cutoff. While it provides a consistent and accurate description of known particle interactions (excluding gravity), several empirical observations and theoretical limitations point compellingly toward the existence of new physics beyond its scope. Below we summarize the most pressing motivations for extending the SM.

The Hierarchy Problem

As discussed in details in section 2.1.3, one of the most significant theoretical challenges in the SM is the hierarchy problem, which concerns the stability of the electroweak scale against radiative corrections. The mass of the Higgs boson receives quadratically divergent contributions from quantum loops involving the top quark, electroweak gauge bosons, and the Higgs itself. These corrections scale as $\delta m_H^2 \sim \Lambda^2$, where Λ is the energy scale at which new physics enters. If Λ is taken to be close to the Planck scale ($M_{\text{Pl}} \sim 10^{19}$ GeV), an extreme fine-tuning of parameters is required to maintain the observed Higgs mass near 125 GeV. This tension suggests the need for a stabilizing mechanism. Proposed solutions include low-scale supersymmetry [34], composite Higgs models [35], and extra-dimensional scenarios [36], each introducing new degrees of freedom that soften or cancel the dangerous quadratic divergences.

Dark Matter

Multiple lines of astrophysical and cosmological evidence point to the existence of dark matter – a form of matter that interacts gravitationally but not (or extremely weakly) via electromagnetic or strong forces. Observations such as galactic rotation curves, gravitational lensing, the dynamics of galaxy clusters, and the Cosmic Microwave Background require a non-luminous, non-baryonic matter component that comprises roughly 27% of the Universe's energy density. The SM does not contain a viable dark matter candidate: neutrinos are too light and too hot to account for the observed structure formation. This motivates a rich array of BSM possibilities, including Weakly Interacting Massive Particles [37], axions [38, 39], and sterile neutrinos [40], each being actively explored through direct detection experiments, indirect astrophysical probes, and collider searches.

Dark Energy and the cosmological constant problem

The late-time accelerated expansion of the Universe, confirmed through Type Ia supernovae and precision cosmology, points to the presence of dark energy – a component with negative pressure comprising about 70% of the cosmic energy budget. In QFT, the simplest candidate is a cosmological constant, corresponding to vacuum energy. However, theoretical estimates of the vacuum energy density exceed the observed value by some 120 orders of magnitude, making this arguably the most severe fine-tuning problem in theoretical physics [41]. Resolving this mismatch likely requires input from a deeper framework, possibly involving new symmetries, dynamical adjustment mechanisms, or quantum gravity effects – none of which are incorporated in the SM.

Neutrino masses and mixing

Neutrino oscillation experiments have established that neutrinos have small but non-zero masses and undergo flavor mixing – phenomena that the minimal SM cannot accommodate, as it predicts massless neutrinos. Generating neutrino masses requires extending the SM in one of several ways: by introducing right-handed neutrinos and Dirac mass terms, or via Majorana masses through the seesaw mechanism [42–45]. These mechanisms not only explain the smallness of neutrino masses but also open the door to new physics scales and possible connections to baryogenesis via leptogenesis. Their experimental signatures include neutrinoless double beta decay and deviations in neutrino oscillation patterns – key probes of BSM physics.

Matter-antimatter asymmetry

The observed baryon asymmetry of the Universe, quantified by the baryon-to-photon ratio $\eta_B \sim 6 \times 10^{-10}$, remains unexplained within the SM. While the SM satisfies the three Sakharov conditions – baryon number violation, C and CP violation, and departure from thermal equilibrium – the amount of CP violation provided (mainly through the CKM phase) is insufficient by several orders of magnitude. This suggests the need for additional CP-violating phases and new dynamics beyond the SM. Prominent scenarios include electroweak baryogenesis [46] and leptogenesis [47], both of which require BSM ingredients such as new scalar sectors, heavy neutrinos, or extended Higgs structures.

Unification and Quantum Gravity

As already described in section 2.2.3, the SM does not provide a unified description of all interactions. While it successfully unifies the electromagnetic and weak forces, it fails to incorporate gravity and does not unify all three gauge couplings at a single energy scale. However, the running of the gauge couplings suggests a near unification around 10^{15}-10^{16} GeV, inspiring GUTs such as $SU(5)$, $SO(10)$, or E_6 [24, 25]. These frameworks predict new particles, such as leptoquarks and GUT-scale gauge bosons, and typically lead to testable phenomena like proton decay. A complete unification also requires a quantum theory of gravity. Candidates include string theory and loop quantum gravity, as well as newer approaches based on asymptotic safety, all of which provide avenues to embed the SM into a more fundamental UV-complete theory. In this thesis, the idea of asymptotic safety is going to be explored in details.

3

Phenomenological approach to VLF

This chapter marks the beginning of the original research contributions presented in this thesis. Adopting a phenomenological perspective, it investigates an extension of the SM that includes VLFs, focusing on their implications for low-energy observables and collider phenomenology. Particular attention is given to the muon anomalous magnetic moment, within a model that aims to address the mass generation mechanism for SM fermions through the dynamics of VLFs.

3.1 Global analysis and LHC study of a vector-like extension of the Standard Model with extra scalars

This chapter is based on "Global analysis and LHC study of a vectorlike extension of the standard model with extra scalars" by A. E. Carcamo Hernandez, K. Kowalska, H. Lee, D. Rizzo, [1].

3.1.1 Introduction

The origin of the flavor structure of the SM, i.e. the observed hierarchy between fermion masses and mixing angles of the CKM matrix, is one of the greatest mysteries of particle physics that still lacks a convincing and commonly accepted explanation. A number of New Physics (NP) ideas have been put forward in recent decades to address the flavor puzzle, among which the Froggatt-Nielsen (FN) mechanism [48] and extra dimensions [49–51] are those that admittedly received the most attention and applications. The underlying concept is to introduce a new quantity that in some sense would be "larger" than the electroweak symmetry breaking (EWSB) scale. This could be the vev of a flavon field, or a distance of a fermion field from the infra-red brane. Such a hierarchy of scales can be then translated into a hierarchy of masses and mixing angles of the SM quarks and leptons. A similar idea gave rise to the famous seesaw mechanism of neutrino mass generation [42, 52–57], where tiny values of the SM neutrino masses arise as a result of suppression of the EWSB scale by a very large Majorana mass.

In Ref. [58] a FN-inspired model was proposed to explain the observed masses and mixing patterns of the SM fermions. The SM Yukawa interactions are forbidden in this setup by an extra abelian symmetry $\mathrm{U}(1)_X$, which could be either global or local. The particle content of the model corresponds to the two-Higgs-doublet model (2HDM) extended by a full family of VL fermions charged under $\mathrm{U}(1)_X$, and one $\mathrm{U}(1)_X$-breaking singlet scalar which plays the role of a FN flavon. The large third-family Yukawa couplings are then effectively generated via mixing of the SM quarks and leptons with the $\mathrm{SU}(2)_L$ doublet VL fermions, while the Yukawa couplings of the second family emerge from a seesaw-like construction, mediated by the heavy VL $\mathrm{SU}(2)_L$ singlets.
In this study, we provide benchmark points that could account for the muon $(g-2)$ anomaly and, at the same time, give rise to the mass and mixing patterns of the SM fermions. We discuss the impact of the most recent bounds from direct NP searches at the LHC on the allowed parameter space of the model. While we show that the model is not currently tested by any collider experiment, we point out that decays of a heavy Higgs boson into two tau leptons may offer a smoking gun signature for the detection of the model in the upcoming runs of the LHC.
Secondly, we demonstrate that the quartic and Yukawa couplings of the model are subject to strong constraints from their RG running. The breakdown of perturbativity usually calls for an extension of the theoretical setup by extra degrees of freedom in order to cure pathological behavior of the running couplings, or/and for an inclusion of non-perturbative effects (like bound-state formation). If any of those arose at the scale specific to the original NP model, they would most likely affect its phenomenological predictions. Therefore, we apply the perturbativity bounds to the running couplings evaluated at an energy scale which is high enough that the phenomenology of the specific NP model can be trusted. Last but not least, we derive the stability conditions for the scalar potential.
In this work, we identify three benchmark scenarios that satisfy our theoretical and experimental requirements. While these best-fit points emerge from a random numerical scan, they present features that are generic for the model in study. Most importantly, we point out that a charged Higgs/heavy neutrino loop is a dominant contribution to the muon $(g-2)$ anomaly. This results from the fact that the competing neutral scalar/heavy charged lepton contributions are governed by the same Yukawa coupling that determines the tree-level muon mass and is thus required to be small.

3.1.2 Generation of fermion masses and mixing

We begin our study by reviewing the structure and the main properties of the model introduced in Ref. [58]. In the following, we focus mostly on these features of the model which play a pivotal role in the subsequent phenomenological analysis. Technical details of the model, including the analytical diagonalization of the fermion mass matrices and the derivation of the interaction vertices in the mass basis, can be found in Refs. [58–61].
The particle content of the model is summarized in Table 3.1. The SM fermion sector, collectively denoted as ψ_i ($\psi_i = Q_{iL}$, u_{iR}, d_{iR}, L_{iL}, e_{iR} and $i = 1,2,3$ stands for a generation index) is extended by one full family of VL fermions, indicated collectively as $(\psi_4,\ \widetilde{\psi}_4)$. We adopt the convention of using the left-chiral two-component Weyl spinors, therefore the subscripts L, R indicate the names of the fermions, not the chiralities. The scalar sector contains, besides the usual $\mathrm{SU}(2)_L$ Higgs doublet dubbed as H_u, an extra scalar doublet H_d and a scalar singlet ϕ. Note that all the NP particles and the Higgs doublet H_u are charged under an extra global gauge symmetry $\mathrm{U}(1)_X$, while the SM fermions are $\mathrm{U}(1)_X$ singlets. As a result, the ordinary SM Yukawa interactions are forbidden.

Field	$SU(3)_C$	$SU(2)_L$	$U(1)_Y$	$U(1)_X$
Q_{iL}	$\mathbf{3}$	$\mathbf{2}$	$\frac{1}{6}$	0
u_{iR}	$\bar{\mathbf{3}}$	$\mathbf{1}$	$-\frac{2}{3}$	0
d_{iR}	$\bar{\mathbf{3}}$	$\mathbf{1}$	$\frac{1}{3}$	0
L_{iL}	$\mathbf{1}$	$\mathbf{2}$	$-\frac{1}{2}$	0
e_{iR}	$\mathbf{1}$	$\mathbf{1}$	1	0
Q_{4L}	$\mathbf{3}$	$\mathbf{2}$	$\frac{1}{6}$	1
u_{4R}	$\bar{\mathbf{3}}$	$\mathbf{1}$	$-\frac{2}{3}$	1
d_{4R}	$\bar{\mathbf{3}}$	$\mathbf{1}$	$\frac{1}{3}$	1
L_{4L}	$\mathbf{1}$	$\mathbf{2}$	$-\frac{1}{2}$	1
e_{4R}	$\mathbf{1}$	$\mathbf{1}$	1	1
ν_{4R}	$\mathbf{1}$	$\mathbf{1}$	0	1
$\widetilde{Q}_{4R}$	$\bar{\mathbf{3}}$	$\mathbf{2}$	$-\frac{1}{6}$	-1
$\widetilde{u}_{4L}$	$\mathbf{3}$	$\mathbf{1}$	$\frac{2}{3}$	-1
$\widetilde{d}_{4L}$	$\mathbf{3}$	$\mathbf{1}$	$-\frac{1}{3}$	-1
$\widetilde{L}_{4R}$	$\mathbf{1}$	$\mathbf{2}$	$\frac{1}{2}$	-1
$\widetilde{e}_{4L}$	$\mathbf{1}$	$\mathbf{1}$	-1	-1
$\widetilde{\nu}_{4L}$	$\mathbf{1}$	$\mathbf{1}$	0	-1
ϕ	$\mathbf{1}$	$\mathbf{1}$	0	1
H_u	$\mathbf{1}$	$\mathbf{2}$	$\frac{1}{2}$	-1
H_d	$\mathbf{1}$	$\mathbf{2}$	$-\frac{1}{2}$	-1

TABLE 3.1: The particle content of the NP model considered in this study.

All the renormalizable Yukawa interactions between the SM and NP fermions which are allowed by the extended gauge symmetry can be schematically written as:

$$\mathcal{L}_{\text{ren}}^{\text{Yukawa}} = y^{\psi}_{i4}\psi_{iL}H\psi_{4R} + y^{\psi}_{4j}\psi_{4L}H\psi_{jR} + x^{\psi}_{i4}\psi_{iL}\phi\,\widetilde{\psi}_{4R} + x^{\psi}_{4j}\widetilde{\psi}_{4L}\phi\,\psi_{jR} + M_4^{\psi}\,\psi_{4L}\widetilde{\psi}_{4R} + M_4^{\widetilde{\psi}}\,\widetilde{\psi}_{4L}\psi_{4R} + \text{h.c.}, \quad (3.1)$$

where H is either H_u or H_d and M_4^{ψ} ($M_4^{\widetilde{\psi}}$) denotes the VL doublet (singlet) mass parameter. Note that with the $U(1)_X$ charges given in Table 3.1 the scalar H_u only couples to the up-type quarks, while H_d to the down-type quarks and charged leptons, reminiscent of the 2HDM Type-II model.

3.1.2.1 Hierarchy of masses

Once the neutral components of the scalar fields develop their vevs, the 5×5 fermions mass matrices are generated. Since their upper 3×3 blocks contain only zeros (we recall that the SM Yukawa couplings are forbidden by the $U(1)_X$ symmetry), one has the freedom to rotate the first three families. It can easily be shown [58] that this allows one to choose a flavor basis in which the fermion mass matrices acquire the following form:

$$\mathcal{M}_\psi = \begin{array}{c|ccccc} & \psi_{1R} & \psi_{2R} & \psi_{3R} & \psi_{4R} & \widetilde{\psi}_{4R} \\ \hline \psi_{1L} & 0 & 0 & 0 & (y^\psi_{14}\langle H^0\rangle) & 0 \\ \psi_{2L} & 0 & 0 & 0 & y^\psi_{24}\langle H^0\rangle & 0 \\ \psi_{3L} & 0 & 0 & 0 & y^\psi_{34}\langle H^0\rangle & x^\psi_{34}\langle\phi\rangle \\ \psi_{4L} & 0 & 0 & y^\psi_{43}\langle H^0\rangle & 0 & M^\psi_4 \\ \widetilde{\psi}_{4L} & 0 & x^\psi_{42}\langle\phi\rangle & x^\psi_{43}\langle\phi\rangle & M^{\widetilde{\psi}}_4 & 0 \end{array} . \tag{3.2}$$

In the above, the term in parentheses assumes a non-zero value in the mass matrix of the down-type quarks, while it is zero for the up-type quarks and charged leptons. The exact forms of the matrices $\mathcal{M}_u$, $\mathcal{M}_d$ and $\mathcal{M}_e$ are presented in Appendix 3.A.
In order to calculate the masses of the physical quarks and leptons, the 5×5 matrices of Eq. (3.2) need to be diagonalized. Due to a large number of free parameters in the Yukawa sector one may expect that the resulting functional dependence of the eigenvalues of $\mathcal{M}_\psi$ on the couplings y^ψ_{i4}, y^ψ_{43}, x^ψ_{4i}, x^ψ_{34} and the masses $M_4^{\psi(\widetilde{\psi})}$ is highly nontrivial. It turns out, however, that it is not necessarily the case and that simplified expressions for the fermion masses can be derived. Denoting the scalar vevs as

$$\langle H_u^0\rangle = v_u/\sqrt{2}, \qquad \langle H_d^0\rangle = v_d/\sqrt{2}, \qquad \langle\phi\rangle = v_\phi/\sqrt{2} \tag{3.3}$$

and defining $\tan\beta = v_u/v_d$, the masses of the third and second family quarks and leptons are approximately given by (see also Ref. [58] for a related derivation)

$$m_t \approx \frac{1}{\sqrt{2}}\frac{y^u_{43}x^Q_{34}v_\phi v_u}{\sqrt{(x^Q_{34}v_\phi)^2+2(M^Q_4)^2}}, \qquad m_c \approx \frac{y^u_{24}x^u_{42}v_\phi v_u}{2\,M^u_4} \tag{3.4}$$

$$m_b \approx \frac{1}{\sqrt{2}}\frac{y^d_{43}x^Q_{34}v_\phi v_d}{\sqrt{(x^Q_{34}v_\phi)^2+2(M^Q_4)^2}}, \qquad m_s \approx \frac{y^d_{24}x^d_{42}v_\phi v_d}{2\,M^d_4} \tag{3.5}$$

$$m_\tau \approx \frac{1}{\sqrt{2}}\frac{y^e_{43}x^L_{34}v_\phi v_d}{\sqrt{(x^L_{34}v_\phi)^2+2(M^L_4)^2}}, \qquad m_\mu \approx \frac{y^e_{24}x^e_{42}v_\phi v_d}{2\,M^e_4}\,. \tag{3.6}$$

While Eqs. (3.4)-(3.6) allow determination of the SM fermion masses with an accuracy within a factor of $2-3$ only, they can be used to gain intuition of which NP Yukawa couplings play a dominant role in establishing the correct masses of particular fermions. For example, large x^Q_{34} and y^u_{43} are expected to fit m_t, while $y^u_{24}\ll 1$ or $x^u_{42}\ll 1$ would be required to suppress the charm mass. Similarly, large y^d_{43} is needed to generate $m_b = 4.18$ GeV. Additionally, in order to obtain the correct value of the top quark mass, the singlet scalar vev v_ϕ should be of the same order as the VL mass parameter M^Q_4. Note, however, that in our phenomenological analysis we always perform the numerical diagonalization of the mass matrices (3.66), (3.69) and (3.72).
One important observation which can be deduced from Eqs. (3.4) and (3.5) is that the ratio of the top and bottom masses, $m_t/m_b \approx 34$, puts relevant constraints on the allowed parameter space of the model. In fact, we have

$$\frac{m_t}{m_b} \approx \frac{y^u_{43}}{y^d_{43}}\tan\beta\,. \tag{3.7}$$

The relation (3.7) leads to two distinct classes of solutions. In the first one, with both the

Yukawa couplings of order one, $\tan\beta \sim \mathcal{O}(10)$ is required. In the other one, with $\tan\beta \sim \mathcal{O}(1)$, a large hierarchy between the up and down sector couplings, $y^d_{43} \ll y^u_{43}$, must be imposed.
The masses of VL fermions are given, to a very good approximation, by the corresponding VL mass parameters with small contributions stemming from their mixing with the second and the third family,

$$M_{U_1} \approx \sqrt{(M_4^Q)^2 + \frac{1}{2}(v_\phi x_{34}^Q)^2 - \frac{(M_4^Q y_{43}^u v_u)^2}{(x_{34}^Q v_\phi)^2 + 2(M_4^Q)^2}} \tag{3.8}$$

$$M_{U_2} \approx \sqrt{(M_4^u)^2 + \frac{1}{2}(v_\phi x_{43}^u)^2 + \frac{1}{2}(v_\phi x_{42}^u)^2 + \frac{2(M_4^u y_{43}^u v_u)^2}{2(M_4^u)^2 + (v_\phi x_{43}^u)^2 + (v_\phi x_{42}^u)^2}} \tag{3.9}$$

$$M_{D_1} \approx \sqrt{(M_4^Q)^2 + \frac{1}{2}(v_\phi x_{34}^Q)^2}, \qquad M_{D_2} = \sqrt{(M_4^d)^2 + \frac{1}{2}(v_\phi x_{43}^d)^2 + \frac{1}{2}(v_\phi x_{42}^d)^2} \tag{3.10}$$

$$M_{E_1} \approx \sqrt{(M_4^L)^2 + \frac{1}{2}(v_\phi x_{34}^L)^2}, \qquad M_{E_2} = \sqrt{(M_4^e)^2 + \frac{1}{2}(v_\phi x_{43}^e)^2 + \frac{1}{2}(v_\phi x_{42}^e)^2}. \tag{3.11}$$

In the neutrino sector, the corresponding mass matrix is 7×7 and its explicit form can be found in Eq. (3.76). The resulting masses of the heavy neutrinos read

$$M_{N_1} = M_{N_2} \approx M_4^\nu, \qquad M_{N_3} = M_{N_4} \approx \sqrt{(M_4^L)^2 + \frac{1}{2}(v_\phi x_{34}^L)^2}. \tag{3.12}$$

By comparing Eq. (3.12) with Eq. (3.11), we can pinpoint two generic features of the model considered in this study: heavy neutrinos $N_{1,2}$ are the lightest VL leptons in the spectrum, while the pair $N_{3,4}$ is mass-degenerate (at the tree level) with the charged VL lepton E_1. We will later see that this mass pattern has important consequences for the resulting phenomenology.
As a final remark, let us notice that one complete VL family allows us to give masses to the second and third family of the SM fermions only. To generate the masses for the first family as well, one extra VL family is required (for an example of such a construction, see Ref. [60]). Since such an extension would only increase the number of free parameters in the model without affecting any phenomenological findings, in this study we limit ourselves to its most economical version.

3.1.2.2 CKM mixing matrix

The full 5×5 mixing matrix takes the following form [59]:

$$V_{\rm mixing} = V_L^u .\, \mathrm{diag}\,(1,1,1,1,0)\,.V_L^{d\dagger} \tag{3.13}$$

where V_L^u and V_L^d are the left-handed mixing matrices of Eqs. (3.70) and (3.73) which diagonalize the up- and down-type quark mass matrices $\mathcal{M}_u$ and $\mathcal{M}_d$. The zero element of the matrix (3.13) indicates the fact that the singlet VL quarks do not interact with the SM gauge bosons $W^\pm$. Following the strategy of Ref. [59] and working under the assumption that $v_{u,d}/M_4^{Q,u,d} \ll 1$, we can approximate the 3×3 CKM matrix as

$$V_{\rm CKM}^{3\times 3} \approx \begin{pmatrix} 1 - x_{ud}^2/2 & x_{ud} & x_{ud}x_d \\ -x_{ud} & 1 - x_{ud}^2/2 & x_d - x_u \\ -x_u x_{ud} & x_u - x_d & 1 \end{pmatrix}, \tag{3.14}$$

where

$$x_d = \frac{y^d_{24} x^d_{43} M^Q_4}{y^d_{43} x^Q_{34} M^d_4}\,, \qquad x_u = \frac{y^u_{24} x^u_{43} M^Q_4}{y^u_{43} x^Q_{34} M^u_4}\,, \qquad x_{ud} = \frac{y^d_{14}}{y^d_{24}}\,. \tag{3.15}$$

Based on the conclusions from Sec. 3.1.2.1 one expects $x_u, x_d \ll 1$. Note also that:

- The element V_{us} of the CKM matrix is given by y^d_{14}/y^d_{24} in our model. The presence of a non-zero coupling y^d_{14} is thus crucial to generate the Cabibbo angle of the right size. We also expect $y^d_{14} \approx 0.22\, y^d_{24}$.
- The correct value of the element V_{ud} is generated automatically once the Cabibbo angle is set.
- To reproduce the correct value of the element V_{ub}, one needs $x_d \approx 0.017$. It then follows that $x_u \approx -0.023$ is required in order to fit the element V_{cb} (it also implies x^u_{43} of order one).
- The only element of the CKM matrix that can not be accurately reproduced is V_{td}.

To analzye this issue more quantitatively, it is convenient to rewrite the CKM matrix (3.14) in terms of the Wolfenstein parameters [62]. Defining, for example,

$$x_d = A\,\lambda^3 \sqrt{\eta^2+\rho^2}\,, \qquad x_u = A\,\lambda^2 \left(\sqrt{\eta^2+\rho^2} - 1\right)\,, \qquad x_{ud} = \frac{x_u\, x_d}{\lambda}\,, \tag{3.16}$$

one obtains

$$|V^{3\times 3}_{\rm CKM}| = \begin{pmatrix} 1-\lambda^2/2 & \lambda & A\,\lambda^3\sqrt{\eta^2+\rho^2} \\ \lambda & 1-\lambda^2/2 & A\,\lambda^2 \\ A\,\lambda^3\left(1-\sqrt{\eta^2+\rho^2}\right) & A\,\lambda^2 & 1 \end{pmatrix} + \mathcal{O}(\lambda^4)\,. \tag{3.17}$$

Plugging the Wolfenstein parameters extracted from the global fit [63] into Eq. (3.17) and comparing it with the experimental determination of the CKM matrix elements reported in Ref. [63], one can estimate to what extent the measured structure of the CKM matrix can be reproduced in our model. One obtains

$$\frac{|V^{\rm exp}_{\rm CKM}| - |V^{3\times 3}_{\rm CKM}|}{\delta |V^{\rm exp}_{\rm CKM}|} = \begin{pmatrix} 0 & 0 & 0 \\ 0 & 0.04 & 0 \\ 8.88 & 0.23 & 0.01 \end{pmatrix}\,. \tag{3.18}$$

It results from Eq. (3.18) that in the framework of our model we may not be able to correctly reproduce all the elements of the CKM matrix (this observation will be later confirmed by our numerical scan).[1] Once more, this issue could be solved by introducing an extra VL family.

3.1.3 Scalar potential constraints

In this section, we discuss the constraints stemming from the scalar potential of the model. In particular, we define the alignment limit of the SM-like Higgs boson, we derive the conditions for the scalar potential to be bounded from below in the presence of three independent scalar fields, and we verify whether the electroweak (EW) vacuum is stable.

[1] Note that modifying the definitions of the parameters x_u, x_d and x_{ud} in Eq. (3.16), one could be able to fit better the element V_{td}, but at the price of losing the accuracy in reproducing V_{cb}.

3.1.3.1 Scalar masses in the alignment limit

In the interaction basis, the most generic renormalizable scalar potential of the model defined in Table 3.1 takes the form [60]:

$$\begin{aligned} V = &\mu_u^2(H_u^\dagger H_u) + \mu_d^2(H_d^\dagger H_d) + \mu_\phi^2(\phi^*\phi) - \frac{1}{2}\mu_{\rm sb}^2\left(\phi^2 + \phi^{*2}\right) \\ &+ \frac{1}{2}\lambda_1(H_u^\dagger H_u)^2 + \frac{1}{2}\lambda_2(H_d^\dagger H_d)^2 + \lambda_3(H_u^\dagger H_u)(H_d^\dagger H_d) + \lambda_4(H_u^\dagger H_d)(H_d^\dagger H_u) \\ &- \frac{1}{2}\lambda_5(\epsilon_{ij}H_u^i H_d^j \phi^2 + \text{H. c.}) + \frac{1}{2}\lambda_6(\phi^*\phi)^2 + \lambda_7(\phi^*\phi)(H_u^\dagger H_u) + \lambda_8(\phi^*\phi)(H_d^\dagger H_d), \end{aligned} \tag{3.19}$$

where $\mu^2_{u,d,\phi}$ are dimensionful mass parameters, $\lambda_{1,2,\cdots,8}$ denote dimensionless quartic coupling constants, and $\mu^2_{\rm sb}$ is an extra mass term which softly violates the global $\mathrm{U}(1)_X$ symmetry. The main reason to introduce the latter is to prevent a massless Goldstone boson of the spontaneously broken $\mathrm{U}(1)_X$ to appear in the spectrum. As we will see below, the soft-breaking term does not affect the CP-even and the charged scalar masses since it only enters the mass matrix of the pseudoscalars.

Expanding the fields H_u, H_d and ϕ around their vacuum states,

$$\begin{aligned} H_u = \begin{pmatrix} H_u^+ \\ \frac{1}{\sqrt{2}}\left(v_u + \mathrm{Re}\,H_u^0 + i\,\mathrm{Im}\,H_u^0\right)\end{pmatrix}, \qquad H_d = \begin{pmatrix} \frac{1}{\sqrt{2}}\left(v_d + \mathrm{Re}\,H_d^0 + i\,\mathrm{Im}\,H_d^0\right) \\ H_d^- \end{pmatrix}, \\ \phi = \frac{1}{\sqrt{2}}\left(v_\phi + \mathrm{Re}\,\phi + i\,\mathrm{Im}\,\phi\right), \end{aligned} \tag{3.20}$$

where the vevs are defined in Eq. (3.3), one can use the minimization conditions for the scalar potential (3.19) to express the dimensionful mass parameters in terms of the quartic couplings and the vevs,

$$\begin{aligned} \mu_u^2 &= -\frac{1}{2}\left(\lambda_1 v_u^2 + \lambda_3 v_d^2 + \lambda_7 v_\phi^2\right) - \frac{1}{4}\lambda_5\left(\frac{v_d}{v_u}\right)v_\phi^2, \\ \mu_d^2 &= -\frac{1}{2}\left(\lambda_2 v_d^2 + \lambda_3 v_u^2 + \lambda_8 v_\phi^2\right) - \frac{1}{4}\lambda_5\left(\frac{v_u}{v_d}\right)v_\phi^2, \\ \mu_\phi^2 &= -\frac{1}{2}\left(\lambda_6 v_\phi^2 + \lambda_5 v_d v_u + \lambda_7 v_u^2 + \lambda_8 v_d^2\right) + \mu_{\rm sb}^2\,. \end{aligned} \tag{3.21}$$

One must have

$$\mu_u^2 < 0\,, \qquad \mu_d^2 < 0\,, \qquad \mu_\phi^2 < 0\,. \tag{3.22}$$

in order to generate the non-zero vevs for all the scalar fields.

The real parts of the scalar fields, $\mathrm{Re}\,H_u^0$, $\mathrm{Re}\,H_d^0$ and $\mathrm{Re}\,\phi$, account for three CP-even Higgs bosons. The masses of three physical neutral scalars, h_1, h_2 and h_3, correspond to the eigenvalues of $\mathbf{M}^2_{\text{CP-even}}$,

$$\mathrm{diag}\{M_{h_1}^2, M_{h_2}^2, M_{h_3}^2\} = R_h(\mathbf{M}^2_{\text{CP-even}})R_h^T\,. \tag{3.23}$$

In the following, we will want to identify the SM Higgs boson with the lightest neutral scalar h_1. To this end, we choose to work in the so-called alignment limit, defined as a set of constraints on the quartic couplings λ_i under which h_1 features the same tree-level couplings with the SM particles as the SM Higgs. This assumption requires

$$\lambda_8\,\cos^2\beta + \lambda_7\,\sin^2\beta + \lambda_5\,\sin\beta\cos\beta \;=\; 0 \tag{3.24}$$

$$\lambda_2\,\cos^2\beta - \lambda_1\,\sin^2\beta - \lambda_3(\cos^2\beta - \sin^2\beta) \;=\; 0\,, \tag{3.25}$$

where the equality imposes a perfect alignment condition. The masses of the CP-even scalars in the alignment limit read

$$M_{h_1}^2 = v^2 \left(\lambda_1 \sin^2\beta + \lambda_3 \cos^2\beta\right) \tag{3.26}$$

$$M_{h_2}^2 = \lambda_6 v_\phi^2 - \frac{1}{8\sin\beta\cos\beta}\left(B_{23} + \sqrt{4A_{23}^2 + B_{23}^2}\right) \tag{3.27}$$

$$M_{h_3}^2 = \lambda_6 v_\phi^2 - \frac{1}{8\sin\beta\cos\beta}\left(B_{23} - \sqrt{4A_{23}^2 + B_{23}^2}\right), \tag{3.28}$$

where we define

$$A_{23} = 2\, v\, v_\phi s_\beta (c_\beta \lambda_5 + 2\lambda_7 s_\beta) \tag{3.29}$$

$$B_{23} = \lambda_5 v_\phi^2 + 4 s_\beta c_\beta \left(\lambda_6 v_\phi^2 - (\lambda_1 - \lambda_3) v^2 s_\beta^2\right), \tag{3.30}$$

and $v = \sqrt{v_u^2 + v_d^2} = 246$ GeV.

The CP-odd scalar mass matrix in the basis $(\mathrm{Im}\, H_u^0, \mathrm{Im}\, H_d^0, \mathrm{Im}\, \phi)$, $\mathbf{M}^2_{\text{CP-odd}}$, after diagonalization, gives the physical CP-odd spectrum, consisting of one massless Goldstone boson and two massive pseudoscalars, a_1 and a_2,

$$M_{a_1}^2 = -\frac{\lambda_5}{2\sin 2\beta}\left(v^2 \sin^2 2\beta + v_\phi^2\right) \tag{3.31}$$

$$M_{a_2}^2 = 2\,\mu_{\text{sb}}^2\,. \tag{3.32}$$

Note that $\lambda_5 < 0$ and $\mu_{\text{sb}}^2 > 0$ are required to guarantee the positivity of $M_{a_1}^2$ and $M_{a_2}^2$. Finally, the charged scalar mass matrix in the basis $(H_u^\pm, H_d^\mp)$, $\mathbf{M}^2_{\text{Charged}}$, after diagonalization, gives a massless charged Goldstone boson and a charged Higgs boson,

$$M_{h^\pm}^2 = \frac{\lambda_4 v^2}{2} - \frac{\lambda_5 v_\phi^2}{2\sin 2\beta}\,. \tag{3.33}$$

As a closing remark, let us notice that the alignment condition (3.25) indicates

$$\lambda_2 = \lambda_3 + \tan^2\beta(\lambda_1 - \lambda_3)\,. \tag{3.34}$$

In order to preserve the perturbativity of λ_2 (more on this in Sec. 3.1.5), the term in parentheses needs to be fine-tuned with a precision $\mathcal{O}(1/\tan^2\beta)$ or better, effectively fixing $\lambda_3 \approx \lambda_1$ with the same accuracy. On the other hand, Eq. (3.26) implies that we can identify λ_1 with the quartic coupling of the SM, $\lambda_1 = 0.258$, as long as $\tan\beta \gtrsim 3$. Similarly, the alignment condition (3.24) gives

$$\lambda_8 = -\tan\beta\,(\lambda_7 \tan\beta + \lambda_5)\,. \tag{3.35}$$

Perturbativity of λ_8 then requires $\lambda_7 \sim \mathcal{O}(1/\tan^2\beta)$ and $\lambda_5 \sim \mathcal{O}(1/\tan\beta)$.

3.1.3.2 Bounded-from-below limits and vacuum stability

To guarantee that the minimum around which we expand the scalar potential (3.19) is physically meaningful, we must ensure that the potential is bounded from below, which means that it cannot tend to negative infinity along any direction in the field space. This requirement puts additional restrictions on the allowed values of the couplings λ_i. To derive the 'bounded-from-below' constraints, one should analyze all possible directions along which the scalar fields H_u, H_d and ϕ can flow towards arbitrarily large values. The details of our derivation are presented in Appendix 3.C. Here we summarize our findings in the form of inequality conditions which need to be satisfied by the quartic couplings of the potential (3.19):

$$\begin{aligned} \lambda_8 + \sqrt{\lambda_2\lambda_6} &> 0 \\ \lambda_7 + \sqrt{\lambda_1\lambda_6} &> 0 \\ \lambda_3 + \sqrt{\lambda_2\lambda_1} &> 0 \\ \lambda_3 + \lambda_4 + \sqrt{\lambda_2\lambda_1} &> 0 \\ -\frac{1}{4}\frac{(\mathrm{Re}\,\lambda_5)^2 + (\mathrm{Im}\,\lambda_5)^2}{\lambda_a} + \lambda_4 &> 0 \\ 4\lambda_b^2 - (\mathrm{Re}\,\lambda_5)^2 + \mathrm{Re}\,\lambda_5\,\mathrm{Im}\,\lambda_5 &> 0 \\ 4\lambda_b^2 - (\mathrm{Im}\,\lambda_5)^2 + \mathrm{Re}\,\lambda_5\,\mathrm{Im}\,\lambda_5 &> 0 \end{aligned} \tag{3.36}$$

where $\lambda_a = \frac{3}{2}\lambda_6 + \lambda_3\frac{\lambda_6}{\sqrt{\lambda_1\lambda_2}} + \lambda_7\sqrt{\frac{\lambda_6}{\lambda_1}} + \lambda_8\sqrt{\frac{\lambda_6}{\lambda_2}}$ and $\lambda_b = \sqrt{\lambda_a\lambda_4}$. Since in this study we do not investigate the CP violation, we assume that all the parameters of the lagrangian are real, indicating $\mathrm{Im}\,\lambda_5 = 0$.

In theories which feature an extended scalar sector, the scalar potential can easily develop more than one local minimum. As a result, the theory may tunnel from one minimum to another. In principle, color and charge breaking minima deeper than the EWSB minimum of Eq. (3.3) can arise in our model (see, e.g. [64]). Moreover, several charge and color conserving minima can coexist, in which case we do not know *a priori* which of them corresponds to the desired EWSB minimum. The strong vacuum stability condition for the scalar potential requires that the EWSB vacuum corresponds to a global minimum. In such a case the potential is said to be stable. If, on the other hand, the EWSB minimum is a local minimum but the tunneling time to a true global minimum exceeds the age of the Universe, the potential is said to be metastable. In this study we employ the publicly available numerical package `Vevacious++` [65] (the C++ version of [66]) to find all tree- and one-loop level minima of the scalar potential defined in Eq. (3.19) and to calculate the tunneling time from the EWSB minimum to the deepest minimum found.

3.1.4 Flavor physics constraints

In this section, we review additional constraints which may affect the allowed parameter space of the analyzed model. These extra restrictions come from the experimental measurements of several flavor observables, including the anomalous magnetic moment of the muon, the lepton flavor violating decays of the tau lepton, and the elements of the CKM matrix. We discuss them in the following one by one.

3.1.4.1 Muon anomalous magnetic moment

The discrepancy between the SM prediction [67–88] and the experimental measurement of the anomalous magnetic moment of the muon has been confirmed separately by the Brookhaven National Laboratory [89] and the Fermilab experimental groups [90, 91], giving rise to the combined 5.1 σ anomaly:

$$\Delta a_\mu = a_\mu^{\mathrm{exp}} - a_\mu^{\mathrm{SM}} = (2.49 \pm 0.48) \times 10^{-9}. \tag{3.37}$$

It is important to note that recent developments in lattice QCD have led to updated determinations of the leading-order hadronic vacuum polarization (HVP) contribution to a_μ. In particular, the BMW Collaboration has reported a value that is in closer agreement with the experimental result [92], potentially reducing or even eliminating the previously observed tension between theory and experiment. However, this result is in mild tension with the values obtained from the data-driven (dispersive) approach [81, 82], which continues to predict a discrepancy. As of now, this situation remains under scrutiny, and future theoretical and experimental input will be crucial in resolving this tension.

In a generic NP model which features heavy scalars ϕ_i and fermions ψ_j coupled to the SM muons via the Yukawa-type interactions $y_L^{ij}\phi_i\,\bar\psi_j P_L\,\mu$ and $y_R^{ij}\phi_i\,\bar\psi_j P_R\,\mu$ (where $P_{L,R} = (1 \mp \gamma^5)/2$ are the usual projection operators), a well-known one-loop contribution to the muon anomalous magnetic moment reads

$$\begin{aligned}\Delta a_\mu = \sum_{i,j}\Bigg\{ & -\frac{m_\mu^2}{16\pi^2 M_{\phi_i}^2}\left(|y_L^{ij}|^2+|y_R^{ij}|^2\right)\left[Q_j\mathcal{F}_1\left(x_{ij}\right)-Q_i\mathcal{G}_1\left(x_{ij}\right)\right]\\ & -\frac{m_\mu\,M_{\psi_j}}{16\pi^2 M_{\phi_i}^2}\mathrm{Re}\left(y_L^{ij}y_R^{ij*}\right)\left[Q_j\mathcal{F}_2\left(x_{ij}\right)-Q_i\mathcal{G}_2\left(x_{ij}\right)\right]\Bigg\}\,,\end{aligned} \tag{3.38}$$

where M_{ϕ_i} is the physical mass of a heavy scalar, M_{ψ_j} is the physical mass of a heavy fermion, $x_{ij} = M_{\psi_j}^2/M_{\phi_i}^2$, and the electric charges of ϕ_i and ψ_j are related as $Q_i + Q_j = -1$. The loop functions are defined in the following way:

$$\begin{aligned}\mathcal{F}_1(x) &= \frac{1}{6\,(1-x)^4}\left(2+3x-6x^2+x^3+6x\ln x\right)\\ \mathcal{F}_2(x) &= \frac{1}{(1-x)^3}\left(-3+4x-x^2-2\ln x\right)\\ \mathcal{G}_1(x) &= \frac{1}{6\,(1-x)^4}\left(1-6x+3x^2+2x^3-6x^2\ln x\right)\\ \mathcal{G}_2(x) &= \frac{1}{(1-x)^3}\left(1-x^2+2x\ln x\right)\,.\end{aligned} \tag{3.39}$$

The first addend in Eq. (3.38) captures the loop chirality-conserving contributions to Δa_μ. These are known to be generically too small to account for the anomaly (3.37) when the most recent LHC bounds on the NP masses are taken into account [93, 94]. We will thus focus on the second addend in Eq. (3.38), which corresponds to the loop chirality-flipping contributions to Δa_μ.
In the framework of the model defined in Table 3.1, two classes of contributions to the anomalous magnetic moment of the muon can arise, induced by one-loop diagrams with an exchange of neutral (pseudo)scalars and charged VL leptons, as shown in Fig. 3.1(a), or charged scalars and neutral VL leptons, as shown in Fig. 3.1(b). In the first case, the chirality-flipping contributions to Δa_μ read

$$\Delta a_\mu^{Eh^0} \approx \frac{1}{16\pi^2}\sum_{j=1}^{2}\sum_{i=1}^{3}\left[\frac{m_\mu\,M_{E_j}}{M_{h_i^0}^2}\mathrm{Re}\left(c_L c_R^*\right)^{E_j,h_i^0}\mathcal{F}_2\left(M_{E_j}^2/M_{h_i^0}^2\right)\right] \tag{3.40}$$

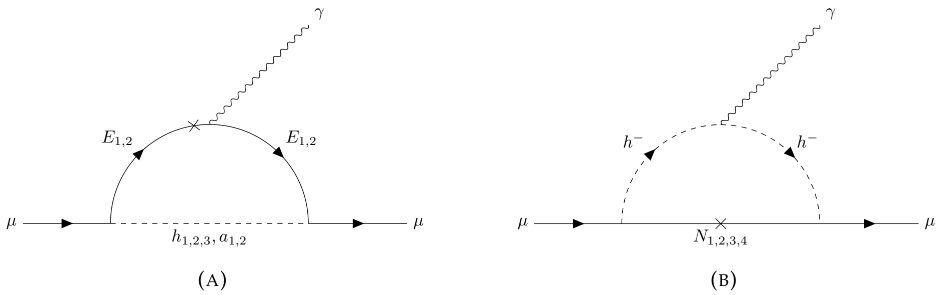

FIGURE 3.1: The one-loop chirality-flipping contributions to Δa_μ mediated by (a) a neutral (pseudo)scalar/charged lepton exchange, and (b) a charged scalar/neutral lepton exchange.

for the CP-even scalars and

$$\Delta a_\mu^{Ea} \approx \frac{1}{16\pi^2} \sum_{j=1}^{2} \sum_{i=1}^{2} \left[\frac{m_\mu M_{E_j}}{M_{a_i}^2} \mathrm{Re}\,(c_L c_R^*)^{E_j, a_i}\, \mathcal{F}_2\left(M_{E_j}^2 / M_{a_i}^2 \right) \right] \tag{3.41}$$

for the CP-odd scalars. The one-loop contributions to Δa_μ from the neutral leptons and charged scalars are given by

$$\Delta a_\mu^{Nh^\pm} \approx -\frac{1}{16\pi^2} \sum_{j=1}^{4} \left[\frac{m_\mu M_{N_j}}{M_{h^\pm}^2} \mathrm{Re}\,(c_L c_R^*)^{N_j, h^\pm}\, \mathcal{G}_2\left(M_{N_j}^2 / M_{h^\pm}^2 \right) \right]. \tag{3.42}$$

The parameters $c_{L/R}$ denote the effective couplings arising from the muon-(pseudo)scalar-VL fermion vertices in the mass basis. They depend on the lepton Yukawa couplings, as well as on the elements of the mixing matrices R_h, R_a, and $V_{L/R}^e$. The explicit forms of $c_{L/R}$ are rather complex and we refrain from showing them here. Note, however, that in our numerical analysis we are going to compute all the contributions to Δa_μ with the numerical package `SPheno` [95, 96].

3.1.4.2 Lepton flavor violating decays

Due to the non-zero mixing between the second and the third generation of fermions, charged lepton flavour violating processes may occur. The $\tau \to \mu\gamma$ decay receives contributions from the one-loop diagrams analogous to those of Δa_μ. The corresponding branching ratio (BR) is given by [97]

$$\mathrm{BR}(\tau \to \mu\gamma) = \frac{\alpha_{\mathrm{em}} m_\tau^3}{4\,\Gamma_\tau} \sum_{i,j} \left(|A_L^{ij}|^2 + |A_R^{ij}|^2 \right), \tag{3.43}$$

where $\Gamma_\tau = 2.3 \times 10^{-12}$ [63] indicates the total decay width of the tau, α_{em} is the fine structure constant, and the decay amplitude A_L^{ij} reads

$$A_L^{ij} = \frac{1}{32\pi^2 M_{\phi_i}^2} \Big\{ m_\tau \left(y_{\tau,L}^{ij} y_{\mu,L}^{ij*} \right) \left[Q_j \mathcal{F}_1\left(x_{ij}\right) - Q_i \mathcal{G}_1\left(x_{ij}\right) \right] + M_{\psi_j} \left(y_{\tau,L}^{ij} y_{\mu,R}^{ij*} \right) \left[Q_j \mathcal{F}_2\left(x_{ij}\right) - Q_i \mathcal{G}_2\left(x_{ij}\right) \right] \Big\}. \tag{3.44}$$

The corresponding amplitude A_R^{ij} is obtained from Eq. (3.44) by replacing $L \leftrightarrow R$. Just like it was in the Δa_μ case, the main contribution to $\mathrm{BR}(\tau \to \mu\gamma)$ originates from the second addend in Eq. (3.44). The current experimental 90% confidence level (C.L.) upper bound on

BR $(\tau \to \mu\gamma)$ from the Belle collaboration reads [98]:

$$\mathrm{BR}\,(\tau \to \mu\gamma)_{\mathrm{exp}} < 4.2 \times 10^{-8}\,. \tag{3.45}$$

The $\tau \to 3\,\mu$ decay can proceed through the one-loop penguin and box diagrams. The latter are subdominant in our model as they do not receive the chiral enhancement. The corresponding formulae for the penguin-diagram BRs are lengthy and not particularly enlightening. They can be found, for example, in Eq. (37) of Ref. [97]. The 90% C.L. upper bound on BR $(\tau \to 3\,\mu)$ by the Belle collaboration reads [99]:

$$\mathrm{BR}\,(\tau \to 3\,\mu)_{\mathrm{exp}} < 2.1 \times 10^{-8}\,. \tag{3.46}$$

3.1.4.3 CKM anomaly

Among the experimental puzzles which are not explained by the SM we should also mention various tensions between three different determinations of the Cabibbo angle. This observable can be extracted from the short distance radiative corrections to the β decay, from the experimental data on kaon decays, and from the lattice calculations [100–103]. All these measurements are in tension with each other, giving rise to two interesting anomalies.
The first anomaly is related to the violation of the CKM matrix unitarity when one compares the values of $|V_{ud}|$ and $|V_{us}|$ resulting from the β decay and from the kaon decays. The second anomaly originates from two different measurements of $|V_{us}|$: from the semileptonic $K \to \pi l \nu$ and the leptonic $K \to \mu\nu$ decay, respectively.
The experimental upper bound on the CKM deviation from the unitarity reads [63]

$$\Delta_{\mathrm{CKM}} = \sqrt{1 - V_{ud}^2 - V_{us}^2 - V_{ub}^2} < 0.05. \tag{3.47}$$

To explain the anomaly of Eq. (3.47), one can consider extensions of the SM in which the fermion sector is enlarged by VL quarks mixing at the tree level with the SM quarks [101, 104–106]. In such a setting deviations from the unitarity of the three-dimensional CKM matrix can arise quite naturally. Since the model defined in Table 3.1 contains all the necessary ingredients to account for the CKM anomaly, we include it in our list of constraints.

3.1.5 Perturbativity constraints

The model defined in Table 3.1 is intended as a phenomenological scenario which correctly describes the physics around the energy scale determined by the typical masses in the NP sector. Nevertheless, it is important to understand what is the range of validity of such a model or, in other words, what is the energy scale at which the model can not be trusted anymore and should be embedded in some more fundamental UV completion. While such a "cut-off" scale lacks a truly rigorous definition, one can try to estimate it by simply requiring that whatever extra degrees of freedom emerge in the theory above this scale to make the model UV complete, they do not affect its phenomenological predictions.
As an example, let us consider the muon anomalous magnetic moment operator, which in the low-energy EFT reads

$$\frac{e}{2\,m_\mu}\Delta a_\mu \left(\bar{\mu}\,\sigma_{\mu\nu}\,F^{\mu\nu}\mu\right) \equiv \frac{C}{\Lambda}\left(\bar{\mu}\,\sigma_{\mu\nu}\,F^{\mu\nu}\mu\right)\,. \tag{3.48}$$

Here Λ is a cut-off scale of the examined EFT while C denotes a generic Wilson coefficient. Note that since the operator in Eq. (3.48) is chirality flipping, it is more convenient to define

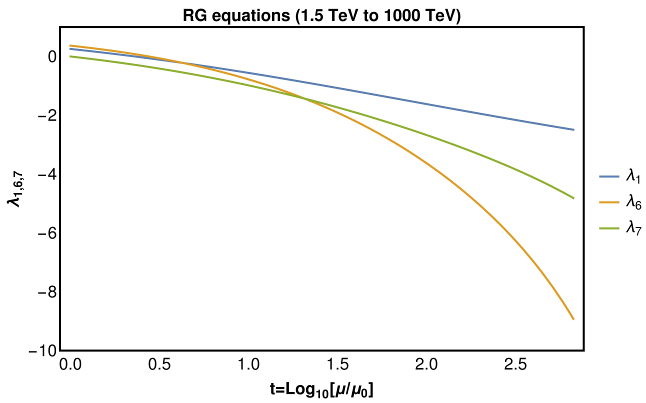

FIGURE 3.2: The RG running of the quartic couplings λ_1, λ_6 and λ_7 for a randomly chosen benchmark point which satisfies all the constraints discussed in Secs. 3.1.2 and 3.1.3. The renormalisation scale μ ranges from 1.5 TeV to 1000 TeV. $\mu_0 = 1.5$ TeV is a reference scale. We do not show the RG evolution of other quartic and Yukawa couplings as it is very slow in the considered energy range.

$C = \tilde{C}\, m_\mu/\Lambda$. One can now derive from Eq. (3.48) rough estimates of the energy scale associated with a hypothetical NP contributing to Δa_μ at different loop orders,

$$\text{tree level}: \quad \tilde{C} \approx 1, \qquad \Lambda \approx 3000 \text{ GeV} \tag{3.49}$$

$$1 \text{ loop}: \quad \tilde{C} \approx 1/16\pi^2, \qquad \Lambda \approx 230 \text{ GeV} \tag{3.50}$$

$$2 \text{ loop}: \quad \tilde{C} \approx (1/16\pi^2)^2, \quad \Lambda \approx 20 \text{ GeV} \tag{3.51}$$

and so on. Going beyond the EFT approximation, let us investigate a one-loop chirality flipping contribution to Δa_μ like the one in Eq. (3.38). Assuming that it arises from an unspecified UV completion of our model above the scale Λ, it can be estimated by the corresponding UV mass m_Λ and the UV Yukawa couplings $y_{L/R}(\Lambda)$ as

$$\Delta a_\mu^\Lambda \sim \frac{1}{16\pi^2} \frac{m_\mu\, v}{m_\Lambda^2} y_L(\Lambda)\, y_R(\Lambda). \tag{3.52}$$

By demanding that the new contribution (3.52) does not shift our phenomenological predictions for Δa_μ by more than $3\,\sigma$, we can derive a lower bound on the UV mass,

$$m_\Lambda \gtrsim \sqrt{y_L(\Lambda) y_R(\Lambda)}\, 15\,\text{TeV}\,. \tag{3.53}$$

For the Yukawa couplings at the upper edge of perturbativity, $y_L(\Lambda) = y_R(\Lambda) = \sqrt{4\pi}$, Eq. (3.53) translates into a conservative estimation of the scale of validity of our phenomenological model,

$$m_\Lambda \gtrsim 50 \text{ TeV}. \tag{3.54}$$

In other words, the model can not be UV completed below m_Λ.
To implement the RG-based perturbativity constraints, we follow the RG flow of all the coupling constants from the scale $\mu_0 = 1.5$ TeV, which is a proxy for the NP scale in our model, to $\Lambda = 50$ TeV. The one-loop RGEs were computed using the publicly available numerical code `SARAH` [107, 108] and are summarized in Appendix 3.D. Due to a large number of Yukawa and quartic interactions in our model, it is not possible to perform the perturbativity analysis in a generic way as the RGEs are non-linear differential equations that can not be solved analytically. On the other hand, the perturbativity bounds are expected to be relevant

Scalar sector									
$\tan\beta$	$[2, 50]$	v_ϕ	$[1000, 1500]$	μ_{sb}^2	$[4, 64] \times 10^4$	λ_2	$[-2.0, +2.0]$	λ_3	$[0.24, 0.28]$
λ_4	$[-2.0, +2.0]$	λ_5	$[-0.2, 0.0]$	λ_6	$[-2.0, +2.0]$	λ_7	$[-0.01, +0.01]$	λ_8	$[-1.0, +1.0]$
Lepton sector									
y_{24}^e	$[-0.7, +0.7]$	y_{43}^e	$[-1.0, +1.0]$	y_{14}^ν	$[-1.0, +1.0] \times 10^{-10}$	$y_{14}'^\nu$	$[-1.0, +1.0]$	M_4^e	$\pm [200, 1000]$
y_{34}^e	$[-1.0, +1.0]$	x_{42}^e	$[-1.0, +1.0]$	y_{24}^ν	$[-1.0, +1.0] \times 10^{-10}$	$y_{24}'^\nu$	$[-1.0, +1.0]$	M_4^ν	$\pm [200, 1000]$
x_{34}^L	$[-1.0, +1.0]$	x_{43}^e	$[-1.0, +1.0]$	y_{34}^ν	$[-1.0, +1.0] \times 10^{-10}$	$y_{34}'^\nu$	$[-1.0, +1.0]$	M_4^L	$\pm [200, 1000]$
Quark sector									
y_{24}^u	$[-1.0, +1.0]$	y_{43}^u	$[-1.4, +1.4]$	y_{14}^d	$[-0.7, +0.7]$	y_{43}^d	$[-1.0, +1.0]$	M_4^d	$\pm [1200, 4000]$
y_{34}^u	$[-1.4, +1.4]$	x_{42}^u	$[-1.0, +1.0]$	y_{24}^d	$[-1.0, +1.0]$	x_{42}^d	$[-1.0, +1.0]$	M_4^u	$\pm [1200, 4000]$
x_{34}^Q	$[-1.0, +1.0]$	x_{43}^u	$[-1.4, +1.4]$	y_{34}^d	$[-1.0, +1.0]$	x_{43}^d	$[-1.0, +1.0]$	M_4^Q	$\pm [1200, 4000]$

TABLE 3.2: Scanning ranges for the input parameters of the model defined in Table 3.1. The alignment limit (cf. Sec. 3.1.3), the RGE perturbativity constraints (cf. Sec. 3.1.5) and a tentative lower bound on the VL mass parameters (see the text) are imposed. In the Yukawa sector only the non-zero couplings are shown. Dimensionful quantities are given in GeV and GeV^2.

only for those couplings whose values must be of order 1 (or larger) for phenomenological reasons. This observation allows us to reduce the RGE system and to simplify the analysis. In the Yukawa sector, the couplings of interest are x_{34}^Q, y_{43}^u, y_{34}^u and x_{43}^u (see Sec. 3.1.2 for the discussion). We find that the modulus of their value cannot exceed 1.4 at μ_0 if they are to remain perturbative up to 50 TeV. This conclusion is derived under the assumption that all the other couplings (but two) are set to 1 at the initial scale μ_0. The two exceptions are y_{14}^d and y_{24}^e (expected to be much smaller than 1 as the Yukawas of the second generation), whose values at μ_0 are set to 0.7.
In the scalar sector, the perturbativity bounds are presumably most relevant for the couplings λ_1, λ_6 and λ_7, whose RGEs feature a power-four dependence on the large Yukawa couplings y_{43}^u, x_{43}^u and x_{34}^Q. In Fig. 3.2 we illustrate the RG running of λ_1, λ_6 and λ_7 for a randomly chosen benchmark point which satisfies all the constraints discussed in Secs. 3.1.2 and 3.1.3. The running of all the remaining quartic couplings is very slow in the considered energy range and does not pose any danger from the point of view of their perturbativity. Once the whole system is analyzed with the alignment conditions (3.24) and (3.25) in place, it turns out that the perturbativity requires the modulus of the quartic couplings to be smaller than 2. A straightforward consequence of this result is that all the benchmark points found previously in Ref. [60] are disfavored.

3.1.6 Numerical analysis and benchmark scenarios

In this section we perform a global numerical analysis of the model. We begin by discussing the employed scanning methodology, the definition of the chi-square (χ^2) statistics and the initial ranges for all the model's parameters. Next, we present three best-fit benchmark scenarios which arise from the minimization of the χ^2 function. Finally, we provide a discussion of some experimental signatures that these benchmark scenarios could produce.

3.1.6.1 Scanning methodology

In Table 3.2 we summarize the scanning ranges for all the parameters of the model. These include the quartic couplings and the soft-breaking term of the scalar potential (3.19), the non-zero Yukawa couplings and the mass parameters of the lagrangian (3.1), the vev of the singlet scalar, and $\tan\beta$.

In the scalar sector the alignment conditions (3.24) and (3.25) are imposed, leading to the limited scanning ranges for λ_3, λ_5 and λ_7 (cf. Eqs. (3.34) and (3.35)). For all the other quartic couplings the perturbativity bounds discussed in Sec. 3.1.5 are enforced. Similarly, the Yukawa couplings are scanned in the ranges consistent with their RGE perturbativity constraints. Finally, small values of some of the neutrino coupling constants are necessary to generate tiny masses for the SM neutrinos.

A tentative lower bound of 1200 GeV is imposed on the VL quark mass parameters. This is a rough (and conservative) approximation of the constraints from the direct NP searches at the LHC, which will be discussed in more details in Sec. 3.1.7.1. The scanning range for v_ϕ then follows from the requirement of reproducing the correct mass of the top quark, as discussed in Sec. 3.1.2.1. Similarly, we adopt 200 GeV lower bounds on the VL lepton mass parameters in order to be roughly consistent with the corresponding LHC constraints, which we examine in Sec. 3.1.7.2. Finally, the range for μ_{sb}^2 was chosen to make sure that the mass of the associated CP-odd state (cf. Eq. (3.32)) is not excluded by the current experimental searches [63].

The experimental constraints employed in our numerical scan are listed in Table 3.3. The central values and the experimental errors for the quark and lepton masses and for the CKM matrix elements are quoted after the PDG report [63]. Since the uncertainties for m_μ and m_τ are very small, rendering the fitting procedure numerically challenging, we adopt an error of 10% for these two observables. The experimental constraints from the flavor physics were discussed in Sec. 3.1.4.

We construct the χ^2-statistic function as

$$\chi^2 = \sum_i \frac{\left(\mathcal{O}_i^{\text{model}} - \mathcal{O}_i^{\text{cen}}\right)^2}{(\mathcal{O}_i^{\text{err}})^2}\,, \tag{3.55}$$

where $\mathcal{O}_i^{\text{model}}$ indicates the value of an observable calculated in our model, $\mathcal{O}_i^{\text{cen}}$ is the central value of its experimental measurement, $\mathcal{O}_i^{\text{err}}$ is the corresponding experimental error, and the sum runs over all the measured observables listed in Table 3.3. The upper bounds, corresponding to the last three rows of Table 3.3, are not included in the χ^2 function, but applied as hard-cuts instead (a point in the parameter space is rejected if such a condition is not satisfied). Benchmark points are obtained by minimization of the χ^2 function.

3.1.6.2 Benchmark scenarios

In Table 3.4 we present input parameters for three best-fit benchmark scenarios identified by performing the numerical scan discussed in Sec. 3.1.6.1. The corresponding mass spectra are summarized in Table 3.5 while the breakdown of individual contributions to the χ^2 function is shown in Table 3.6.

In general, the three benchmark scenarios demonstrate quite similar features, both in terms of the input parameters and of the resulting NP spectra. This is largely due to the fact that we aim at reproducing masses and mixings of the SM fermions and this, as we discussed in Sec. 3.1.2, puts strong constraints on (some of) the model's parameters. For example, the Yukawa couplings which link the VL sector with the SM fermions of the third generation are in general larger than those associated with the second generation.

On the other hand, fitting the CKM matrix is a little bit more tricky and the bulk of the total χ^2 stems from this very sector. As anticipated in Sec. 3.1.2.2, the main contribution to the χ^2 function is given by the element $|V_{td}|$, with the corresponding $\chi^2_{V_{td}}$ ranging from 16 for BP1 to 25 for BP3. Smaller yet still relevant contributions come from the entries $|V_{ub}|$ and $|V_{ts}|$.

	Central Value	Exp. Error		Central Value	Exp. Error
m_μ	0.10566	10%	$\lvert V_{ud}\rvert$	0.97370	0.00014
m_τ	1.77686	10%	$\lvert V_{us}\rvert$	0.22450	0.00080
m_c	1.270	0.020	$\lvert V_{ub}\rvert$	0.00382	0.00024
m_s	0.0934	0.0034	$\lvert V_{cd}\rvert$	0.22100	0.00400
m_b	4.18	0.02	$\lvert V_{cs}\rvert$	0.98700	0.01100
m_t	172.76	0.30	$\lvert V_{cb}\rvert$	0.04100	0.00140
Δa_μ	2.49×10^{-9}	0.48×10^{-9}	$\lvert V_{td}\rvert$	0.00800	0.00030
			$\lvert V_{ts}\rvert$	0.03880	0.00110
			$\lvert V_{tb}\rvert$	1.01300	0.03000
	Upper bound				
$\mathrm{BR}\,(\tau \to \mu\gamma)$	$< 4.2 \times 10^{-8}$				
$\mathrm{BR}\,(\tau \to 3\mu)$	$< 2.1 \times 10^{-8}$				
Δ_{CKM}	< 0.05				

TABLE 3.3: The experimental measurements which we employ in our numerical scan. Masses are in GeV.

Finally, an order 10 contribution to the χ^2 function from the element $|V_{us}|$ is mainly due to a very small experimental error associated with this particular observable. All other elements of the CKM matrix are fitted within their 1σ experimental ranges. The two remaining best-fit points follow the same pattern. Incidentally, note that the CKM anomaly is $\mathcal{O}(10^{-4})$ in our setup, well below the experimental upper bound of Eq. (3.47).

Interestingly, in all three cases each quartic (Yukawa) coupling remains smaller than 4π ($\sqrt{4\pi}$) up to 1000 TeV. We can therefore conclude that the validity range of our model extends well beyond the putative scale of 50 TeV.

Masses of the NP leptons are determined, to a large extent, by correctly fitting the experimental value of Δa_μ (an overall contribution from this observable to the total χ^2 function does not exceed 0.7 in all the benchmark scenarios). Contributions to Δa_μ from the individual one-loop diagrams of Fig. (3.1) are summarized in Table 3.7. We present separately fractions of Δa_μ generated by the charged scalars $h^\pm$ and the neutral leptons $N_{1,2,3,4}$, by the CP-odd scalars $a_{1,2}$ and the charged leptons $E_{1,2}$, and by the CP-even scalars $h_{1,2,3}$ and the charged leptons $E_{1,2}$. We also show the sum of all the contributions of a given type, indicated by a subscript "tot".

We observe that the largest contributions to Δa_μ arise from the charged scalar/heavy neutrino loops. As we show in our analysis, all possible one-loop diagrams contributing to Δa_μ should be treated at equal footing and none of them should be discarded *a priori*.

Even more interestingly, the observed dominance of the heavy neutrino contributions to the anomalous magnetic moment of the muon seems to be a generic feature of the model which does not pertain exclusively to the identified benchmark scenarios. The charged scalar/heavy neutrino loops are determined, among other parameters, by combinations of the y'^{ν} couplings which are not constrained by any SM masses and mixing and thus can become relatively large. Contrarily, the same Yukawa coupling is responsible for the generation of the neutral (pseudo)scalar/charged lepton loops and for the correct tree-level mass of the muon. It is thus required to be small and the corresponding contributions to Δa_μ are

Scalar sector							
	BP1	BP2	BP3		BP1	BP2	BP3
$\tan\beta$	13	8	12	λ_1	0.258	0.258	0.258
v_u	245.3	244.3	245.2	λ_2	0.514	0.153	0.623
v_d	18.9	30.5	20.4	λ_3	0.257	0.260	0.256
v_ϕ	1015	1077	1012	λ_4	0.552	0.304	0.167
μ_u^2	-7.8×10^3	-6.6×10^3	-7.6×10^3	λ_5	-0.039	-0.072	-0.061
μ_d^2	-8.2×10^3	-8.6×10^4	-3.4×10^4	λ_6	0.370	0.487	0.663
μ_ϕ^2	-4.9×10^4	-9.4×10^4	-2.3×10^5	λ_7	0.001	0.002	0.002
$\mu_{\rm sb}^2$	1.4×10^5	1.9×10^5	1.1×10^5	λ_8	0.254	0.423	0.417
Quark sector				Lepton sector			
	BP1	BP2	BP3		BP1	BP2	BP3
y_{24}^u	-0.051	-0.049	0.050	y_{24}^e	0.028	-0.015	0.022
y_{34}^u	-0.980	1.185	-1.024	y_{34}^e	-0.895	0.612	0.790
x_{34}^Q	0.924	-0.842	-0.877	x_{34}^L	0.616	-0.729	0.724
y_{43}^u	1.382	1.093	-1.337	y_{43}^e	-0.223	0.144	-0.191
x_{42}^u	0.550	0.821	-0.595	x_{42}^e	0.156	0.165	0.188
x_{43}^u	1.286	1.261	1.263	x_{43}^e	-0.168	0.228	-0.205
y_{14}^d	-0.022	0.035	0.026	y_{14}^ν	-2×10^{-11}	5×10^{-11}	3×10^{-11}
y_{24}^d	0.096	0.151	-0.113	y_{24}^ν	3×10^{-11}	8×10^{-12}	6×10^{-11}
y_{34}^d	-0.684	0.274	0.267	y_{34}^ν	-5×10^{-11}	9×10^{-11}	9×10^{-11}
y_{43}^d	-0.672	-0.489	0.656	$y_{14}^{\prime\nu}$	-0.824	-0.674	-0.674
x_{42}^d	-0.371	-0.110	0.225	$y_{24}^{\prime\nu}$	-0.895	-0.874	-0.896
x_{43}^d	-0.160	0.072	-0.127	$y_{34}^{\prime\nu}$	0.701	0.744	-0.812
Mass parameters							
	BP1	BP2	BP3		BP1	BP2	BP3
M_4^u	-1317	1405	1334	M_4^e	-517	-575	533
M_4^d	-3644	3068	-2882	M_4^ν	204	-212	217
M_4^Q	-1384	1443	1322	M_4^L	-206	-222	-202

TABLE 3.4: Input parameters for three best-fit benchmark scenarios. Dimensionful quantities are given in GeV and GeV^2.

suppressed. Additionally, one also observes cancellations between the individual contributions to Δa_μ stemming from the (pseudo)scalar diagrams with different VL leptons, which is a known and common feature of many NP models with the VL fermions (see, e.g., [109, 110] for a discussion).

Finally, we should mention the size of the BRs for the lepton flavor violating decays $\tau \to \mu\gamma$ and $\tau \to 3\mu$ in our model, which are of the order $(3-4)\times10^{-8}$ for the former and $(6-9)\times10^{-10}$ for the latter. Given that in the future the Belle-II collaboration is expected to improve their current exclusion bounds by an order of magnitude or more [111, 112], it may turn out that the tau leptonic decays offer the best experimental way of verifying the predictions of the NP model analyzed in this study.

		SM fermions					
	BP1	BP2	BP3		BP1	BP2	BP3
m_c	1.262	1.282	1.259	m_μ	0.110	0.110	0.110
m_t	172.7	172.8	172.6	m_τ	1.864	1.756	1.765
m_s	0.089	0.093	0.091	m_{ν_2} $[10^{-10}]$	4.659	6.587	0.252
m_b	4.169	4.196	4.175	m_{ν_3} $[10^{-10}]$	8.253	18.38	20.95
			NP fermions				
		Quark sector				Lepton sector	
	BP1	BP2	BP3		BP1	BP2	BP3
M_{U_1}	1495	1561	1440	M_{E_1}	487	596	554
M_{U_2}	1708	1842	1704	M_{E_2}	543	615	570
M_{D_1}	1534	1579	1464	$M_{N_{1,2}}$	205	214	218
M_{D_2}	3655	3070	2888	$M_{N_{3,4}}$	488	598	556
			Scalars				
	BP1	BP2	BP3		BP1	BP2	BP3
M_{h_1}	125	125	125	M_{a_1}	362	411	433
M_{h_2}	362	412	435	M_{a_2}	532	614	469
M_{h_3}	617	752	824	$M_{h^\pm}$	384	423	440

TABLE 3.5: Mass spectra for three best-fit benchmark scenarios. All masses are in GeV.

3.1.7 LHC study of the benchmark scenarios

In this section we confront the benchmark scenarios identified in Sec. 3.1.6 with the null results of the direct NP searches at the LHC. We analyze, one by one, the constraints originating from considering the production of VL quarks, VL leptons, and exotic scalars.

3.1.7.1 Vector-like quarks

The VL quarks (VLQs) can be copiously produced at the LHC, either in pairs through the strong interactions or singly through an exchange of the EW gauge bosons. In the former case, the dominant production channels at the leading order are gluon fusion and quark-antiquark annihilation, whose production cross sections depend on the VLQ mass and its $SU(3)_C$ quantum numbers only (see Refs. [113, 114] for analytical formulae). Therefore, the experimental lower bounds on VLQ masses are expected to be, to a large extent, model independent, baring only a slight dependence on the relative strength of the individual VLQ decay channels.

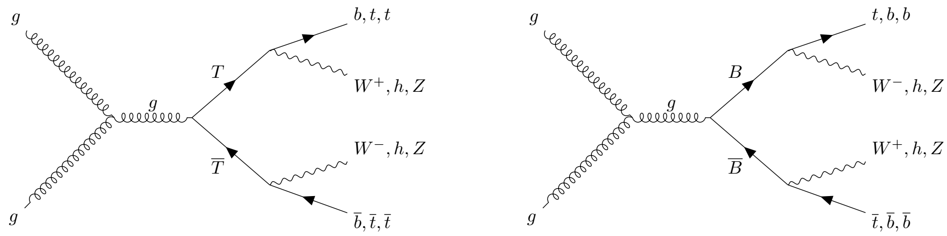

FIGURE 3.3: Pair production of the VLQs T and B via the gluon fusion at the LHC considered by the ATLAS collaboration in Ref. [115].

Quarks masses				CKM elements			
	BP1	BP2	BP3		BP1	BP2	BP3
χ_c^2	0.154	0.360	0.280	$\chi_{V_{us}}^2$	8.225	8.290	5.986
χ_t^2	0.022	0.018	0.119	$\chi_{V_{ub}}^2$	12.33	10.36	9.327
χ_s^2	1.569	0.014	0.450	$\chi_{V_{td}}^2$	15.69	18.30	24.58
χ_b^2	0.330	0.640	0.052	$\chi_{V_{ts}}^2$	10.45	9.796	6.559
χ_Q^2	2.075	1.031	0.901	χ_V^2	55.45	55.26	55.92
Charged leptons masses				Δa_μ			
χ_μ^2	0.210	0.170	0.207	$\chi_{\Delta a_\mu}^2$	0.328	0.657	0.375
χ_τ^2	0.241	0.014	0.004	Total			
χ_L^2	0.451	0.183	0.211	χ_{TOT}^2	58.30	57.31	57.41

TABLE 3.6: Breakdown of the χ^2 contributions from various observables implemented in the χ^2 function of Eq. (3.55). The CKM contributions which are smaller than 3 are not shown. χ_Q^2, χ_L^2 and χ_V^2 indicate total χ^2 contributions from the quark masses, lepton masses, and the CKM matrix elements, respectively. χ_{TOT}^2 stands for the total χ^2 function of each best-fit scenario.

The most recent analysis from ATLAS, based on the data from proton-proton collisions at a centre-of-mass energy of $\sqrt{s} = 13$ TeV, corresponding to an integrated luminosity of 139 fb^{-1} [115], considered the pair production of VL top partners T and VL bottom partners B with the decay channels $T \to Zt, ht, Wb$ and $B \to Zb, hb, Wt$ and with large missing transverse momentum. The corresponding Feyman diagrams are depicted in Fig. 3.3. The strongest 95% C.L. lower bounds on the VLQ mass derived in Ref. [115] read

$$M_{T/B} > 1.41\,\mathrm{TeV} \tag{3.56}$$

for the EW doublets[2] and

$$M_T > 1.26\,\mathrm{TeV}, \qquad M_B > 1.33\,\mathrm{TeV} \tag{3.57}$$

for the EW singlets.[3] The analogous results from CMS can be found in Ref. [116]. Similarly, by assuming that at least one of the VLQs decays into a Z boson with the BR=100%, the 13 TeV ATLAS search [117] obtained even stronger bounds,

$$M_T > 1.60\,\mathrm{TeV}, \qquad M_B > 1.42\,\mathrm{TeV}\;. \tag{3.58}$$

At first glance it may seem that all our benchmark scenarios are consistent with the VLQ exclusion bounds. On the other hand, in the model considered in this study the couplings of the physical heavy quarks $U_{1,2}$ and $D_{1,2}$ with the third-generation SM quarks and the EW gauge (Higgs) bosons are generated via tree-level mixing after the EW and $\mathrm{U}(1)_X$ symmetries are spontaneously broken (cf. Sec. 3.1.2 and Appendix 3.A). Since there is *a priori* no reason for the resulting BRs to correspond to any of the benchmark cases considered by ATLAS and CMS in their analyses (exotic decays to the charged Higgs are possible, for example), we need to reexamine the experimental results in the framework of our model.

[2] For the VLQ mass larger than 800 GeV this indicates BR($T \to Zt$)=BR($T \to ht$) = 50% and BR($B \to Wt$) = 100% [115].

[3] For the VLQ mass larger than 800 GeV this indicates BR($T \to Zt$) = 25%, BR($T \to ht$) = 25%, BR($T \to Wb$) = 50%, BR($B \to Zb$) = 25%, BR($B \to hb$) = 25% and BR($B \to Wt$) = 50% [115].

Contributions to $\Delta a_\mu \times 10^9$							
Charged scalars				CP-even scalars			
Loop	BP1	BP2	BP3	Loop	BP1	BP2	BP3
$h^\pm, N_{1,2}$	-1.076	-0.792	-0.942	h_1, E_1	-0.003	-0.001	-0.009
$h^\pm, N_{3,4}$	3.300	2.898	3.153	h_1, E_2	0.003	0.001	0.009
$h^\pm, N_{\text{tot}}$	2.225	2.106	2.211	h_2, E_1	-0.409	-0.520	-0.969
CP-odd scalars				h_2, E_2	0.437	0.548	0.994
a_1, E_1	0.425	0.528	0.938	h_3, E_1	0.018	0.115	0.076
a_1, E_2	-0.544	-0.611	-1.529	h_3, E_2	-0.017	-0.127	-0.076
a_2, E_1	-0.033	-0.135	-0.071	h, E_{tot}	0.032	0.027	0.025
a_2, E_2	0.110	0.196	0.621	Total			
a, E_{tot}	-0.015	-0.023	-0.041	Δa_μ	2.215	2.101	2.196

TABLE 3.7: Contributions to Δa_μ from the individual one-loop diagrams shown in Fig. (3.1). The subscript "tot" indicates the sum of all the contributions of a given type.

	M_{U_1}	$\sigma(pp \to U_1U_1)$	M_{U_2}	$\sigma(pp \to U_2U_2)$	M_{D_1}	$\sigma(pp \to D_1D_1)$	M_{D_2}	$\sigma(pp \to D_2D_2)$
BP1	1495	1.3×10^{-3}	1708	3.9×10^{-4}	1534	1.0×10^{-3}	3655	4.5×10^{-9}
BP2	1561	8.9×10^{-4}	1842	1.9×10^{-4}	1579	8.1×10^{-4}	3070	1.6×10^{-7}
BP3	1440	1.8×10^{-3}	1704	4.0×10^{-4}	1464	1.6×10^{-3}	2888	5.0×10^{-7}

TABLE 3.8: Cross sections (in pb) for the pair production of the VLQs for our three benchmark scenarios. Masses are in GeV.

To this end, we calculate with `MadGraph5 MC@NLO` [118] the cross sections for the pair production of U_1, U_2, D_1 and D_2. The results are presented in Table 3.8. By comparing these numbers with the observed experimental 95% C.L. upper bounds on the signal cross section from Ref. [115] (to give an example, $\sigma^{\text{exp}}_{95\%}(p\,p \to \bar{T}T) = 4 \times 10^{-3}$ pb for $M_{\text{VLQ}} = 1.5$ TeV) we conclude that our benchmark scenarios are indeed not excluded by the current LHC searches for the VLQs, irrespectively of the actual sizes of their BRs.
It is instructive to investigate the prospects of testing our model in future runs at the LHC. The total cross section for the VLQ pair production, followed by a decay into the third generation quarks and the EW gauge/Higgs bosons, can be expressed using the narrow width approximation (NWA) as

$$\tilde{\sigma}\left(pp \to \overline{Q}Q \to f\bar{f}\,VV\right) \approx \sigma\left(pp \to Q\overline{Q}\right) \text{BR}\left(Q \to fV\right) \text{BR}\left(\overline{Q} \to \bar{f}V\right), \tag{3.59}$$

where $Q = U_{1,2}, D_{1,2}$, $f = t, b$ and $V = W, Z, h_1$. Under the assumption that $\text{BR}\left(Q \to fV\right) = \text{BR}\left(Q \to h_1 t/b\right) + \text{BR}\left(Q \to Zt/b\right) + \text{BR}\left(Q \to Wb/t\right) = 1$, the cross section (3.59) reduces to the signal cross section constrained by the experimental collaborations, $\sigma^{\text{exp}}_{95\%} \approx \sigma\left(pp \to Q\overline{Q}\right)$. If, on the other hand, the three BRs do not sum to one, we expect the resulting exclusion bounds to be weaker than the bounds reported by ATLAS and CMS.
The lightest VLQ in our model, U_1, is characterized by the following BRs:

$$\begin{aligned}
\text{BP1}: &\quad \text{BR}\left(U_1 \to h_1 t\right) = 0.188, \quad \text{BR}\left(U_1 \to Zt\right) = 0.146, \quad \text{BR}\left(U_1 \to Wb\right) = 0.040\\
\text{BP2}: &\quad \text{BR}\left(U_1 \to h_1 t\right) = 0.135, \quad \text{BR}\left(U_1 \to Zt\right) = 0.101, \quad \text{BR}\left(U_1 \to Wb\right) = 0.044\\
\text{BP3}: &\quad \text{BR}\left(U_1 \to h_1 t\right) = 0.209, \quad \text{BR}\left(U_1 \to Zt\right) = 0.165, \quad \text{BR}\left(U_1 \to Wb\right) = 0.037
\end{aligned} \tag{3.60}$$

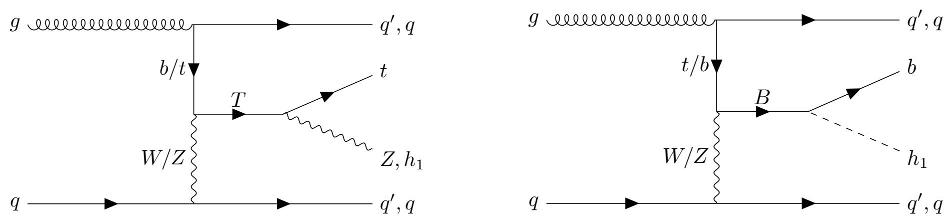

FIGURE 3.4: Single production of the VLQs T and B via the EW gauge boson exchange at the LHC, as considered by the ATLAS collaboration in Refs. [119–121] for T and in Ref. [122] for B.

with the resulting cross sections $\widetilde{\sigma}^{\mathrm{BP1}} = 1.8 \times 10^{-4}$ pb, $\widetilde{\sigma}^{\mathrm{BP2}} = 7.0 \times 10^{-5}$ pb and $\widetilde{\sigma}^{\mathrm{BP3}} = 3.0 \times 10^{-4}$ pb. The second-to-the-lightest VLQ, D_1, has

$$\begin{aligned}
\mathrm{BP1}: &\quad \mathrm{BR}\,(D_1 \to h_1 b) = 0.001, \quad \mathrm{BR}\,(D_1 \to Zb) = 0.001, \quad \mathrm{BR}\,(D_1 \to Wt) = 0.375 \\
\mathrm{BP2}: &\quad \mathrm{BR}\,(D_1 \to h_1 b) = 0.001, \quad \mathrm{BR}\,(D_1 \to Zb) = 0.001, \quad \mathrm{BR}\,(D_1 \to Wt) = 0.221 \\
\mathrm{BP3}: &\quad \mathrm{BR}\,(D_1 \to h_1 b) = 0.001, \quad \mathrm{BR}\,(D_1 \to Zb) = 0.001, \quad \mathrm{BR}\,(D_1 \to Wt) = 0.387
\end{aligned} \tag{3.61}$$

with $\widetilde{\sigma}^{\mathrm{BP1}} = 1.4 \times 10^{-4}$ pb, $\widetilde{\sigma}^{\mathrm{BP2}} = 4.1 \times 10^{-5}$ pb and $\widetilde{\sigma}^{\mathrm{BP3}} = 2.4 \times 10^{-4}$ pb. We can thus conclude that in order to probe the VL masses featured by our benchmark scenarios, at least one order of magnitude enhancement of the experimental sensitivity in the VLQ searches is required.

Finally, we analyze the possibility of testing the model via processes in which the VLQs are produced one at the time. The single VL T quark production was analyzed by ATLAS in Refs. [119–121], while the single VL B quark production in Ref. [122]. The corresponding Feynman diagrams are shown in Fig. 3.4. The 95% C.L. experimental upper bounds on the relevant signal cross sections are of the order $(10^{-2} - 10^{-1})$ pb.

We calculated the cross sections for the VLQ single productions of our three benchmark points using the NWA. The hadronic cross sections were obtained with `MadGraph5 MC@NLO` and the BRs with `SPheno`. We found that the cross section for a single production of the VLQs U_1 is $\mathcal{O}(10^{-5})$ pb, while for D_1 it amounts to $\mathcal{O}(10^{-7})$ pb. We can thus conclude that in our model the single production is a less promising search strategy than the pair production. This was to be expected as the single production is in general less competitive than the pair production for the Yukawa couplings smaller than 1, see e.g. [123, 124].

3.1.7.2 Vector-like leptons

At the tree level, the VL leptons (VLLs) are pair produced at the LHC via the Drell-Yan processes. The corresponding cross sections for our three benchmark scenarios are collected in Table 3.9. The analysis of all the possible experimental signatures is in this case much more involved than for the VLQs as the lepton decay BRs strongly depend on the presence in the spectrum of the exotic scalars lighter than the VLLs. The following mass hierarchies are observed:

$$\begin{aligned}
\mathrm{BP1}: &\quad M_{N_{1,2}} < M_{h_2}, M_{a_1}, M_{h^\pm} < M_{E_1}, M_{N_{3,4}} < M_{a_2} < M_{E_2} < M_{h_3} \\
\mathrm{BP2}: &\quad M_{N_{1,2}} < M_{h_2}, M_{a_1}, M_{h^\pm} < M_{E_1}, M_{N_{3,4}} < M_{a_2} < M_{E_2} < M_{h_3} \\
\mathrm{BP3}: &\quad M_{N_{1,2}} < M_{h_2}, M_{a_1}, M_{h^\pm} < M_{a_2} < M_{E_1}, M_{N_{3,4}} < M_{E_2} < M_{h_3}\,.
\end{aligned} \tag{3.62}$$

In all the cases the lightest VLLs, neutrinos $N_{1,2}$, originate predominantly from the $\mathrm{SU(2)}_L$ singlets and their production cross section at the LHC is suppressed, $\mathcal{O}(10^{-5})$ pb.

	M_{E_2}	$\sigma(pp \to \bar{E}_2 E_2)$	M_{E_1}	$\sigma(pp \to \bar{E}_1 E_1)$	$M_{N_{3,4}}$	$\sigma(pp \to N_{3,4} N_{3,4})$	$\sigma(pp \to E_1 N_{3,4})$
BP1	543	1.5×10^{-3}	487	5.7×10^{-3}	488	2.7×10^{-5}	3.6×10^{-3}
BP2	615	8.0×10^{-4}	596	1.8×10^{-3}	598	8.5×10^{-6}	1.2×10^{-3}
BP3	570	1.2×10^{-3}	554	2.8×10^{-3}	556	2.8×10^{-5}	1.8×10^{-3}

TABLE 3.9: Cross sections (in pb) for the pair production of the VLLs for our three benchmark scenarios. Masses are in GeV.

The second-to-the-lightest VLLs, E_1 and heavy neutrinos $N_{3,4}$, come from the same SU(2)$_L$ doublets and are almost degenerate in mass. Therefore, three production channels should be considered simultaneously: $p\,p \to Z/\gamma \to E_1 \bar{E}_1$, $p\,p \to Z/\gamma \to N_{3,4} N_{3,4}$ and $p\,p \to W^\pm \to E_1 N_{3,4}$. The dominant branching ratios for the subsequent decays of E_1 and $N_{3,4}$, evaluated with `SPheno`, are collected in Table 3.10. In all three cases the VLLs decay predominantly to the SM muons, which is a direct consequence of the fact that we impose Δa_μ as a constraint in our likelihood function and the largish muon-lepton-scalar Yukawa couplings are preferred. A closer look at Table 3.10 reveals that the relative strengths of various VLL decay channels are, to some extent, scenario dependent. Moreover, the final experimental signatures hinge on the subsequent decay channels of the scalar particles, which are also pretty complex (we discuss it in more details in Sec. 3.1.7.3). As an example, let us consider a process $p\,p \to E_1\,\bar{E}_1 \to \mu\,\bar{\mu}\,a_1\,a_1$ for the benchmark scenario BP1. The lightest pseudoscalar can decay in this case either to a $b\,\bar{b}$ pair (with the BR of 28%) or to $\nu\,N_{1,2}$ (with the BR of 69%). The decay of the heavy neutrinos then proceeds as $N_{1,2} \to e^\pm/\mu^\pm\,W^\pm$ with the BR of 56%, or $N_{1,2} \to \nu\,Z$ with the BR of 28%. We can thus expect the following distinctive experimental signatures emerging from the $p\,p \to E_1\,\bar{E}_1 \to \mu\,\bar{\mu}\,a_1\,a_1$ process: a) 2 muons + (b)-jets, b) multileptons + missing energy, c) multileptons + jets + missing energy, with the total signal cross section reduced w.r.t. the production cross section reported in Table 3.9 by the product of the subsequent BRs.

To make the things even worse, there are not many LHC analysis that would explicitly look for the VLLs. The only dedicated ATLAS search, based on the 139 fb^{-1} of data from the 13 TeV run [125], looks for the VLLs coupled predominantly to taus. The analogous CMS analysis based on the 77.4 fb^{-1} of data can be found in Ref. [126]. The decay chains considered by the two collaborations are shown in Fig. 3.5. In both cases, the total cross sections for the VLL production can be probed down to 10^{-3} pb (of course, the actual value is mass dependent).

In our model all three benchmark scenarios feature very low BRs for E_1 and $N_{3,4}$ decaying to taus, which do not exceed 10%. We can thus expect a strong suppression of the resulting

BR	BP1	BR	BP2	BR	BP3
$E_1 \to \mu\,a_1$	37%	$E_1 \to \mu\,a_1$	23%	$E_1 \to \mu\,a_1$	21%
$E_1 \to \mu\,h_2$	37%	$E_1 \to \mu\,h_2$	24%	$E_1 \to \mu\,h_2$	25%
		$E_1 \to N_{1,2}\,W^\pm$	26%	$E_1 \to \tau\,a_1$	11%
BR	BP1	BR	BP2	BR	BP3
$N_{3,4} \to \mu\,h^\pm$	70%	$N_{3,4} \to \mu\,h^\pm$	51%	$N_{3,4} \to \mu\,h^\pm$	56%
		$N_{3,4} \to N_{1,2}\,Z$	12%		
		$N_{3,4} \to N_{1,2}\,h_1$	11%		

TABLE 3.10: Dominant BRs for the decays of E_1 and $N_{3,4}$.

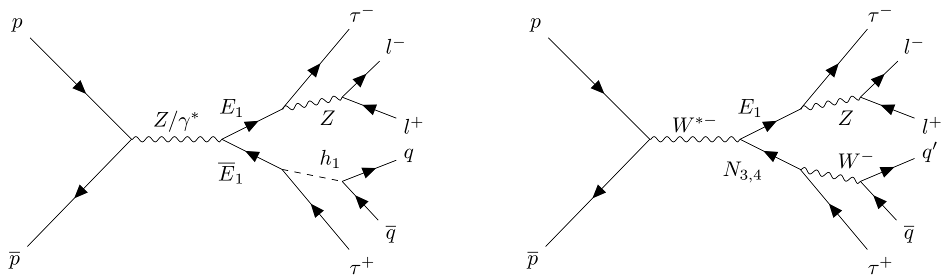

FIGURE 3.5: Pair production of the VLLs E_1 and $N_{3,4}$ at the LHC, as considered by the ATLAS [125] and CMS [126] collaborations.

signal w.r.t. the experimental analysis. Indeed, using the NWA the total cross section for the process considered in Refs. [125] and [126] can be written as follows:

$$\begin{aligned} \sigma\left(p\,p \to \tau^-\tau^+l^-l^+q\,\overline{q}\right) \;&\approx\; \sigma\left(p\,p \to E_1\overline{E}_1\right) \mathrm{BR}\left(E_1 \to \tau^-l^-l^+\right) \mathrm{BR}\left(\overline{E}_1 \to \tau^+q\,\overline{q}\right) \\ &+\; \sigma\left(p\,p \to E_1N_{3,4}\right) \mathrm{BR}\left(E_1 \to \tau^-l^-l^+\right) \mathrm{BR}\left(N_{3,4} \to \tau^+q\,\overline{q}\right) \end{aligned} \tag{3.63}$$

Combining the cross sections from Table 3.9 with the relevant BRs calculated with `SPheno`, we obtain

$$\begin{aligned} \mathrm{BP1}: \quad \sigma\left(p\,p \to \tau^-\tau^+l^-l^+q\,\overline{q}\right) \; &= 8.3 \times 10^{-7}\ \mathrm{pb} \\ \mathrm{BP2}: \quad \sigma\left(p\,p \to \tau^-\tau^+l^-l^+q\,\overline{q}\right) \; &= 8.1 \times 10^{-6}\ \mathrm{pb} \\ \mathrm{BP3}: \quad \sigma\left(p\,p \to \tau^-\tau^+l^-l^+q\,\overline{q}\right) \; &= 5.3 \times 10^{-7}\ \mathrm{pb}\,. \end{aligned} \tag{3.64}$$

If we now compare the predictions of Eq. (3.64) with the corresponding experimental 95% C.L. exclusion cross sections from Ref. [125], we can conclude that the benchmark scenarios identified in Sec. 3.1.6 are not excluded by the dedicated LHC searches for the VLLs.[4] Moreover, it may also be challenging to test the VLL sector of our model in future runs at the LHC, if no dedicated experimental strategies for the muon final state signatures are proposed.

3.1.7.3 Exotic scalars

Finally, we investigate the possibility of testing the predictions of our model via the LHC searches in the scalar sector. There is a plethora of experimental analyses, both by ATLAS and CMS, that look for the non-SM Higgs bosons (see Ref. [128] for a recent review in the framework of the 2HDM). At the same time, in our benchmark scenarios the exotic scalars can decay through a variety of channels (the dominant BRs, obtained with `SPheno`, are collected in Table 3.11).

To facilitate the analysis, we use the publicly available code `HiggsTools` [129], a toolbox for evaluating bounds from the direct searches for the exotic scalar particles at LEP and the LHC, whose database contains 258 different limits. We find that all our benchmark scenarios are tagged as "allowed" by `HiggsTools`.

It is instructive to take a closer look at the output of `HiggsTools`, as it indicates which searches are most sensitive to the spectra featured by our best-fit scenarios. This is quantified by a parameter called "observed ratio", R_{obs}, which is the ratio of the predicted cross section and the experimental limit at the 95% C.L. The point in the parameter space is excluded if $R_{\mathrm{obs}} > 1$. We observe that the highest values of R_{obs} (0.6 for BP1 and BP3, 0.14

[4] In principle, some of the SUSY searches looking for the chargino/neutralino production, e.g. Ref. [127], analyze signatures that could be generated in our model. However, the resulting cross section for such a process is way too low to allow the derivation of any constraints.

Process	BP1	BP2	BP3
$a_1 \to \nu\, N_{1,2}$	69%	82%	72%
$a_1 \to \bar{b}\, b$	28%	14%	25%
$a_2 \to \bar{t}\, t$	73%	73%	36%
$a_2 \to \bar{b}\, b$			15%
$a_2 \to \nu\, N_{1,2}$			46%
$h_2 \to \nu\, N_{1,2}$	69%	84%	72%
$h_2 \to \bar{b}\, b$	28%	14%	25%
$h_3 \to \bar{t}\, t$	50%	43%	34%
$h_3 \to \bar{\tau}\, E_1$	10%	9%	20%
$h^{\pm} \to \bar{\mu}\, N_{1,2}$	41%	51%	48%
$h^{\pm} \to \bar{e}\, N_{1,2}$	34%	30%	26%
$h^{\pm} \to \bar{b}\, t$	19%	13%	19%

TABLE 3.11: Dominant BRs ($> 5\%$) for the decays of the exotic scalars.

for BP2) are reached for the $h_2 \to \tau^+\tau^-$ and $a_1 \to \tau^+\tau^-$ decays constrained by the ATLAS 139 fb^{-1} analysis [130], despite very low decay BRs in this channel.
To investigate it in more details, we calculated the $a_1/h_2 \to \tau^+\tau^-$ cross sections with `MadGraph5 MC@NLO`. The results are reported in the last three columns of Table 3.12. These are to be compared with the 95% C.L. experimental lower bounds on the cross section reported in the third column of Table 3.12. We find a very good agreement with the output of `HiggsTools` in terms of the parameter $R_{\rm obs}$, thus confirming that the decays of the exotic scalars into taus are going to be the most promising way of testing the predictions of the model at the LHC.
In Table 3.12 we also present other decay channels of a_1 and h_2 that feature the high sensitivity. While the current experimental bounds on those searches are weaker that those relative to the $\tau^-\tau^+$ final state, they may offer complementary signatures of the model in future LHC runs.
Incidentally, note that the BRs for the decays of h_2 and a_1 to the EW gauge bosons, $\gamma\gamma$, ZZ and WW, are $\mathcal{O}(10^{-8})$ and $\mathcal{O}(10^{-9})$, respectively, which is orders of magnitude below the current experimental bounds.
Finally, let us comment on the possibility of testing the $a_1/h_2 \to t^+t^-$ decay through the measurement of an effective coupling $g_{a_1/h_2 tt}$. This scenario was investigated by CMS in Ref. [131]. Comparing the values of the $g_{a_1/h_2 tt}$ coupling evaluated with `SPheno` (0.084 for BP2, 0.096 for BP3) with the experimental 95% C.L. upper bounds (0.80 for BP2 and 0.70 for BP3)[5] we conclude that no additional constraint on our model arises from this particular search.

3.1.8 Conclusions

In this study, we performed a global analysis of an extension of the SM which contains one full family of VL fermions, an extra $SU(2)_L$ scalar doublet and an $SU(2)_L$ scalar singlet. It also features a $U(1)_X$ global symmetry spontaneously broken by the singlet scalar vev. This

[5] The CMS analysis [131] does not cover the scalar masses below 400 GeV.

Channel	Experiment	$\sigma^{\rm exp}_{95\%}$ (BP1, BP2, BP3)			$\sigma^{\rm BP1}$	$\sigma^{\rm BP2}$	$\sigma^{\rm BP3}$
$a_1/h_2 \to \tau^+\tau^-$	CMS [132]	0.060	0.030	0.020	0.037	0.004	0.011
	ATLAS [130]	0.050	0.020	0.016			
$a_1/h_2 \to \mu^+\mu^-$	CMS [133]	0.007	0.006	0.005	1.3×10^{-4}	1.4×10^{-5}	4.4×10^{-5}
	ATLAS [134]	0.009	0.004	0.003			
$a_1/h_2 \to b^+b^-$	CMS [135]	6.0	3.5	3.0	0.554	0.061	0.061
	ATLAS [136]	–	–	–			
$h^\pm \to \bar{t}b$	CMS [137]	0.40	0.30	0.25	7.6×10^{-3}	2.1×10^{-3}	4.5×10^{-3}
	ATLAS [138]	0.45	0.30	0.25			

TABLE 3.12: An overview of the LHC scalar searches which present the highest sensitivity to the benchmark scenarios identified in Sec. 3.1.6. The columns show, respectively, the decay channel, the experimental analyses investigating this channel, the experimental 95% C.L. upper bound on the cross section for the mass corresponding to the mass of the scalar in a benchmark scenario, the actual cross section calculated in the benchmark scenario.

scenario was originally proposed in Ref. [58] to generate the masses of the third and the second family of the SM fermions, as well as to account correctly for their mixing patterns.
In our analysis we confronted the model with the experimental bounds from the flavor physics observables, which include the anomalous magnetic moment of the muon and the rare decays of the tau lepton. Additionally, the model was subjected to the theoretical constraints stemming from the stability of the scalar potential and from the perturbativity of the renormalized couplings. Importantly, we revisited and corrected the bounded-from-below and the alignment limits, which in the context of the same model were previously discussed in Refs. [60, 61]. In particular, we showed that additional constraints on the quartic couplings arise if the full three-scalar potential is considered. We also argued that the perturbativity bounds should not be imposed on the low-scale parameters of the lagrangian but on the running couplings evaluated at the renormalisation scale which sets an upper limit of the model's validity. These RG-based perturbativity conditions require the low-scale scalar couplings to be smaller than 2 and the Yukawa couplings smaller than 1.5.
With all the constraints in place, we performed a numerical scan of the model's parameter space and we identified three benchmark scenarios that satisfied all the theoretical and experimental requirements. One distinctive feature of these solutions is that the charged scalar/heavy neutrino loops provide dominant contributions to the observable Δa_μ. This finding is qualitatively different from the conclusions obtained in Refs. [60, 61] where only the charged lepton loops were considered. We would like to emphasize that the dominance of the heavy neutrino contribution to Δa_μ is a generic characteristic of the model and not a mere artifact of the specific benchmark scenarios. The main reason behind this feature is that the same coupling which generates the neutral scalar/charged lepton loops is also responsible for the correct tree-level mass of the muon and thus it is required to be small.
We also performed a detailed LHC analysis of our three best-fit scenarios. We investigated the experimental constraints stemming from the direct searches for VLQs, VLLs and exotic scalars. We found that none of the currently available exclusion bounds can test the spectra featured by the benchmark scenarios. This provides a proof of concept that the model in

study is feasible as an explanation of both the SM masses and mixings and of the relevant experimental phenomena.
Regarding future prospects for experimental verification of the model, several observations can be made. Firstly, both charged and neutral VLLs decay predominantly to muons in our framework. On the other hand, all currently available LHC analyses focus on taus in the final state, for which the cross sections obtained in our model are several orders of magnitude below the experimental sensitivity. Therefore, we would like to encourage the experimental collaborations to provide dedicated analyses of the VLLs coupled to the second family of the SM fermions. Such a study would not only allow to test the predictions of our model, but it would prove very useful in any phenomenological research that aims at explaining the muon $(g-2)$ anomaly in a NP framework with the VLLs.
Secondly, the experimental searches for the VLQs can become a fruitful testing ground for our model already in the current run of the LHC. The cross sections for the pair production of VLQs featured by the benchmark scenarios are one order of magnitude smaller than the current experimental upper bounds and should be in reach of the dedicated VLQs searches based on the larger data samples.
Finally, we observed that the most constraining decay channel for the exotic scalars is $a_1/h_2 \to \tau^+\tau^-$, for which the ratio of the predicted to the experimental cross sections is close to 1. It may thus provide complementary signatures of our model in future runs at the LHC.
However, the ultimate verification of the NP scenario considered in this study may come from the flavor physics. The Belle-II collaboration plans on improving, by at least one order of magnitude, their experimental bounds on the rare leptonic decays of the tau lepton. As the corresponding branching ratios featured by our three benchmark scenarios are very close to the current 90% C.L. exclusion limits, the rare decays could be the first experimental signatures to be tested.

Appendix 3.A: Fermion mass matrices

Charged leptons The mass matrix for the charged leptons, $\mathcal{M}_e$, can be derived from Eq. (3.1) after identifying the generic fermions ψ with the corresponding lepton fields from Table 3.1 and the generic scalar H with H_d. One thus has

$$\psi_{iR} = e_{iR}, \qquad \psi_{iL} = L_{iL}, \qquad \psi_{4R} = e_{4R}, \qquad \psi_{4L} = L_{4L}, \qquad \widetilde{\psi}_{4R} = \widetilde{L}_{4R}, \qquad \widetilde{\psi}_{4L} = \widetilde{e}_{4L} \tag{3.65}$$

with the following components of the SU(2)$_L$ doublets: $L_{iL} = (\nu_{iL}, e_{iL})^T$, $L_{4L} = (\nu_{4L}, e_{4L})^T$ and $\widetilde{L}_{4R} = (\widetilde{\nu}_{4R}, \widetilde{e}_{4R})^T$. As a result, the mass matrix reads

$$\mathcal{M}_e = \begin{array}{cc} & \begin{matrix} e_{1R} & e_{2R} & e_{3R} & e_{4R} & \widetilde{e}_{4R} \end{matrix} \\ \begin{matrix} e_{1L} \\ e_{2L} \\ e_{3L} \\ e_{4L} \\ \widetilde{e}_{4L} \end{matrix} & \begin{pmatrix} 0 & 0 & 0 & 0 & 0 \\ 0 & 0 & 0 & y^e_{24}\frac{v_d}{\sqrt{2}} & 0 \\ 0 & 0 & 0 & y^e_{34}\frac{v_d}{\sqrt{2}} & -x^L_{34}\frac{v_\phi}{\sqrt{2}} \\ 0 & 0 & y^e_{43}\frac{v_d}{\sqrt{2}} & 0 & -M^L_4 \\ 0 & x^e_{42}\frac{v_\phi}{\sqrt{2}} & x^e_{43}\frac{v_\phi}{\sqrt{2}} & M^e_4 & 0 \end{pmatrix} \end{array}, \tag{3.66}$$

where M^L_4 (M^e_4) denotes the mass of the VL lepton doublet (singlet) and $x^L_{34} \equiv x^e_{34}$. To facilitate the comparison with the corresponding mass matrix defined in SARAH, we adopt the sign convention used in the code. Note, however, that such a choice does not affect the

conclusions drawn in our study as we allow all the Yukawa couplings and all the VL mass parameters to assume both positive and negative values in our numerical scan.
The 5×5 charged lepton mass matrix $\mathcal{M}_e$ can be diagonalized by means of two unitary transformations V_L^e and V_R^e,

$$V_L^e \mathcal{M}_e V_R^{e\dagger} = \mathrm{diag}\left(0, m_\mu, m_\tau, M_{E_1}, M_{E_2}\right). \tag{3.67}$$

In Sec. 3.1.2 the approximate expressions for the eigenvalues m_μ and m_τ were provided in Eq. (3.6), whereas the analogous formulae for the eigenvalues M_{E_1} and M_{E_2} were given in Eq. (3.11). While those equations are very useful to get a general idea on which lagrangian parameters are relevant for generating the physical charged lepton masses, in our numerical analysis we diagonalize all the fermion mass matrices numerically, employing the `SPheno` code generated by `SARAH`.

Up-type quarks In analogy to the charged lepton sector, the mass matrix for the up-type quarks, $\mathcal{M}_u$, can be derived from Eq. (3.1) after taking $H = H_u$ and making the following identification:

$$\psi_{iR} = u_{iR}, \qquad \psi_{iL} = Q_{iL}, \qquad \psi_{4R} = u_{4R}, \qquad \psi_{4L} = Q_{4L}, \qquad \widetilde{\psi}_{4R} = \widetilde{Q}_{4R}, \qquad \widetilde{\psi}_{4L} = \widetilde{u}_{4L}. \tag{3.68}$$

In Eq. (3.68) the SU(2)$_L$ doublets have the following components: $Q_{iL} = (u_{iL}, d_{iL})^T$, $Q_{4L} = (u_{4L}, d_{4L})^T$ and $\widetilde{Q}_{4R} = (\widetilde{u}_{4R}, \widetilde{d}_{4R})^T$. The corresponding mass matrix with the `SARAH` sign convention reads

$$\mathcal{M}_u = \left(\begin{array}{c|ccccc} & u_{1R} & u_{2R} & u_{3R} & u_{4R} & \widetilde{u}_{4R} \\ \hline u_{1L} & 0 & 0 & 0 & 0 & 0 \\ u_{2L} & 0 & 0 & 0 & -y_{24}^u \frac{v_u}{\sqrt{2}} & 0 \\ u_{3L} & 0 & 0 & 0 & -y_{34}^u \frac{v_u}{\sqrt{2}} & x_{34}^Q \frac{v_\phi}{\sqrt{2}} \\ u_{4L} & 0 & 0 & -y_{43}^u \frac{v_u}{\sqrt{2}} & 0 & -M_4^Q \\ \widetilde{u}_{4L} & 0 & x_{42}^u \frac{v_\phi}{\sqrt{2}} & x_{43}^u \frac{v_\phi}{\sqrt{2}} & M_4^u & 0 \end{array}\right), \tag{3.69}$$

with $x_{34}^Q \equiv x_{34}^u$. The up-type quark mass matrix $\mathcal{M}_u$ can be diagonalized via the mixing matrices V_L^u and V_R^u as

$$V_L^u \mathcal{M}_u V_R^{u\dagger} = \mathrm{diag}\left(0, m_c, m_t, M_{U_1}, M_{U_2}\right). \tag{3.70}$$

The approximate expressions for the eigenvalues m_c and m_t can be found in Eq. (3.4), and for the eigenvalues M_{U_1} and M_{U_2} in Eqs. (3.8) and (3.9), respectively.

Down-type quarks The down-type quark lagrangian can be obtained from the generic lagrangian (3.1) by taking $H = H_d$ and making the following replacements of the fermion fields,

$$\psi_{iR} = d_{iR}, \qquad \psi_{iL} = Q_{iL}, \qquad \psi_{4R} = d_{4R}, \qquad \psi_{4L} = Q_{4L}, \qquad \widetilde{\psi}_{4R} = \widetilde{Q}_{4R}, \qquad \widetilde{\psi}_{4L} = \widetilde{d}_{4L}. \tag{3.71}$$

The corresponding down-type quark mass matrix with the SARAH sign convention reads

$$\mathcal{M}_d = \begin{array}{c|ccccc} & d_{1R} & d_{2R} & d_{3R} & d_{4R} & \widetilde{d}_{4R} \\ \hline d_{1L} & 0 & 0 & 0 & y^d_{14}\frac{v_d}{\sqrt{2}} & 0 \\ d_{2L} & 0 & 0 & 0 & y^d_{24}\frac{v_d}{\sqrt{2}} & 0 \\ d_{3L} & 0 & 0 & 0 & y^d_{34}\frac{v_d}{\sqrt{2}} & -x^Q_{34}\frac{v_\phi}{\sqrt{2}} \\ d_{4L} & 0 & 0 & y^d_{43}\frac{v_d}{\sqrt{2}} & 0 & M^Q_4 \\ \widetilde{d}_{4L} & 0 & x^d_{42}\frac{v_\phi}{\sqrt{2}} & x^d_{43}\frac{v_\phi}{\sqrt{2}} & M^d_4 & 0 \end{array} . \tag{3.72}$$

Note that, unlike in the case of the up-type quarks and charged leptons, it is impossible to rotate away the $(1,4)$ element of the matrix $\mathcal{M}_d$. The reason is that the mixing between the SM doublets Q_{1L} and Q_{2L} has already been used in the up-quark sector to rotate away the corresponding entry of $\mathcal{M}_u$ [58]. As a result, the Yukawa coupling y^d_{14} is present in $\mathcal{M}_d$. The down-type quark mass matrix can be diagonalized by the unitary matrices V^d_L and V^d_R,

$$V^d_L \mathcal{M}_d V^{d\dagger}_R = \mathrm{diag}\left(0, m_s, m_b, M_{D_1}, M_{D_2}\right) . \tag{3.73}$$

The approximate formulae for the eigenvalues m_s and m_b can be found in Eq. (3.5), and for the eigenvalues M_{D_1} and M_{D_2} in Eq. (3.10).
Incidentally, the presence of the matrix element $y^d_{14}v_d$ has important consequences for the phenomenology of the model defined in Table 3.1. As it was discussed in Sec. 3.1.2, the first generation of the SM fermions remains massless if only one complete VL family is added to the spectrum. On the other hand, the mixing of the d quark with the strange and bottom quarks is mediated by $y^d_{14}v_d$. As a result, the full CKM matrix can be generated in this setup and one needs to include its elements in the global fit.

Neutrino sector Finally, we discuss the neutrino mass matrix which emerges from the particle content given in Table 3.1. The corresponding lagrangian can be deduced from Eq. (3.1) after the following identification:

$$\psi_{iL} = L_{iL}, \qquad \psi_{4R} = \nu_{4R}, \qquad \psi_{4L} = L_{4L}, \qquad \widetilde{\psi}_{4R} = \widetilde{L}_{4R}, \qquad \widetilde{\psi}_{4L} = \widetilde{\nu}_{4L}, \qquad H = H_u , \tag{3.74}$$

where the SU(2)$_L$ doublets L_{iL}, L_{4L} and $\widetilde{L}_{4R}$ are defined above. Note that since there is no ν_{iR} field in our model, the couplings y^ν_{4j} and x^ν_{4j} vanish. On the other hand, the VL neutrino ν_{4R} is a singlet under the SM gauge symmetry, so an extra term with H^*_d replacing H_u arises. In the end, the neutrino lagrangian reads:

$$\mathcal{L}^{\text{Yukawa}}_{\text{ren},\nu} = y^\nu_{i4} L_{iL} H_u \nu_{4R} + x^L_{i4} L_{iL}\phi \widetilde{L}_{4R} + y'^\nu_{i4} L_{iL} H^*_d \widetilde{\nu}_{4L} + M^L_4 L_{4L}\widetilde{L}_{4R} + M^\nu_4 \widetilde{\nu}_{4L}\nu_{4R} + \text{h. c.} . \tag{3.75}$$

Eq. (3.75) defines a mixed Majorana-Dirac neutrino sector, which after the EWSB gives rise to a 7×7 Majorana neutrino mass matrix

$$\mathcal{M}_\nu = \begin{array}{c|ccccccc} & \nu_{1L} & \nu_{2L} & \nu_{3L} & \nu_{4L} & \nu_{4R} & \widetilde{\nu}_{4L} & \widetilde{\nu}_{4R} \\ \hline \nu_{1L} & 0 & 0 & 0 & 0 & -y^\nu_{14}\frac{v_u}{\sqrt{2}} & y'^\nu_{14}\frac{v_d}{\sqrt{2}} & 0 \\ \nu_{2L} & 0 & 0 & 0 & 0 & -y^\nu_{24}\frac{v_u}{\sqrt{2}} & y'^\nu_{24}\frac{v_d}{\sqrt{2}} & 0 \\ \nu_{3L} & 0 & 0 & 0 & 0 & -y^\nu_{34}\frac{v_u}{\sqrt{2}} & y'^\nu_{34}\frac{v_d}{\sqrt{2}} & x^L_{34}\frac{v_\phi}{\sqrt{2}} \\ \nu_{4L} & 0 & 0 & 0 & 0 & 0 & 0 & M^L_4 \\ \nu_{4R} & -y^\nu_{14}\frac{v_u}{\sqrt{2}} & -y^\nu_{24}\frac{v_u}{\sqrt{2}} & -y^\nu_{34}\frac{v_u}{\sqrt{2}} & 0 & 0 & M^\nu_4 & 0 \\ \widetilde{\nu}_{4L} & y'^\nu_{14}\frac{v_d}{\sqrt{2}} & y'^\nu_{24}\frac{v_d}{\sqrt{2}} & y'^\nu_{34}\frac{v_d}{\sqrt{2}} & 0 & M^\nu_4 & 0 & 0 \\ \widetilde{\nu}_{4R} & 0 & 0 & x^L_{34}\frac{v_\phi}{\sqrt{2}} & M^L_4 & 0 & 0 & 0 \end{array} , \tag{3.76}$$

where once again we chose to work with the SARAH sign convention.
The neutrino mass matrix is symmetric, it can thus be diagonalized via an orthogonal mixing matrix V^ν,

$$V^\nu \mathcal{M}_\nu V^{\nu\dagger} = \mathrm{diag}\left(0, m_{\nu_2}, m_{\nu_3}, M_{N_1}, M_{N_2}, M_{N_3}, M_{N_4}\right). \tag{3.77}$$

Appendix 3.B: Scalar mass matrices

In this Appendix we collect the explicit formulae for the scalar mass matrices derived from the scalar potential (3.19) under the spontaneous symmetry breaking conditions (3.3).
The CP-even scalar mass matrix in the basis $(\mathrm{Re}\,H_u^0,\ \mathrm{Re}\,H_d^0,\ \mathrm{Re}\,\phi)$ evaluated at the vacuum reads

$$\mathbf{M}^2_{\text{CP-even}} = \begin{pmatrix} \lambda_1 v_u^2 - \lambda_5 \frac{v_d v_\phi^2}{4 v_u} & \lambda_3 v_u v_d + \lambda_5 \frac{v_\phi^2}{4} & \lambda_7 v_u v_\phi + \lambda_5 \frac{v_d v_\phi}{2} \\ \lambda_3 v_u v_d + \lambda_5 \frac{v_\phi^2}{4} & \lambda_2 v_d^2 - \lambda_5 \frac{v_u v_\phi^2}{4 v_d} & \lambda_8 v_d v_\phi + \lambda_5 \frac{v_u v_\phi}{2} \\ \lambda_7 v_u v_\phi + \lambda_5 \frac{v_d v_\phi}{2} & \lambda_8 v_d v_\phi + \lambda_5 \frac{v_u v_\phi}{2} & \lambda_6 v_\phi^2 \end{pmatrix}. \tag{3.78}$$

The matrix (3.78) can be diagonalized by an orthogonal matrix R_h parameterized with three mixing angles. We will denote them as α_{12} for the (H_u, H_d) mixing, α_{13} for the (H_u, ϕ) mixing, and α_{23} for the (H_d, ϕ) mixing. In this parametrization, the mixing matrix R_h is given by

$$R_h = \begin{pmatrix} c_{12}c_{13} & s_{12}c_{13} & s_{13} \\ -s_{12}c_{23} - c_{12}s_{13}s_{23} & c_{12}c_{23} - s_{12}s_{13}s_{23} & c_{13}s_{23} \\ s_{12}s_{23} - c_{12}s_{13}c_{23} & -c_{12}s_{23} - s_{12}s_{13}c_{23} & c_{13}c_{23} \end{pmatrix}, \tag{3.79}$$

with the standard notation $s_{ij} = \sin\alpha_{ij}$ and $c_{ij} = \cos\alpha_{ij}$.
The elements of the matrix R_h determine the couplings of the physical Higgs bosons with the SM particles. It is convenient to define a reduced coupling as the ratio between the coupling of the physical Higgs scalar h_i and the corresponding coupling of the SM Higgs,

$$c_{h_i XX} = \frac{g_{h_i XX}}{g_{h_{\mathrm{SM}} XX}}, \tag{3.80}$$

where X stands for the SM fermions and gauge bosons. For the model defined in Table 3.1, the reduced couplings to quarks and charged leptons are given by

$$c_{h_i tt} = \frac{(R_h)_{i1}}{\sin\beta}, \qquad c_{h_i bb} = \frac{(R_h)_{i2}}{\cos\beta} \qquad c_{h_i \tau\tau} = \frac{(R_h)_{i2}}{\cos\beta}, \tag{3.81}$$

while the reduced couplings to the EW gauge bosons read

$$c_{h_i ZZ} = c_{h_i WW} = (R_h)_{i1} \sin\beta + (R_h)_{i2} \cos\beta \,. \tag{3.82}$$

In this study we choose to work in the alignment limit, which is defined as a set of constraints on the quartic couplings λ_i under which the lightest CP-even scalar h_1 has the same tree-level couplings with the SM particles as the SM Higgs. This means that the reduced couplings to fermions should be very close to 1,

$$\frac{\cos\alpha_{12}\cos\alpha_{13}}{\sin\beta} \approx 1, \qquad \frac{\sin\alpha_{12}\cos\alpha_{13}}{\cos\beta} \approx 1 \,. \tag{3.83}$$

It can be easily verify that Eq. (3.83) leads to the following conditions on the CP-even scalars mixing angles,

$$\alpha_{12} + \beta = \frac{\pi}{2} + n\,\pi, \qquad \alpha_{13} = 2\,n\pi\,, \quad \text{with } n = 0, 1, 2 \ldots \tag{3.84}$$

indicating no mixing between the doublet H_u and the singlet ϕ. In this setting, the two $\mathrm{SU}(2)_L$ scalar doublets mix with the mixing angle $\frac{\pi}{2} - \beta$, while the doublet H_d mixes with the singlet ϕ with the mixing angle α_{23}. The CP-even scalars mixing matrix thus reduces to

$$R_h^{\text{alignment}} = \begin{pmatrix} s_\beta & c_\beta & 0 \\ -c_\beta c_{23} & s_\beta c_{23} & s_{23} \\ c_\beta s_{23} & -s_\beta s_{23} & c_{23} \end{pmatrix} = \begin{pmatrix} 1 & 0 & 0 \\ 0 & c_{23} & s_{23} \\ 0 & -s_{23} & c_{23} \end{pmatrix} \times \begin{pmatrix} s_\beta & c_\beta & 0 \\ -c_\beta & s_\beta & 0 \\ 0 & 0 & 1 \end{pmatrix} . \tag{3.85}$$

The alignment conditions (3.83) translates into the non-trivial relations between the scalar potential couplings,

$$\lambda_8\, c_\beta^2 + \lambda_7\, s_\beta^2 + \lambda_5\, s_\beta c_\beta \;=\; 0 \tag{3.86}$$
$$\lambda_2\, c_\beta^2 - \lambda_1\, s_\beta^2 - \lambda_3 (c_\beta^2 - s_\beta^2) \;=\; 0 \,. \tag{3.87}$$

The CP-odd mass matrix in the basis $\left(\mathrm{Im}\, H_u^0, \mathrm{Im}\, H_d^0, \mathrm{Im}\,\phi\right)$ reads

$$\mathbf{M}^2_{\text{CP-odd}} = -\lambda_5 \begin{pmatrix} \frac{v_d v_\phi^2}{4 v_u} & \frac{v_\phi^2}{4} & \frac{v_d v_\phi}{2} \\ \frac{v_\phi^2}{4} & \frac{v_u v_\phi^2}{4 v_d} & \frac{v_u v_\phi}{2} \\ \frac{v_d v_\phi}{2} & \frac{v_u v_\phi}{2} & v_u v_d - 2\frac{\mu_{\text{sb}}^2}{\lambda_5} \end{pmatrix} . \tag{3.88}$$

Finally, the charged scalar mass matrix is given by

$$\mathbf{M}^2_{\text{Charged}} = \begin{pmatrix} \lambda_4 \frac{v_d^2}{2} - \lambda_5 \frac{v_d v_\phi^2}{4 v_u} & \lambda_4 \frac{v_u v_d}{2} - \lambda_5 \frac{v_\phi^2}{4} \\ \lambda_4 \frac{v_u v_d}{2} - \lambda_5 \frac{v_\phi^2}{4} & \lambda_4 \frac{v_u^2}{2} - \lambda_5 \frac{v_u v_\phi^2}{4 v_d} \end{pmatrix} . \tag{3.89}$$

Appendix 3.C: Derivation of the bounded-from-below conditions

In this Appendix, we derive the scalar potential bounded-from-below conditions shown in Eq. (3.36). In doing so, we follow the approach of Ref. [139] and we extend it to the three-field case.

In order to determine the shape of the scalar potential (3.19) in the limit of the large fields, it is enough to investigate the behavior of the quartic terms,

$$\begin{aligned} V_4 = & \frac{1}{2}\lambda_1(H_u^\dagger H_u)^2 + \frac{1}{2}\lambda_2(H_d^\dagger H_d)^2 + \lambda_3(H_u^\dagger H_u)(H_d^\dagger H_d) + \lambda_4(H_u^\dagger H_d)(H_d^\dagger H_u) \\ & - \frac{1}{2}\lambda_5(\epsilon_{ij}H_u^i H_d^j \phi^2 + \text{H. c.}) + \frac{1}{2}\lambda_6(\phi^*\phi)^2 + \lambda_7(\phi^*\phi)(H_u^\dagger H_u) + \lambda_8(\phi^*\phi)(H_d^\dagger H_d). \end{aligned} \tag{3.90}$$

It is convenient to parameterize each quartic term in the following way,

$$\begin{aligned} a &= H_u^\dagger H_u \\ b &= H_d^\dagger H_d \\ c &= \phi^*\phi \\ d &= \text{Re}\, H_u^\dagger H_d \\ e &= \text{Im}\, H_u^\dagger H_d \\ f &= \text{Re}\, \epsilon_{ij} H_u^i H_d^j \phi^2 \\ g &= \text{Im}\, \epsilon_{ij} H_u^i H_d^j \phi^2 \,. \end{aligned} \tag{3.91}$$

To make our results more general, we allow λ_5 to be complex. Note that $a, b, c \geq 0$ by definition, and

$$\begin{aligned} a\, b &\geq d^2 + e^2 \\ a\, b\, c^2 &\geq f^2 + g^2 \geq 2fg. \end{aligned} \tag{3.92}$$

In terms of the new parameters, the scalar potential (3.90) can be rewritten as

$$\begin{aligned} V_4 = & \frac{1}{4}\left(\sqrt{\lambda_1}a - \sqrt{\lambda_2}b\right)^2 + \left(\frac{1}{2}\sqrt{\lambda_1\lambda_2} + \lambda_3\right) a\, b \\ & + \frac{1}{4}\left(\sqrt{\lambda_1}a - \sqrt{\lambda_6}c\right)^2 + \left(\frac{1}{2}\sqrt{\lambda_1\lambda_6} + \lambda_7\right) a\, c \\ & + \frac{1}{4}\left(\sqrt{\lambda_2}b - \sqrt{\lambda_6}c\right)^2 + \left(\frac{1}{2}\sqrt{\lambda_2\lambda_6} + \lambda_8\right) b\, c \\ & + \lambda_4\left(d^2 + e^2\right) - \left(\text{Re}\,\lambda_5 f - \text{Im}\,\lambda_5 g\right) \,. \end{aligned} \tag{3.93}$$

We are now ready to analyze the asymptotic behaviour of the potential (3.93) in different field directions.

$a = 0$.

The parameters d, e, f, g automatically vanish, see Eq. (3.92), and the global potential reduces to

$$V_4\left(a = d = e = f = g = 0\right) = \frac{1}{2}\left(\sqrt{\lambda_2}b - \sqrt{\lambda_6}c\right)^2 + \left(\lambda_8 + \sqrt{\lambda_2\lambda_6}\right) bc\,, \tag{3.94}$$

giving rise to the condition

$$\lambda_8 + \sqrt{\lambda_2\lambda_6} > 0. \tag{3.95}$$

$b = 0$.

In analogy to the previous case, one obtains

$$V_4\left(b = d = e = f = g = 0\right) = \frac{1}{2}\left(\sqrt{\lambda_1}a - \sqrt{\lambda_6}c\right)^2 + \left(\lambda_7 + \sqrt{\lambda_1\lambda_6}\right) ac, \tag{3.96}$$

which gives

$$\lambda_7 + \sqrt{\lambda_1 \lambda_6} > 0. \tag{3.97}$$

$c = 0$.
This time, only the parameters f and g vanish and the reduced scalar potential reads

$$V_4\left(c = f = g = 0\right) = \frac{1}{2}\left(\sqrt{\lambda_1}a - \sqrt{\lambda_2}b\right)^2 + \left(\lambda_3 + \sqrt{\lambda_1\lambda_2}\right)ab + \lambda_4\left(d^2 + e^2\right). \tag{3.98}$$

In order to determine the fate of the scalar potential V_4 at the large field values, we need to analyze additional directions in the field space. We first choose a direction along which $a = \sqrt{\frac{\lambda_2}{\lambda_1}}b$ and $d = e = 0$. Inserting these expressions into Eq. (3.98), we arrive to the following condition

$$\lambda_3 + \sqrt{\lambda_1\lambda_2} > 0. \tag{3.99}$$

Choosing another direction, $a = \sqrt{\frac{\lambda_2}{\lambda_1}}b$ and $ab = d^2 + e^2$, we obtain

$$\lambda_3 + \lambda_4 + \sqrt{\lambda_1\lambda_2} > 0. \tag{3.100}$$

$a = \sqrt{\frac{\lambda_6}{\lambda_1}}c$, $b = \sqrt{\frac{\lambda_6}{\lambda_2}}c$.
Under this assumption the scalar potential (3.93) reduces to

$$V_4 = \lambda_a c^2 + \lambda_4\left(d^2 + e^2\right) - \left(\mathrm{Re}\,\lambda_5 f - \mathrm{Im}\,\lambda_5 g\right), \tag{3.101}$$

where one defines

$$\lambda_a = \frac{3}{2}\lambda_6 + \lambda_3\frac{\lambda_6}{\sqrt{\lambda_1\lambda_2}} + \lambda_7\frac{\lambda_6}{\lambda_1} + \lambda_8\frac{\lambda_6}{\lambda_2}. \tag{3.102}$$

From Eq. (3.92) one has

$$c^2 \geq \frac{f^2 + g^2}{d^2 + e^2}, \tag{3.103}$$

leading to

$$V_4 \geq \lambda_a\frac{f^2 + g^2}{d^2 + e^2} + \lambda_4\left(d^2 + e^2\right) - \left(\mathrm{Re}\,\lambda_5\, f - \mathrm{Im}\,\lambda_5',g\right). \tag{3.104}$$

The r.h.s. of Eq. (3.104) can now be rewritten as

$$\mathrm{R.H.S} = \left(f - \frac{\mathrm{Re}\,\lambda_5}{c_1}\right)^2 + \left(g + \frac{\mathrm{Im}\,\lambda_5}{c_1}\right)^2 - \frac{1}{4c_1}\left((\mathrm{Re}\,\lambda_5)^2 + (\mathrm{Im}\,\lambda_5)^2\right) + \lambda_4\left(d^2 + e^2\right), \tag{3.105}$$

where

$$c_1 = \frac{\lambda_a}{d^2 + e^2}. \tag{3.106}$$

Choosing an additional direction in the field space, $f = \frac{\mathrm{Re}\,\lambda_5}{c_1}$ and $g = -\frac{\mathrm{Im}\,\lambda_5}{c_1}$, we can derive the following condition,

$$-\frac{1}{4}\frac{(\mathrm{Re}\,\lambda_5)^2 + (\mathrm{Im}\,\lambda_5)^2}{\lambda_a} + \lambda_4 > 0. \tag{3.107}$$

Finally, let us rewrite the r.h.s. of Eq. (3.104) in yet another way,

$$\mathrm{R.H.S} = \left(\frac{\sqrt{c_2}}{\sqrt{d^2 + e^2}} - \sqrt{\lambda_4\left(d^2 + e^2\right)}\right)^2 + 2\sqrt{c_2\lambda_4} - \left(\mathrm{Re}\,\lambda_5 f - \mathrm{Im}\,\lambda_5 g\right), \tag{3.108}$$

where

$$c_2 = \lambda_a \left(f^2 + g^2\right), \quad \lambda_b = \sqrt{\lambda_a \lambda_4}. \tag{3.109}$$

Analyzing the quartic potential along the direction $\sqrt{c_2} = \sqrt{\lambda_4}(d^2 + f^2)$, we obtain

$$V_4 \geq \left(4\lambda_b^2 - (\mathrm{Re}\,\lambda_5)^2 + \mathrm{Re}\,\lambda_5\,\mathrm{Im}\,\lambda_5\right) f^2 + \left(4\lambda_b^2 - (\mathrm{Im}\,\lambda_5)^2 + \mathrm{Re}\,\lambda_5\,\mathrm{Im}\,\lambda_5\right) g^2, \tag{3.110}$$

leading straightforwardly to the last two conditions,

$$\begin{aligned} 4\lambda_b^2 - (\mathrm{Re}\,\lambda_5)^2 + \mathrm{Re}\,\lambda_5\,\mathrm{Im}\,\lambda_5 > 0 \\ 4\lambda_b^2 - (\mathrm{Im}\,\lambda_5)^2 + \mathrm{Re}\,\lambda_5\,\mathrm{Im}\,\lambda_5 > 0. \end{aligned} \tag{3.111}$$

Appendix 3.D: Renormalisation group equations

In this Appendix, we collect the one-loop RGEs of our model computed with SARAH [107, 108]. We denote

$$\beta(X) \equiv \mu \frac{dX}{d\mu} \equiv \frac{1}{16\pi^2} \beta^{(1)}(X). \tag{3.112}$$

$$\beta^{(1)}(g_1) = \frac{103 g_1^3}{15} \tag{3.113}$$

$$\beta^{(1)}(g_2) = -\frac{g_2^3}{3} \tag{3.114}$$

$$\beta^{(1)}(g_3) = -\frac{13 g_3^3}{3} \tag{3.115}$$

$$\begin{aligned} \beta^{(1)}(\lambda_1) = &-\frac{9}{5} g_1^2 \lambda_1 - 9 g_2^2 \lambda_1 + \frac{27 g_1^4}{100} + \frac{9 g_2^4}{4} + \frac{9}{10} g_1^2 g_2^2 + 12\lambda_1^2 + 4\lambda_3^2 + 2\lambda_4^2 + 2\lambda_7^2 + 4\lambda_3\lambda_4 \\ &+ 12\lambda_1 (y_{43}^u)^2 + 12\lambda_1 \left[(y_{24}^u)^2 + (y_{34}^u)^2\right] - 12 (y_{43}^u)^4 - 12 \left[(y_{24}^u)^2 + (y_{34}^u)^2\right]^2 \\ &+ 4\lambda_1 \left[(y_{14}^\nu)^2 + (y_{24}^\nu)^2 + (y_{34}^\nu)^2\right] - 4 \left[(y_{14}^\nu)^2 + (y_{24}^\nu)^2 + (y_{34}^\nu)^2\right]^2 \end{aligned} \tag{3.116}$$

$$\begin{aligned} \beta^{(1)}(\lambda_2) = &-\frac{9}{5} g_1^2 \lambda_2 - 9 g_2^2 \lambda_2 + \frac{27 g_1^4}{100} + \frac{9 g_2^4}{4} + \frac{9}{10} g_1^2 g_2^2 + 12\lambda_2^2 + 4\lambda_3^2 + 2\lambda_4^2 + 2\lambda_8^2 + 4\lambda_3\lambda_4 \\ &+ 12\lambda_2 (y_{43}^d)^2 + 12\lambda_2 \left[(y_{14}^d)^2 + (y_{24}^d)^2 + (y_{34}^d)^2\right] - 12 (y_{43}^d)^4 - 12 \left[(y_{14}^d)^2 + (y_{24}^d)^2 + (y_{34}^d)^2\right]^2 \\ &+ 4\lambda_2 (y_{43}^e)^2 + 4\lambda_2 \left[(y_{24}^e)^2 + (y_{34}^e)^2\right] - 4 (y_{43}^e)^4 - 4 \left[(y_{24}^e)^2 + (y_{34}^e)^2\right]^2 \\ &+ 4\lambda_2 \left[(x_{14}^\nu)^2 + (x_{24}^\nu)^2 + (x_{34}^\nu)^2\right] - 4 \left[(x_{14}^\nu)^2 + (x_{24}^\nu)^2 + (x_{34}^\nu)^2\right]^2 \end{aligned} \tag{3.117}$$

$$\begin{aligned} \beta^{(1)}(\lambda_3) = &-\frac{9}{5} g_1^2 \lambda_3 - 9 g_2^2 \lambda_3 + \frac{27 g_1^4}{100} + \frac{9 g_2^4}{4} + \frac{9}{10} g_1^2 g_2^2 + 4\lambda_3^2 + 2\lambda_4^2 + \lambda_5^2 + 6\lambda_1\lambda_3 + 6\lambda_2\lambda_3 + 2\lambda_1\lambda_4 \\ &+ 2\lambda_2\lambda_4 + 2\lambda_7\lambda_8 + 6\lambda_3 (y_{43}^d)^2 + 6\lambda_3 \left[(y_{14}^d)^2 + (y_{24}^d)^2 + (y_{34}^d)^2\right] + 2\lambda_3 \left[(y_{24}^e)^2 + (y_{34}^e)^2\right] \\ &+ 2\lambda_3 (y_{43}^e)^2 + 6\lambda_3 (y_{43}^u)^2 + 6\lambda_3 \left[(y_{24}^u)^2 + (y_{34}^u)^2\right] + 2\lambda_3 \left[(x_{14}^\nu)^2 + (x_{24}^\nu)^2 + (x_{34}^\nu)^2\right] \\ &- 4 \left[x_{14}^\nu y_{14}^\nu + x_{24}^\nu y_{24}^\nu + x_{34}^\nu y_{34}^\nu\right]^2 + 2\lambda_3 \left[(y_{14}^\nu)^2 + (y_{24}^\nu)^2 + (y_{34}^\nu)^2\right] \end{aligned} \tag{3.118}$$

$$\begin{aligned} \beta^{(1)}(\lambda_4) = &-\frac{9}{5} g_1^2 \lambda_4 - 9 g_2^2 \lambda_4 - \frac{9}{5} g_1^2 g_2^2 + 4\lambda_4^2 - \lambda_5^2 + 2\lambda_1\lambda_4 + 2\lambda_2\lambda_4 + 8\lambda_3\lambda_4 + 6\lambda_4 (y_{43}^u)^2 + 6\lambda_4 (y_{43}^d)^2 \\ &+ 6\lambda_4 \left[(y_{24}^u)^2 + (y_{34}^u)^2\right] - 12 (y_{43}^d)^2 (y_{43}^u)^2 - 12 \left[y_{24}^d y_{24}^u + y_{34}^d y_{34}^u\right]^2 + 6\lambda_4 \left[(y_{14}^d)^2 + (y_{24}^d)^2 + (y_{34}^d)^2\right] \end{aligned}$$

$$+2\lambda_4 (y^e_{43})^2 + 2\lambda_4 \left[(y^e_{24})^2 + (y^e_{34})^2\right] - 4\left[y^e_{24}y^\nu_{24} + y^e_{34}y^\nu_{34}\right]^2 + 2\lambda_4 \left[(x^\nu_{14})^2 + (x^\nu_{24})^2 + (x^\nu_{34})^2\right]$$
$$+4\left[x^\nu_{14}y^\nu_{14} + x^\nu_{24}y^\nu_{24} + x^\nu_{34}y^\nu_{34}\right]^2 + 2\lambda_4 \left[(y^\nu_{14})^2 + (y^\nu_{24})^2 + (y^\nu_{34})^2\right] \quad (3.119)$$

$$\beta^{(1)}(\lambda_5) = \lambda_5 \Big\{ -\frac{9}{20}g_1^2 - \frac{9}{4}g_2^2 + \lambda_3 - \lambda_4 + \lambda_6 + 2\lambda_7 + 2\lambda_8 + 6(x^Q_{34})^2 + 3\left[(x^u_{42})^2 + (x^u_{43})^2\right]$$
$$+\frac{3}{2}(y^u_{43})^2 + \frac{3}{2}\left[(y^u_{24})^2 + (y^u_{34})^2\right] + 3\left[(x^d_{42})^2 + (x^d_{43})^2\right] + \frac{3}{2}(y^d_{43})^2 + \frac{3}{2}\left[(y^d_{14})^2 + (y^d_{24})^2 + (y^d_{34})^2\right]$$
$$+2(x^L_{34})^2 + \left[(x^e_{42})^2 + (x^e_{43})^2\right] + \frac{1}{2}(y^e_{43})^2 + \frac{1}{2}\left[(y^e_{24})^2 + (y^e_{34})^2\right] + \frac{1}{2}\left[(x^\nu_{14})^2 + (x^\nu_{24})^2 + (x^\nu_{34})^2\right]$$
$$+\frac{1}{2}\left[(y^\nu_{14})^2 + (y^\nu_{24})^2 + (y^\nu_{34})^2\right]\Big\} \quad (3.120)$$

$$\beta^{(1)}(\lambda_6) = 2\lambda_5^2 + 10\lambda_6^2 + 4\lambda_7^2 + 4\lambda_8^2 + 24\lambda_6 (x^Q_{34})^2 - 24(x^Q_{34})^4 + 12\lambda_6\left[(x^u_{42})^2 + (x^u_{43})^2\right]$$
$$-12\left[(x^u_{42})^2 + (x^u_{43})^2\right]^2 + 12\lambda_6\left[(x^d_{42})^2 + (x^d_{43})^2\right] - 12\left[(x^d_{42})^2 + (x^d_{43})^2\right]^2$$
$$+8\lambda_6 (x^L_{34})^2 - 8(x^L_{34})^4 + 4\lambda_6\left[(x^e_{42})^2 + (x^e_{43})^2\right] - 4\left[(x^e_{42})^2 + (x^e_{43})^2\right]^2 \quad (3.121)$$

$$\beta^{(1)}(\lambda_7) = -\frac{9}{10}g_1^2\lambda_7 - \frac{9}{2}g_2^2\lambda_7 + 2\lambda_5^2 + 4\lambda_7^2 + 6\lambda_1\lambda_7 + 4\lambda_6\lambda_7 + 4\lambda_3\lambda_8 + 2\lambda_4\lambda_8$$
$$-12(x^Q_{34})^2(y^u_{34})^2 + 12\lambda_7(x^Q_{34})^2 + 6\lambda_7\left[(x^u_{42})^2 + (x^u_{43})^2\right] - 12(x^u_{43})^2(y^u_{43})^2 + 6\lambda_7(y^u_{43})^2$$
$$+6\lambda_7\left[(y^u_{24})^2 + (y^u_{34})^2\right] + 6\lambda_7\left[(x^d_{42})^2 + (x^d_{43})^2\right] + 4\lambda_7(x^L_{34})^2 - 4(x^L_{34})^2(y^\nu_{34})^2$$
$$+2\lambda_7\left[(x^e_{42})^2 + (x^e_{43})^2\right] + 2\lambda_7\left[(y^\nu_{14})^2 + (y^\nu_{24})^2 + (y^\nu_{34})^2\right] \quad (3.122)$$

$$\beta^{(1)}(\lambda_8) = -\frac{9}{10}g_1^2\lambda_8 - \frac{9}{2}g_2^2\lambda_8 + 2\lambda_5^2 + 4\lambda_8^2 + 4\lambda_3\lambda_7 + 2\lambda_4\lambda_7 + 6\lambda_2\lambda_8 + 4\lambda_6\lambda_8 - 12(y^d_{34})^2(x^Q_{34})^2$$
$$+12\lambda_8(x^Q_{34})^2 + 6\lambda_8\left[(x^u_{42})^2 + (x^u_{43})^2\right] + 6\lambda_8\left[(x^d_{42})^2 + (x^d_{43})^2\right] - 12(x^d_{43})^2(y^d_{43})^2 + 6\lambda_8(y^d_{43})^2$$
$$+6\lambda_8\left[(y^d_{14})^2 + (y^d_{24})^2 + (y^d_{34})^2\right] + 4\lambda_8(x^L_{34})^2 - 4(x^L_{34})^2(y^e_{34})^2 - 4(x^L_{34})^2(x^\nu_{34})^2$$
$$+2\lambda_8\left[(x^e_{42})^2 + (x^e_{43})^2\right] - 4(x^e_{43})^2(y^e_{43})^2 + 2\lambda_8(y^e_{43})^2 + 2\lambda_8\left[(y^e_{24})^2 + (y^e_{34})^2\right]$$
$$+2\lambda_8\left[(x^\nu_{14})^2 + (x^\nu_{24})^2 + (x^\nu_{34})^2\right] \quad (3.123)$$

$$\beta^{(1)}(y^d_{43}) = -\frac{1}{4}g_1^2y^d_{43} - \frac{9}{4}g_2^2y^d_{43} - 8g_3^2y^d_{43} + y^d_{43}\left[(x^\nu_{14})^2 + (x^\nu_{24})^2 + (x^\nu_{34})^2\right] + \frac{1}{2}(x^d_{43})^2y^d_{43} + \frac{1}{2}y^d_{43}(y^u_{43})^2$$
$$+3y^d_{43}\left[(y^d_{14})^2 + (y^d_{24})^2 + (y^d_{34})^2\right] + y^d_{43}\left[(y^e_{24})^2 + (y^e_{34})^2\right] + y^d_{43}(y^e_{43})^2 + \frac{9}{2}(y^d_{43})^3 \quad (3.124)$$

$$\beta^{(1)}(y^d_{14}) = -\frac{1}{4}g_1^2y^d_{14} - \frac{9}{4}g_2^2y^d_{14} - 8g_3^2y^d_{14} + y^d_{14}\left[(x^\nu_{14})^2 + (x^\nu_{24})^2 + (x^\nu_{34})^2\right]$$
$$+\frac{9}{2}y^d_{14}\left[(y^d_{14})^2 + (y^d_{24})^2 + (y^d_{34})^2\right] + y^d_{14}\left[(y^e_{24})^2 + (y^e_{34})^2\right] + 3y^d_{14}(y^d_{43})^2 + y^d_{14}(y^e_{43})^2 \quad (3.125)$$

$$\beta^{(1)}(y^d_{24}) = -\frac{1}{4}g_1^2y^d_{24} - \frac{9}{4}g_2^2y^d_{24} - 8g_3^2y^d_{24} + y^d_{24}\left[(x^\nu_{14})^2 + (x^\nu_{24})^2 + (x^\nu_{34})^2\right]$$
$$+\frac{9}{2}y^d_{24}\left[(y^d_{14})^2 + (y^d_{24})^2 + (y^d_{34})^2\right] + y^d_{24}\left[(y^e_{24})^2 + (y^e_{34})^2\right] + \frac{1}{2}y^d_{24}(y^u_{24})^2$$
$$+3y^d_{24}(y^d_{43})^2 + y^d_{24}(y^e_{43})^2 + \frac{1}{2}y^u_{24}y^d_{34}y^u_{34} \quad (3.126)$$

$$\beta^{(1)}(y^d_{34}) = -\frac{1}{4}g_1^2y^d_{34} - \frac{9}{4}g_2^2y^d_{34} - 8g_3^2y^d_{34} + y^d_{34}\left[(x^\nu_{14})^2 + (x^\nu_{24})^2 + (x^\nu_{34})^2\right] + \frac{1}{2}(x^Q_{34})^2y^d_{34}$$

$$+\frac{9}{2}y^d_{34}\left[(y^d_{14})^2+(y^d_{24})^2+(y^d_{34})^2\right]+\frac{1}{2}y^d_{24}y^u_{24}y^u_{34}+y^d_{34}\left[(y^e_{24})^2+(y^e_{34})^2\right]$$
$$+\frac{1}{2}y^d_{34}(y^u_{34})^2+3y^d_{34}(y^d_{43})^2+y^d_{34}(y^e_{43})^2 \quad (3.127)$$

$$\beta^{(1)}(y^u_{43})=-\frac{17}{20}g_1^2y^u_{43}-\frac{9}{4}g_2^2y^u_{43}-8g_3^2y^u_{43}+\frac{1}{2}(x^u_{43})^2y^u_{43}+y^u_{43}\left[(y^\nu_{14})^2+(y^\nu_{24})^2+(y^\nu_{34})^2\right]$$
$$+3y^u_{43}\left[(y^u_{24})^2+(y^u_{34})^2\right]+\frac{1}{2}(y^d_{43})^2y^u_{43}+\frac{9}{2}(y^u_{43})^3 \quad (3.128)$$

$$\beta^{(1)}(y^u_{24})=-\frac{17}{20}g_1^2y^u_{24}-\frac{9}{4}g_2^2y^u_{24}-8g_3^2y^u_{24}+y^u_{24}\left[(y^\nu_{14})^2+(y^\nu_{24})^2+(y^\nu_{34})^2\right]+\frac{1}{2}(y^d_{24})^2y^u_{24}$$
$$+\frac{1}{2}y^d_{24}y^d_{34}y^u_{34}+\frac{9}{2}y^u_{24}\left[(y^u_{24})^2+(y^u_{34})^2\right]+3y^u_{24}(y^u_{43})^2 \quad (3.129)$$

$$\beta^{(1)}(y^u_{34})=-\frac{17}{20}g_1^2y^u_{34}-\frac{9}{4}g_2^2y^u_{34}-8g_3^2y^u_{34}+\frac{1}{2}(x^Q_{34})^2y^u_{34}+y^u_{34}\left[(y^\nu_{14})^2+(y^\nu_{24})^2+(y^\nu_{34})^2\right]$$
$$+\frac{1}{2}y^d_{24}y^u_{24}y^d_{34}+\frac{9}{2}y^u_{34}\left[(y^u_{24})^2+(y^u_{34})^2\right]+\frac{1}{2}(y^d_{34})^2y^u_{34}+3y^u_{34}(y^u_{43})^2 \quad (3.130)$$

$$\beta^{(1)}(x^d_{42})=-\frac{2}{5}g_1^2x^d_{42}-8g_3^2x^d_{42}+2(x^L_{34})^2x^d_{42}+6(x^Q_{34})^2x^d_{42}+x^d_{42}(x^e_{42})^2+3x^d_{42}\left[(x^u_{42})^2+(x^u_{43})^2\right]$$
$$+4x^d_{42}\left[(x^d_{42})^2+(x^d_{43})^2\right]+x^d_{42}(x^e_{43})^2 \quad (3.131)$$

$$\beta^{(1)}(x^d_{43})=-\frac{2}{5}g_1^2x^d_{43}-8g_3^2x^d_{43}+2(x^L_{34})^2x^d_{43}+6(x^Q_{34})^2x^d_{43}+4x^d_{43}\left[(x^d_{42})^2+(x^d_{43})^2\right]+(x^e_{42})^2x^d_{43}$$
$$+3x^d_{43}\left[(x^u_{42})^2+(x^u_{43})^2\right]+x^d_{43}(x^e_{43})^2+x^d_{43}(y^d_{43})^2 \quad (3.132)$$

$$\beta^{(1)}(x^Q_{34})=-\frac{1}{10}g_1^2x^Q_{34}-\frac{9}{2}g_2^2x^Q_{34}-8g_3^2x^Q_{34}+2(x^L_{34})^2x^Q_{34}+3x^Q_{34}\left[(x^d_{42})^2+x^d_{43})^2\right]+x^Q_{34}(x^e_{42})^2$$
$$+3x^Q_{34}\left[(x^u_{42})^2+(x^u_{43})^2\right]+x^Q_{34}(x^e_{43})^2+\frac{1}{2}x^Q_{34}(y^d_{34})^2+\frac{1}{2}x^Q_{34}(y^u_{34})^2+7(x^Q_{34})^3 \quad (3.133)$$

$$\beta^{(1)}(x^u_{42})=-\frac{8}{5}g_1^2x^u_{42}-8g_3^2x^u_{42}+2(x^L_{34})^2x^u_{42}+6(x^Q_{34})^2x^u_{42}+3x^u_{42}\left[(x^d_{42})^2+(x^d_{43})^2\right]$$
$$+x^u_{42}(x^e_{42})^2+x^u_{42}(x^e_{43})^2+4x^u_{42}\left[(x^u_{42})^2+(x^u_{43})^2\right] \quad (3.134)$$

$$\beta^{(1)}(x^u_{43})=-\frac{8}{5}g_1^2x^u_{43}-8g_3^2x^u_{43}+2(x^L_{34})^2x^u_{43}+6(x^Q_{34})^2x^u_{43}+3x^u_{43}\left[(x^d_{42})^2+(x^d_{43})^2\right]$$
$$+(x^e_{42})^2x^u_{43}+4x^u_{43}\left[(x^u_{42})^2+(x^u_{43})^2\right]+(x^e_{43})^2x^u_{43}+x^u_{43}(y^u_{43})^2 \quad (3.135)$$

$$\beta^{(1)}(y^e_{24})=-\frac{9}{4}g_1^2y^e_{24}-\frac{9}{4}g_2^2y^e_{24}+y^e_{24}\left[(x^\nu_{14})^2+(x^\nu_{24})^2+(x^\nu_{34})^2\right]-\frac{3}{2}x^\nu_{24}x^\nu_{34}y^e_{34}-\frac{3}{2}(x^\nu_{24})^2y^e_{24}$$
$$+\frac{1}{2}y^e_{24}(y^\nu_{24})^2+3y^e_{24}\left[(y^d_{14})^2+(y^d_{24})^2+(y^d_{34})^2\right]+\frac{5}{2}y^e_{24}\left[(y^e_{24})^2+(y^e_{34})^2\right]$$
$$+3y^e_{24}(y^d_{43})^2+y^e_{24}(y^e_{43})^2+\frac{1}{2}y^\nu_{24}y^e_{34}y^\nu_{34} \quad (3.136)$$

$$\beta^{(1)}(y^e_{34})=-\frac{9}{4}g_1^2y^e_{34}-\frac{9}{4}g_2^2y^e_{34}+y^e_{34}\left[(x^\nu_{14})^2+(x^\nu_{24})^2+(x^\nu_{34})^2\right]-\frac{3}{2}x^\nu_{24}x^\nu_{34}y^e_{24}-\frac{3}{2}(x^\nu_{34})^2y^e_{34}$$
$$+\frac{1}{2}x^L_{34}x^Q_{34}y^e_{34}+3y^e_{34}\left[(y^d_{14})^2+(y^d_{24})^2+(y^d_{34})^2\right]+\frac{1}{2}y^e_{24}y^\nu_{24}y^\nu_{34}+\frac{5}{2}y^e_{34}\left[(y^e_{24})^2+(y^e_{34})^2\right]$$
$$+\frac{1}{2}y^e_{34}(y^\nu_{34})^2+3y^e_{34}(y^d_{43})^2+y^e_{34}(y^e_{43})^2 \quad (3.137)$$

$$\beta^{(1)}(y^e_{43})=-\frac{9}{4}g_1^2y^e_{43}-\frac{9}{4}g_2^2y^e_{43}+y^e_{43}\left[(x^\nu_{14})^2+(x^\nu_{24})^2+(x^\nu_{34})^2\right]+\frac{1}{2}(x^e_{43})^2y^e_{43}$$

$$+y^e_{43}\left[(y^e_{24})^2+(y^e_{34})^2\right]+3y^e_{43}\left[(y^d_{14})^2+(y^d_{24})^2+(y^d_{34})^2\right]+3(y^d_{43})^2y^e_{43}+\frac{5}{2}(y^e_{43})^3 \tag{3.138}$$

$$\begin{aligned}\beta^{(1)}(y^\nu_{14}) &= -\frac{9}{20}g_1^2y^\nu_{14}-\frac{9}{4}g_2^2y^\nu_{14}+\frac{1}{2}x^\nu_{14}x^\nu_{24}y^\nu_{24}+\frac{1}{2}x^\nu_{14}x^\nu_{34}y^\nu_{34}+\frac{1}{2}(x^\nu_{14})^2y^\nu_{14}\\ &+\frac{5}{2}y^\nu_{14}\left[(y^\nu_{14})^2+(y^\nu_{24})^2+(y^\nu_{34})^2\right]+3y^\nu_{14}\left[(y^u_{24})^2+(y^u_{34})^2\right]+3y^\nu_{14}(y^u_{43})^2\end{aligned} \tag{3.139}$$

$$\begin{aligned}\beta^{(1)}(y^\nu_{24}) &= -\frac{9}{20}g_1^2y^\nu_{24}-\frac{9}{4}g_2^2y^\nu_{24}+\frac{1}{2}x^\nu_{14}x^\nu_{24}y^\nu_{14}+\frac{1}{2}x^\nu_{24}x^\nu_{34}y^\nu_{34}+\frac{1}{2}(x^\nu_{24})^2y^\nu_{24}+3y^\nu_{24}\left[(y^u_{24})^2+(y^u_{34})^2\right]\\ &+\frac{5}{2}y^\nu_{24}\left[(y^\nu_{14})^2+(y^\nu_{24})^2+(y^\nu_{34})^2\right]+\frac{1}{2}(y^e_{24})^2y^\nu_{24}+\frac{1}{2}y^e_{24}y^e_{34}y^\nu_{34}+3y^\nu_{24}(y^u_{43})^2\end{aligned} \tag{3.140}$$

$$\begin{aligned}\beta^{(1)}(y^\nu_{34}) &= -\frac{9}{20}g_1^2y^\nu_{34}-\frac{9}{4}g_2^2y^\nu_{34}+\frac{1}{2}x^\nu_{14}x^\nu_{34}y^\nu_{14}+\frac{1}{2}x^\nu_{24}x^\nu_{34}y^\nu_{24}+\frac{1}{2}(x^L_{34})^2y^\nu_{34}+\frac{1}{2}(x^\nu_{34})^2y^\nu_{34}+3y^\nu_{34}(y^u_{43})^2\\ &+\frac{5}{2}y^\nu_{34}\left[(y^\nu_{14})^2+(y^\nu_{24})^2+(y^\nu_{34})^2\right]+\frac{1}{2}y^e_{24}y^\nu_{24}y^e_{34}+3y^\nu_{34}\left[(y^u_{24})^2+(y^u_{34})^2\right]+\frac{1}{2}(y^e_{34})^2y^\nu_{34}\end{aligned} \tag{3.141}$$

$$\begin{aligned}\beta^{(1)}(x^e_{42}) &= -\frac{18}{5}g_1^2x^e_{42}+2(x^L_{34})^2x^e_{42}+6(x^Q_{34})^2x^e_{42}+2x^e_{42}(x^e_{43})^2+2(x^e_{42})^3\\ &+3x^e_{42}\left[(x^d_{42})^2+(x^d_{43})^2\right]+3x^e_{42}\left[(x^u_{42})^2+(x^u_{43})^2\right]\end{aligned} \tag{3.142}$$

$$\begin{aligned}\beta^{(1)}(x^e_{43}) &= -\frac{18}{5}g_1^2x^e_{43}+2(x^L_{34})^2x^e_{43}+6(x^Q_{34})^2x^e_{43}+3x^e_{43}\left[(x^d_{42})^2+(x^d_{43})^2\right]+2(x^e_{42})^2x^e_{43}\\ &+3x^e_{43}\left[(x^u_{42})^2+(x^u_{43})^2\right]+x^e_{43}(y^e_{43})^2+2(x^e_{43})^3\end{aligned} \tag{3.143}$$

$$\begin{aligned}\beta^{(1)}(x^L_{34}) &= -\frac{9}{10}g_1^2x^L_{34}-\frac{9}{2}g_2^2x^L_{34}+\frac{1}{2}x^L_{34}(x^\nu_{34})^2+6x^L_{34}(x^Q_{34})^2+3x^L_{34}\left[(x^d_{42})^2+(x^d_{43})^2\right]+x^L_{34}(x^e_{42})^2\\ &+3x^L_{34}\left[(x^u_{42})^2+(x^u_{43})^2\right]+x^L_{34}(x^e_{43})^2+\frac{1}{2}x^L_{34}(y^e_{34})^2+\frac{1}{2}x^L_{34}(y^\nu_{34})^2+3(x^L_{34})^3\end{aligned} \tag{3.144}$$

$$\begin{aligned}\beta^{(1)}(x^\nu_{14}) &= -\frac{9}{20}g1^2x^\nu_{14}-\frac{9}{4}g2^2x^\nu_{14}+\frac{5}{2}x^\nu_{14}\left[(x^\nu_{14})^2+(x^\nu_{24})^2+(x^\nu_{34})^2\right]+3x^\nu_{14}\left[(y^d_{14})^2+(y^d_{24})^2+(y^d_{34})^2\right]\\ &+\frac{1}{2}x^\nu_{14}(y^\nu_{14})^2+x^\nu_{14}\left[(y^e_{24})^2+(y^e_{34})^2\right]+3x^\nu_{14}(y^d_{43})^2+x^\nu_{14}(y^e_{43})^2+\frac{1}{2}x^\nu_{24}y^\nu_{14}y^\nu_{24}+\frac{1}{2}x^\nu_{34}y^\nu_{14}y^\nu_{34}\end{aligned} \tag{3.145}$$

$$\begin{aligned}\beta^{(1)}(x^\nu_{24}) &= -\frac{9}{20}g1^2x^\nu_{24}-\frac{9}{4}g2^2x^\nu_{24}+\frac{5}{2}x^\nu_{24}\left[(x^\nu_{14})^2+(x^\nu_{24})^2+(x^\nu_{34})^2\right]+3x^\nu_{24}\left[(y^d_{14})^2+(y^d_{24})^2+(y^d_{34})^2\right]\\ &+\frac{1}{2}x^\nu_{14}y^\nu_{14}y^\nu_{24}+x^\nu_{24}\left[(y^e_{24})^2+(y^e_{34})^2\right]-\frac{3}{2}x^\nu_{24}(y^e_{24})^2+\frac{1}{2}x^\nu_{24}(y^\nu_{24})^2+3x^\nu_{24}(y^d_{43})^2+\\ &x^\nu_{24}(y^e_{43})^2-\frac{3}{2}x^\nu_{34}y^e_{24}y^e_{34}+\frac{1}{2}x^\nu_{34}y^\nu_{24}y^\nu_{34}\end{aligned} \tag{3.146}$$

$$\begin{aligned}\beta^{(1)}(x^\nu_{34}) &= -\frac{9}{20}g1^2x^\nu_{34}-\frac{9}{4}g2^2x^\nu_{34}+\frac{5}{2}x^\nu_{34}\left[(x^\nu_{14})^2+(x^\nu_{24})^2+(x^\nu_{34})^2\right]+\frac{1}{2}x^\nu_{14}y^\nu_{14}y^\nu_{34}-\frac{3}{2}x^\nu_{24}y^e_{24}y^e_{34}\\ &+\frac{1}{2}x^\nu_{24}y^\nu_{24}y^\nu_{34}+\frac{1}{2}(x^L_{34})^2x^\nu_{34}+3x^\nu_{34}\left[(y^d_{14})^2+(y^d_{24})^2+(y^d_{34})^2\right]-\frac{3}{2}x^\nu_{34}(y^e_{34})^2\\ &+x^\nu_{34}\left[(y^e_{24})^2+(y^e_{34})^2\right]+\frac{1}{2}x^\nu_{34}(y^\nu_{34})^2+3x^\nu_{34}(y^d_{43})^2+x^\nu_{34}(y^e_{43})^2\end{aligned} \tag{3.147}$$

4

Theoretical approach to VLF

After the phenomenological analysis of VLFs in the previous chapter, we now shift to a more theoretical perspective. This chapter explores the UV behavior of gauge theories with VLFs using FRG techniques. In particular, we study a toy model consisting of an infinite number of quarks and gluons in the large-N_F, large-N_c limit with fixed ratio. This setup enables a non-perturbative analysis of the RG flow and the identification of interacting UV fixed points.

4.1 Non-perturbative fixed point of gauge-Yukawa theories

This chapter is based on a work that will soon appear on the ArXiv, performed in collaboration with D. Litim and T. Büyükbese.

4.1.1 Introduction

UV fixed points are essential in providing a rigorous foundation for QFTs. Their presence guarantees UV completeness, ensuring that theories remain predictive and mathematically consistent at arbitrarily high energies. This contrasts with effective field theories, which lose their predictive power beyond specific energy thresholds. Analogous to critical points observed in continuous phase transitions in condensed matter physics, UV fixed points in particle physics often indicate an underlying conformal field theory. Historically, the existence of non-interacting UV fixed points – known as asymptotic freedom – has been well-established. More recently, however, the identification of interacting UV fixed points, termed AS, has significantly broadened the landscape, prompting extensive exploration of potential UV-complete theories BSM.

A notable example of a UV-complete particle theory featuring an interacting fixed point is provided by a model consisting of N_F fermions interacting with $SU(N_c)$ gauge fields and scalar fields through gauge and Yukawa couplings [140]. In scenarios lacking asymptotic freedom, quantum fluctuations play a crucial role, balancing the growth in gauge coupling via the Yukawa interactions and thereby stabilizing the theory at an interacting UV fixed point. Perturbative control over this fixed point is achieved in the large-N limit, where detailed properties of the theory can be systematically calculated using perturbation theory. The small parameter facilitating this perturbative approach is called *Veneziano parameter* and it is defined as $\epsilon = N_F/N_c - 11/2$. To date, precise computations of critical couplings, scaling exponents, and the extent of the "conformal window" have been carried out up to third-order accuracy in ϵ [141].

In this work, the inclusion of an infinite set of perturbative non-renormalisable operators is considered in the EAA, and the UV fixed point of corresponding couplings are computed at leading order in the Veneziano parameter ϵ. Incidentally, the leading order power scales with the canonical mass dimension of the operator under consideration, with anomalous dimension giving a sub-leading effect. Because of such power counting argument, it is possible to re-sum this infinite tower of operators into a closed form.

The chapter is structured as follows: after introducing the renormalisable version of the model and reporting the main results of the perturbative calculations in 4.1.2, we extend the model by including beyond marginal operators in 4.1.3 and compute their flow equation. In 4.1.4, the fixed point solution is computed analytically and numerically, explicitly showing the power counting argument aforementioned. In 4.1.5 the anomalous dimensions of the operators is computed and in 4.1.6 a closed form of the scalar potential is given. Conclusions are given in 4.1.7.

4.1.2 Model

Let us consider a four-dimensional QFT with $SU(N_c)$ gauge group, N_F coloured quark-like fermion and a complex uncharged scalar. The theory has a global $U(N_F)_L \times U(N_F)_R$ flavour symmetry. The most generic perturbatively renormalizable Lagrangian is then:

$$\begin{aligned}\mathcal{L} = &-\frac{1}{2}\mathrm{Tr}\, F^a_{\mu\nu}F^{a\mu\nu} + \mathrm{Tr}\left(\partial_\mu H^\dagger \partial^\mu H\right)\\ &- m^2 \mathrm{Tr}\left(H^\dagger H\right) - u\,\mathrm{Tr}\left(H^\dagger H\right)^2 - v\left(\mathrm{Tr}\, H^\dagger H\right)^2\\ &+ \mathrm{Tr}\left(\bar{\psi}\, i\not{D}\, \psi\right) - y\,\mathrm{Tr}\left(\bar{\psi}_L H \psi_R + \bar{\psi}_R H^\dagger \psi_L\right),\end{aligned} \tag{4.1}$$

where $\psi = \psi_L + \psi_R$ is understood and the trace Tr is to be intended over all the internal indices. The fixed points of the Lagrangian (4.1) have been studied within the perturbative expansion in [140–142]. In [140] the four marginal couplings given by the gauge coupling, the Yukawa coupling, the "single trace" and the "double trace" have been rescale respectively as

$$\alpha_g = \frac{g^2 N_c}{4\pi^2}, \qquad \alpha_y = \frac{y^2 N_c}{4\pi^2}, \qquad \alpha_u = \frac{u N_F}{4\pi^2}, \qquad \alpha_v = \frac{v N_F^2}{4\pi^2}, \tag{4.2}$$

so that the proper power of N_F and N_c is taken into account. The Veneziano parameter

$$\epsilon = \frac{N_F}{N_c} - \frac{11}{2} \tag{4.3}$$

was introduced and the limit in which both N_F and N_c are large while their ratio is fixed has been employed. In such limit, it is possible to show that the theory at the UV fixed point is parametric in ϵ. Even more interestingly, it was shown PT can be traded for a power series expansion in ϵ. The widely used terminology and systematic in PT with Veneziano limit is detailed *e.g.* in [141]: the zero-th order ϵ^0 corresponds to the loop order `100`, where no fixed point is present. The leading order ϵ^1 corresponds to 211 loop expansion and this is the lowest order where a fixed point appears, as described in [140]. The next-to-leading order ϵ^2 relates to the 322 loop expansion and this is the first non-trivial order where bounds on the conformal window arise [142]. Finally, the next-to-next-to-leading order, ϵ^3, has been recently studied in [141], modifying the previous bounds on the conformal window. This way, the interacting fixed point for the couplings in equation 4.2 is given by:

$$\begin{aligned} \alpha_g &= +0.456\epsilon + 0.781\epsilon^2 + 6.610\epsilon^3\,, \\ \alpha_y &= +0.211\epsilon + 0.508\epsilon^2 + 3.322\epsilon^3\,, \\ \alpha_u &= +0.200\epsilon + 0.440\epsilon^2 + 2.693\epsilon^3\,, \\ \alpha_v &= -0.137\epsilon - 0.632\epsilon^2 - 4.313\epsilon^3\,. \end{aligned} \tag{4.4}$$

The structure of the fixed point is then determined by linearizing the system of RGEs. Let us define $\{\alpha_i\}$ as the set of all coupling constants in the theory. One thus computes in the vicinity of the fixed point the stability matrix M_{ij} :

$$M_{kj} = \left[\frac{\partial \beta_k(\alpha_i)}{\partial \alpha_j}\right]_{\alpha_i=\alpha_i^*}\,, \tag{4.5}$$

whose eigenvalues define the opposite of the critical exponents θ_i. If $\theta_i > 0$ the corresponding eigendirection is UV-attractive and dubbed as *relevant*. All RG trajectories along this direction asymptotically reach the fixed point, thus a deviation of a relevant coupling from the fixed point introduces a free parameter in the theory. One can then use this freedom to adjust the coupling at some high trans-Planckian scale to match an eventual measurement in the IR. If $\theta_i < 0$ is negative, the corresponding eigendirection is UV-repulsive and dubbed as *irrelevant*. In such a case only one trajectory exists that the coupling's flow can follow towards the IR, thus providing potentially a specific prediction for its value at the experimentally accessible scale. Finally, $\theta_i = 0$ corresponds to a *marginal* eigendirection characterized by the RG flow that is logarithmically slow and one needs to go beyond the linear approximation to determine whether a fixed point is attractive or repulsive.
The critical exponent of this model have been computed in previously mentioned works and here we report the result at 433 loop accuracy:

$$\begin{aligned} \theta_1 &= +0.608\,\epsilon^2 - 0.707\,\epsilon^3 - 6.947\,\epsilon^4, \\ \theta_2 &= -2.737\,\epsilon - 6.676\,\epsilon^2 - 22.120\,\epsilon^3, \\ \theta_3 &= -2.941\,\epsilon - 1.041\,\epsilon^2 - 5.137\,\epsilon^3, \\ \theta_4 &= -4.039\,\epsilon - 9.107\,\epsilon^2 - 38.646\,\epsilon^3. \end{aligned} \tag{4.6}$$

The theory has a single relevant eigenvalue, while the other three are irrelevant. As already mentioned, we only consider the LO in ϵ for our analysis, while NLO and NNLO calculations will be studied in future works.
As it will become important later, we provide results for the anomalous dimensions associated with the fermions and scalars [140]. We report here the 1-loop results for the anomalous dimensions

$$\gamma_H = \alpha_y \qquad\qquad \gamma_Q = \left(\frac{11}{2} + \epsilon\right)\alpha_y\,, \tag{4.7}$$

Next, we report the anomalous dimension for the scalar mass term from the composite operator $\mathrm{Tr}(H^\dagger H)$ at 1-loop:

$$\gamma_\rho \equiv \frac{d\ln M^2}{d\ln\mu} = 8\alpha_u + 4\alpha_v + 2\alpha_y\,, \tag{4.8}$$

as well as the anomalous dimension for the composite operator $\mathrm{Tr}(H^\dagger H)^2$ at 1-loop:

$$\gamma_\tau = -8\alpha_v\,. \tag{4.9}$$

At the classical level, the moduli space has been studied in [140], and here we report the main results. The scalar potential

$$V = u\,\mathrm{Tr}\left(H^\dagger H\right)^2 + v\left(\mathrm{Tr}\,H^\dagger H\right)^2 \tag{4.10}$$

can be studied at a classical field configuration $H_c = \mathrm{diag}(h_1, ..., h_{N_F})$ after a chiral $U(N_F)_L \times U(N_F)_R$ rotation

$$V = u\sum_{i=1}^{N_F} h_i^4 + v\left(\sum_{i=1}^{N_F} h_i^2\right)\,. \tag{4.11}$$

Extremising such potential and requiring vacuum stability gives two possible solutions. The first solution is obtained for a field configuration $h_1 = 1$, $h_{i>1} = 0$, provided that $u < 0$ and $v + u \geq 0$. As we will see later when studying the theory at the UV fixed point, such condition is not met, as $u > 0$. The second solution is given by all fields being equal, $h_i = 1$, provided that $u \geq 0$ and $(N_F\,v) + u \geq 0$. Vacuum stability at the UV fixed point translates into the following conditions:

$$H_c = \mathrm{diag}(1, ..., 1)/\sqrt{N_F}\,, \qquad \alpha_u^* \geq 0 \qquad \alpha_v^* + \alpha_u^* \geq 0\,. \tag{4.12}$$

4.1.3 Beyond marginal operators

In this work, we start the exploration of beyond marginal operators (BMO) and their influence in the model at hand. The reason is that the theory at the UV fixed point is a (weakly, but still) interacting theory, and as such it switches on all the BMO. It is then important to compute the fixed point solution of such BMO couplings and their scaling dimensions. To achieve so, we employ functional renormalisation, as introduced in 2.2.5, and compute the scale dependence of Γ_k as

$$\partial_t\Gamma_k = \frac{1}{2}\,\mathrm{STr}\left[\partial_t R_k \cdot \left(\Gamma_k^{(2)} + R_k\right)^{-1}\right]\,. \tag{4.13}$$

We use optimised regulator [143] for both the bosonic and fermionic propagators:

$$R_k^B(q) = (k^2 - q^2)\,\theta(k^2 - q^2)\,, \qquad R_k^F(q) = \not{q}\left(\sqrt{\frac{k^2}{q^2}} - 1\right)\theta(k^2 - q^2)\,, \tag{4.14}$$

where ^{B} and ^{F} respectively stands for the regulator function used for bosons and fermions. In this work we make the choice to not compute the contributions coming from the gauge sector using FRG, and simply retain the results from PT. As an ansatz for the effective action Γ_k, we retain the first order in the derivative expansion, working in what is knows as the

Local Potential Approximation (LPA):

$$\Gamma_k\left[H,\psi,\bar{\psi}\right] = \int d^d x \left[-\frac{1}{4} G^a_{\mu\nu} G^{\mu\nu}_a + Z^H_k \,\mathrm{Tr}\left((D_i H)^\dagger (D^i H) \right) + V_k + Z^\psi_k \bar{\psi} \left(i \not{D} + Y_k H_5 \right) \psi \right] \tag{4.15}$$

where the scalar fields are in the basis of the generators of $U(N_F)$, $H = (\sigma_a + i\pi_a)\, T_a$ and $H_5 = (\sigma_a + i\gamma_5 \pi_a)\, T_a$. The action is chirality invariant, so that any field configuration needs to reflect such symmetry. A possible set of independent chiral invariants is given by:

$$\begin{aligned} P_1 &= \mathrm{Tr}\left(H^\dagger H\right), \\ P_2 &= \mathrm{Tr}\left(H^\dagger H - \mathrm{Tr}(H^\dagger H)/N_F\right)^2, \\ &\dots \\ P_{N_F} &= \mathrm{Tr}\left(H^\dagger H - \mathrm{Tr}(H^\dagger H)/N_F\right)^{N_F}. \end{aligned} \tag{4.16}$$

The working approximation given by computing the EAA in LPA has been shown to be exact within large-N limit.
Following [144], we parameterize the potential $V_k(H)$ in terms of only the first two invariants. Specifically, we want to study an ansatz that is very general in the first invariant and retain only a linear term in the second invariant. Concerning the Yukawa interaction, in this first analysis, we restrict ourselves to a function of the first invariant only:

$$\begin{aligned} V_k(H) &\equiv U_k(P_1) + P_2\, C_k(P_1), \\ Y_k(H) &\equiv Y_k(P_1). \end{aligned} \tag{4.17}$$

It is important to notice that on the flat direction in equation 4.12, we have $P_{i\neq 1} = 0$, so that vacuum stability is determined by studying $U_k(P_1)$. However, as we will see in the following sections, the flow equation of the function $U_k(P_1)$ depends on the other functions $C_k(P_1)$, $Y_k(P_1)$, so that we have to take them into consideration in our study.
Regarding the anomalous dimensions $Z_{H,k}$ and $Z_{\psi,k}$, in this first analysis, we do not compute their flow with FRG, and retain the results obtained using PT, equations 4.4. Moreover, the running of the gauge coupling α_g is also taken from perturbative calculations, so that we can simply use the fixed point result, up to the leading order in ϵ.
The fields and invariants are rescaled as

$$\begin{gathered} H_i \to k^{(d-2)/2} H_i, \qquad \psi \to k^{(d-1)/2} \psi, \\ P_n = k^{(d-2)n} \rho_n, \end{gathered} \tag{4.18}$$

while the couplings are rescaled as:

$$V_k = k^d v, \;\; Y_k = y, \;\; U_k = k^d u, \;\; C_k = c, \tag{4.19}$$

where we have dropped the sub-fix k in the rescaled functions. Since in this study we are focusing on just the first two invariants, we are going to rename them as $\rho_1 \equiv \rho$ and $\rho_2 \equiv \tau$. The most generic flow equations for the dimension-less functions u, c, y are extremely complicated, so here we report the flow equations in the Veneziano limit, using the optimized regulator:

$$\partial_t u = -4u + (2+\eta_\phi)\,\rho\, u' + \frac{1}{2}\left(\frac{1}{1+u'+4\rho c} + \frac{1}{1+u'} - \frac{4}{\frac{11}{2}+\epsilon}\, \frac{1}{1+(\frac{11}{2}+\epsilon)\,\rho\, y_k^2} \right), \tag{4.20}$$

$$\begin{aligned}
\partial_t c = +4\eta_\phi\, c + (2+\eta_\phi)\rho c' + \frac{1}{2}\Bigg(& \frac{8(2c-\rho\, c')c}{(1+4\rho c+u')^3} - \frac{128\rho^3 c^5}{(1+u')^3\,(1+4\rho c+u')^3} \\
& + \frac{64\rho^2 c^3\,(c-\rho c')}{(1+u')^2\,(1+4\rho c+u')^3} - \frac{48\rho^2 c^2 c'}{(1+u')\,(1+4\rho c+u')^3} \\
& - \frac{2c'}{(1+4\rho c+u')^2} - \frac{(\frac{11}{2}+\epsilon)y^4}{\left(1+(\frac{11}{2}+\epsilon)\rho y^2\right)^3}\Bigg),
\end{aligned} \tag{4.21}$$

$$\begin{aligned}
\partial_t y = -3\alpha_g y(0) + \frac{1}{2}(2\eta_\psi+\eta_H)y + (2+\eta_\phi)\rho y' - \frac{1}{2}\left(\frac{y'}{(1+4\,\rho\, c+u')^2} + \frac{y'}{(1+u')^2}\right) \\
+ \frac{y^3}{2\,(1+\rho y^2)\,(1+4\rho\, c+u')}\left(\frac{1}{1+4\rho\, c+u'} + \frac{1}{1+\rho y^2}\right) \\
- \frac{y^3}{2\,(1+u')\,(1+\rho y^2)}\left(\frac{1}{1+\rho y^2} + \frac{1}{1+u'}\right).
\end{aligned} \tag{4.22}$$

Studying the flow of these functions in their most generic functional form is possible only within numerical calculations, and we postpone this task to a future work. In the following, we will consider power series of the functions u, c, y around some field configuration. In the literature, for physical relevancy, the options usually taken into accounts are of two types. A first type of expansion is around a null-field configuration

$$u(\rho) = \sum_{n=0}^{M} u_n\, \rho^{n+1}, \qquad c(\rho) = \sum_{n=1}^{M} c_n\, \rho^{n-1}, \qquad y(\rho) = \sum_{n=1}^{M} y_n\, \rho^{n-1}. \tag{4.23}$$

Here, the first summation starts from zero, so that a mass term $m^2 \equiv u_0$ is taken into account. A second possible expansion is around the RGE flowing minimum of the potential κ:

$$u(\rho) = \sum_{n=0}^{M} u_n(\rho-\kappa)^{n+1}, \qquad c(\rho) = \sum_{n=1}^{M} c_n(\rho-\kappa)^{n-1}, \qquad y(\rho) = \sum_{n=1}^{M} y_n(\rho-\kappa)^{n-1}. \tag{4.24}$$

In both expansions, the starting point of the summation is chosen such that couplings with subscript 1 are associated with dimension-4 operators, couplings with subscript 2 are associated with dimension-6 operators and so on. The relation between the quartic u and v and the new couplings u_1 and c_1 is $\alpha_u = c_1$ and $\alpha_v = u_1 - c_1$. The perturbatively renormalizable Yukawa coupling α_y is identified with y_1^2.
In appendix 4.A we show that the fixed point solutions for the coupling constants of the model, at LO in ϵ, do not depend on the expansion point for the functions u, c, y. In what follows, we will always refer to results for the expansion around a massive null-field configuration, equation 4.23, but analogue results can be obtained for the RGE flowing minimum.

4.1.4 Ultraviolet fixed point

In this section, we want to study the flow equations 4.20-4.22 at the UV fixed point. As previously described, the fixed point is induced by the interplay between the gauge coupling α_g and the yukawa coupling α_y and so it is important to retain the fixed point value for the gauge coupling as from equation 4.4. Clearly, a full FRG calculation would reproduce the same LO term for the gauge coupling, as this is universal.

4.1.4.1 A generic argument for the leading order calculation

In this section we will show how the fixed point at leading order in ϵ is computed. For simplicity and to keep the equations as light as possible, the expansion around a null field configuration and a potential with no mass term is going to be analyzed, corresponding to $u_0 = 0$ in 4.23. By setting $M = 0$, we obtain the set of β-functions for the canonically marginal couplings. The fixed point solution, at LO in ϵ, is well known:

$$u_1 \sim \epsilon\,, \qquad c_1 \sim \epsilon\,, \qquad y_1 \sim \sqrt{\epsilon}\,. \tag{4.25}$$

In order to study the fixed point of dimension 6 operators, we need to truncate the series at $M = 1$. Without loss of generality, we can focus on the β-function for the coupling c_2:

$$\partial_t c_2 = +2c_2 + c_2\left(4u_1 + 20c_1 + 6y_1^2\right) + \left(\frac{363}{2}y_1^6 - 48u_1c_1^2 - 96c_1^3\right) + \ldots\,. \tag{4.26}$$

In the former equation, the first term represents the contribution coming from the canonical mass dimension, while the second term is given by the anomalous dimension. The big bracket in the second line represents the quantum corrections given by the right-hand side of the Wetterich equation and depends only on lower dimensional couplings wrt c_2. Finally, the ellipsis represent higher dimensional couplings, which in this truncation are not retained. To solve the equation at the fixed point, we immediately notice that the contribution coming from the anomalous dimension is of order ϵ and so it is negligible compared to the contribution from the canonical dimension, which is of order unity. For such reason, the fixed point for c_2 is determined by the big bracket in the last term, which is of order ϵ^3. The latter result can be generalized for the other dimension 6 operators and can be summarized by saying that their fixed point at leading order in the Veneziano parameter is given by the corresponding dimension 4 operators fixed point plus 2:

$$u_2 \sim \epsilon^3\,, \qquad c_2 \sim \epsilon^3\,, \qquad y_2 \sim \sqrt{\epsilon^5}\,. \tag{4.27}$$

Such argument can be schematically generalized to compute the fixed point of a dimension $2n$ operator as follows. The β-function of the operator:

$$\partial_t \lambda_{2n} = (2n-4)\lambda_{2n} + A\,\epsilon\,\lambda_{2n} + B\,\epsilon^n\,, \tag{4.28}$$

where A is the anomalous dimension with the dependence on ϵ made explicit and B is some combination of lower dimensional operators, again with the dependency on ϵ made explicit. Solving this equation at the fixed point for λ_{2n} gives

$$\lambda_{2n} = \frac{B\,\epsilon^n}{(2n-4) + A\,\epsilon}\,. \tag{4.29}$$

If $n \neq 2$, the anomalous dimension term can be neglected, exactly as in the previous case and the LO in ϵ for operators of dimension $2n$ is $\lambda_{2n} \sim \epsilon^n$. For canonically marginal couplings, $n = 2$, the first term in the denominator disappears and the anomalous dimension term reduces the LO by one unit, making the fixed point for operators of dimension $2n$ of order $\lambda_{2n=4} \sim \epsilon^{n-1} = \epsilon$. Incidentally, also a mass term, $n = 1$, would have as LO ϵ. This simple argument is confirmed numerically, as shown in Table 4.1. As perhaps obvious, the calculation of the fixed point of the marginal couplings gives back the well-known result from perturbation theory, equation 4.4.

Coupling	Fixed point	Coupling	Fixed point	Coupling	Fixed point
c_2	$-0.404135\epsilon^3$	u_2	$-0.0844283\epsilon^3$	y_2	$+0.318417\sqrt{\epsilon^5}$
c_3	$+0.558651\epsilon^4$	u_3	$+0.0721923\epsilon^4$	y_3	$-0.468528\sqrt{\epsilon^7}$
c_4	$-0.812282\epsilon^5$	u_4	$-0.0699564\epsilon^5$	y_4	$+0.626392\sqrt{\epsilon^9}$
c_5	$+1.16104\epsilon^6$	u_5	$+0.0706016\epsilon^6$	y_5	$-0.798058\sqrt{\epsilon^{11}}$

TABLE 4.1: The values of the interactive fixed point solution of the first few beyond marginal operators.

4.1.4.2 Independence of the fixed point on the expansion point

It is also interesting to show that regardless of the expansion point for the power series of the coupling functions u, c, y, the fixed point solution at LO in ϵ does not change. Starting with the null-field configuration with a mass term in the potential, the terms of the β-function of (for example and without any loss of generality) c_1 that contains the mass u_0 reads:

$$\partial_t c_1 \supset \frac{8\,c_1^2}{(1+u_0)^3} - \frac{c_2}{(1+u_0)^2}\,. \tag{4.30}$$

In the previous section we have shown that the LO in ϵ for a non-marginal operator of dimension $2n$ is ϵ^n, while for marginal operators it is $\epsilon^{n-1} = \epsilon$, which means that $u_0 \approx \epsilon$, $c_2 \approx \epsilon^3$ but $c_1 \approx \epsilon$ rather than ϵ^2. It is then clear that, at LO in ϵ, contributions given by u_0 are negligible and so the fixed points of marginal and beyond marginal operators do not depend on the presence and value of a mass term in the potential. If we were to compute the NLO term in the Veneziano limit, the mass term would give a non-negligible contribution.
Similarly, we can ask whether an expansion around the true minimum of the potential, at the fixed point, can influence the fixed point at LO in ϵ. Taking again into consideration the β-function of c_1, as from appendix 4.A, we note that terms including κ are sub-leading with respect to the LO of the fixed point calculation.

4.1.5 Scaling dimensions

In this section, we want to study the behaviour of the theory close to the UV fixed point, by computing the critical exponents associated to the couplings of the theory. To do so, we follow standard procedures by calculating the stability matrix and the critical exponents, as defined in 4.5.
For simplicity and without loss of generality, we show the results for the expansion around a null-field configuration, for the truncation $M = 1$, meaning for operators up to canonical mass dimension 6

$$M = \begin{pmatrix} -2+1.47\epsilon & -2-0.21\epsilon & 0 & -2-0.21\epsilon & 0 & 1.84\sqrt{\epsilon} & 0 \\ 0 & 2.94\epsilon & -3-0.31\epsilon & 3.70\epsilon & -2-0.21\epsilon & 0 & 1.84\sqrt{\epsilon} \\ 0 & 0 & 2+4.41\epsilon & 0 & 3.70\epsilon & 0 & 0 \\ 0 & 0 & 0 & 4.04\epsilon & -1-0.10\epsilon & 0 & 0 \\ 0 & 0 & 0 & 0 & 2+5.51\epsilon & 0 & 0 \\ 0 & 0 & 0 & 0 & 0 & 2.74\epsilon & -1-0.10\epsilon \\ 0 & 0 & 0 & 0 & 0 & 0 & 2+2.84\epsilon \end{pmatrix},$$

where we have ordered the couplings (and accordingly the β-functions) as α_0, α_1, α_2, γ_1, γ_2, y_1, y_2. It is perhaps not surprising that the eigenvalues (at leading order in ϵ) are sitting on the diagonal of this matrix, with off-diagonal terms giving corrections starting from next to leading order in ϵ. Because of such simple form of the stability matrix, we can associate its eigenvalues (the critical exponents of the theory) directly to couplings in the theory:

$$\begin{aligned} &\theta_{u_0} = +2 - 1.47\epsilon\,, \\ \theta_{u_1} &= -2.94\epsilon\,, & \theta_{u_2} &= -2 - 4.41\epsilon\,, \\ \theta_{c_1} &= -4.04\epsilon\,, & \theta_{c_2} &= -2 - 5.51\epsilon\,, \\ \theta_{y_1} &= -2.74\epsilon\,, & \theta_{y_2} &= -2 - 2.84\epsilon\,. \end{aligned} \tag{4.31}$$

From now on, we will comment on results for the couplings u_n, but the generalization to c_n and y_n is straightforward. Let us start by noticing that the difference between the critical exponents of subsequent couplings of the same function is constant:

$$\theta_{u_n} - \theta_{u_{n-1}} = -2 - 1.47\epsilon\,. \tag{4.32}$$

To get a better understanding of this result, let us focus on the critical exponents of couplings u_n and let us look at the flow equation for the function u, equation 4.20. Since the critical exponents are sitting on the diagonal of the stability matrix, to extract the critical exponent related to the coupling u_n we can simply take n derivatives of the flow equation with respect to ρ and then retain only the terms that are linear in u_n:

$$\partial_t u_n \supset (2n-4)\, u_n + 4n \left(u_1 + c_1 + \frac{1}{2} y_1^2 \right) u_n\,. \tag{4.33}$$

Computing the derivative of such equation with respect to u_n gives the negative of the critical exponents

$$\theta_{u_n} = (4-2n) - n\gamma_\rho\,, \tag{4.34}$$

where we have used the previously defined anomalous dimension for the operator ρ at 1-loop, equation 4.8. Similarly, we can compute the critical exponents for the couplings c_n and y_n:

$$\theta_{c_n} = (4-2n) - n\gamma_\rho - \gamma_\tau\,, \tag{4.35}$$

$$\theta_{y_n} = -2n - 2\gamma_\rho - \eta_\psi - \frac{1}{2}\eta_\phi\,, \tag{4.36}$$

where we have used the previously defined anomalous dimension of the operator τ, equation 4.9 and for the fermion and scalar fields, equations 4.7. Perhaps not surprisingly, the result is that the critical exponents associated to a certain operator are given by the mass dimension (canonical plus anomalous) of the corresponding operator.

4.1.6 Effective potential at the interacting fixed point

In section 4.1.4 we have computed the fixed point solution of a infinite tower of beyond marginal couplings and we have found that the leading order in ϵ has an increasing power with the dimension of the operator, $\lambda_{2n} \approx \epsilon^n$, for an operator of dimension $2n$. When looking at the numerical results from table 4.1, we also notice that the sign of higher-dimensional couplings is alternating. One may try to take the limit of the truncation order M going to infinity and perform a re-summation of the series u, c, y at the fixed point. Before doing so,

it is important to understand to what extent the power series expansions 4.23 can be trusted, by computing the radius of convergence.
To estimate the radius of convergence we use the root test $r = \lim_{n\to\infty} |a_n|^{-1/n}$, where a_n is the coefficient of the n-th order term of the power series. Without loss of generality, we focus on the flow equation of the function u and notice how the quantum corrections coming from the right hand side of the Wetterich equation have the well-known form $(1+m_i^2)^{-1}$, with m_i the rescaled, dimensionless mass for some particle i. Dropping corrections coming from the anomalous dimension, we can rewrite the flow equation in general as

$$\partial_t u = -4u + 2\rho u' + \frac{1}{2}\sum_i \frac{1}{1+m_i^2(\rho)} \,. \tag{4.37}$$

Similarly to the calculation for the critical exponent, we can compute the β-function for the coupling u_n as the n-th derivative of the flow with respect to ρ, by using the Faà di Bruno formula:

$$\frac{d^n}{dx^n} f(g(x)) = \sum_{\{m_k\}} \frac{n!}{m_1!m_2!\cdots m_n!} \cdot f^{(m_1+m_2+\cdots+m_n)}(g(x)) \cdot \prod_{k=1}^{n} \left(\frac{g^{(k)}(x)}{k!}\right)^{m_k} , \tag{4.38}$$

where $m_1 + 2m_2 + 3m_3 + \cdots + nm_n = n$. We can identify $f(x) = (1+x)^{-1}$ and $g(\rho) = m_i^2(\rho)$ in which case the Faà di Bruno formula can be written as:

$$\frac{d^n}{d\rho^n}\frac{1}{1+m_i^2(\rho)} = \sum_{\{m_k\}} \frac{n!}{m_1!m_2!\cdots m_n!} \cdot \frac{(-1)^{1+m_1+m_2+\cdots+m_n}}{(1+m_i^2(\rho))^{1+m_1+m_2+\cdots+m_n}} \cdot \prod_{k=1}^{n} \left(\frac{1}{k!}\frac{d^k}{d\rho^k} m_i^2(\rho)\right)^{m_k} . \tag{4.39}$$

Since m_i has in general some power series expansion in ϵ, it is not too difficult to understand that in the denominator we can neglect the term m_i^2 against the unity. In the same way, in the product symbol, the leading order term in ϵ is given by the "first" term of the summation, when $m_1 = n$ and all other $m_i = 0$:

$$\frac{d^n}{d\rho^n}\frac{1}{1+m_i^2(\rho)} = \left(\frac{d}{d\rho} m_i^2(\rho)\right)^n . \tag{4.40}$$

This way, the n-th derivative of the flow equation 4.20 takes the form:

$$\partial_t u_k^{(n)} = (2n-4)u_k^{(n)} + \frac{(-1)^n}{2} n! \left((u_k'')^n + (u_k'' + 4c_k)^n - \frac{8}{11}\left(\frac{11}{2} y_k^2\right)^n \right)$$

where in the right hand side we have retained only terms that have the same power of ϵ as the left hand side. The fixed point for the coupling u_n can be extracted by setting $\partial_t u_k^{(n)} = 0$ and using the power series expansion 4.23 to extract the coupling u_n from the function u_k:

$$u_n^* = \frac{(-1)^{n+1}}{n(2n-4)} \left((2u_1^*)^n + (2u_1^* + 4c_1^*)^n - \frac{8}{11}\left(\frac{11}{2} y_1^{*2}\right)^n \right) . \tag{4.41}$$

Some comments are in order. Firstly, the factor $(-1)^n$ explains the alternating sign for the numerical values of the fixed points from table 4.1. Secondly, the fixed point value of arbitrarily higher dimensional couplings (remember that n can in principle run until infinity) is determined by increasing powers of the marginal couplings. This is once again a manifestation of the power counting argument in ϵ as described in section 4.1.4.1. Notice how the latter equation represents a_n of the root test, so that we can compute the radius of convergence:

$$r^{-1} = \mathrm{Max}\left(2u_1^*, 2u_1^* + 4c_1^*, \frac{11}{2}y_1^{*2}\right) = \frac{11}{2}y_1^{*2} \approx 1.16\epsilon\,. \tag{4.42}$$

As perhaps obvious, the smaller ϵ, the bigger the radius of convergence, which also means we can trust the power series expansion to higher field values ρ. However, by using power series approximations, we are not entitled to explore arbitrarily large field values. To solve such problem, we insert the fixed point solution 4.41 in the expansion 4.23 and perform a re-summation of the full function u:

$$u^*(\rho) = u_0^*\rho + u_1^*\rho^2 + \frac{\rho^2}{4}\left(A^2\log(1+A\,\rho) + B^2\log(1+B\,\rho) - \frac{4N_c}{N_F}D^2\log(1+D\,\rho)\right) \tag{4.43}$$

where we have defined

$$A = 2u_1^*\,, \qquad B = 2u_1^* + 4c_1^*\,, \qquad D = \frac{N_F}{N_c}y_1^{*2}\,. \tag{4.44}$$

Similarly, a resummation for the expansion 4.24 can be performed and the result can be obtained from the previous formula, by setting $u_0^* = 0$ and making the simple replacement $\rho \to \rho - \rho_0^*$, where $\rho_0^* = 0.414$, cf. 4.A. Interestingly, the function u depends only on four numbers, which are combinations of the marginal coupling constants. The main result, therefore, is that once we have determined the marginal couplings, the non-perturbative corrections are also determined through log functions of the marginal couplings. Even more interestingly, our result is in agreement with the one in [145], in which the Callan-Symanzik equation is used to compute the effective potential.
Similar closed expressions can be obtained for the functions c and y:

$$\begin{aligned} c^*(\rho) = \gamma_1^* &- \frac{1}{32}(3A^2+8AB+B^2)\log(1+A\rho) + \frac{1}{32}(11A^2-8AB+9B^2)\log(1+B\rho) \\ &+ \frac{(A-B)(6A^2+48AB-30B^2)\rho}{64(1+A\rho)^2(1+B\rho)^2} + \frac{(A-B)(7A^3+103A^2B-19AB^2-19B^3)\rho^2}{64(1+A\rho)^2(1+B\rho)^2} \\ &+ \frac{(A-B)(58A^3B+48A^2B^2-34AB^3)\rho^3}{64(1+A\rho)^2(1+B\rho)^2} + \frac{(A-B)(40A^3B^2-16A^2B^3)\rho^4}{64(1+A\rho)^2(1+B\rho)^2} \\ &- \frac{1}{2}\frac{N_c}{N_F}\frac{D^3(4+3D\rho)\,\rho}{(1+D\rho)^2} - \frac{N_c}{N_F}D^2\log(1+D\rho)\,, \end{aligned} \tag{4.45}$$

$$\begin{aligned} y^*(\rho) = y_0^*\Bigg(1 &- \frac{AD}{2(A-D)}\log(1+A\rho) + \frac{BD}{2(B-D)}\log(1+B\rho) \\ &+ \frac{(A-B)D^2}{2(A-D)(D-B)}\log(1+D\rho) - \frac{(A-B)D\rho}{4(1+A\rho)(1+B\rho)(1+D\rho)}\Bigg)\,. \end{aligned} \tag{4.46}$$

While the closed expressions for the functions c and y look more complicated than the one for u, they share some important features. Firstly, they all depend only on the combinations of marginal couplings defined in equation 4.44. Secondly, the logarithmic terms 1-loop corrections that appeared in the function u are also present in the functions c and y, but with different coefficients, that are combinations of A, B and D. Finally, the latter expressions have extra terms, rational in the field value ρ: the interesting property those terms share is that they are negligible in both the low- and high- field value limit, and become feasible only for finite, non-zero values of the field. Therefore, they do not determine the asymptotic behaviour of the functions c and y, which is instead determined by the sole logarithmic terms.

4.1.7 Conclusions

In this work, we have investigated the UV behavior of a class of gauge-Yukawa theories featuring a large number of fermions and gauge fields. These theories are known to exhibit interacting UV fixed points – realizing the scenario of asymptotic safety – through a delicate interplay between gauge and Yukawa interactions in the Veneziano limit, under which the number of both fermions and gauge fields is taken to infinity, while keeping the ratio fixed. Building upon prior studies that focused on the renormalisable sector, we have extended the analysis by systematically incorporating an infinite tower of perturbatively non-renormalisable operators and computed the UV fixed point of the relative couplings, within the FRG approach.

Our key result is the identification of fixed points for this extended operator basis at leading order in the expansion parameter $\epsilon = N_F/N_c - 11/2$. We showed that the scaling behavior of these higher-dimensional operators is dominated by their canonical mass dimensions, while anomalous dimensions provide only sub-leading corrections. This hierarchy enabled a power-counting resummation of the entire tower into a compact, closed-form scalar potential. The analytical and numerical fixed point solutions confirmed the consistency of this approach. Furthermore, we explicitly computed the anomalous dimensions of the beyond-marginal operators and demonstrated that their contributions do not destabilize the UV fixed point structure obtained at leading order. The results support the robustness of asymptotic safety in this class of theories even when extended to include an infinite set of perturbatively irrelevant operators.

Overall, our findings reinforce the viability of asymptotically safe QFTs beyond the renormalisable paradigm and provide new tools for analyzing the structure of UV completions in gauge-Yukawa systems.

Appendix 4.A: First β-functions in polynomial expansions

In this subsection we report the β-functions of the first terms in the power series expansion 4.20, for the two different expansion point described in the main text: an expansion point around null field configuration is going to be discussed firstly and then an expansion around the RGE flowing minimum of the potential. In both cases, we will discuss the importance of the expansion point on the fixed point value.

Expansion around null-field configuration We report the β-functions of the first terms in the power series expansion 4.23, including the mass term u_0, for the three functions u_k, c_k, y_k. The equations need to be considered already as a LO results. Starting from the mass term u_0:

$$\partial_t u_0 = -2u_0 + \frac{1}{2}\left(-\frac{2u_1}{(1+u_0)^2} - \frac{2(u_1+2c_1)}{(1+u_0)^2}\right) + 2(1+u_0)y_1^2 . \tag{4.47}$$

Let us discuss the fixed point value for u_0: since u_1, c_1 and y_1^2 have a fixed point value at LO linear in ϵ, we can immediately deduce that also the LO fixed point value for the mass term is linear in ϵ, $u_0^* = -0.0518\epsilon$. Notice how this is perfectly in line with the power counting argument for the fixed point at leading order in ϵ, as detailed in section 4.1.4.1.
We now move to the β-functions for the first terms of u_k, c_k, y_k. Starting from the β-functions

for the dimension 4 operators:

$$\partial_t u_1 = \frac{2u_1^2}{(1+u_0)^3} + \frac{2(u_1+2c_1)^2}{(1+u_0)^3} - 11y_1^4 + 4u_1y_1^2 \approx 2u_1^2 + 2(u_1+2c_1)^2 - 11y_1^4 + 4u_1y_1^2\,,$$

$$\partial_t c_1 = \frac{8c_1^2}{(1+u_0)^3} + 4c_1y_1^2 - 11y_1^4 \approx 8c_1^2 + 4c_1y_1^2 - 11y_1^4\,,$$

$$\partial_t y_1 = -3\alpha_g y_1 + \frac{13y_1^3}{2}\,,$$

where the $\approx$ signifies that we are neglecting the u_0 terms in the denominator, as they are sub-leading. Clearly, these are exactly the β-functions at *211* loop order, as already computed and studied in [140].

Next, we move to operators at dimension 6:

$$\begin{aligned}\partial_t u_2 = -4u_2 - \frac{4u_1^3}{(1+u_0)^4} + \frac{6u_1u_2}{(1+u_0)^3} - \frac{4(u_1+2c_1)^3}{(1+u_0)^4} + \frac{2(u_1+2c_1)(3u_2+4c_2)}{(1+u_0)^3} \\ + \frac{121y_1^6}{2} + 6u_2(1+y_1^2) - 44y_1^3y_2 + 2y_2^2\,,\end{aligned} \tag{4.48}$$

$$\partial_t c_2 = -\frac{48(2c_1+u_1)c_1^2}{(1+u_0)^4} + 2c_2 + \frac{4(5c_1+u_1)c_2}{(1+u_0)^3} + \frac{363y_1^6}{2} - 44y_1^3y_2\,, \tag{4.49}$$

$$\partial_t y_2 = -\frac{11c_1y_1^3}{(1+u_0)^2} + 2\left(1+\frac{17y_1^2}{4}\right)y_2 + \frac{8u_1y_2 - 4c_1(11y_1^3 - 2y_2)}{2(1+u_0)^3}\,. \tag{4.50}$$

Again, the contribution given by the mass terms is sub-leading, showing what mentioned in the main text: the presence of a mass term does not modify the value of the fixed point at leading order in ϵ. Moreover, it is quite straightforward to notice that the fixed point for coupling of dimension 6 operators is of order ϵ^3.

Expansion around the true minimum We report the β-functions of the first terms in the power series expansion 4.24, around the RGE flowing minimum ρ_0. Starting from the β-function for ρ_0:

$$\partial_t \rho_0 = -u_1 + 4u_1(1+y_1^2)\rho_0 + \frac{2y_1^2}{(1+\frac{11}{2}y_1^2\rho_0)^2} - \frac{u_1+2c_1}{(1+4c_1\rho_0)^2} \approx -u_1 + 4u_1\rho_0 + 2y_1^2 - u_1 + 2c_1\,, \tag{4.51}$$

where $\approx$ signifies dropping terms that are sub-leading in ϵ. Notice how the above equation depends only on marginal operators, which are linear in ϵ. The fixed point solution is then order unity:

$$\rho_0^* = \frac{c_1 + u_1 - y_1^2}{2u_1} = 0.414\,. \tag{4.52}$$

The β-functions for dimension 4 operators read:

$$\partial_t u_1 = 2u_1^2 + 4u_1y_1^2 + \frac{2(u_1+2c_1)^2}{(1+4c_1\rho_0)^3} - \frac{11y_1^4}{\left(1+\frac{11}{2}y_1^2\rho_0\right)^3} \approx 2u_1^2 + 4u_1y_1^2 + 2(u_1+2c_1)^2 - 11y_1^4\,,$$

$$\partial_t c_1 = 4c_1y_1^2 + \frac{8c_1^2}{(1+4c_1\rho_0)^3} - \frac{11y_1^4}{\left(1+\frac{11}{2}y_1^2\rho_0\right)^3} + \frac{32c_1^4\rho_0^2}{(1+4c_1\rho_0)^3} - \frac{64c_1^5\rho_0^3}{(1+4c_1\rho_0)^3} \approx 4c_1y_1^2 + 8c_1^2 - 11y_1^4\,,$$

$$\partial_t y_1 = -3\alpha_g y_1 + \frac{13y_1^3}{2} - \frac{11y_1^3(4+11y_1^2\rho_0)}{2(2+11y_1^2\rho_0)^2} + \frac{11y_1^3(4+8c_1\rho_0+11y_1^2\rho_0)}{2(1+4c_1\rho_0)^2(2+11y_1^2\rho_0)^2} \approx -3\alpha_g y_1 + \frac{13y_1^3}{2}\,.$$

Contributions proportional to ρ_0 are always sub-leading, so that the choice of expanding the potential around the RGE flowing minimum of the potential does not affect the value of the fixed point at leading order in ϵ.

5

Asymptotically safe gravity confronts VLF phenomenology

As explained in chapter 4, AS is the property of a QFT to develop UV fixed points of the RG flow of the action [146]. Following the development of FRG techniques three decades ago [32, 147], it was shown in numerous papers that AS may arise quite naturally in quantum gravity and provide the key ingredient for the non-perturbative renormalizability of the theory. Fixed points for the rescaled Newton coupling and the cosmological constant were identified initially in the Einstein-Hilbert truncation of the effective action [148–150], based on two operators, and later confirmed in the presence of gravitational operators of increasing mass dimension [151–159], and of matter-field operators [160–162].

From the point of view of particle physics in four space-time dimensions, a particularly exciting possibility is that not only the gravitational action but the full system of gravity and matter may feature UV fixed points in the energy regime where gravitational interactions become strong [163–174]. A trans-Planckian fixed point may provide in that case specific boundary conditions for some of the *a priori* free couplings of the matter Lagrangian, as long as they correspond to *irrelevant* directions in theory space. In this context, indications of AS emerging in U(1) gauge theories have led to discovering a gravity-driven solution to the triviality problem of the SM hypercharge coupling [175–177]. Early achievements of embedding realistic matter systems in AS include the ballpark prediction for the value of the Higgs mass (more precisely, of the quartic coupling of the Higgs potential) obtained a few years ahead of its discovery [178] (see also Refs. [179–181]), and the retroactive "postdiction" of the top-mass value [182].

In order to properly complete a matter system with trans-Planckian AS, one should consistently calculate gravitational corrections to the matter beta function using the formalism of the FRG. The ensuing high-scale boundary conditions for the matter couplings, obtained this way from first principles, should be then compared with observations (cross sections, decay rates, etc.) after running the couplings to the low scale. It has been long known, however, that calculations based on the FRG can be subject to large theoretical uncertainties, stemming from a variety of sources – from the choice of truncation in the gravity action [151, 156, 183–185], to cutoff-scheme dependence [150, 186], to the backreaction of matter, which may introduce a dependence of the gravitational fixed point on the specifics of the matter sector [187–189]. Various results can differ by up to 50–60% [189] so that, often, a precise quantitative determination of the high-scale value of the matter couplings is not possible. Moreover, it has been recently pointed out [190, 191] that some conceptual questions regarding the appropriateness of the FRG itself as the right tool for investigating/enforcing AS in quantum gravity remain open.

On the other hand, because of the universal nature of trans-Planckian interactions, and thanks to the "rigidity" of the dynamics in the vicinity of an interactive fixed point – by virtue of which all quantities can be predicted except for a handful of relevant parameters that will have to be determined experimentally – a first-principle calculation of the gravitational contribution to the matter couplings is not necessarily needed to prove the consistency of certain low-energy predictions with quantum gravity. Often one is content with establishing a heuristic framework in which the trans-Planckian interactions are parameterized by coefficients that are eventually obtained from low-energy observations [2, 110, 192–200].

Such heuristic embedding of a gauge-Yukawa system in trans-Planckian AS has been used in the SM to attempt a prediction of the top/bottom mass ratio [192], the CKM [195], and PMNS [197] matrix elements. In the context of neutrino mass generation, this effective approach was employed to theorize the interesting possibility that the tiny Yukawa couplings of Dirac-type right-handed neutrinos may find their origin in the dynamics of the trans-Planckian flow [197, 200]. NP predictions were extracted for neutrino masses [193], leptoquarks [196], vector-like fermions [110], and γ/Z' kinetic mixing [2]. Following this, predictions were made for the relic abundance of dark matter [194, 201], baryon number [198, 199], as well as axion models [202]. Note, however, that whether gravitational corrections to the running couplings of the scalar potential are multiplicative or not remains a model-dependent issue, as some truncations of the gravitational action can generate additive contributions to the matter beta functions of the scalar potential [201].

5.1 The heuristic approach

The framework of AS we adopt in this work is based on the assumption that the SM and the NP particles couple above the Planck scale, at energy $k \geq M_{\rm Pl} = 10^{19}$ GeV, to quantum gravity or some other NP responsible for generating a fixed point in the trans-Planckian RG flow of the beta functions of all dimensionless couplings. The beta functions of the SM and NP receive in the trans-Planckian regime parametric corrections,

$$\beta_g = \beta_g^{\rm SM+NP} - g\, f_g, \tag{5.1}$$

$$\beta_y = \beta_y^{\rm SM+NP} - y\, f_y, \tag{5.2}$$

$$\beta_\lambda = \beta_\lambda^{\rm SM+NP} - \lambda\, f_\lambda, \tag{5.3}$$

where $\beta_x \equiv dx/d\log k$, and g, y, λ are the set of all gauge, Yukawa and scalar couplings, respectively. The effects of new trans-Planckian interactions are parameterized with fixed effective couplings f_g, f_y, and f_λ. In agreement with theoretical computations in asymptotically safe gravity, the latter are assumed to be universal, in the sense that they differ according to the type of matter interaction (gauge, Yukawa, scalar) but do not change with the quantum numbers of the particles involved.

The parameters f_g, f_y, and f_λ should be eventually determined from the gravitational dynamics [160, 162, 169–174]. In the framework of quantum gravity, calculations utilizing the functional RG have shown that f_g is likely to be non-negative, irrespective of the chosen RG scheme [172], and that $f_g > 0$ is required to make the gauge sector asymptotically free.

On the other hand, the status of the leading-order gravitational correction to the Yukawa couplings, f_y, remains to some extent more uncertain. A number of simplified models were analyzed in the literature [160, 168, 169, 173], but no definite conclusions regarding the size and sign of f_y are available to our knowledge. The same level of ignorance applies to the gravity contribution to the scalar coupling beta function, f_λ [179, 181, 201, 203–206].
As mentioned in the previous section, one ought to keep in mind that the theoretical determination of the parameters f_g, f_y, and f_λ is marred by large uncertainties, which are related to the choice of truncation of the gravitational action and, within a chosen truncation, the cutoff-scheme dependence [150, 186]. Depending on the number of operators considered in the effective action [151, 156, 183–185] various determinations can differ by up to 50-60% [189]. To bypass these obstacles, in the first section, we follow the *heuristic approach* adopted in some recent articles [110, 182, 192, 194–197], in which f_g, f_y, and f_λ are treated as free parameters to be determined by matching the SM couplings onto their low-energy measurements, and postpone the problem of computing the uncertainties of such approach to the second section of this chapter. The ensuing fixed point analysis of the matter beta functions defines in turn a set of boundary conditions for the NP couplings which, unlike the SM ones, have not been directly measured yet.

5.2 Constraints on Z′ solutions to the flavor anomalies with trans-Planckian asymptotic safety

This section is based on "Constraints on Z' solutions to the flavor anomalies with trans-Planckian asymptotic safety" by A. Chikkaballi, W. Kotlarski, K. Kowalska, D. Rizzo, E. M. Sessolo, [2].

In the last few years several "flavor" anomalies have appeared in data published by the LHCb and other experimental collaborations. The most intriguing and statistically significant involve semileptonic $b \to s$ transitions with muons in the final state. In particular, the measurement of the ratios $R_K = \mathrm{BR}(B \to K\mu^+\mu^-)/\mathrm{BR}(B \to Ke^+e^-)$ [207] and $R_{K^*} = \mathrm{BR}(B \to K^*\mu^+\mu^-)/\mathrm{BR}(B \to K^*e^+e^-)$ [16, 208] each deviates from the SM prediction approximately at the $3\,\sigma$ level. While strong deviations in these two "clean" observables would provide a smoking gun for the violation of lepton-flavor universality, the overall empirical frame is buttressed by the concurrent emergence of numerous anomalies in other measurements of branching ratios and angular observables mediated by the $b \to s\,\mu^+\mu^-$ transition [209–218]. A global picture has surfaced, pointing to the potential presence of NP, whose contribution is currently statistically favored compared to the SM prediction alone at the level of more than $5\,\sigma$ – see, *e.g.*, Refs. [18, 219–230] for recent analyses.

However, as detailed in section 2.1.5, the new LHCb's updated analysis in 2022, based on the full Run 1 and 2 datasets [17], has shown how both R_K and R_{K^*} are consistent with the SM within 1σ uncertainties. For the purpose of this section, we are going to consider these anomalies from a theoretical perspective, as a historical motivation for specific BSM scenarios that remain of interest irrespective of the current experimental status.

Global EFT studies of the $b \to s$ anomalous data have confidently shown that some NP states ought to be able to generate the four-fermion operators $\mathcal{O}_9^{(\prime)\mu}, \mathcal{O}_{10}^{(\prime)\mu}$ of the Weak Effective Theory (WET),with different combinations of the corresponding Wilson coefficients being equivalently favored as long as $C^{\mu}_{9,\mathrm{NP}}$ remains large and negative. A handful of simple models were thus identified early on, which could give rise to one or more of these flavor non-diagonal vector operators already at the tree level. Popular choices include leptoquarks (see, *e.g.*,Ref. [231] for a recent review) and new abelian gauge bosons (early studies include Refs. [232–241]).

In this section, we perform a trans-Planckian fixed-point analysis of minimal SM extensions with a new abelian gauge boson Z', which can lead to a solution for the flavor anomalies. The phenomenology of some U(1) extensions of the SM giving a solution to the flavor anomalies and being, at the same time, constrained in an asymptotically safe framework *not* based on quantum gravity was recently investigated in Ref. [242]. In Ref. [198] trans-Planckian AS inspired from quantum gravity was applied to a SM extension with gauged baryon number, without direct connection to the flavor anomalies. Because the Z' is expected to be massive and to couple to the b-s current, the Lagrangians we consider feature Yukawa interactions of a new scalar field S with the SM and VL heavy fermions with color charge. The scalar's vev breaks the abelian gauge symmetry giving mass to the Z' and the mixing of VL and SM quarks generates the flavor non-diagonal gauge coupling. Moreover, because of the presence of VL fermions charged under both the new abelian and the SM gauge groups, the Z' is subject to kinetic mixing with the SM photon and Z boson.

In Sec. 5.2.1 we introduce NP models with an extra U(1) symmetry and VL fermions in the context of the flavor anomalies and recall their general structure. In Sec. 5.2.2 we perform a full fixed-point analysis of the scenarios introduced in Sec. 5.2.1. The resulting predictions for the low-scale physics and the related phenomenology are discussed in Sec. 5.2.3, were we also derive the most recent LHC constraints applying to our models.

5.2.1 Minimal Z' models for the flavor anomalies

In model-independent global analyses the anomalous flavor data is confronted with the operators of an effective Hamiltonian for the $b \to sl^+l^-$ transition (where $l = e, \mu, \tau$). One writes

$$\mathcal{H}_{\text{eff}} = -\frac{4G_F}{\sqrt{2}} V_{tb} V_{ts}^* \sum_{i,l} (C_i^l O_i^l + C_i'^l O_i'^l) + \text{H.c.}\,, \tag{5.4}$$

where G_F is the Fermi constant and V_{tb}, V_{ts} are elements of the CKM matrix. The short-distance physics is encoded in the Wilson coefficients $C_i^{(\prime)l}$, whereas the long-distance physics is described by the four-fermion dimension-six interaction operators $O_i^{(\prime)l}$, invariant under the $\mathrm{SU(3)_c} \times \mathrm{U(1)_{em}}$ gauge group.

The flavor anomalies strongly hint to NP emerging in the coefficients of a few semi-leptonic operators with muons in the final state,

$$\begin{aligned} O_9^{(\prime)\mu} &= \frac{\alpha_{\text{em}}}{4\pi} \left(\bar{s}\gamma^\rho P_{L(R)} b\right) \left(\bar{\mu}\gamma_\rho \mu\right), \\ O_{10}^{(\prime)\mu} &= \frac{\alpha_{\text{em}}}{4\pi} \left(\bar{s}\gamma^\rho P_{L(R)} b\right) \left(\bar{\mu}\gamma_\rho \gamma_5 \mu\right), \end{aligned} \tag{5.5}$$

where α_{em} is the fine-structure constant in the Thomson limit and $P_{L,R} = (1 \mp \gamma_5)/2$ are the standard chiral projectors. We limit ourselves in this work to NP models that can give rise to the left-chiral (unprimed) pair of Wilson coefficients $C_{9,\text{NP}}^\mu$, $C_{10,\text{NP}}^\mu$, and to CP-conserving NP effects (real Wilson coefficients). Global analyses have shown that the fit to the flavor anomalies does not improve significantly by adding the right-chiral components or considering their imaginary part.

The 2σ region consistent with the flavor anomalies reads [229]

$$-1.03 \leq C^{\mu}_{9,\mathrm{NP}} \leq -0.43 \tag{5.6}$$

when $C^{\mu}_{10,\mathrm{NP}} = 0$, and

$$-0.53 \leq C^{\mu}_{9,\mathrm{NP}} \left(= -C^{\mu}_{10,\mathrm{NP}}\right) \leq -0.25 \tag{5.7}$$

when $C^{\mu}_{9,\mathrm{NP}} = -C^{\mu}_{10,\mathrm{NP}}$. The parameter space allowed in the case when $C^{\mu}_{9,\mathrm{NP}}$ and $C^{\mu}_{10,\mathrm{NP}}$ are independent objects can be found, *e.g.*, in Ref. [229].

The Hamiltonian of 5.4 can be completed in the UV with new massive states above the EWSB scale. We focus in this work on scenarios with a Z' gauge boson. The most generic Lagrangian parameterizing Z' interactions with the b-s current and the muons is given by

$$\mathcal{L} \supset Z'_{\rho} \left[\left(g_L^{sb}\, \bar{s}\gamma^{\rho} P_L\, b + g_R^{sb}\, \bar{s}\gamma^{\rho} P_R\, b + \text{H.c.} \right) + g_L^{\mu\mu}\, \bar{\mu}\gamma^{\rho} P_L\, \mu + g_R^{\mu\mu}\, \bar{\mu}\gamma^{\rho} P_R\, \mu \right], \tag{5.8}$$

in terms of *a priori* free effective couplings $g^{sb}_{L,R}$, $g^{\mu\mu}_{L,R}$. The Wilson coefficients of the WET can be then expressed in terms of the effective couplings as

$$C^{\mu}_{9,\mathrm{NP}} = -2\, \frac{g_L^{sb} g_V^{\mu\mu}}{V_{tb} V^*_{ts}} \left(\frac{\Lambda_v}{m_{Z'}} \right)^2, \qquad C^{\mu}_{10,\mathrm{NP}} = -2\, \frac{g_L^{sb} g_A^{\mu\mu}}{V_{tb} V^*_{ts}} \left(\frac{\Lambda_v}{m_{Z'}} \right)^2, \tag{5.9}$$

where $g^{\mu\mu}_V \equiv (g^{\mu\mu}_R + g^{\mu\mu}_L)/2$, $g^{\mu\mu}_A \equiv (g^{\mu\mu}_R - g^{\mu\mu}_L)/2$, $m_{Z'}$ indicates the mass of the Z' boson, $V_{tb} = 0.999$, $V_{ts} = -0.0404$, and

$$\Lambda_v = \left(\frac{\pi}{\sqrt{2} G_F \alpha_{\mathrm{em}}} \right)^{1/2} \approx 4.94\,\text{TeV} \tag{5.10}$$

defines the typical effective scale of the NP states. Note that to simplify the notation we will drop the subscript "NP" from the Wilson coefficients C^{μ}_9, C^{μ}_{10} hereafter.

5.2.1.1 Quark sector couplings

In order to render the model renormalizable and gauge-invariant, we extend the gauge symmetry of the SM by an additional abelian gauge factor, $\mathrm{U}(1)_X$, with gauge coupling denoted by g_X. The couplings of the Z' boson with gauge eigenstates are by definition flavor-conserving, therefore an additional structure is required to generate the flavor-violating couplings g^{sb}_L and g^{sb}_R. One minimal solution invokes extending the particle content by a singlet scalar field S and a VL pair of left-chiral Weyl spinor doublets, $Q = (U_L, D_L)^T$ and $Q' = (U_R, D_R)$, collectively charged under $\mathrm{SU}(3)_c \times \mathrm{SU}(2)_L \times \mathrm{U}(1)_Y \times \mathrm{U}(1)_X$ as

$$S : (\mathbf{1}, \mathbf{1}, 0, Q_S)\,, \tag{5.11}$$

$$Q : (\mathbf{3}, \mathbf{2}, 1/6, Q_S) \qquad Q' : (\bar{\mathbf{3}}, \bar{\mathbf{2}}, -1/6, -Q_S)\,, \tag{5.12}$$

where Q_S is the $\mathrm{U}(1)_X$ charge of scalar field S. New Yukawa and VL mass terms are then generated in the Lagrangian which, in the basis where the SM fields are diagonal, can be written as

$$\mathcal{L} \supset -\lambda_{Q,i} S D_R\, d_{L,i} - \lambda_{Q,k} (V^{\dagger}_{\mathrm{CKM}})_{ki}\, S\, U_R u_{L,i} - m_Q\, (D_R D_L + U_R U_L) + \text{H.c.}\,, \tag{5.13}$$

with $u_{L,i}$, $d_{L,i}$ being the SM left-chiral quarks and $V_{\rm CKM}$ the CKM matrix. A sum over repeated indices $k, i = 1, 2, 3$, labeling the quark generations, is implied.
As is shown in greater detail in Appendix 5.A, after the $\mathrm{U}(1)_X$ symmetry is spontaneously broken by the vev of the scalar field, v_S, the Lagrangian (5.13) is rotated to the physical basis, leading to flavor non-diagonal interactions of the Z' boson with the SM quarks. One finds

$$g_L^{sb} \approx \pm g_X Q_S \frac{\sqrt{2}\, m_Q\, \lambda_{Q,2}\, \lambda_{Q,3}\, v_S^2}{\left(2m_Q^2 + \lambda_{Q,2}^2\, v_S^2\right)\sqrt{2\, m_Q^2 + \left(\lambda_{D,2}^2 + \lambda_{D,3}^2\right) v_S^2}}\,, \tag{5.14}$$

$$g_R^{sb} \approx 0\,. \tag{5.15}$$

A coupling $g_R^{sb} \neq 0$ can be easily generated by adding an extra VL spinor pair with the quantum numbers of the SM down-type quarks.

5.2.1.2 Direct lepton couplings: $L_\mu - L_\tau$ symmetry

The flavor-conserving effective couplings of Z' to the muon, $g_L^{\mu\mu}$ and $g_R^{\mu\mu}$, can be generated either directly, or by the mixing of the muon with extra VL leptons. We will discuss the first possibility in this subsection and the second in Sec. 5.2.1.3.
Direct Z' couplings to the muons emerge if the SM is charged under $\mathrm{U}(1)_X$. We employ the well known $L_\mu - L_\tau$ gauge symmetry [234, 243–245] to provide an anomaly-free SM extension generating the desired couplings. The SM lepton doublets, $l_{i=1,2,3}$, and singlets, e_R, μ_R, τ_R, carry the following quantum numbers:

$$l_1 : (\mathbf{1}, \mathbf{2}, -1/2, 0) \qquad e_R : (\mathbf{1}, \mathbf{1}, 1, 0) \tag{5.16}$$

$$l_2 : (\mathbf{1}, \mathbf{2}, -1/2, 1) \qquad \mu_R : (\mathbf{1}, \mathbf{1}, 1, -1) \tag{5.17}$$

$$l_3 : (\mathbf{1}, \mathbf{2}, -1/2, -1) \qquad \tau_R : (\mathbf{1}, \mathbf{1}, 1, 1)\,. \tag{5.18}$$

Since the Z' interaction with the muon is VL in $\mathrm{U}(1)_X$ one gets, straightforwardly,

$$g_V^{\mu\mu} = g_X \qquad g_A^{\mu\mu} = 0\,. \tag{5.19}$$

One can insert Eqs. (5.14) and (5.19) into 5.9 to obtain the WET Wilson coefficients. By recalling that $m_{Z'}^2 = g_X^2 Q_S^2 v_S^2$ one gets

$$C_9^\mu \approx \mp \frac{1}{Q_S} \frac{2\Lambda_v^2}{V_{tb}V_{ts}^*} \frac{\sqrt{2}\, m_Q\, \lambda_{Q,2}\, \lambda_{Q,3}}{\left(2m_Q^2 + \lambda_{Q,2}^2\, v_S^2\right)\sqrt{2\, m_Q^2 + \left(\lambda_{Q,2}^2 + \lambda_{Q,3}^2\right) v_S^2}}\,, \qquad C_{10}^\mu = 0\,. \tag{5.20}$$

In this case, the bound of 5.6 applies. Assuming, for example, $Q_S = 1$ and $|\lambda| \equiv |\lambda_{Q,i}|$, one gets

$$14\,\mathrm{TeV} \lesssim m_Q/|\lambda| \lesssim 22\,\mathrm{TeV} \tag{5.21}$$

for $m_Q/|\lambda| \approx m_{Z'}/g_X$. One gets instead

$$20\,\mathrm{TeV} \lesssim m_Q/|\lambda| \lesssim 32\,\mathrm{TeV} \tag{5.22}$$

for $m_{Z'}/g_X \ll m_Q/|\lambda|$. Taken at face value, these solutions may be difficult to constrain directly at the LHC.

5.2.1.3 Couplings through mixing: VL leptons with a $\mathrm{U}(1)_X$ charge

Alternatively, the effective couplings $g_L^{\mu\mu}$ and $g_R^{\mu\mu}$ can be generated in the same way as the quark couplings $g_{L,R}^{sb}$ in Sec. 5.2.1.1. Unlike in Sec. 5.2.1.2 we now keep the SM leptons uncharged under $\mathrm{U}(1)_X$ and instead introduce a VL pair of left-chiral Weyl spinor doublets transforming under the total gauge group as

$$L : (\mathbf{1}, \mathbf{2}, -1/2, Q_L) \qquad L' : (\mathbf{1}, \bar{\mathbf{2}}, 1/2, -Q_L)\,. \tag{5.23}$$

For $Q_L = Q_S$ ($Q_L = -Q_S$) the particle content allows for new Yukawa and mass terms

$$\mathcal{L} \supset \lambda_{L,i} S^{(*)} L' l_i + m_L L' L + \text{H.c.}\,, \tag{5.24}$$

where $l_{i=1,2,3}$ are the SM lepton doublets (uncharged under $\mathrm{U}(1)_X$) and, again, a sum over SU(2) and repeated flavor indices is implied.
Once the $\mathrm{U}(1)_X$ symmetry is broken, the effective muon couplings take the form

$$g_L^{\mu\mu} \approx g_X\, Q_L \frac{\lambda_{L,2}^2 v_S^2}{2m_L^2 + \lambda_{L,2}^2 v_S^2}\,, \tag{5.25}$$

$$g_R^{\mu\mu} \approx 0\,, \tag{5.26}$$

which lead to

$$C_9^\mu = -C_{10}^\mu \approx \mp \frac{Q_L}{Q_S} \frac{\Lambda_v^2}{V_{tb} V_{ts}^*} \left[\frac{\sqrt{2}\, m_Q\, \lambda_{Q,2}\, \lambda_{Q,3}}{\left(2m_Q^2 + \lambda_{Q,2}^2\, v_S^2\right) \sqrt{2\, m_Q^2 + \left(\lambda_{Q,2}^2 + \lambda_{Q,3}^2\right) v_S^2}} \right] \left(\frac{\lambda_{L,2}^2 v_S^2}{2m_L^2 + \lambda_{L,2}^2 v_S^2} \right). \tag{5.27}$$

In this case, the bound of 5.7 applies. Assuming for example, $|\lambda| \equiv |\lambda_{Q,i}| \approx |\lambda_{L,i}|$, one gets,

$$8\,\text{TeV} \lesssim m_{Q,L}/|\lambda| \lesssim 12\,\text{TeV} \tag{5.28}$$

for $m_{Q,L}/|\lambda| \approx m_{Z'}/g_X$. In the limit $m_{Z'}/g_X \approx m_L/|\lambda| \ll m_Q/|\lambda|$,

$$11\,\text{TeV} \lesssim m_Q/|\lambda| \lesssim 17\,\text{TeV}\,, \tag{5.29}$$

while typical scales for $m_{Z'}/g_X$, $m_L/|\lambda|$ are expected to be in the 1-to-few TeV range.

We conclude this section by pointing out that we have introduced in Eqs. (5.12), (5.17), (5.18), and (5.23) fermions that are charged under both the abelian $\mathrm{U}(1)_Y$ and $\mathrm{U}(1)_X$ gauge groups. As a direct consequence, abelian kinetic mixing will be generated in the Lagrangian and the Z' will mix at the tree level with the neutral gauge bosons of the SM, as reviewed briefly in Appendix 5.A. The size of the kinetic mixing in turn determines how sensitive the models described in this section end up being to existing LHC searches for Z' production with leptons in the final states. Finally, the rotations of the scalar fields from the gauge to the physical mass basis are presented in Appendix 5.A.

5.2.2 Fixed-point analysis of the Z' models

5.2.2.1 Gauge-Yukawa system

The one-loop RGEs of the gauge and Yukawa couplings for the models defined in Sec. 5.2.1 are presented in Appendix 5.B and Appendix 5.C. We work in the basis where the quark

Model	Sec. reference	Fermion charges	$\widetilde{Q}_{YX}$
1A	Sec. 5.2.1.3	$Q_{\rm SM}=0$, $Q_L=Q_S$	0
1B	Sec. 5.2.1.3	$Q_{\rm SM}=0$, $Q_L=-Q_S$	$8/3\,Q_S$
2	Sec. 5.2.1.2	$Q_\mu=1$, $Q_\tau=-1$	$4/3\,Q_S$

TABLE 5.1: The effective charge $\widetilde{Q}_{YX}$, introduced in 5.88 of Appendix 5.B, determines the fixed-point value of kinetic mixing for the three scenarios considered in this study.

mass is diagonal in flavor space, since it facilitates the matching of the quark Yukawa couplings onto the experimentally measured values. Consequently, we take into account the running of the elements of the CKM matrix [246–249]. Since we are mainly interested in the parameters affecting $b\to s$ transitions, we reduce the quark Yukawa RGE system to two generations, the second and the third, in the “down-origin” approach (see Appendix 5.C). The CKM matrix is thus approximated by an orthogonal 2×2 matrix, parameterized by one single rotation angle.

The scalar potential couplings do not affect the running of the gauge-Yukawa system at one loop and therefore they can be treated separately. We will come back to discussing the fixed-point structure of the scalar potential in Sec. 5.2.2.2.

The minimal set of couplings pertinent to the analysis of the gauge-Yukawa system is the following:

$$\text{SM}: \qquad g_3\,,\ g_2\,,\ g_Y\,,\ y_t\,,\ y_b\,,\ V_{33}\,, \tag{5.30}$$

$$\text{NP}: \qquad g_D,\ g_\epsilon,\ \lambda_{Q,2},\ \lambda_{Q,3},\ \lambda_{L,2}\,, \tag{5.31}$$

where g_3, g_2, and g_Y are the gauge couplings of $\mathrm{SU}(3)_c$, $\mathrm{SU}(2)_L$, and $\mathrm{U}(1)_Y$, respectively, y_t and y_b indicate the Yukawa couplings of the top and bottom quarks, and V_{33} belongs to the CKM matrix. The running NP gauge couplings g_D and g_ϵ are related to the gauge coupling g_X and abelian gauge boson kinetic mixing ϵ as defined in Appendix 5.B. The Yukawa couplings of the quarks of the first two generations and of the leptons are not included in the system, as their impact on the running of the parameters defined in 5.30 and 5.31 is negligible. We associate all of them with relevant directions of a Gaussian fixed point in the trans-Planckian UV [195] and so their IR values can always be reached.

Let us start the fixed-point analysis by focusing on the gauge sector. In what follows, we will indicate the fixed-point values of dimensionless couplings with an asterisk. Given the expectation that $f_g>0$, the non-abelian gauge couplings develop non-interactive (or Gaussian) fixed points,

$$g_3^*=0, \qquad g_2^*=0\,, \tag{5.32}$$

as required by the low-energy phenomenology. Both of them correspond to relevant directions in the coupling space.

The abelian sector is described by the three couplings g_Y, g_D, and g_ϵ. Following the AS ansatz, we assume that quantum gravitational interactions are going to tame their pathological UV behavior. The system thus develops a fully interactive fixed point,

$$g_Y^*=4\pi\sqrt{\frac{f_g}{\widetilde{Q}_Y}}\,,\quad g_D^*=4\pi\sqrt{\frac{f_g\widetilde{Q}_Y}{\widetilde{Q}_Y\widetilde{Q}_X-\widetilde{Q}_{YX}^2}}\,,\quad g_\epsilon^*=-4\pi\widetilde{Q}_{YX}\sqrt{\frac{f_g}{\widetilde{Q}_Y^2\widetilde{Q}_X-\widetilde{Q}_Y\widetilde{Q}_{YX}^2}}\,, \tag{5.33}$$

corresponding to irrelevant directions in the coupling space. Incidentally, a fixed point with

	f_g	f_y	g_Y^*	g_D^*	g_ϵ^*	y_t^*	$\lambda_{Q,3}^*$	$\lambda_{Q,2}^*$	$\lambda_{L,2}^*$
$\mathrm{FP}_{1\mathrm{A},a}$	0.012	0.0025	0.498	0.418	0	0.406	0	0.072	0.648
$\mathrm{FP}_{1\mathrm{A},b}$	0.012	0.0029	0.498	0.418	0	0.424	0.200	0	0.610
$\mathrm{FP}_{1\mathrm{B},a}$	0.012	0.0026	0.498	0.436	0.151	0.417	0	0.163	0.586
$\mathrm{FP}_{1\mathrm{B},b}$	0.012	0.0034	0.498	0.436	0.151	0.452	0.264	0	0.547
$\mathrm{FP}_{2,a}$	0.010	0.0018	0.479	0.366	0.069	0.356	0	0.302	–
$\mathrm{FP}_{2,b}$	0.010	0.0037	0.479	0.366	0.069	0.453	0.379	0	–

TABLE 5.2: Trans-Planckian fixed-point values for the gauge and Yukawa couplings and the corresponding gravity parameters f_g and f_y for the scenarios investigated in this work.

$g_D^* = 0$ is also allowed, but it is not phenomenologically interesting as it would imply a non-interacting Z'. The quantities $\widetilde{Q}_Y$, $\widetilde{Q}_X$, and $\widetilde{Q}_{YX}$ are defined in Eqs. (5.86)–(5.88) in Appendix 5.B. It is possible to make the kinetic mixing vanish at the fixed point, provided $\widetilde{Q}_{YX} = 0$. One may use 5.88 to determine whether or not this happens in the models introduced in Sec. 5.2.1. We analyze three cases, summarized in Table 5.1:

- Model 1A, with VL leptons introduced in 5.23 of Sec. 5.2.1.3 and $Q_L = Q_S$
- Model 1B, same as above but $Q_L = -Q_S$
- Model 2, with $L_\mu - L_\tau$ symmetry as described in Sec. 5.2.1.2.

In Model 1A the kinetic mixing g_ϵ vanishes at the fixed point. Moreover, it is not generated through the running, as the corresponding beta function is multiplicative in g_ϵ, see 5.85 in Appendix 5.B.

With no loss of generality, we shall henceforth set $Q_S = 1$. The gravity parameter f_g is uniquely determined by matching g_Y onto its phenomenological value in the IR, $g_Y(M_t) = 0.358$. One obtains $f_g = 0.012$ in models 1A, 1B, and $f_g = 0.010$ in Model 2.

The second quantum gravity parameter, f_y, is fixed by postulating that at least one of the SM Yukawa couplings presents a UV interactive fixed point [192],

$$y_t^* = F_t\left(f_g, f_y\right) \qquad \text{and/or} \qquad y_b^* = F_b\left(f_g, f_y\right)\,. \tag{5.34}$$

The flow along an irrelevant direction, from the fixed point down to the IR, is then matched onto the value of the corresponding quark mass. Finally, we associate the CKM matrix element V_{33} with a relevant direction and assume it is zero at the fixed point [195]:

$$V_{33}^* = 0\,. \tag{5.35}$$

Once the f_g, f_y parameters are extracted by matching the SM couplings to their IR value, one proceeds to determine the UV fixed points of the NP Yukawa couplings in 5.31. The process will eventually lead to specific low-scale predictions, as long as those couplings correspond to irrelevant directions in theory space. Out of the full set of fixed points, we extract those with maximal predictivity, which belong to two classes of trans-Planckian solutions,

$$\begin{aligned} \mathrm{FP}_{M,a}: &\quad \lambda_{Q,2}^* \neq 0,\ \lambda_{Q,3}^* = 0\,, \\ \mathrm{FP}_{M,b}: &\quad \lambda_{Q,2}^* = 0,\ \lambda_{Q,3}^* \neq 0\,, \end{aligned} \tag{5.36}$$

where the subscript M = 1A, 1B, 2 spans the models in Table 5.1. Moreover, in models 1A, 1B we require

$$\lambda_{L,2}^* \neq 0\,. \tag{5.37}$$

	$g_Y(k_0)$	$g_D(k_0)$	$g_\epsilon(k_0)$	$y_t(k_0)$	$\lambda_{Q,3}(k_0)$	$\lambda_{Q,2}(k_0)$	$\lambda_{L,2}(k_0)$
$\text{FP}_{1\text{A},a}$	0.364	0.305	0	1.08	-0.381	0.016	0.823
$\text{FP}_{1\text{A},b}$	0.364	0.305	0	1.09	0.034	0.803	0.606
$\text{FP}_{1\text{B},a}$	0.363	0.318	0.110	1.05	-0.612	0.296	0.652
$\text{FP}_{1\text{B},b}$	0.363	0.318	0.110	1.08	0.004	0.874	0.499
$\text{FP}_{2,a}$	0.363	0.277	0.052	1.03	-0.700	0.638	–
$\text{FP}_{2,b}$	0.363	0.277	0.052	1.10	0.040	0.988	–

TABLE 5.3: Values of the gauge and Yukawa couplings of the scenarios investigated in this work at the reference "collider" scale of $k_0 = 2\,\text{TeV}$.

Note that a fully interactive solution with *real* Yukawa couplings $\lambda^*_{Q,2} \neq \lambda^*_{Q,3} \neq 0$ does not exist. Conversely, we neglect the solution $\lambda^*_{Q,2} = \lambda^*_{Q,3} = 0$ along a relevant direction because that choice would not lead to an enhancement in predictivity with respect to the simplified model approach.

The list of all fixed points of phenomenological interest, together with the values assumed by f_g and f_y for the three scenarios considered in this study is presented in Table 5.2. We can only reproduce the IR value of the bottom mass if $y_b^* = 0$ (relevant). Conversely, the top Yukawa coupling at the fixed point is irrelevant and thus in principle the parameter f_y should be determined by the top quark mass like in 5.34. However, there exists a minimum f_y allowing $y_b^* = 0$ to be relevant and therefore we adopt that as the f_y value of choice.

Once the quantum gravity contribution to the RGEs is turned off below M_{Pl}, the system of the couplings is run down to an indicative "collider" scale, which we set at $k_0 = 2\,\text{TeV}$. For the models considered in this work, the values of the couplings at k_0 are presented in Table 5.3. Note that in the two-family approximation adopted here we do not generate radiatively $\lambda_{Q,1}$. However, one should bear in mind that in the more realistic three-family approach a small $\lambda_{Q,1}(k_0) \lesssim 10^{-5}$ can arise due to the additive contributions in its RGE,

$$\frac{d\lambda_{Q,1}}{dt} \simeq -\frac{y_t^2\, V_{31}}{16\,\pi^2}\left(V_{32}\lambda_{Q,2} + V_{33}\lambda_{Q,3}\right) . \tag{5.38}$$

An attentive look at the low-scale predictions in Table 5.3 shows that the running kinetic mixing coupling g_ϵ vanishes at all scales in Model 1A but is instead different from zero in models 1B and 2, in agreement with the corresponding value of $\widetilde{Q}_{YX}$ reported in Table 5.1. One can thus compute with 5.82 in Appendix 5.B the corresponding $\epsilon(k_0) = 0.29$ in Model 1B, and $\epsilon(k_0) = 0.14$ in Model 2. As will be discussed in detail in Sec. 5.2.3, these values lead to the direct exclusion of Model 1B and Model 2 at the LHC. For this reason, we shall focus entirely on Model 1A for the remainder of this subsection.

We show the trans-Planckian flow from $\text{FP}_{1\text{A},a}$ in Fig. 5.1(a) and the flow from $\text{FP}_{1\text{A},b}$ in Fig. 5.1(b). At the fixed point $\text{FP}_{1\text{A},a}$ coupling $\lambda_{Q,2}$ is of the irrelevant type. Conversely, the system of couplings $(V_{33}, \lambda_{Q,3})$ spans a 2-dimensional submanifold in theory space, on which both couplings are relevant but do not correspond to eigendirections of the stability matrix. An attentive look at Fig. 5.1(a) shows the likely appearance, on the left-hand side of the plot, where the flow approaches from above the Planck scale, of an additional IR-attractive fixed point for the RGE trajectories, distinct from $\text{FP}_{1\text{A},a}$. This fixed point, confirmed by the numerical analysis, is characterized by $V^*_{33} = 1$, $\lambda^*_{Q,3} = -0.1$, $\lambda^*_{Q,2} = 0$, $y^*_b = 0$, all of them irrelevant. An IR-attractive fixed point of similar features was already observed for the leptoquark case in Ref. [196]; it effectively washes out much of the freedom associated with relevant directions in the Yukawa-coupling theory space and sets the typical value the couplings of the system take at the Planck scale.

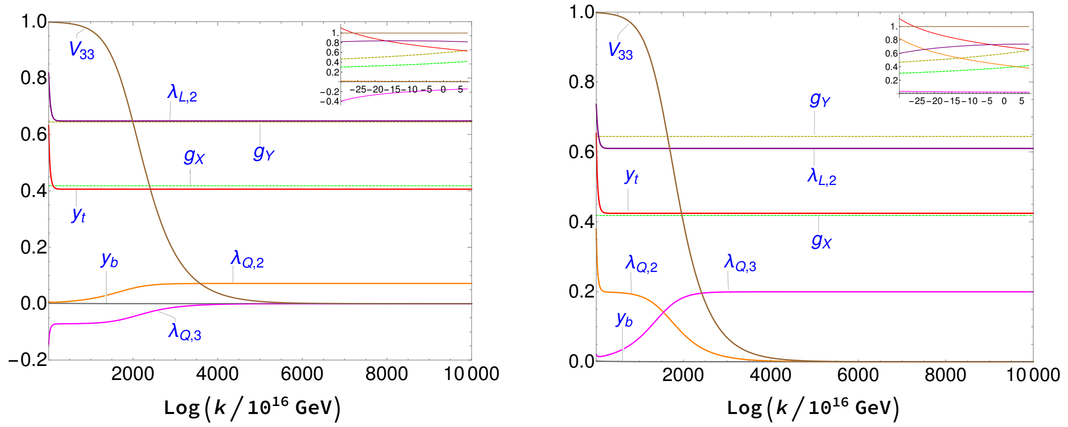

(A) (B)

FIGURE 5.1: (a) RG flow of the gauge and Yukawa couplings from trans-Planckian energies down to the EWSB scale for a scenario characterized by UV fixed point $\mathrm{FP}_{1\mathrm{A},a}$. The sub-Planckian flow is shown in the inset panel. (b) The same for $\mathrm{FP}_{1\mathrm{A},b}$.

Note also that the exact mass of the top quark cannot be exactly matched at the EWSB scale. Because there is a minimum f_y value required to make $y_b^* = 0$ relevant, the running y_t always overshoots the SM measurement by about 20%. This is unfortunate, but it seems to be a feature appearing in other studies of trans-Planckian boundary conditions, in the SM and NP alike, see, *e.g.*, Refs. [195, 196]. Possibly, a detailed analysis of the RGEs at higher loop order may shed some light on this issue. However, since a precise determination of the top mass is not essential to the extraction of the predictions of these Z' models for flavor and collider physics, we will leave the investigation of this topic to future work.

At the fixed point of type $\mathrm{FP}_{1\mathrm{A},b}$ both the NP Yukawa couplings of the quark sector span irrelevant directions. While $\lambda_{Q,3}$ corresponds to an eigenvector of the stability matrix, the flow of $\lambda_{Q,2}$ close to the fixed point is entirely dictated by the UV hypercritical surface relating it with the (relevant) CKM matrix element V_{33}, $\lambda_{Q,2}(t) = \mathcal{F}(V_{33}(t))$. The trans-Planckian flow of the parameters of the system is presented in Fig. 5.1(b). As was the case for $\mathrm{FP}_{1\mathrm{A},a}$, the trajectories eventually cross over to the basin of attraction of an IR-attractive fixed point characterized by $V_{33}^* = 1, \lambda_{Q,2}^* = 0.2, \lambda_{Q,3}^* = 0, y_b^* = 0$. Note, however, that in neither Model 1A, a nor Model 1A, b the new IR-attractive fixed point is ever fully reached, as the requirement of reproducing the low-energy value of the CKM matrix element V_{33} implies that the gravitational effects decouple before the system stabilizes. As was the case in Model 1A, a, the IR value of the top Yukawa coupling is overshot in Model 1A, b by about 20%.

5.2.2.2 Scalar potential

The scalar potential of the models considered in this work is given by

$$V\left(|h|^2, |S|^2\right) = -\mu_h^2 h^\dagger h + \lambda_h \left(h^\dagger h\right)^2 + \mu_S^2\, S^\dagger S + \lambda_S \left(S^\dagger S\right)^2 + \lambda_{hS} \left(S^\dagger S\right)\left(h^\dagger h\right), \quad (5.39)$$

where μ_h^2 and λ_h are the mass parameter and the quartic coupling of the SM Higgs boson doublet h, μ_S^2 and λ_S are the mass parameter and the quartic coupling of the scalar S, and λ_{hS} is the portal coupling. The 1-loop RGEs of the dimensionless parameters of the potential are given in Appendices 5.C-5.C.

As was mentioned above, the quartic couplings of the scalar potential do not enter at one loop the RGEs of the gauge-Yukawa system and as such their fixed-point properties will not

	λ_h^*	λ_S^*	λ_{hS}^*	θ_h	θ_S	θ_{hS}
FP_A	> 0	> 0	$\approx 0^+$	$-$	$-$	$-$
FP_B	> 0	< 0	$\approx 0^+$	$-$	$+$	$-$
FP_C	< 0	> 0	$\approx 0^+$	$+$	$-$	$-$
FP_D	< 0	< 0	> 0	$+$	$+$	$-$

TABLE 5.4: The sign of real fixed points of the system $(\lambda_h, \lambda_S, \lambda_{hS})$ (left-hand side box) and the signs of the corresponding critical exponents (right-hand side box) for $f_\lambda < 0$.

impact the flavor phenomenology in a significant way. On the other hand, predictions can be derived for the mass of the heavy scalar m_{H_2}, where H_2 is a mixture of the the SM Higgs and the scalar S (dominated by the latter, see Appendix 5.A).
The qualitative properties of the fixed-point $(\lambda_h^*, \lambda_S^*, \lambda_{hS}^*)$ are the same in all the considered scenarios. The sign of the real fixed points and corresponding critical exponents are presented in Table 5.4 for $f_\lambda < 0$. In three out of the four points the portal coupling develops a quasi-Gaussian fixed point, $|\lambda_{hS}^*| \ll 10^{-2}$. In all four points λ_{hS}^* is positive and IR attractive for $f_\lambda < 0$ and negative and UV attractive for $f_\lambda > 0$.
The actual value of the couplings depends on the model at hand and, most importantly, on the eventual size and sign of f_λ. This is shown in Fig. 5.2. In both panels the fixed points of Table 5.4 are marked with color dots. The arrows always point towards the UV.
In Fig. 5.2(a) the phase diagram is shown for a negative value $f_\lambda = -0.1$, which is large compared to the typical size of the terms involving the gauge and Yukawa couplings in the RGEs of Appendix 5.C (recall that $f_g, f_y \lesssim 10^{-2}$, see Table 5.2). It forces the appearance of a pseudo-Gaussian fixed point, FP_A, fully irrelevant, which makes the potential stable at the Planck scale. Infrared-attractive fixed points of the scalar potential are often discussed in the literature for their predictivity [178, 179, 204]. However, since in these models we overshoot the top mass value at low energies – see discussion above – we also overshoot the Higgs mass at the EWSB scale. The behavior of y_t and λ_h is strongly connected and does not depend much on the specific form of the Higgs quartic-coupling RGE which, if anything, features in these models additional positive terms with respect to the SM, allowing for an easier running. As was the case for the top mass determination, a full two-loop analysis may be required to shed more light on this issue.
As one increases f_λ, towards less negative values, to zero and then positive values, the four fixed points move up and to the right with respect to Fig. 5.2(a). In Fig. 5.2(b) we show the case of positive $f_\lambda = 0.05$, which is also relatively large with respect to the typical size of the RGE terms of the gauge and Yukawa couplings. In this case, one can refer to the fully relevant fixed point FP_D, which implies that the three quartic couplings become effectively free parameters and issues with the IR value of the Higgs mass do not arise. The scalar potential, on the other hand, may possibly become unstable at the Planck scale or, in the best-case scenario, metastable in a fashion similar to the SM [29]. A detailed analysis of stability of the scalar potential exceeds the scope of this paper.
We conclude, finally, by pointing out that λ_S^* assumes different values in the two panels in Fig. 5.2, depending on the selected f_λ. Nevertheless, a unique low-scale prediction for $\lambda_S(M_t)$ (and therefore m_{H_2}) can be extracted, as the sub-Planckian flow of λ_S is predominantly determined by the top and NP Yukawa couplings and is quite insensitive to the exact value of λ_S at the Planck scale (as long as it remains small). In Model 1A, a we obtain the NP

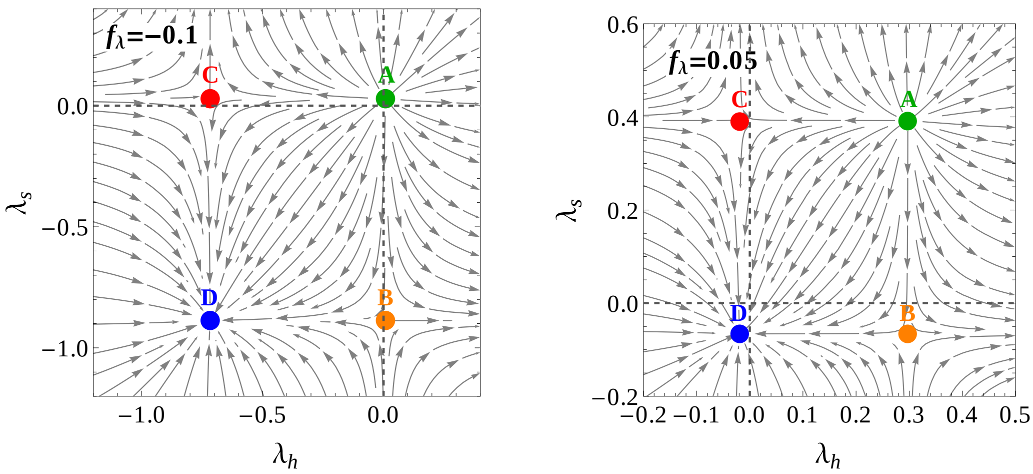

(A) (B)

FIGURE 5.2: (a) Phase space diagram in the (λ_h, λ_S) plane for $f_\lambda = -0.1$ and the couplings set at $\text{FP}_{1\text{A},a}$ in Table 5.2. (b) Phase space diagram for $f_\lambda = 0.05$. The RG flow directions point towards the UV. Color dots correspond to the fixed points listed in Table 5.4.

couplings

$$\lambda_S(173\,\text{GeV}) = 0.18\,, \qquad \lambda_{hS}(173\,\text{GeV}) = 0.1\,, \tag{5.40}$$

which lead to a prediction for the heavy scalar mass

$$m_{H_2} \approx 2.02\, m_{Z'}\,. \tag{5.41}$$

A non-zero value of the portal coupling λ_{hS} introduces mixing between the SM Higgs and the scalar singlet S. For the values of the scalar potential couplings given in 5.40, 5.73 in Appendix 5.A can be used to obtain

$$\sin\alpha_H \approx \frac{20\,\text{GeV}}{m_{Z'}}. \tag{5.42}$$

This is far below the experimental upper bound which reads $\sin\alpha_H < 0.2$ [250].

5.2.3 Experimental constraints on the Z' models

Since the new fermions introduced in Sec. 5.2.1 are VL they neither generate gauge anomalies nor induce via loops new axial-vector contributions to the decay of the SM gauge bosons, which are strongly constrained. Moreover, since the $\text{U}(1)_X$ symmetry is broken by the vev of a SM singlet, we do not expect large contributions to the oblique parameters. In other words, the minimal models we have chosen are safe from the precision physics constraints. The trans-Planckian fixed-point analysis of the gauge-Yukawa system allows one to predict the low-scale values of the irrelevant couplings. Since the RG flow of the NP Yukawa couplings is very slow over the phenomenologically interesting $\sim$TeV range, these can effectively be treated as constants at the low scale, which leaves the VL fermion masses m_Q, m_L, and the Z' mass $m_{Z'}$ as the only remaining free parameters. This is in agreement with the fact that Lagrangian mass parameters are canonically relevant in AS.
The parameter space of the Z' models is subject to several constraints. These include: $m_{Z'}$-dependent bounds on the kinetic mixing of neutral gauge bosons; flavor bounds on B_s-meson mixing; neutrino trident production; and direct bounds on the mass of the VL fermions

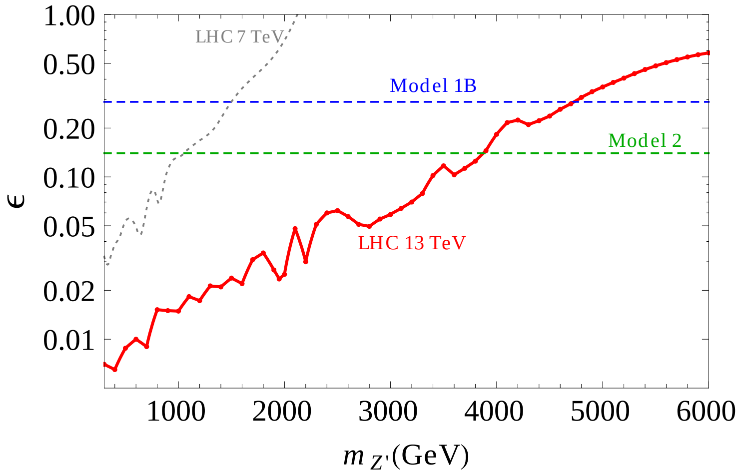

FIGURE 5.3: Our computation of the experimental bound on the kinetic mixing parameter ϵ as a function of the Z' mass. In solid red the results based on the 13 TeV analysis by ATLAS [252] are shown. In dashed gray we show for comparison the 7 TeV exclusion bound derived in Ref. [251]. Dashed blue and green line indicate the predictions of Models 1B and 2, respectively.

and Z' boson from NP searches at the LHC.

Kinetic mixing

The kinetic mixing of heavy Z' ($m_{Z'} > m_Z$) can be experimentally tested by looking for narrow Z' resonances decaying to muons and/or electrons [251]. The dominant production channels proceed through the couplings to the first quark generation which, in the limit $m_Q, m_L \gg m_{Z'}$, are given in 5.68 of Appendix 5.A. The most recent measurements by ATLAS [252] and CMS [253], based on 140/fb data set in proton-proton collisions at the centre-of-mass energy of $\sqrt{s} = 13$ TeV provide upper bounds on the $p\,p \to Z' \to l^+\,l^-$ cross-section as a function of the Z' boson mass. These in turn can be translated onto the limit on the kinetic mixing ϵ.
We compute for the first time the lower bound on $m_{Z'}$, based on the ATLAS 13 TeV search. It is presented in Fig. 5.3 as a red solid line. The cross section for the process $p\,p \to Z' \to l^+\,l^-$, where $l = e, \mu$, is simulated with `MadGraph5_aMC@NLO` v3.4.1 [118]. Note that our computation is completely model-independent. For comparison, we show as a gray dotted line the 7 TeV exclusion bound derived in Ref. [251]. The bounds on the kinetic mixing parameter in Model 1B and Model 2, which is computed with 5.82 in Appendix 5.B, are superimposed in the plot as a dashed blue (1B) and a dashed green line (2).

B-meson mixing and neutrino trident production

$B_s - \bar{B}_s$ transitions can constrain directly the mass parameters. We use [254]

$$R_{\Delta M_s} = \frac{\Delta M_s^{\text{exp.}}}{\Delta M_s^{\text{SM}}} - 1 = -0.09 \pm 0.08 \tag{5.43}$$

to impose a bound on $m_Q, m_{Z'}$. The quantity of interest is parameterized as [255]

$$R_{\Delta M_s} = \frac{v_h^2 \left(g_L^{sb}\right)^2}{m_{Z'}^2} \left[\frac{g_2^2}{16\pi^2} \left(V_{tb} V_{ts}^*\right)^2 S_0\right]^{-1}, \tag{5.44}$$

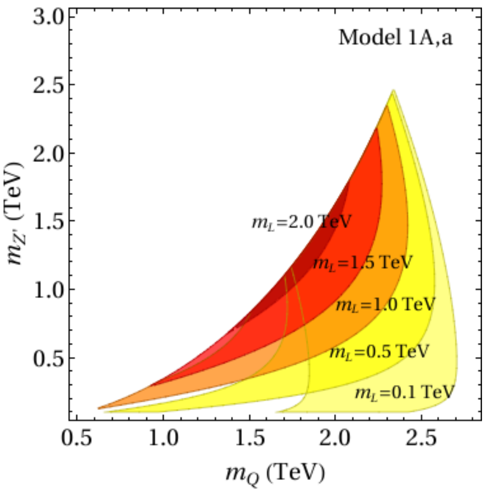

(A)

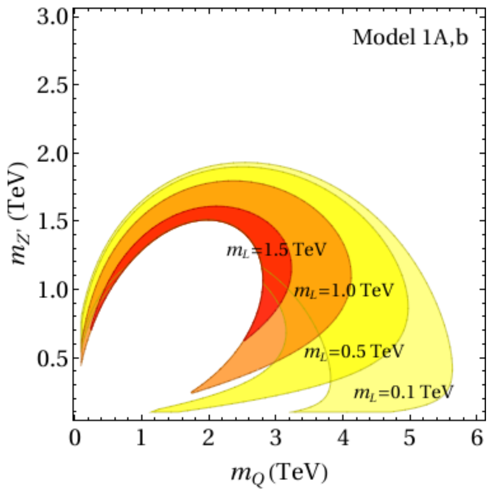

(B)

FIGURE 5.4: (a) The parameter space of Model 1A, a allowed by the flavor anomalies and the constraints from B_s-meson mixing and neutrino trident production in the $(m_Q, m_{Z'})$ plane. In different colors the parameter space corresponding to selected choices of m_L. (b) Same for Model 1A, b.

where $v_h = 246\,\text{GeV}$ is the SM Higgs vev, g_2 is the SU(2)$_L$ gauge coupling, $S_0 \approx 2.3$ is a loop function, and g_L^{sb} is given in 5.14.

If Z' couples to muon neutrinos, a strong enhancement in the neutrino trident production from scattering on atomic nuclei, N: $N\nu \to \nu N \mu^+\mu^-$, is expected [256]. The corresponding cross section has been measured by the CCFR [257] and CHARM-II [258] collaborations in agreement with the SM prediction. For $m_{Z'} > 1\,\text{GeV}$, these results translate into the universal lower bound on the new gauge boson mass,

$$\left(\frac{m_{Z'}}{g_\nu}\right) > 500\,\text{GeV}, \tag{5.45}$$

where g_ν denotes a generic coupling of Z' to neutrinos. In the case of the $L_\mu - L_\tau$ symmetry (Model 2) one finds $g_\nu = g_X$, while in the scenario where the interactions of Z' with the SM lepton doublet arise through the mixing with VL leptons (Model 1) one finds $g_\nu = g_L^{\mu\mu}$, with $g_L^{\mu\mu}$ given in 5.25.

We present in Fig. 5.4(a), in the (m_Q, $m_{Z'}$) plane for different choices of m_L, the parameter space of Model 1A, a allowed by a combination of the flavor anomalies constraint given in 5.7, the bound from B_s-meson mixing in 5.43, and the neutrino trident production limit in 5.45. In Fig. 5.4(b) we show the corresponding parameter space for Model 1A, b. Note that there exists an upper bound on the Z' mass, $m_{Z'} \lesssim 2.5\,\text{TeV}$, which is known to be mostly due to the B_s-mixing constraint.
The VL fermion mass parameters are bounded as well: $0.5\,\text{TeV} \lesssim m_Q \lesssim 2.7\,\text{TeV}$ in Model 1A, a and $m_Q \lesssim 5.5\,\text{TeV}$ in Model 1A, b; $m_L \lesssim 2.3\,\text{TeV}$ in Model 1A, a and $m_L \lesssim 1.6\,\text{TeV}$ in Model 1A, b. Compare these determinations to the mostly unconstrained parameter space of the simplified model, Eqs. (5.28) and (5.29): the strong predictions for the models' couplings that arise from AS open up the enticing possibility of testing the parameter space entirely in current and future collider searches. We investigate such possibility in Sec. 5.2.3.
By again applying Eqs. (5.6), (5.7), and (5.43) with the coupling values of Table 5.3 one can easily check that a 2σ upper bound on the Z' mass, $m_{Z'} \lesssim 2.6\,\text{TeV}$, exists in models 1B and 2

as well. On the other hand, we read in Fig. 5.3 that the 95% C.L. lower bound on the Z' mass due to the kinetic mixing reads

$$\text{Model 1B:} \qquad m_{Z'} \gtrsim 4.7\,\text{TeV}\,, \tag{5.46}$$

$$\text{Model 2:} \qquad m_{Z'} \gtrsim 3.9\,\text{TeV}\,, \tag{5.47}$$

which unequivocally lead to the full exclusion of Model 1B and Model 2 in the AS framework. Incidentally, the same conclusion does not apply to Model 1A, as the parameter g_ϵ (and thus ϵ) remains identically zero in its run from the Planck scale to the scale of decoupling of the largest VL mass, $\max(m_Q, m_L)$. Below that scale kinetic mixing is loop-generated, proportionally to the product of hypercharge Y_i and $\text{U}(1)_X$ charge Q_i of the fermions of label i transforming under both symmetries. The final result,

$$\epsilon \approx \cos\theta_W \frac{g_Y g_X}{12\pi^2} \sum_{i\,\in\,\text{fermions}} Y_i Q_i \ln\frac{m_Q^2}{m_L^2} \approx 10^{-3}\,, \tag{5.48}$$

remains however too small for Model 1A to be sensitive to the bound in Fig. 5.3.

Collider searches

The Lagrangians of 5.13 and 5.24 imply the presence of NP particles beyond the SM. The theory contains an up and a down quark of the fourth generation, U_4 and D_4, degenerate at the tree level, a charged lepton and Dirac heavy neutrino, E_4 and N_4, again degenerate, as well as a heavy Z' gauge boson and a heavy scalar H_2. These particles can in principle be directly produced at the LHC. In this subsection we briefly discuss the possibility of constraining the parameter space of Model 1A with the results of the LHC Run II, as well as some prospects for the future upgrades.

Z' boson Even in the absence of kinetic mixing, the heavy quark fusion process $u(s)\,u(s) \to Z' \to \mu^+\mu^-$ can impose constraints on the Z' mass, as was observed, *e.g.*, in Ref. [109]. Since quark fusion can only proceed through the mixing of VL quarks with the SM quarks u and s, the corresponding cross section strongly depends on the size of the NP Yukawa couplings $\lambda_{Q,2}$ and $\lambda_{Q,3}$.
Following the strategy described in Sec. 5.2.3, we apply to the process $u(s)\,u(s) \to Z' \to \mu^+\mu^-$ the experimental bounds on the cross section from the ATLAS [252] and CMS [253] 140/fb narrow resonance searches. In Model 1A, b this translates into a 95% C.L. lower bound on the Z' mass,

$$m_{Z'} \gtrsim 5\,\text{TeV}\,. \tag{5.49}$$

The bound is quite strong, the main reason being the large value of the Z' coupling to up and strange quark pairs due to large $\lambda_{Q,2}(k_0) = 0.803$ (see Table 5.3) and $V_{12}\,\lambda_{Q,2}(k_0) \approx 0.18$. As Fig. 5.4(b) shows, the constraints from the flavor anomalies and B_s mixing yield

$$m_{Z'} \lesssim 2\,\text{TeV}\,, \tag{5.50}$$

which makes Model 1A, b excluded. Only Model 1A, a remains untested by the narrow resonance searches as the production cross section is in this case suppressed by four orders of magnitude due to the small value $\lambda_{Q,2}(k_0) = 0.016$.

VL fermions The VL leptons can be pair produced at the LHC via Drell-Yan processes. Their physical mass at the tree level reads

$$m_{E_4,N_4} = \sqrt{m_L^2 + \lambda_{L,2}^2 m_{Z'}^2 / 2g_X^2}\,. \tag{5.51}$$

In Model 1A, *a* this means that $m_{E_4,N_4} > m_{Z'}$ since, given the values in Table 5.3, $\lambda_{L,2}^2/2g_X^2 > 1$. On the other hand, the hierarchy between E_4 and the scalar H_2 depends on the relative size of the Lagrangian parameter m_L with respect to $m_{Z'}$ (recall from Sec. 5.2.2.2 that $m_{Z'} \approx 0.5\, m_{H_2}$). If $m_L \lesssim 0.6\, m_{Z'}$, the scalar is heavier than the VL lepton and the dominant decay channel is $E_4 \to Z'\mu$, followed by $Z' \to \mu^+\mu^-$ and $Z' \to \nu_\mu \nu_\mu$ with a branching ratio of 50% each. These decay chains lead to a characteristic multilepton plus missing energy (MET) signature, reminiscent of that arising in the production of supersymmetric charginos. Conversely, if $m_L > 0.6\, m_{Z'}$, the decay channel $E_4 \to H_2\,\mu$ becomes kinematically allowed, with characteristic leptons and jets in the final state. As for the VL quarks of the fourth generation, their physical mass is given at the tree level by

$$m_{U_4,D_4} \approx \sqrt{m_Q^2 + \left(\lambda_{Q,2}^2 + \lambda_{Q,3}^2\right) m_{Z'}^2 / 2g_X^2}\,. \tag{5.52}$$

They are predominantly produced at the LHC via strong interactions. As long as $m_{U_4,D_4} \gg m_{Z'}$ the dominant decay channels are $U_4(D_4) \to Z'\,t(b)$, $U_4 \to H_2\,t(b)$, resulting in a multijets plus leptons signature which can be tested by the LHC searches tailored to look for supersymmetric gluinos decaying through stops.

In Fig. 5.5(b) we show the lower exclusion bound on the mass of the heavy VL quarks U_4 and D_4. Mainly two searches contribute to the exclusion bound: at $m_{Z'} < m_{U_4,D_4}$ the decay chain $U_4 \to Z't$ is tested by the ATLAS search [259]. At the upper edge, $m_{Z'} \approx m_{U_4,D_4}$, decays to the top quark are not kinematically allowed and the most aggressive bound is placed by the ATLAS search [260]. The dashed blue line shows, again, the reach obtained by the rescaling procedure described above.

We summarize the constraints on the parameter space of Model 1A, *a* in Fig. 5.5(c). The region allowed by the flavor anomalies and B_s-mixing is shown in the $(m_L, m_{Z'})$ plane for different choices of the VL mass m_Q. All parameter space with $m_Q < 1.3$ TeV is excluded by the ATLAS search [259]. For $m_Q > 1.3$ TeV the regions excluded by hadronic production searches are shaded in solid gray. Conversely, the current bound from Drell-Yan production of heavy VL leptons, which is dominated by the CMS 13 TeVanalysis [261], is superimposed on the plot as a solid blue line, and the high-luminosity projections of Fig. 5.5(a) correspond to the dashed blue line. We also cover with dashed shadings the regions corresponding to the high-luminosity projection of Fig. 5.5(b). We evince that future coverage of the hadronic production will exclude the entire parameter space up to approximately $m_Q \approx 1.5$ TeV, and significantly test the regions at higher m_Q values. The regions that remain beyond reach in hadronic production, on the other hand, like the area shaded in red corresponding to $m_Q = 2.6$ TeV, will be probed deeply by the Drell-Yan searches.

5.2.4 Summary and conclusions

In this section, we considered two simple and well-known Z' extensions of the SM providing a solution to the long-standing flavor anomalies in $b \to s\mu^+\mu^-$ transitions. We constrained them with a double "chokehold" consisting, in the deep UV, of well-motivated boundary conditions for the otherwise free parameters of the models and, in the IR, of a comprehensive study of the most recent experimental bounds applying to them.

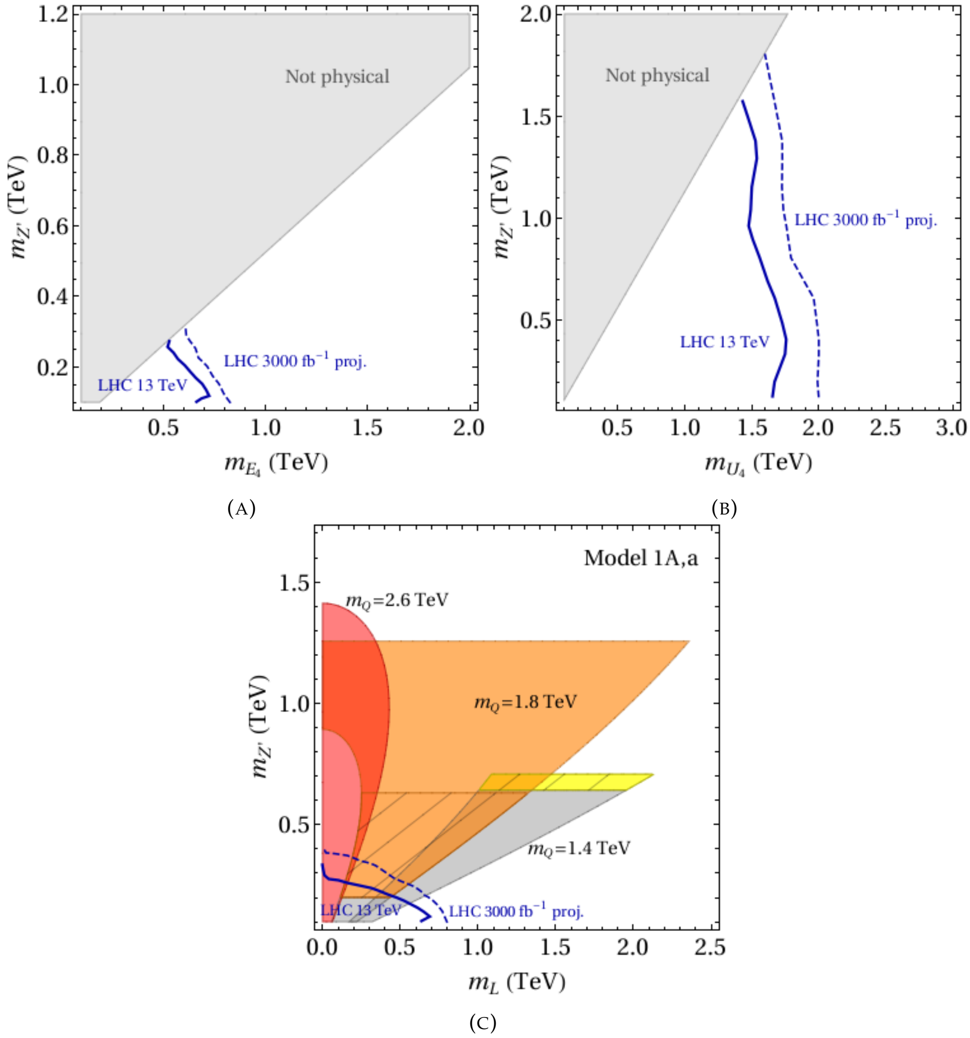

FIGURE 5.5: (a) 95% C.L.lower exclusion bound on the mass of heavy VL leptons E_4 and N_4 from the CMS 13 TeV search [261] (solid blue line) and the projection for the future luminosity of 3000 fb^{-1} (dashed blue line). (b) 95% C.L.lower exclusion bound on the mass of heavy VL quarks U_4 and D_4 from the 13 TeV ATLAS searches [259] and [260] (solid blue line) and the corresponding projection (dashed blue line). (c) In the $(m_L, m_{Z'})$ plane, the parameter space of Model 1A, *a* allowed by the flavor anomalies and the constraints from B_s-meson mixing and neutrino trident production. The present 95% C.L.exclusion bound on the VL quark mass is denoted in solid gray, while the corresponding projection for 3000 fb^{-1} with dashed shadings. The 95% C.L.exclusion bound on the VL lepton mass and corresponding projection are indicated by a solid blue line and a dashed blue line, respectively.

In the models we considered the extra $U(1)_X$ gauge symmetry is broken by the vev of a scalar SM singlet and the flavor non-diagonal couplings of the Z' to the s and b quarks are generated via the mixing with heavy quarks of a VL fourth generation, which carry $U(1)_X$ charge. While in Model 1 we apply the same mechanism to the lepton sector and generate the coupling of the Z' to muons via the mixing of the latter with heavy VL leptons, in Model 2 the $L_\mu - L_\tau$ symmetry is employed to generate the $Z'\mu\mu$ coupling directly. Those two constructions lead to different expectations for the Z'/γ kinetic mixing. Moreover, we considered two different choices of the charges within Model 1 itself, also leading to different expectations for the kinetic mixing, which we dub as Model 1A and Model 1B.
In order to constrain the resulting three scenarios in the UV, we chose to apply the ansatz of trans-Planckian AS. This is based on the assumption that, while the particles at the collider scale should be responsible for the flavor anomalies, a "desert" devoid of any other NP state extends all the way up to the Planck scale. At M_{Pl}, interactions of the matter states with quantum gravity or some other physics lead to the appearance of fixed points for the beta functions of the dimensionless couplings in the Lagrangian. We thus performed a fixed-point analysis of the three models to determine the relevant (UV-attractive) and irrelevant (IR-attractive) directions in theory space. While the former identify the effectively free parameters of the Lagrangian, the latter yield predictions for the couplings, which in turn can be tested experimentally once the gravity interactions are decoupled at M_{Pl} and the system is run back down to the EWSB scale.
Thanks to the trans-Planckian fixed-point analysis we were able to derive a fairly precise determination of the abelian kinetic mixing ϵ, the NP Yukawa couplings, and the scalar quartic couplings. We then compared the obtained results with the Wilson coefficient ranges favored in the global EFT analyses to identify the allowed NP mass ranges. The emerging parameter space was finally subjected to a phenomenological analysis of the most recent ATLAS and CMS constrains, which we simulated numerically. In particular, we computed the most recent 95% C.L. bound on the $(m_{Z'}, \epsilon)$ plane from Z' production searches, based on the 13 TeV data set. We found that this search excludes two out of the three scenarios (1B and 2) due to the insurmountable constraint on the large kinetic mixing generated along the flow from the Planck scale down.
Conversely, the same strong bound can be evaded in Model 1A with an appropriate choice of the $U(1)_X$ charges. We have thus subjected this last scenario to the bounds from direct production of VL heavy quarks and leptons at the LHC. By using `CheckMate`, we identified the parameter space excluded at the 95% C.L., and we computed the projections for the planned increase in luminosity in future runs. We showed that direct NP searches are effective in excluding the parameter space consistent with the flavor anomalies and have the potential to bite into the unconstrained regions in even greater depth.
Overall, this work confirms the findings of several recent studies, from our group and others, pointing to the dramatic boost in predictivity that can be obtained by endowing NP scenarios with UV completions based on the well-motivated assumption of trans-Planckian AS. If the flavor anomalies are eventually confirmed to be real in future experimental data at LHCb and Belle II, the possibility of observing NP particles directly at the LHC rather than in a more powerful, yet-to-be-conceived machine, may point to the existence of a UV completion based on the ultra-high scale properties of quantum gravity.

Appendix 5.A: Rotations to the physical basis

Fermions We construct the mass matrix $\mathcal{M}$ for the Weyl spinor components of generic fermions $f_i' = (f_{L,i}', f_{R,i}'^{\dagger})^T$ of generation i,

$$\mathcal{L} \supset (\mathcal{M})_{ij} f_{R,i}' f_{L,j}' + \text{H.c.}\,, \tag{5.53}$$

where a sum over repeated indices is implied. Following Sec. 5.2.1, the mass matrix takes the generic form

$$\mathcal{M}_{Q(L)} = \frac{1}{\sqrt{2}} \begin{pmatrix} y_1 v_h & 0 & 0 & 0 \\ 0 & y_2 v_h & 0 & 0 \\ 0 & 0 & y_3 v_h & 0 \\ \lambda_{Q(L),1} v_S & \lambda_{Q(L),2} v_S & \lambda_{Q(L),3} v_S & \sqrt{2}\, m_{Q(L)} \end{pmatrix}, \tag{5.54}$$

which can be applied to quarks ($Q = U, D$) and/or to the leptons ($L = E, N$). In 5.54 the SM fermions have been rotated to their diagonal basis already.
We now diagonalize the 4×4 matrix $\mathcal{M}$ ($= \mathcal{M}_Q, \mathcal{M}_L$) by means of 2 unitary matrices $\mathcal{U}_L$, $\mathcal{U}_R$,

$$\mathcal{M}_{\text{diag}} = \mathcal{U}_R^{\dagger} \mathcal{M}\, \mathcal{U}_L\,, \tag{5.55}$$

and express the fermion "gauge" eigenstates (primed) as function of the physical eigenstates (unprimed) as

$$f_{L,i}' = (\mathcal{U}_L)_{ik}\, f_{L,k} \tag{5.56}$$

$$f_{R,i}' = (\mathcal{U}_R)_{ik}^{*}\, f_{R,k}\,, \tag{5.57}$$

where, again, a sum over repeated indices is implied.
A VL fermion of generation $\bar{k}$, charged under the $\text{U}(1)_X$ symmetry with $Q_X \neq 0$, develops a gauge interaction with the Z' boson,

$$\mathcal{L} \supset g_X Q_X \left(\bar{f}_{\bar{k}}' \gamma^{\mu} f_{\bar{k}}' \right) \tilde{Z}_{\mu}'\,. \tag{5.58}$$

One can insert Eqs. (5.56), (5.57) into 5.58 to extract the couplings of the Z' to the physical particles. One gets

$$\mathcal{L} \supset \bar{f}_i \gamma^{\mu} \left(g_L^{ij} P_L + g_R^{ij} P_R \right) f_j\, \tilde{Z}_{\mu}'\,, \tag{5.59}$$

where

$$g_L^{ij} = g_X Q_X (\mathcal{U}_L^{\dagger})_{i\bar{k}}\, (\mathcal{U}_L)_{\bar{k}j}\,, \qquad g_R^{ij} = g_X Q_X (\mathcal{U}_R^{\dagger})_{i\bar{k}}\, (\mathcal{U}_R)_{\bar{k}j}\,. \tag{5.60}$$

Note that the specific texture considered in 5.54 leads to $g_R^{ij} = 0$ for $i, j \neq \bar{k}$, in agreement with the results of Sec. 5.2.1.1 and Sec. 5.2.1.3.

Neutral gauge bosons In the presence of fermions charged under the $\text{U}(1)_Y$ and $\text{U}(1)_X$ gauge groups kinetic mixing of the abelian gauge bosons, ϵ, will be generated in the Lagrangian. Let us consider

$$\mathcal{L} \supset -\frac{1}{4} W_{\mu\nu}^i W^{i\mu\nu} - \frac{1}{4} B_{\mu\nu} B^{\mu\nu} - \frac{1}{4} X_{\mu\nu} X^{\mu\nu} - \frac{\epsilon}{2} B_{\mu\nu} X^{\mu\nu}, \tag{5.61}$$

where $W_{\mu\nu}^i$, $B_{\mu\nu}$ and $X_{\mu\nu}$ are the field strength tensors of $\text{SU}(2)_L$, $\text{U}(1)_Y$, and $\text{U}(1)_X$, respectively. After both the electroweak and $\text{U}(1)_X$ symmetries are spontaneously broken, the three neutral gauge bosons mix at the tree level. Once the kinetic terms are canonically normalized the relation between the gauge and physical bases up to $\mathcal{O}(\epsilon)$ reads [262]

$$\tilde{Z}_\mu = Z_\mu \cos\theta_M + Z'_\mu \sin\theta_M\,, \tag{5.62}$$

$$\tilde{A}_\mu = A_\mu + \epsilon\cos\theta_W (Z\sin\theta_M - Z'_\mu\cos\theta_M)\,, \tag{5.63}$$

$$\tilde{Z}'_\mu = Z_\mu(-\sin\theta_M + \epsilon\cos\theta_M\sin\theta_W) + Z'_\mu(\cos\theta_M + \epsilon\sin\theta_M\sin\theta_W)\,, \tag{5.64}$$

where we indicate the fields in the unrotated basis with a tilde and those in the physical basis without tilde. Here $\sin\theta_W$ is the Weinberg angle and we define the mixing angle $\tan\theta_M = 1/(\beta \pm \sqrt{\beta^2+1})$ as

$$\beta = \frac{m^2_{Z,\mathrm{SM}}\left(1-\epsilon^2\cos^2\theta_W\right)^2 - m^2_{Z'}\left(1-\epsilon^2-\epsilon^2\sin^2\theta_W\right)}{2\,m^2_{Z'}\,\epsilon\sin\theta_W\sqrt{1-\epsilon^2}}\,, \tag{5.65}$$

where $m^2_{Z,\mathrm{SM}} = (g_2^2+g_Y^2)\,v_h^2/4$ and $m^2_{Z'} = g_X^2 Q_S^2 v_S^2$ like in Sec. 5.2.1.[1] The $+(-)$ sign in the line above 5.65 applies to the case $m_{Z,\mathrm{SM}} > m_{Z'}$ ($m_{Z,\mathrm{SM}} < m_{Z'}$).
The flavor-diagonal couplings of the SM gauge bosons $\tilde{A}_\mu$ and $\tilde{Z}_\mu$ to a fermion $f = (f_L, f_R^\dagger)^T$, of electric charge $\tilde{Q}_f$, read

$$\mathcal{L} \supset g_Y\cos\theta_W\tilde{Q}_f\left(\bar{f}\gamma^\mu f\right)\tilde{A}_\mu + \frac{g_2}{\cos\theta_W}\bar{f}\gamma^\mu\left(c_L^f P_L + c_R^f P_R\right) f\tilde{Z}_\mu\,, \tag{5.66}$$

where

$$c^f_{L,R} = \left(T_3^{f_{L,R}} - \tilde{Q}_f\sin^2\theta_W\right), \tag{5.67}$$

with $T_3^{f_{L,R}}$ denoting the third component of weak isospin. From Eqs. (5.62), (5.63) and 5.65 one can read off the coupling of the physical Z' boson to the SM fermions. Up to $\mathcal{O}(\epsilon)$ one obtains

$$\mathcal{L} \supset -\epsilon\, g_Y\cos^2\theta_W\tilde{Q}_f\left(\bar{f}\gamma^\mu f\right)Z'_\mu + \epsilon\, g_2\tan\theta_W\frac{m^2_{Z'}}{m^2_{Z'}-m^2_{Z,\mathrm{SM}}}\bar{f}\gamma^\mu\left(c_L^f P_L + c_R^f P_R\right) f Z'_\mu\,. \tag{5.68}$$

Due to the flavor construction described in Appendix 5.A the model also features interactions of the $\tilde{Z}'_\mu$ boson with fermions of different generations i, j. Consider the Lagrangian in 5.59 which, to provide a solution for the flavor anomalies, must apply in particular to the quarks of the second and third generation, and to the leptons of the second generation. After plugging in 5.64 one can extract the off-diagonal couplings of the physical Z' boson to the fermions. Equation (5.59) remains unchanged at $\mathcal{O}(\epsilon)$.

Scalars The scalar potential of the models considered in this study takes the form

$$V\left(|h|^2, |S|^2\right) = -\mu_h^2\, h^\dagger h + \lambda_h\left(h^\dagger h\right)^2 + \mu_S^2\, S^\dagger S + \lambda_S\left(S^\dagger S\right)^2 + \lambda_{hS}\left(S^\dagger S\right)\left(h^\dagger h\right), \tag{5.69}$$

where

$$h : (\mathbf{1}, \mathbf{2}, 1/2, 0)\,, \tag{5.70}$$

is the SM Higgs doublet.
After the breaking of the electroweak and $\mathrm{U}(1)_X$ symmetries, respectively by the vev's v_h and v_S, the mass matrix for the real part of the neutral component of the Higgs doublet h

[1] Note that the these expressions have to be further modified at $\mathcal{O}(\epsilon^2)$ by the rotation (5.65) – the full form of the Z and Z' physical masses can be found, *e.g.*, in Ref. [262].

and the real part of the scalar S takes the form

$$m_H^2 = \begin{pmatrix} -\mu_h^2 + 3\lambda_h v_h^2 + \frac{1}{2}\lambda_{hS} v_S^2 & \lambda_{hS} v_S v_h \\ \lambda_{hS} v_S v_h & \mu_S^2 + 3\lambda_S v_S^2 + \frac{1}{2}\lambda_{hS} v_h^2 \end{pmatrix}. \tag{5.71}$$

Equation (5.71) can be diagonalized by an orthogonal matrix $\mathcal{Z}_H$ such that

$$(m_H^2)_{\text{diag}} = \mathcal{Z}_H m_H^2 \mathcal{Z}_H^T. \tag{5.72}$$

The mixing angle α_H parameterizing the matrix $\mathcal{Z}_H$ is given by

$$\sin\alpha_H = \frac{\lambda_{hS}\, v_h\, v_S}{2\sqrt{\lambda_h^2 v_h^4 + \lambda_{hS}^2 v_h^2 v_S^2 - 2\lambda_h\lambda_S v_h^2 v_S^2 + \lambda_S^2 v_S^4}}, \tag{5.73}$$

and the physical masses of the scalars H_1 and H_2 can be expressed in terms of the parameters in 5.69 as

$$\begin{aligned} m_{H_1} &= \sqrt{\lambda_h v_h^2 + \lambda_S v_S^2 - \sqrt{\lambda_h^2 v_h^4 + \lambda_{hS}^2 v_h^2 v_S^2 - 2\lambda_h\lambda_S v_h^2 v_S^2 + \lambda_S^2 v_S^4}}, \\ m_{H_2} &= \sqrt{\lambda_h v_h^2 + \lambda_S v_S^2 + \sqrt{\lambda_h^2 v_h^4 + \lambda_{hS}^2 v_h^2 v_S^2 - 2\lambda_h\lambda_S v_h^2 v_S^2 + \lambda_S^2 v_S^4}}. \end{aligned} \tag{5.74}$$

Appendix 5.B: RGEs in the presence of two U(1) group factors

Let us consider a gauge theory with a symmetry group $\mathrm{U}(1)_Y \times \mathrm{U}(1)_X$, with the corresponding gauge couplings denoted as g_Y and g_X. If the theory contains a fermion f transforming under both symmetry factors with charges Q_Y, Q_X, kinetic mixing ϵ is generated between the two abelian groups. The gauge part of the Lagrangian takes the form

$$\begin{aligned} \mathcal{L} \supset\; & -\frac{1}{4}B_{\mu\nu}B^{\mu\nu} - \frac{1}{4}X_{\mu\nu}X^{\mu\nu} - \frac{\epsilon}{2}B_{\mu\nu}X^{\mu\nu} \\ & + i\bar{f}\left(\partial^\mu - i g_Y Q_Y \tilde{B}^\mu - i g_X Q_X \tilde{X}^\mu\right)\gamma_\mu f, \end{aligned} \tag{5.75}$$

where we indicate with $\tilde{B}^\mu$ and $\tilde{X}^\mu$ the gauge bosons of $\mathrm{U}(1)_Y$ and $\mathrm{U}(1)_X$, respectively, and $B_{\mu\nu}$ and $X_{\mu\nu}$ are the corresponding field strength tensors.

In order to modify the RGEs with trans-Planckian corrections linear in the gauge couplings it is convenient to work in a basis in which the gauge fields are canonically normalized. This can be achieved by a rotation [263, 264]

$$\begin{pmatrix} \tilde{B}^\mu \\ \tilde{X}^\mu \end{pmatrix} = \begin{pmatrix} 1 & -\epsilon/\sqrt{(1-\epsilon^2)} \\ 0 & 1/\sqrt{(1-\epsilon^2)} \end{pmatrix} \begin{pmatrix} V^\mu \\ D^\mu \end{pmatrix}, \tag{5.76}$$

which parameterizes the gauge interaction vertices of Lagrangian (5.75) in terms of a "visible" gauge boson V^μ and a "dark" gauge boson D^μ:

$$(Q_Y\, Q_X) \begin{pmatrix} g_Y & 0 \\ 0 & g_X \end{pmatrix} \begin{pmatrix} \tilde{B}^\mu \\ \tilde{X}^\mu \end{pmatrix} \;\to\; (Q_Y\, Q_X) \begin{pmatrix} g_V & g_\epsilon \\ 0 & g_D \end{pmatrix} \begin{pmatrix} V^\mu \\ D^\mu \end{pmatrix}. \tag{5.77}$$

The elements g_V, g_D, and g_ϵ are related to the original gauge couplings g_Y, g_X and the kinetic mixing ϵ as

$$g_V = g_Y, \quad g_D = \frac{g_X}{\sqrt{1-\epsilon^2}}, \quad g_\epsilon = -\frac{\epsilon g_Y}{\sqrt{1-\epsilon^2}}. \tag{5.78}$$

Generic sub-Planckian RGEs in the g_V, g_D and g_ϵ basis are given by [264]

$$\frac{dg_V}{dt} = \frac{1}{16\pi^2}\frac{2}{3}d(R_{F3})d(R_{F2})\,Q_Y^2\,g_V^3 \tag{5.79}$$

$$\frac{dg_D}{dt} = \frac{1}{16\pi^2}\frac{2}{3}d(R_{F3})d(R_{F2})\left(Q_Y^2 g_\epsilon^2 + 2Q_Y Q_X g_\epsilon g_D + Q_X^2 g_D^2\right) g_D \tag{5.80}$$

$$\frac{dg_\epsilon}{dt} = \frac{1}{16\pi^2}\frac{2}{3}d(R_{F3})d(R_{F2})\left[Q_Y^2(2g_V^2\,g_\epsilon + g_\epsilon^3) + 2Q_Y Q_X g_D(g_D^2 + g_\epsilon^2) + Q_X^2 g_D^2 g_\epsilon\right] \tag{5.81}$$

where $d(R_{F3})$ is the dimension of the SU(3)$_c$ representation R_{F3} under which the fermion f transforms and $d(R_{F2})$ is the corresponding dimension of the SU(2)$_L$ representation R_{F2}. While Eqs. (5.79) and (5.80) are multiplicative in the respective gauge couplings, 5.81 shows that g_ϵ may be generated additively, if and only if both charges Q_Y, Q_X are different from zero. It is easy to invert 5.78 and read off the kinetic mixing from the running couplings:

$$\epsilon = \frac{g_\epsilon}{\sqrt{g_\epsilon^2 + g_V^2}}\,. \tag{5.82}$$

In the presence of multiple fields charged under U(1)$_Y$, U(1)$_X$, or both, Eqs. (5.79)-(5.81) can be rewritten in compact form,

$$\frac{dg_V}{dt} = \frac{1}{16\pi^2}\widetilde{Q}_Y\,g_V^3 \tag{5.83}$$

$$\frac{dg_D}{dt} = \frac{1}{16\pi^2}\left(\widetilde{Q}_Y g_\epsilon^2 + 2\,\widetilde{Q}_{YX} g_\epsilon g_D + \widetilde{Q}_X g_D^2\right) g_D \tag{5.84}$$

$$\frac{dg_\epsilon}{dt} = \frac{1}{16\pi^2}\left[\widetilde{Q}_Y\left(2\,g_V^2 g_\epsilon + g_\epsilon^3\right) + 2\,\widetilde{Q}_{YX} g_D\left(g_V^2 + g_\epsilon^2\right) + \widetilde{Q}_X g_D^2 g_\epsilon\right], \tag{5.85}$$

where the one-loop coefficients $\widetilde{Q}_Y$, $\widetilde{Q}_X$ and $\widetilde{Q}_{YX}$ are defined as

$$\widetilde{Q}_Y = \frac{2}{3}\sum_i d(R_{i3})d(R_{i2})Q_{Yi}^2 + \frac{1}{3}\sum_j d(R_{j3})d(R_{j2})Q_{Yj}^2 \tag{5.86}$$

$$\widetilde{Q}_X = \frac{2}{3}\sum_i d(R_{i3})d(R_{i2})Q_{Xi}^2 + \frac{1}{3}\sum_j d(R_{j3})d(R_{j2})Q_{Xj}^2 \tag{5.87}$$

$$\widetilde{Q}_{YX} = \frac{2}{3}\sum_i d(R_{i3})d(R_{i2})Q_{Yi}Q_{Xi} + \frac{1}{3}\sum_j d(R_{j3})d(R_{j2})Q_{Yj}Q_{Xj}\,, \tag{5.88}$$

where $Q_{Yi(j)}$ and $Q_{Xi(j)}$ are the abelian charges of a fermion (scalar) particle of index i (j) under U(1)$_Y$ and U(1)$_X$, respectively, and the sums run over all the fermions and scalars in the theory.

Appendix 5.C: RGEs of the gauge-Yukawa-quartic system

The elements of the SM and NP Yukawa matrices are all subject to modifications due to RGE running. When working in the mass basis the scale dependence of the rotation matrices is encapsulated in the running of the elements of the CKM matrix, see, *e.g.*, Appendices A and B of Ref. [196] and references therein for a discussion. Following the procedure detailed there, we compute the RGEs in the flavor basis with `SARAH v4.14.0` [265] and `RGBeta` [266] and then transform them to the quark mass basis. We work in the "down-origin" approach, in which the NP Yukawa couplings of the up-type quarks are related to the more "fundamental" down-type Yukawa couplings $\lambda_{Q,i}$ by a CKM rotation. We then employ the 2-family approximation, in which the CKM matrix is orthogonal and defined by one independent parameter,

$$V_{22} = V_{33}\,, \qquad V_{23} = -V_{32} = \sqrt{1 - {V_{33}}^2}\,. \tag{5.89}$$

In the following we present the trans-Planckian RGEs of the models defined in Table 5.1. All parameters that are not shown explicitly are considered to be zero and relevant at the UV fixed point. We restrict our analysis to one loop and consider only trans-Planckian corrections to the RGEs that are linear in the coupling constants, neglecting the effects of higher order terms. Note that $t = \log k$.

Model 1 (VL leptons)

Gauge sector Model 1A

$$\frac{dg_3}{dt} = -\frac{17}{3}\frac{g_3^3}{16\pi^2} - f_g g_3 \tag{5.90}$$

$$\frac{dg_2}{dt} = -\frac{1}{2}\frac{g_2^3}{16\pi^2} - f_g g_2 \tag{5.91}$$

$$\frac{dg_Y}{dt} = \frac{139}{18}\frac{g_Y^3}{16\pi^2} - f_g g_Y \tag{5.92}$$

$$\frac{dg_D}{dt} = \frac{1}{16\pi^2}\left(11 g_D^2 + \frac{139}{18} g_\epsilon^2\right) g_D - f_g g_D \tag{5.93}$$

$$\frac{dg_\epsilon}{dt} = \frac{1}{16\pi^2}\left(11 g_D^2 g_\epsilon + \frac{139}{9} g_Y^2 g_\epsilon + \frac{139}{18} g_\epsilon^3\right) - f_g g_\epsilon \tag{5.94}$$

Gauge sector Model 1B

$$\frac{dg_3}{dt} = -\frac{17}{3}\frac{g_3^3}{16\pi^2} - f_g g_3 \tag{5.95}$$

$$\frac{dg_2}{dt} = -\frac{1}{2}\frac{g_2^3}{16\pi^2} - f_g g_2 \tag{5.96}$$

$$\frac{dg_Y}{dt} = \frac{139}{18}\frac{g_Y^3}{16\pi^2} - f_g g_Y \tag{5.97}$$

$$\frac{dg_D}{dt} = \frac{1}{16\pi^2}\left(11 g_D^2 + \frac{139}{18} g_\epsilon^2 - \frac{16}{3} g_D g_\epsilon\right) g_D - f_g g_D \tag{5.98}$$

$$\frac{dg_\epsilon}{dt} = \frac{1}{16\pi^2}\left(11 g_D^2 g_\epsilon + \frac{139}{9} g_Y^2 g_\epsilon + \frac{139}{18} g_\epsilon^3 - \frac{16}{3} g_D g_Y^2 - \frac{16}{3} g_D g_\epsilon^2\right) - f_g g_\epsilon \tag{5.99}$$

Yukawa and scalar sector

$$\begin{aligned}\frac{dy_t}{dt} = \frac{1}{16\pi^2}\Bigg[&3y_b^2 + \frac{9}{2}y_t^2 - \frac{17}{12}g_Y^2 - \frac{17}{12}g_\epsilon^2 - \frac{9}{4}g_2^2 - 8g_3^2 - \frac{3}{2}{V_{33}}^2 y_b^2 \\ &+\frac{1}{2}{V_{32}}^2(\lambda_{Q,2})^2 + V_{32}V_{33}\lambda_{Q,3}\lambda_{Q,2} + \frac{1}{2}{V_{33}}^2(\lambda_{Q,3})^2\Bigg] y_t - f_y y_t\end{aligned} \tag{5.100}$$

$$\frac{dy_b}{dt} = \frac{1}{16\pi^2}\left[\frac{9}{2}y_b^2 + 3y_t^2 - \frac{5}{12}g_Y^2 - \frac{5}{12}g_\epsilon^2 - \frac{9}{4}g_2^2 - 8g_3^2 - \frac{3}{2}{V_{33}}^2 y_t^2 + \frac{1}{2}(\lambda_{Q,3})^2\right] y_b - f_y y_b \tag{5.101}$$

$$\frac{d\lambda_{Q,2}}{dt} = \frac{1}{16\pi^2}\left\{\left[7(\lambda_{Q,2})^2 + \frac{13}{2}(\lambda_{Q,3})^2 + 2(\lambda_{L,2})^2 + \frac{1}{2}y_t^2 {V_{32}}^2 - \frac{9}{2}g_2^2 - 8g_3^2 \right.\right.$$
$$\left.\left. -\frac{1}{6}g_Y^2 - \frac{1}{6}g_\epsilon^2 - 3g_D^2 + g_D g_\epsilon\right]\lambda_{Q,2} + 2y_t^2 V_{32}V_{33}\lambda_{Q,3}\right\} - f_y\lambda_{Q,2} \quad (5.102)$$

$$\frac{d\lambda_{Q,3}}{dt} = \frac{1}{16\pi^2}\left\{\left[\frac{15}{2}(\lambda_{Q,2})^2 + 7(\lambda_{Q,3})^2 + 2(\lambda_{L,2})^2 + \frac{1}{2}y_b^2 + \frac{1}{2}y_t^2 {V_{33}}^2 - \frac{9}{2}g_2^2 - 8g_3^2 \right.\right.$$
$$\left.\left. -\frac{1}{6}g_Y^2 - \frac{1}{6}g_\epsilon^2 - 3g_D^2 + g_D g_\epsilon\right]\lambda_{Q,3} - y_t^2 V_{32}V_{33}\lambda_{Q,2}\right\} - f_y\lambda_{Q,3} \quad (5.103)$$

$$\frac{d\lambda_{L,2}}{dt} = \frac{1}{16\pi^2}\left[6(\lambda_{Q,2})^2 + 6(\lambda_{Q,3})^2 + 3(\lambda_{L,2})^2 - \frac{9}{2}g_2^2 - \frac{3}{2}g_Y^2 - \frac{3}{2}g_\epsilon^2 - 3g_D^2 \right.$$
$$\left. + 3g_D g_\epsilon\right]\lambda_{L,2} - f_y\lambda_{L,2} \quad (5.104)$$

$$\frac{d|V_{33}|}{dt} = \frac{V_{23}}{16\pi^2}\left[-\frac{3}{2}V_{23}V_{33}y_b^2 + \frac{1}{2}\Big(V_{22}V_{32}(\lambda_{Q,2})^2 \right.$$
$$\left. + V_{22}V_{33}\lambda_{Q,2}\lambda_{Q,3} + V_{23}V_{32}\lambda_{Q,2}\lambda_{Q,3} + V_{23}V_{33}(\lambda_{Q,3})^2\Big)\right]$$
$$- \frac{V_{32}}{16\pi^2}\left[\frac{3}{2}V_{32}V_{33}y_t^2 - \frac{1}{2}\lambda_{Q,2}\lambda_{Q,3}\right] \quad (5.105)$$

$$\frac{d\lambda_h}{dt} = \frac{1}{16\pi^2}\left[\frac{3}{8}(g_Y^2 + g_\epsilon^2)^2 + \frac{3}{4}(g_Y^2 + g_\epsilon^2)g_2^2 + \frac{9}{8}g_2^4 - 3g_Y^2\lambda_h - 3g_\epsilon^2\lambda_h - 9g_2^2\lambda_h \right.$$
$$\left. + 24\lambda_h^2 + \lambda_{hS}^2 + 12y_b^2\lambda_h + 12y_t^2\lambda_h - 6y_b^4 - 6y_t^4)\right] - f_\lambda\lambda_h \quad (5.106)$$

$$\frac{d\lambda_S}{dt} = \frac{1}{16\pi^2}\left[6g_D^4 g_Y^2/(g_Y^2 + g_\epsilon^2) + 2\lambda_{hS}^2 - 12g_D^2\lambda_S + 20\lambda_S^2 + 8(\lambda_{L,2})^2\lambda_S - 4(\lambda_{L,2})^4 \right.$$
$$\left. + 24(\lambda_{Q,2})^2\lambda_S + 24(\lambda_{Q,3})^2\lambda_S - 12\left((\lambda_{Q,2})^2 + (\lambda_{Q,3})^2\right)^2\right] - f_\lambda\lambda_S \quad (5.107)$$

$$\frac{d\lambda_{hS}}{dt} = \frac{1}{16\pi^2}\left[-\frac{3}{2}g_Y^2\lambda_{hS} - \frac{9}{2}g_2^2\lambda_{hS} - 6g_D^2\lambda_{hS} + 12\lambda_h\lambda_{hS} + 4\lambda_{hS}^2 + 8\lambda_{hS}\lambda_S \right.$$
$$+ 4(\lambda_{L,2})^2\lambda_{hS} + 12(\lambda_{Q,2})^2\lambda_{hS} + 12(\lambda_{Q,3})^2\lambda_{hS} + 6y_b^2\lambda_{hS} + 6y_t^2\lambda_{hS}$$
$$- 12y_b^2(\lambda_{Q,3})^2 - 12y_t^2{V_{32}}^2(\lambda_{Q,2})^2 - 12y_t^2{V_{33}}^2(\lambda_{Q,3})^2$$
$$\left. - 12y_t^2 V_{32}V_{33}\lambda_{Q,2}\lambda_{Q,3}\right] - f_\lambda\lambda_{hS}\,. \quad (5.108)$$

Model 2 ($L_\mu - L_\tau$)

$$\frac{dg_3}{dt} = -\frac{17}{3}\frac{g_3^3}{16\pi^2} - f_g g_3 \quad (5.109)$$

$$\frac{dg_2}{dt} = -\frac{7}{6}\frac{g_2^3}{16\pi^2} - f_g g_2 \quad (5.110)$$

$$\frac{dg_Y}{dt} = \frac{127}{18}\frac{g_Y^3}{16\pi^2} - f_g g_Y \quad (5.111)$$

$$\frac{dg_D}{dt} = \frac{1}{16\pi^2}\left[\frac{37}{3}g_D^2 - \frac{8}{3}g_D g_\epsilon + \frac{127}{18}g_\epsilon^2\right]g_D - f_g g_D \tag{5.112}$$

$$\frac{dg_\epsilon}{dt} = \frac{1}{16\pi^2}\left[\frac{37}{3}g_D^2 g_\epsilon - \frac{8}{3}g_D g_\epsilon^2 - \frac{8}{3}g_D g_Y^2 + \frac{127}{18}g_\epsilon^3 + \frac{127}{9}g_\epsilon g_Y^2\right] - f_g g_\epsilon \tag{5.113}$$

$$\begin{aligned}\frac{dy_t}{dt} = \frac{1}{16\pi^2}&\left[3y_b^2 + \frac{9}{2}y_t^2 - \frac{17}{12}g_Y^2 - \frac{17}{12}g_\epsilon^2 - \frac{9}{4}g_2^2 - 8g_3^2 - \frac{3}{2}{V_{33}}^2 y_b^2\right.\\ &\left.+\frac{1}{2}\left({V_{32}}^2(\lambda_{Q,2})^2 + 2V_{32}V_{33}\lambda_{Q,3}\lambda_{Q,2} + {V_{33}}^2(\lambda_{Q,3})^2\right)\right] y_t - f_y y_t\end{aligned} \tag{5.114}$$

$$\frac{dy_b}{dt} = \frac{1}{16\pi^2}\left[\frac{9}{2}y_b^2 + 3y_t^2 - \frac{5}{12}g_Y^2 - \frac{5}{12}g_\epsilon^2 - \frac{9}{4}g_2^2 - 8g_3^2 - \frac{3}{2}{V_{33}}^2 y_t^2 + \frac{1}{2}(\lambda_{Q,3})^2\right] y_b - f_y y_b \tag{5.115}$$

$$\begin{aligned}\frac{d\lambda_{Q,2}}{dt} = \frac{1}{16\pi^2}&\left\{\left[7(\lambda_{Q,2})^2 + \frac{13}{2}(\lambda_{Q,3})^2 - \frac{1}{6}g_Y^2 - \frac{1}{6}g_\epsilon^2 - 3g_D^2 + g_D g_\epsilon - \frac{9}{2}g_2^2 - 8g_3^2\right.\right.\\ &\left.\left.+\frac{1}{2}y_t^2{V_{32}}^2\right]\lambda_{Q,2} + 2y_t^2 V_{32}V_{33}\lambda_{Q,3}\right\} - f_y\lambda_{Q,2}\end{aligned} \tag{5.116}$$

$$\begin{aligned}\frac{d\lambda_{Q,3}}{dt} = \frac{1}{16\pi^2}&\left\{\left[\frac{15}{2}(\lambda_{Q,2})^2 + 7(\lambda_{Q,3})^2 - \frac{1}{6}g_Y^2 - \frac{1}{6}g_\epsilon^2 - 3g_D^2 + g_D g_\epsilon - \frac{9}{2}g_2^2 - 8g_3^2\right.\right.\\ &\left.\left.+\frac{1}{2}y_b^2 + \frac{1}{2}y_t^2{V_{33}}^2\right]\lambda_{Q,3} - y_t^2 V_{32}V_{33}\lambda_{Q,2}\right\} - f_y\lambda_{Q,3}\end{aligned} \tag{5.117}$$

$$\begin{aligned}\frac{d|V_{33}|}{dt} = \frac{V_{23}}{16\pi^2}&\left[-\frac{3}{2}V_{23}V_{33}y_b^2 + \frac{1}{2}\left(V_{22}V_{32}(\lambda_{Q,2})^2\right.\right.\\ &\left.\left.+V_{22}V_{33}\lambda_{Q,2}\lambda_{Q,3} + V_{23}V_{32}\lambda_{Q,2}\lambda_{Q,3} + V_{23}V_{33}(\lambda_{Q,3})^2\right)\right]\\ &- \frac{V_{32}}{16\pi^2}\left[\frac{3}{2}V_{32}V_{33}y_t^2 - \frac{1}{2}\lambda_{Q,2}\lambda_{Q,3}\right]\end{aligned} \tag{5.118}$$

$$\begin{aligned}\frac{d\lambda_h}{dt} = \frac{1}{16\pi^2}&\left[\frac{3}{8}(g_Y^2 + g_\epsilon^2)^2 + \frac{3}{4}(g_Y^2 + g_\epsilon^2)g_2^2 + \frac{9}{8}g_2^4 - 3g_Y^2\lambda_h - 3g_\epsilon^2\lambda_h - 9g_2^2\lambda_h\right.\\ &\left.+24\lambda_h^2 + \lambda_{hS}^2 + 12y_b^2\lambda_h + 12y_t^2\lambda_h - 6y_b^4 - 6y_t^4)\right] - f_\lambda\lambda_h\end{aligned} \tag{5.119}$$

$$\begin{aligned}\frac{d\lambda_S}{dt} = \frac{1}{16\pi^2}&\left[6g_D^4 g_Y^2/(g_Y^2 + g_\epsilon^2) + 2\lambda_{hS}^2 - 12g_D^2\lambda_S + 20\lambda_S^2 + 24(\lambda_{Q,2})^2\lambda_S + 24(\lambda_{Q,3})^2\lambda_S\right.\\ &\left.-12\left((\lambda_{Q,2})^2 + (\lambda_{Q,3})^2\right)^2\right] - f_\lambda\lambda_S\end{aligned} \tag{5.120}$$

$$\begin{aligned}\frac{d\lambda_{hS}}{dt} = \frac{1}{16\pi^2}&\left[-\frac{3}{2}g_Y^2\lambda_{hS} - \frac{9}{2}g_2^2\lambda_{hS} - 6g_D^2\lambda_{hS} + 12\lambda_h\lambda_{hS} + 4\lambda_{hS}^2 + 8\lambda_{hS}\lambda_S\right.\\ &+12(\lambda_{Q,2})^2\lambda_{hS} + 12(\lambda_{Q,3})^2\lambda_{hS} + 6y_b^2\lambda_{hS} + 6y_t^2\lambda_{hS}\\ &-12y_b^2(\lambda_{Q,3})^2 - 12y_t^2{V_{32}}^2(\lambda_{Q,2})^2 - 12y_t^2{V_{33}}^2(\lambda_{Q,3})^2\\ &\left.-12y_t^2 V_{32}V_{33}\lambda_{Q,2}\lambda_{Q,3}\right] - f_\lambda\lambda_{hS}\,.\end{aligned} \tag{5.121}$$

5.3 How robust are particle physics predictions in asymptotic safety?

This section is based on "How robust are particle physics predictions in asymptotic safety?" by W. Kotlarski, K. Kowalska, D. Rizzo, E. M. Sessolo, [3].

5.3.1 Introduction

While in the absence of a fully developed theory of quantum gravity the heuristic approach described in section 5.1 has proven to be extremely fruitful for phenomenological studies in particle physics, it is also important to be aware that it is based on several simplifying approximations:

- The dimensional regularization matter beta functions are typically computed at 1-loop
- The Planck scale is set arbitrarily at $M_{\text{Pl}} = 10^{19}$ GeV
- The scale dependence of f_g and f_y, which should parameterize the cross-over from the interactive to non-interactive regime of quantum gravity, is neglected. f_g and f_y are treated as constants above the Planck scale and are set to zero below. In other words, gravity decouples instantaneously at $M_{\text{Pl}} = 10^{19}$ GeV.

The question then naturally arises as to how robust the predictions derived in this way can be considered, and to what extent dropping any of the approximations listed above may affect a potential observational strategy to test these predictions at the low scale.
In this section we attempt to address the issue in a systematic way. We analyze the effects of discarding one by one the approximations of the minimal parametric setup. Specifically we consider

- the inclusion of higher-order corrections in the matter sector
- changing the position of the Planck scale by a few orders of magnitude
- the non-trivial functional dependence of the running gravitational couplings, $f_{g,y}(t)$, resulting in the non-instantaneous decoupling of the trans-Planckian UV completion.

We limit ourselves to the study of gauge-Yukawa systems of the type (5.1) and (5.2). As we have mentioned above, the dimensionless parameters of the scalar potential lie on a slightly different footing. Besides the issue of whether the gravitational correction is multiplicative or not, it has also been shown that in the SM [180] and some models of NP [2] it is difficult to obtain the precise value of the Higgs mass if the flow originates from a UV irrelevant fixed point, so that the predictivity of AS for the scalar potential is often in question and a model-dependent issue. On the other hand, from the point of view of the RG flow, the parameters of the scalar potential result somewhat "decoupled" from the gauge-Yukawa system, as they can only affect 5.1 from the third-loop level up, and 5.2 from the second loop. We shall quantify, when necessary, the size of the corrections that unknown parameters of the scalar potential induce on the gauge-Yukawa system via higher-order contributions.
Our main finding is that the predictions in the gauge sector are extremely robust. Each and every one of the effects listed above induce an uncertainty that does not exceed the one percent level. The situation is slightly more intricate in the Yukawa sector, where the uncertainty strongly depends on the size of the predicted coupling itself. We find that, while Yukawas as large as the SM hypercharge coupling are subject to uncertainties not exceeding

the five percent level, if they turn out to be much smaller – as a result of fine tuning – their uncertainties increase significantly.
While the approximations listed above can be abandoned to evaluate the precision of the obtained predictions, the whole heuristic approach relies on a few assumptions which cannot be removed without compromising critically the predictive power of the fixed point analysis:

1. The trans-Planckian UV completion (whether it be gravity of else) should be responsible for the disappearance of the Landau pole in the hypercharge gauge coupling of the SM and for the appearance of an irrelevant fixed point in its place

2. The trans-Planckian UV completion should be responsible for the appearance of an irrelevant fixed point in at least one of the SM Yukawa couplings

3. There is a "desert" with no new state above the typical scale of the NP model, up to the Planck scale where the UV completion kicks in (assumption of minimality). More precisely, new, light or heavy states can actually exist, but they ought to be characterized by feeble interactions with the visible sector [2].

Point 1 and 3 allow one to extract the value of f_g uniquely, by connecting the hypercharge gauge coupling flow from the Planck scale down to the EWSB scale. Point 1, together with the fact that $f_g > 0$, implies that the non-abelian gauge couplings of the SM, g_3 and g_2, remain relevant and asymptotically free. Point 2 implies that one can connect an irrelevant SM direction from the Planck to the EWSB scale and extract uniquely the trans-Planckian value of f_y. All the NP Yukawa couplings for which we seek a prediction should correspond to irrelevant directions, while the SM Yukawa couplings that are not employed for the determination of f_y, as well as other possible couplings (point 3), will vanish in the deep UV and correspond to relevant directions in the coupling space.

5.3.2 Reference model predictions at 1 loop

In order to quantify the theoretical uncertainties originating from the approximations listed in Sec. 5.3.1, one needs a set of "standard candle" predictions to observe how they are modified when those approximations are dropped.
We introduce two models: the $B-L$ model, for which we seek to predict the dark abelian gauge coupling, the kinetic mixing, and the NP Yukawa couplings associated with the right-handed neutrino sector; and a leptoquark (LQ) model, for which we seek to predict the NP Yukawa interaction of the color-charged leptoquark with a SM quark and a lepton. For each of these models we derive the RGEs using `PyR@TE 3` [267, 268].[2] The explicit forms of the beta functions for the models considered in this study are given in Appendix 5.D.

5.3.2.1 Gauged $B-L$

We derive predictions for the NP sector of the gauged $B-L$ model [269, 270]. The SM symmetry is extended by an abelian gauge group $\mathrm{U}(1)_{B-L}$, with gauge coupling g_{B-L}. The particle content of the SM is extended by one or more right-handed neutrinos and a complex scalar field S, whose vev spontaneously breaks $\mathrm{U}(1)_{B-L}$. The abelian charges of the SM and NP fields can be found, *e.g.*, in Refs. [269, 270].

[2] We use the most recent available version of `PyR@TE` (`PyR@TE` master branch). For the gauged $B-L$ we use the model file distributed with `PyR@TE`.

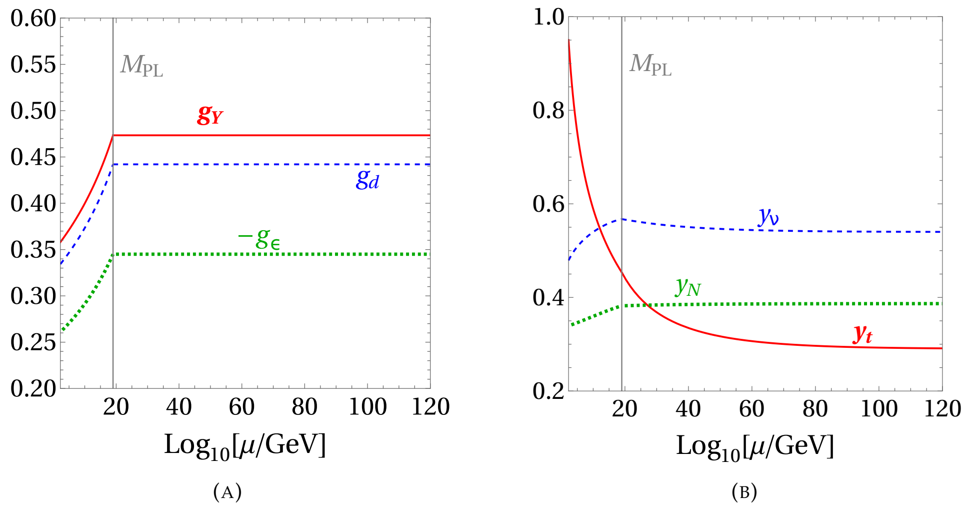

FIGURE 5.6: RG flow of the (a) gauge and (b) Yukawa couplings in the gauged $B-L$ model from trans-Planckian energies down to the EWSB scale, for a scenario characterized by the UV fixed points of 5.128 and 5.129. The gray vertical line indicates the fixed position of the Planck scale, $M_{\rm Pl} = 10^{19}$ GeV.

The Yukawa part of the SM Lagrangian is extended by terms

$$\mathcal{L} \supset -Y_\nu N\,(\epsilon H^*)^\dagger L - \frac{1}{2} Y_N S N N + \text{H.c.}\,, \tag{5.122}$$

where we have used two component spinor notation and $\epsilon = i\sigma_2$. Spinor and SU(2) indices are understood to be contracted trivially, following matrix multiplication rules. H and L are the SM Higgs and lepton doublets, respectively, and N is the SM-singlet right-handed neutrino. Y_ν and Y_N are typically 3-by-3 matrices in flavor space. Here, for simplicity, we will only focus on a single entry of each matrix: $y_\nu \equiv (Y_\nu)_{33}$ and $y_N \equiv (Y_N)_{33}$. When the scalar S acquires a vev, the right-handed neutrino develops a Majorana mass term.
The abelian gauge part of the Lagrangian takes the form

$$\begin{aligned}\mathcal{L} \;\supset\; & -\frac{1}{4} B_{\mu\nu}B^{\mu\nu} - \frac{1}{4} X_{\mu\nu}X^{\mu\nu} - \frac{\epsilon}{2} B_{\mu\nu}X^{\mu\nu} \\ & + i\bar{f}\left(\partial^\mu - i g_Y Q_Y \tilde{B}^\mu - i g_{B-L} Q_{B-L} \tilde{X}^\mu\right)\gamma_\mu f\,,\end{aligned} \tag{5.123}$$

where we indicate with $\tilde{B}^\mu$ and $\tilde{X}^\mu$ the gauge bosons of $\mathrm{U}(1)_Y$ and $\mathrm{U}(1)_{B-L}$, respectively, and $B_{\mu\nu}$ and $X_{\mu\nu}$ are the corresponding field strength tensors. SM fermions f transform under both symmetry factors with charges Q_Y, Q_{B-L} so that kinetic mixing ϵ is generated between the two abelian groups.
It is convenient to work in a basis in which the gauge fields are canonically normalized. This can be achieved by a rotation [263, 264]

$$\begin{pmatrix} \tilde{B}^\mu \\ \tilde{X}^\mu \end{pmatrix} = \begin{pmatrix} 1 & -\epsilon/\sqrt{(1-\epsilon^2)} \\ 0 & 1/\sqrt{(1-\epsilon^2)} \end{pmatrix} \begin{pmatrix} V^\mu \\ D^\mu \end{pmatrix}, \tag{5.124}$$

which parameterizes the gauge interaction vertices of Lagrangian (5.123) in terms of a "visible" gauge boson V^μ and a "dark" gauge boson D^μ:

$$(Q_Y\,, Q_{B-L}) \begin{pmatrix} g_Y & 0 \\ 0 & g_{B-L} \end{pmatrix} \begin{pmatrix} \tilde{B}^\mu \\ \tilde{X}^\mu \end{pmatrix} \;\rightarrow\; (Q_Y\,, Q_{B-L}) \begin{pmatrix} g_Y & g_\epsilon \\ 0 & g_d \end{pmatrix} \begin{pmatrix} V^\mu \\ D^\mu \end{pmatrix}. \tag{5.125}$$

The elements g_Y, g_d, and g_ϵ are related to the original couplings as

$$g_Y \to g_Y, \quad g_d = \frac{g_{B-L}}{\sqrt{1-\epsilon^2}}, \quad g_\epsilon = -\frac{\epsilon\, g_Y}{\sqrt{1-\epsilon^2}}. \tag{5.126}$$

The value of the gravitational parameter f_g is determined by equating the 1-loop RG flow of the hypercharge gauge coupling onto the low-scale $\overline{\text{MS}}$ value in the SM, in agreement with assumption 1 in Sec. 5.3.1. We take $g_Y^{\text{SM},\overline{\text{MS}}}(M_t = 173.1\,\text{GeV}) = 0.36$ [30]. We extract f_y by equating the 1-loop flow of the top Yukawa coupling to its $\overline{\text{MS}}$ value, $y_t^{\text{SM},\overline{\text{MS}}}(M_t) = 0.95$ [271], in agreement with assumption 2 in Sec. 5.3.1. We obtain

$$f_g\,(1\text{ loop}) = 0.0097\,, \quad f_y\,(1\text{ loop}) = 0.0020\,, \tag{5.127}$$

which lead to the following predictions at the irrelevant fixed point:

$$g_Y^*\,(1\text{ loop}) = 0.4734\,, \qquad g_d^*\,(1\text{ loop}) = 0.4420\,, \qquad g_\epsilon^*\,(1\text{ loop}) = -0.3450\,, \tag{5.128}$$

$$y_t^*\,(1\text{ loop}) = 0.2901\,, \qquad y_\nu^*\,(1\text{ loop}) = 0.5398\,, \qquad y_N^*\,(1\text{ loop}) = 0.3868\,. \tag{5.129}$$

The subsequent low-scale predictions for the dark sector coupling and kinetic mixing, at the scale M_t, are

$$g_d\,(M_t, 1\text{ loop}) = 0.3343\,, \qquad g_\epsilon\,(M_t, 1\text{ loop}) = -0.2609\,, \tag{5.130}$$

$$y_\nu\,(M_t, 1\text{ loop}) = 0.4790\,, \qquad y_N\,(M_t, 1\text{ loop}) = 0.3392\,. \tag{5.131}$$

For practicality reasons, we choose to present the low-scale predictions at the EWSB scale as reference. In a realistic neutrino-mass model one should decouple the NP at the scale of the vev of the scalar field S. Note, however, that the dimensionful parameters of the Lagrangian are canonically relevant and as such they do not emerge as predictions of the fixed-point analysis.

In Fig. 5.6(a) we show for illustration the RG flow of the three gauge couplings from their UV fixed point, cf. 5.128, down to the EWSB scale, cf. 5.130. Gravity decouples at the scale $M_{\text{Pl}} = 10^{19}$ GeV, marked as a vertical gray line. The RG flow of the three Yukawa couplings is presented in Fig. 5.6(b). Note the deviation of y_t from its UV fixed-point value, due to the presence of relevant directions associated with the gauge couplings g_3 and g_2.

5.3.2.2 Leptoquark S_3

The SM is extended in this case by a complex scalar that carries both lepton and baryon number [272, 273]. Its $\text{SU}(3)_c\times\text{SU}(2)_L\times\text{U}(1)_Y$ quantum numbers are

$$S_3 : (\bar{\mathbf{3}}, \mathbf{3}, 1/3)\,. \tag{5.132}$$

Following the notation of Ref. [196], we introduce the Yukawa-type interaction of S_3 with SM fermions as follows

$$\mathcal{L} \ni -Y_{\text{LQ}}\, Q^T \epsilon S_3\, L + \text{H.c.}\,, \tag{5.133}$$

where, again, spinor and SU(2) indices are contracted trivially, Q and L are the SM quark and lepton doublets, respectively, and Y_{LQ} is a 3-by-3 matrix in flavor space. For simplicity we shall focus only on the 3rd generation, denoting $y_{\text{LQ}} \equiv (Y_{\text{LQ}})_{33}$.

As before, the gravitational parameters f_g and f_y are determined by equating the 1-loop RG flow of the hypercharge gauge coupling and the top Yukawa coupling onto their low-scale $\overline{\text{MS}}$ values. The resulting gravitational parameters read

$$f_g\,(1\text{ loop}) = 0.0106\,, \qquad f_y\,(1\text{ loop}) = -0.0004\,, \tag{5.134}$$

leading to the following fixed-point values for the irrelevant couplings:

$$g_Y^*\,(1\text{ loop}) = 0.4823\,, \qquad y_t^*\,(1\text{ loop}) = 0.2340\,, \qquad y_{\text{LQ}}^*\,(1\text{ loop}) = 0.1132\,. \tag{5.135}$$

Finally, the low-scale prediction for the LQ coupling y_{LQ} reads

$$y_{\text{LQ}}\,(M_t, 1\text{ loop}) = 0.4270\,. \tag{5.136}$$

5.3.3 Estimation of the uncertainties

The predictions from AS for a specific NP model find perhaps their greatest usefulness when deriving phenomenological bounds on the relevant parameters of the model in question (*e.g.* its masses) [194, 197, 201] or, alternatively, when confronting the model with an experimental anomaly [2, 110, 196]. In particle physics phenomenology it is natural to interpret a new experimental bound (or, in alternative, a deviation from the SM emerging in the precision measurement of a certain process) as an estimate of the NP contribution to the Wilson coefficient of a higher-dimensional operator in the EFT. While the size of a Wilson coefficient generally points to a UV scale of interest, this corresponds to the actual mass of the particles of the UV completion only if the latter generate the Wilson coefficient at the tree level with couplings of order one. In practice the picture is more obscure, due to our complete ignorance of the actual type and strength of UV interactions.
More specifically, the generic EFT matching of a Wilson coefficient $\mathcal{C}_{\text{NP}}$ to a UV Lagrangian with couplings c_i of unknown strength depends possibly on several factors:

$$\frac{\mathcal{C}_{\text{NP}}}{\Lambda^n} \approx \frac{c_i c_j}{m_{\text{NP}}^n} \times \text{loop factor} \times \frac{c_k v_H}{m_{NP}} \times \ldots\,, \tag{5.137}$$

where Λ sets the scale of the UV physics that is integrated out and the last factor, containing the Higgs vev v_H, is meant to indicate effects that depend explicitly on the breaking of electroweak symmetry, *e.g.*, the generation of a neutrino mass in see-saw models, or the presence of a chiral enhancement in dipole operators. As was discussed in Sec. 5.3.2, the assumption of AS can lead to predictions for the dimensionless parameters of the Lagrangian that are not constrained otherwise. Thus, once the l.h.s. of 5.137 is determined following a measurement at the low scale, m_{NP} remains the only unknown variable on the r.h.s., which can be extracted straightforwardly. Following this procedure, under the three assumptions of Sec. 5.3.1, in Ref. [196] a fairly precise prediction for the mass of the S_3 LQ was obtained from a global fit of the Wilson coefficients of the Weak EFT; in Ref. [110] predictions for the mass of two vector-like fermions were obtained from the measurement of leptonic dipole operators; and in Ref. [197] a prediction for the Majorana mass of sterile neutrinos was obtained from the see-saw mechanism.
In this context, pinning down the theoretical uncertainties that mar the predicted couplings c_i, which are then fed into 5.137 to obtain m_{NP}, becomes of crucial importance. Ideally, the error should remain significantly below the experimental uncertainty on the determination of the Wilson coefficient $\mathcal{C}_{\text{NP}}$. To get a quantitative sense of the precision we expect from the

asymptotically safe prediction, we point out that observing, for example, an hypothetical deviation from the SM at the $p\,\sigma$ level in some experiment, would induce a relative uncertainty on a related Wilson coefficient $\mathcal{C}_{\rm NP}$ around its central value, at the level of

$$\frac{\delta\mathcal{C}_{\rm NP}}{\mathcal{C}_{\rm NP}} \approx \frac{1}{p}. \tag{5.138}$$

Thus, in order for this approach to make sense, we expect the theoretical uncertainty on the coupling prediction to remain below the few percent level.

5.3.3.1 Impact of higher-order corrections to the beta functions

In this subsection, we describe how the predictions we obtained in Secs. 5.3.2.1 and 5.3.2.2 are modified when we drop the first approximation listed in Sec. 5.3.1. In other words, we consider the DREG beta functions in the matter sector at perturbation orders higher than 1. Note, however, that assumptions 1, 2, and 3 in Sec. 5.3.1 must hold throughout this analysis.

Comment on threshold corrections Since we impose initial conditions on the solutions of 2-loop RGEs for the SM couplings, consistency requires that we include threshold corrections at the 1-loop order. Such corrections would also reduce the uncertainty associated with the unphysical matching scale.
In the case of an unbroken gauge symmetry, a generic expression for threshold correction exists. For example, in the S_3 LQ model the matching condition for g_3 yields (see for example [274])

$$g_3^{\rm NP} = g_3^{\rm SM} - \frac{g_3^3}{(4\pi)^2}\frac{1}{6}\left(\ln\frac{m_{\phi_{1/3}}}{\mu} + \ln\frac{m_{\phi_{4/3}}}{\mu} + \ln\frac{m_{\phi_{-2/3}}}{\mu}\right). \tag{5.139}$$

Assuming, as we do in this work, that the matching scale is set to $\mu = M_t$, this correction is small even for leptoquarks with masses of a few TeV. If, for example, $m_{\phi_{1/3}} = m_{\phi_{4/3}} = m_{\phi_{-2/3}} = 2$ TeV, the relative shift due to 5.139 is smaller than 1%. In the case of a broken gauge symmetry the expression of threshold corrections is more involved, but the final result is similar to 5.139 in its analytical form, being a sum of terms involving logs of the NP particle masses. Therefore, as long as the NP scale is not much different from the matching scale, threshold corrections remain small.
Matching conditions for the SM Yukawa couplings are obtained by matching the SM fermion masses, which are measured directly. For example, for the top Yukawa coupling one obtains [274]

$$y_t^{\rm NP} = \frac{g_2^{\rm NP} M_t}{\sqrt{2}M_W}\left(1 - \frac{\delta M_W}{M_W} + \frac{\delta M_t}{M_t}\right), \tag{5.140}$$

where M_W is the measured mass of the W boson and δ denotes the finite part of the full self energy. To quantify the impact of threshold corrections on y_t we have created an S_3 LQ model in `FlexibleSUSY` [107, 265, 275–279]. For a parameter point with $m^2_{S_3} = 1$ TeV, $\lambda_{S_3} = \lambda_{HS_3} = 0.1$ (see Eq. (5.178) in Appendix 5.D for the definition of those parameters) and $y_{\rm LQ} = 1$ we obtain $y_t^{\rm NP} = 0.92$, as opposed to 0.95 which is the value we use in this work.
The correct matching of the NP theory to the SM is required to make precise statements about the values of its parameters. This however depends on the mass spectrum of the model and possibly on mixing matrices and cannot be done without discussing also the dimensionful parameters of the matter theory, which are canonically relevant at the fixed point and therefore cannot be predicted. Since none of the statements made in this work depend on the treatment of threshold corrections, we do not lose generality by neglecting

them. In the numerical analysis we will therefore equate the NP equivalents of the SM parameters to their SM values (as was done in Sec. 5.3.2) also at the 2-loop level.

Gauge couplings Given assumptions 1 and 3 in Sec. 5.3.1, one can estimate the numerical value of the gravitational correction f_g at the fixed point. Once this is extracted, the property of universality in gravitational interactions can be invoked to find the irrelevant fixed points of other gauge couplings. As was discussed above, the non-abelian gauge couplings remain relevant, so that we can limit our analysis to the generic system of abelian couplings. In agreement with the $B-L$ example, let us consider $\mathrm{U}(1)_Y\times\mathrm{U}(1)_{B-L}$. It is straightforward to extend our conclusions to any pair of abelian symmetries. As can be seen in Appendix 5.D, the pertinent RGEs take the following parametric form, common to all models with abelian mixing:

$$\frac{dg_Y}{dt} = \frac{1}{16\pi^2}\left(b_Y+\Pi^{(Y)}_{n\geq 2}\right)g_Y^3 - f_g\, g_Y \tag{5.141}$$

$$\frac{dg_d}{dt} = \frac{1}{16\pi^2}\left[\left(b_Y+\Pi^{(Y)}_{n\geq 2}\right)g_d g_\epsilon^2+\left(b_d+\Pi^{(d)}_{n\geq 2}\right)g_d^3+\left(b_\epsilon+\Pi^{(\epsilon)}_{n\geq 2}\right)g_d^2 g_\epsilon\right] - f_g\, g_d \tag{5.142}$$

$$\begin{aligned}\frac{dg_\epsilon}{dt} = &\frac{1}{16\pi^2}\left[\left(b_Y+\Pi^{(Y)}_{n\geq 2}\right)\left(g_\epsilon^3+2g_Y^2 g_\epsilon\right)+\left(b_d+\Pi^{(d)}_{n\geq 2}\right)g_d^2 g_\epsilon\right.\\ &\left.+\left(b_\epsilon+\Pi^{(\epsilon)}_{n\geq 2}\right)\left(g_Y^2 g_d+g_d g_\epsilon^2\right)\right] - f_g\, g_\epsilon\,.\end{aligned} \tag{5.143}$$

Equations (5.141)–(5.143) are given in terms of the one-loop coefficients b_Y, b_d, and b_ϵ, and generic n-loop contributions,

$$\Pi^{(i)}_{n\geq 2} = \frac{1}{16\pi^2}\sum_{l,k}\alpha^{(i)}_{lk}c_l\,c_k+\sum_{n>2}\sum_{l_1\ldots l_{n-1}}\frac{1}{(16\pi^2)^{n-1}}\alpha^{(i)}_{l_1\ldots l_{n-1}}c^2_{l_1}\ldots c^2_{l_{n-1}}\,, \tag{5.144}$$

expressed in terms of loop coefficients $\alpha^{(i)}_{l_1\ldots l_{n-1}}$, with $i=Y,d,\epsilon$. The c_l parameters indicate the gauge and Yukawa couplings of the theory (at perturbation order $n=2$), or the gauge, Yukawa, and (quartic)$^{1/2}$ couplings (at order $n>2$). We require that Eqs. (5.141)–(5.143) develop a zero above the Planck scale.

Assuming for the moment that the fixed point for the gauge couplings is developed sharply at a $M_{\mathrm{Pl}}=10^{19}$ GeV, one can express the value of f_g in terms of the (known) $\mathrm{U}(1)_Y$ trans-Planckian fixed point g_Y^*, with an accuracy that increases at each successive order,

$$f_g(n\text{ loops}) \approx \frac{g_Y^{*2}(n\text{ loops})}{16\pi^2}\left(b_Y+\Pi^{(Y)*}_{n\geq 2}\right)\,, \tag{5.145}$$

where the asterisk refers to all couplings being set at their UV fixed-point value. The predicted ratios of the gauge couplings do not depend explicitly on the value of f_g. One can define

$$r^*_{g,d}(n\text{ loops}) \equiv \frac{g_d^*}{g_Y^*}(n\text{ loops}) \approx \frac{2\tilde{b}_Y}{\sqrt{4\tilde{b}_Y\tilde{b}_d-\tilde{b}_\epsilon^2}}\,, \tag{5.146}$$

$$r^*_{g,\epsilon}(n\text{ loops}) \equiv \frac{g_\epsilon^*}{g_Y^*}(n\text{ loops}) \approx -\frac{\tilde{b}_\epsilon}{\sqrt{4\tilde{b}_Y\tilde{b}_d-\tilde{b}_\epsilon^2}}\,, \tag{5.147}$$

where we have adopted a simplified notation,

$$\tilde{b}_i \equiv b_i+\Pi^{(i)*}_{n\geq 2}\,. \tag{5.148}$$

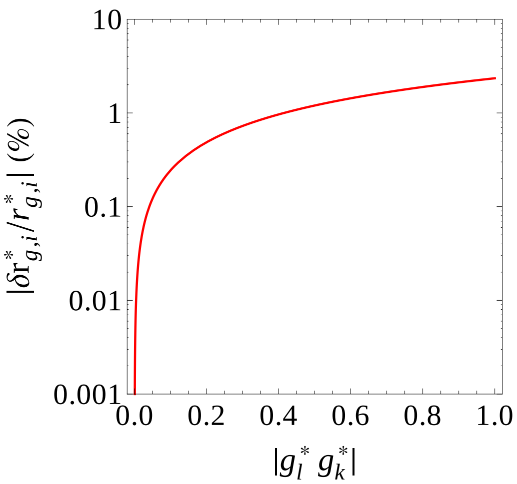

FIGURE 5.7: Estimated percent uncertainty on the predicted fixed-point ratios of abelian gauge couplings $|\delta r^*_{g,i}/r^*_{g,i}|$ in the $B-L$ model due to missing higher-loop contributions. The uncertainty is given as a function of the product of abelian gauge couplings at the fixed point.

In order to obtain some quantitative estimates, let us retain for simplicity only the 2-loop corrections, $\Pi_2^{(i)}$, and quantify the uncertainty on the ratios $r^*_{g,i(=d,\epsilon)}$ by calculating

$$\frac{\delta r^*_{g,i}}{r^*_{g,i}} = \frac{r^*_{g,i}(2\text{ loops}) - r^*_{g,i}(1\text{ loop})}{r^*_{g,i}(1\text{ loop})}\,. \tag{5.149}$$

In the $B-L$ model, the 1-loop coefficients read $b_Y = 41/6$, $b_d = 12$, $b_\epsilon = 32/3$. In general, the dominant coefficients $\alpha^{(i)}_{lk}$ in 5.144 are by far those corresponding to the product of two gauge couplings. Retaining, thus, only the abelian gauge-coupling contributions in the 2-loop RGEs of Appendix 5.D, and assuming in the first approximation that all gauge couplings acquire the same fixed-point value, one can factor out the sums of coefficients $\alpha^{(i)}_{lk}$ and compute them separately keeping track of the relative coupling signs. The percent uncertainty is presented in Fig. 5.7. It is very similar in the two cases $i = d, \epsilon$. It is shown as a function of the generic product of abelian gauge couplings $|g^*_l\, g^*_k|$ at the fixed point. We note that the error remains at the percent level, far below the uncertainty typically associated with Wilson coefficients of higher-dimensional operators of the EFT, see 5.138. Similar levels of uncertainty apply to the UV predictions of gauge couplings in other models with abelian gauge mixing, *e.g.*, those analyzed in Ref. [2].
The precise numerical calculation of the 2-loop uncertainties for the $B-L$ model is reported in Table 5.5. One obtains $\delta r^*_{g,d}/r^*_{g,d} = -0.41\%$ and $\delta r^*_{g,\epsilon}/r^*_{g,\epsilon} = -0.44\%$.

Yukawa couplings The discussion can be repeated with small modifications for the Yukawa couplings. Let us parameterize the full set of Yukawa-coupling RGEs of a generic SM+NP theory in the following way:

$$\frac{dy_r}{dt} = \frac{y_r}{16\pi^2}\left(\sum_j a^{(r)}_j y_j^2 - \sum_{l,k} a'^{(r)}_{lk} g_l g_k + \sum_{n\geq 2}\widetilde{\Pi}^{(r)}_n\right) + \sum_{m,p,q\neq r}\frac{y_m y_p y_q}{16\pi^2}\left(a''_{mpq} + \sum_{n\geq 2}\tilde{\Delta}^{(mpq)}_n\right) - f_y y_r, \tag{5.150}$$

where $y_{r(j)=1,2,\ldots}$ label the set of Yukawa couplings in the Lagrangian and $g_{l(k)}$ label the gauge couplings of the theory. In 5.150 we have defined the generic *multiplicative* n-loop contribution as

$$\widetilde{\Pi}_n^{(r)} \equiv \frac{1}{(16\pi^2)^{n-1}} \sum_{l_1 l_2 \dots l_{2n}} \alpha'^{(r)}_{l_1 l_2 \dots l_{2n}} c_{l_1} c_{l_2} \dots c_{l_{2n}} \,, \tag{5.151}$$

and the generic *additive* n-loop piece as

$$\tilde{\Delta}_n^{(mpq)} \equiv \frac{1}{(16\pi^2)^{n-1}} \sum_{l_1 \dots l_{2n-n}} \alpha''^{(mpq)}_{l_1 \dots l_{2n-n}} c_{l_1} \dots c_{l_{2n-2}} \,, \tag{5.152}$$

in terms of n-loop coefficients $\alpha'^{(r)}_{l_1 \dots l_{2n}}$, $\alpha''^{(mpq)}_{l_1 \dots l_{2n-2}}$, and of all gauge, Yukawa, and (quartic)$^{1/2}$ couplings c_{l_i} entering the Yukawa RGEs at order $n \geq 2$.
Neglecting for the moment the additive part of the beta functions, let us assume we solve the system (5.150) when all the beta functions are equal to zero. Repeating the steps that led to the 1-loop results in Sec. 5.3.2, we express the unknown gravitational contribution f_y in terms of one known "reference" fixed-point Yukawa coupling y_1^*, which is in general the top quark's.[3]
Let us retain, for simplicity, only the 2-loop correction. One gets

$$f_y(2\,\text{loops}) \approx \frac{1}{16\pi^2}\left[y_1^{*2}(2\,\text{loops}) \times F_0\left(a_j^{(r)}\right) + G_0\left(\sum_{l,k} a'^{(r)}_{lk} g_l^* g_k^* (2\,\text{loops})\,;\, a^{(r)}_{j\neq 1}\right) \right.$$
$$\left. + H_0\left(\widetilde{\Pi}_2^{(r)*}\,;\, a^{(r)}_{j\neq 1}\right)\right] \,, \tag{5.153}$$

where F_0, G_0, and H_0 are rational functions of the $a_j^{(r)}$ coefficients, with the latter two being linear in $\sum_{lk} a'^{(r)}_{lk} g_l^* g_k^*$ and $\widetilde{\Pi}_2^{(r)*}$, respectively. Their analytic form is model-dependent and is not needed for the discussion. Note that the reference fixed-point value $y_1^*(2\,\text{loops})$ is obtained by equating the 2-loop RGE flow to the $\overline{\text{MS}}$ values of the couplings at the EWSB scale. As such, it can be significantly shifted with respect to $y_1^*(1\,\text{loop})$, mostly due to the contributions of relevant parameters like g_3 and g_2 to the 2-loops RGEs.
Let us thus define the shift at the fixed point due to relevant parameters in the flow,

$$y_1^{*2}(2\,\text{loops}) = y_1^{*2}(1\,\text{loop}) + \delta y_1^{*2} \,, \tag{5.154}$$

and derive the parametric expression for the fixed point of a second Yukawa coupling of the irrelevant type. This is our prediction, which we indicate as y_2^*. Its value must be a function of f_y. By using 5.153 we trade f_y for y_1^* and plug into the fixed-point solution for y_2^*:

$$y_2^*(2\,\text{loops}) \approx \left[F_1\left(a_j^{(r)}\right)\left(y_1^{*2}(1\,\text{loop}) + \delta y_1^{*2}\right) + G_1\left(\sum_{l,k} a'^{(r)}_{lk} g_l^* g_k^*\,;\, a^{(r)}_{j\neq 1}\right) \right.$$
$$\left. + H_1\left(\widetilde{\Pi}_2^{(r)*}\,;\, a^{(r)}_{j\neq 1}\right)\right]^{1/2} \,, \tag{5.155}$$

where the F_1, G_1, are some other rational functions of coefficients of order one, and the H_1 function carries the 2-loop terms. Using 5.151, one can see that the higher-loop correction H_1 only depends, up to order-one coefficients, on sums of fixed-point products $c^*_{l_1} c^*_{l_2} c^*_{l_3} c^*_{l_4}$. It is thus very similar in size for all the predicted Yukawa couplings – y_2^*, y_3^*, etc. The shift uncertainty δy_1^{*2} also enters in the same way in all predicted Yukawa couplings. However, the relative uncertainties affecting the predictions – $\delta y_2^*/y_2^*$, $\delta y_3^*/y_3^*$, etc. – differ for the different Yukawa couplings because they are very sensitive to the actual size of the coupling itself.

[3] Because of assumption 2 in Sec.5.3.1, in order to estimate f_y all one needs is a fixed point with an irrelevant SM Yukawa coupling. Which fixed point works best for the phenomenology is decided on a case-by-case basis.

If one, for example, had obtained at 1 loop $y_2^* \ll y_1^*, g_k^*$, that would have implied a precise cancellation (fine tuning) between $F_1(a_j^{(r)})\, y_1^{*2}$ and the G_1 function. As a consequence, the uncertainty due to δy_1^{*2} and H_1 on the final result would grow. Conversely, obtaining $y_2^* \approx y_1^*, g_k^*$ at 1 loop would imply that such prediction can be trusted to a very good approximation.

For a quantitative example, let us choose a fixed point with one irrelevant gauge coupling ($l = k = 1$) and two Yukawa couplings ($r, j = 1, 2$). Equation (5.155) becomes

$$y_2^*(2\,\text{loops}) \approx \left[\frac{a_1^{(2)} - a_1^{(1)}}{a_2^{(1)} - a_2^{(2)}} \left(y_1^{*2}(1\,\text{loop}) + \delta y_1^{*2} \right) + \frac{\left(a_{11}^{\prime(1)} - a_{11}^{\prime(2)} \right) g_1^{*2} + \widetilde{\Pi}_2^{(2)*} - \widetilde{\Pi}_2^{(1)*}}{a_2^{(1)} - a_2^{(2)}} \right]^{1/2} . \tag{5.156}$$

This is the case, for example, of the S_3 LQ. With respect to the notation of Sec. 5.3.2.2, here $g_1 \equiv g_Y$, $y_1 \equiv y_t$, and $y_2 \equiv y_{\text{LQ}}$. All other couplings are chosen relevant and zero at the fixed point. The 1-loop coefficients in this model can be found in Appendix 5.D and read $a_1^{(1)} = 9/2$, $a_2^{(1)} = 3/2$, $a_{11}^{\prime(1)} = 17/12$, $a_1^{(2)} = 1/2$, $a_2^{(2)} = 8$, $a_{11}^{\prime(2)} = 5/6$.

The shift in the top Yukawa fixed point can be computed numerically: $\delta y_1^{*2} \approx -9 \times 10^{-3}$. This should be summed to the explicit 2-loop contribution to the beta functions, $\widetilde{\Pi}_2^{(2)*} - \widetilde{\Pi}_2^{(1)*}$, which can be obtained from Appendix 5.D. The latter turns out to be approximately one order of magnitude smaller than δy_1^{*2} when the quartic couplings of the scalar potential are neglected. If the quartic couplings are assumed to be of order one, we get instead $\widetilde{\Pi}_2^{(2)*} - \widetilde{\Pi}_2^{(1)*} \approx -3 \times 10^{-2}$. The first of these determinations leads to the largest uncertainty on the prediction. By plugging the 1-loop coefficients into 5.156, together with the 1-loop fixed-point values given in Sec. 5.3.2.2, one can easily compute the percent deviation,

$$\frac{\delta y_2^*}{y_2^*} = \frac{y_2^*(2\,\text{loops}) - y_2^*(1\,\text{loop})}{y_2^*(1\,\text{loop})} \approx -25\% \,. \tag{5.157}$$

We note that in this example the uncertainty is not negligible. This was expected, since at 1 loop one finds $y_2^* < y_1^*, g_1^*$, see the values in Sec. 5.3.2.2. In the $B - L$ model, on the other hand, one finds $y_2^*, y_3^* \approx y_1^*, g_{k=1,2,3}^*$, and the uncertainty is smaller, cf. Table 5.5.

The discussion can be extended, finally, to cases in which an additive contribution to the Yukawa coupling RGEs – the fourth and fifth addends in 5.150 – is present. It is not difficult to realize that in this case the gauge-Yukawa system only admits a set of real solutions if all the fixed-point values y_r^* are of comparable size. The fixed points can have naturally the size of the gauge couplings, in which case they are not very sensitive to the 2-loop corrections, which are highly suppressed. The fixed points, on the other hand, could also be very small, due to an accidental (fine tuned) cancellation of the terms with $\sum_{l,k} a'_{lk} g_l g_k$ and f_y in 5.150. In that case, 2-loop contributions become important.

Numerical examples We provide quantitative estimates of the higher-loop effects discussed in this section in the two NP models introduced in Sec. 5.3.2.

In Table 5.5 we present the 2-loop determinations of the gravity parameters f_g and f_y, the fixed-point values of the model couplings, as well as their percent uncertainties at the fixed point and at the low-energy scale, $\mu = M_t$. The latter are derived under the assumption that the low-scale value of the reference SM coupling ($g_Y(M_t)$ in the $B - L$ model, $y_t(M_t)$ in the Yukawa sector of the $B - L$ model and in the S_3 LQ model) is not varied when performing the fixed point analysis at 2 loops.

$B-L$	f_g	g_Y^*	g_d^*	g_ϵ^*	$\delta g_Y^*/g_Y^*$	$\delta g_d^*/g_d^*$	$\delta g_\epsilon^*/g_\epsilon^*$	$\delta g_d/g_d(M_t)$	$\delta g_\epsilon/g_\epsilon(M_t)$
	0.0098	0.4748	0.4415	−0.3445	0.3%	−0.1%	−0.1%	−0.4%	−0.5%
	f_y	y_t^*	y_ν^*	y_N^*	$\delta y_t^*/y_t^*$	$\delta y_\nu^*/y_\nu^*$	$\delta y_N^*/y_N^*$	$\delta y_\nu/y_\nu(M_t)$	$\delta y_N/y_N(M_t)$
	0.0016	0.2727	0.5220	0.3813	−6.0%	−3.3%	−1.4%	−1.4%	−0.8%
S_3 LQ	f_y	y_t^*	$y_{\rm LQ}^*$		$\delta y_t^*/y_t^*$	$\delta y_{\rm LQ}^*/y_{\rm LQ}^*$		$\delta y_{\rm LQ}/y_{\rm LQ}(M_t)$	
	−0.0007	0.2133	0.0855		−8.8%	−24.5%		−14.3%	

TABLE 5.5: 2-loop determination of the gravity parameters f_g and f_y, fixed-point values of the reference and the to-be-predicted couplings, percent uncertainty at the fixed point, and percent uncertainty at the low scale for the models introduced in Sec. 5.3.2. The uncertainties are defined w.r.t. the 1-loop results of Sec. 5.3.2, cf. 5.157.

The results shown in Table 5.5 confirm our discussion. The impact of higher-order corrections on the fixed-point value of a coupling is almost negligible for the gauge couplings, while in the Yukawa sector it depends on the relative size of the reference and the predicted couplings. In the $B-L$ model, the fixed-point values of all three couplings are comparable in size. Hence, the impact of 2-loop corrections is small and the uncertainty on the NP couplings is of the order of a few percent. Conversely, in the S_3 LQ model, $y_{\rm LQ}$ is smaller by a factor of 2 than y_t. The impact of the 2-loop corrections is then more pronounced, and the resulting fixed-point uncertainty increases.
Closer inspection of the last column of Table 5.5 reveals that the low-scale uncertainties of the NP Yukawa couplings are smaller than those at the fixed-point. This is not a coincidence and it is intrinsically related to modifications of the RG flow due to higher-order corrections. To get a better understanding of the underlying mechanism, we show in Fig. 5.8(a) the 1-loop (dashed) and 2-loop (solid) running of y_t (red), y_ν (blue) and y_N (green) in the $B-L$ model. The analogous flow of the top (red) and LQ (blue) Yukawa couplings of the S_3 model is presented in Fig. 5.8(b). Due to the negative contribution of the gauge coupling g_3 to the beta functions of the Yukawa couplings of particles carrying the color charge, the running value of y_t at 2 loops is generically smaller than at 1 loop. As was discussed below 5.155, it follows that the fixed-point values of the NP Yukawa couplings also tend to be shifted downwards. The effect is stronger for the couplings that depend on y_t already at 1 loop (y_ν and $y_{\rm LQ}$).
On the other hand, since the same reference low-scale value $y_t(M_t)$ is used in the fixed-point analysis at any loop order, the RG trajectories of the NP Yukawa couplings have the tendency to focus towards their 1-loop value in the infrared, which results in a reduction of the uncertainty with respect to the prediction at the fixed point. A generic rule of thumb thus applies: the uncertainty in the determination of the fixed-point value of a NP Yukawa coupling provides an upper bound on the uncertainty of the same prediction at the low scale.

5.3.3.2 Dependence on the position of the Planck scale

In this subsection, we drop the second of the approximations listed in Sec. 5.3.1, *i.e.*, we consider what happens if gravity decouples from the matter RGEs sharply at a scale that differs from 10^{19} GeV by a few orders of magnitude.

Gauge couplings When assessing the impact of the Planck-scale position on the predictions for gauge couplings one should note that an uncertainty on the position of the Planck scale is effectively equivalent to an uncertainty on the fixed-point value of the hypercharge gauge coupling, g_Y^*, and hence f_g. As a consequence of Eqs. (5.146) and (5.147) one can see

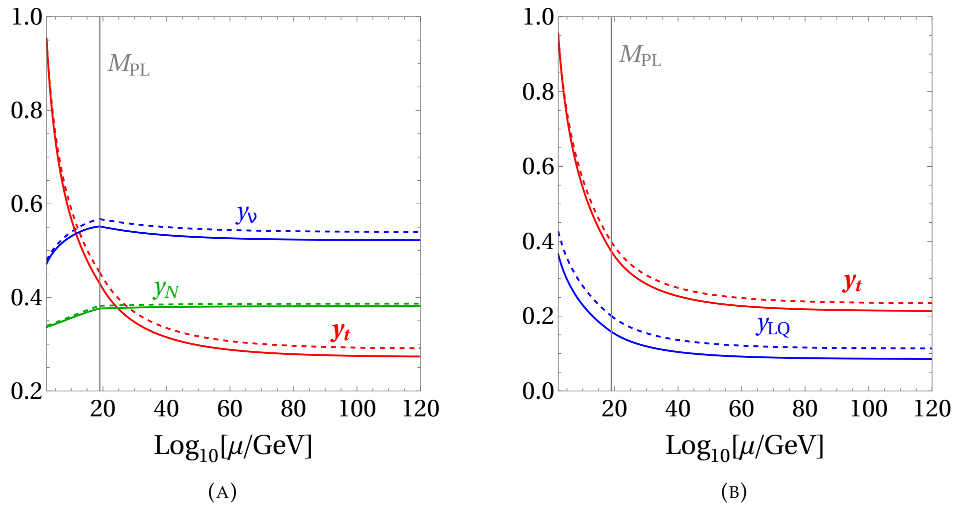

FIGURE 5.8: (a) RG flow of the top (red), Dirac neutrino (blue) and sterile neutrino (green) Yukawa couplings of the gauge $B-L$ model at the 1-loop (dashed) and 2-loop (solid) orders. The gray vertical line indicates the fixed position of the Planck scale, $M_{\rm Pl} = 10^{19}$ GeV. (b) Same as in (a), but for the top (red) and LQ (blue) Yukawa couplings of model S_3.

that moving the Planck scale back and forth does not affect the predicted ratios $r^*_{g,i}$ at the 1-loop order, as the f_g dependence cancels out. This feature is not preserved at higher orders in the perturbative expansion. However, the impact of the Planck scale position remains negligibly small, of $\mathcal{O}(0.01\%)$.

Yukawa couplings On the other hand, since 5.155 depends explicitly on the fixed-point values of the couplings, changing the position of the Planck scale will alter the prediction for the Yukawa couplings, as it changes the fixed-point values of the abelian gauge couplings, which we indicate collectively with $g^*_{k=1,2,...}$, and of the reference Yukawa coupling y^*_1.
Let us define, with slight abuse of notation, $r^*_{g,k} = g^*_k/y^*_1$, $r^*_{y,2} = y^*_2/y^*_1$, and the percent uncertainty

$$\frac{\delta r^*_{g(y),i}}{r^*_{g(y),i}} = \frac{r^*_{g(y),i}(M_{\rm Pl} \neq 10^{19}\,\text{GeV}) - r^*_{g(y),i}(M_{\rm Pl} = 10^{19}\,\text{GeV})}{r^*_{g(y),i}(M_{\rm Pl} = 10^{19}\,\text{GeV})}\,. \tag{5.158}$$

Neglecting for this discussion the 2-loop contribution, the percent uncertainty on the predicted Yukawa-coupling ratios propagates in 5.155 as

$$\frac{\delta r^*_{y,2}}{r^*_{y,2}} = \frac{1}{r^{*2}_{y,2}}\, G_1\left(\sum_{l,k} a'^{(r)}_{lk}\, r^*_{g,l} r^*_{g,k}\cdot\frac{1}{2}\left[\frac{\delta r^*_{g,l}}{r^*_{g,l}} + \frac{\delta r^*_{g,k}}{r^*_{g,k}}\right];\, a^{(r)}_{j\neq 1}\right)\,. \tag{5.159}$$

It is straightforward to re-frame the two cases described in Sec. 5.3.3.1 in light of 5.159. If the predicted Yukawa fixed point is of comparable size to the irrelevant gauge couplings, $r^*_{y,2} \approx r^*_{g,l(k)}$, the uncertainty is dominated by the shifting of the gauge coupling fixed point:

$$\left|\frac{\delta r^*_{y,2}}{r^*_{y,2}}\right| \approx \left|\frac{\delta r^*_{g,l(k)}}{r^*_{g,l(k)}}\right|\,. \tag{5.160}$$

$B-L$	f_g	g_Y^*	g_d^*	g_ϵ^*	$\delta g_Y^*/g_Y^*$	$\delta g_d^*/g_d^*$	$\delta g_\epsilon^*/g_\epsilon^*$	$\delta g_d/g_d(M_t)$	$\delta g_\epsilon/g_\epsilon(M_t)$
10^{20} GeV	0.0102	0.4843	0.4522	−0.3530	2.3%	2.3%	2.3%	0.0%	0.0%
10^{16} GeV	0.0086	0.4445	0.4151	−0.3240	−6.1%	−6.1%	−6.1%	0.0%	0.0%
	f_y	y_t^*	y_ν^*	y_N^*	$\delta y_t^*/y_t^*$	$\delta y_\nu^*/y_\nu^*$	$\delta y_N^*/y_N^*$	$\delta y_\nu/y_\nu(M_t)$	$\delta y_N/y_N(M_t)$
10^{20} GeV	0.0020	0.2914	0.5523	0.3927	0.4%	2.3%	1.5%	1.3%	0.3%
10^{16} GeV	0.0020	0.2869	0.5069	0.3715	−1.1%	−6.1%	−4.0%	−3.7%	−0.9%
S_3 **LQ**	f_y	y_t^*	$y_{\rm LQ}^*$		$\delta y_t^*/y_t^*$	$\delta y_{\rm LQ}^*/y_{\rm LQ}^*$		$\delta y_{\rm LQ}/y_{\rm LQ}(M_t)$	
10^{20} GeV	−0.0006	0.2309	0.1043		−1.3%	−7.8%		−5.1%	
10^{16} GeV	0.00002	0.2422	0.1337		3.5%	18.1%		10.1%	

TABLE 5.6: Impact of the position of the Planck scale on the determination of the gravity parameters f_g and f_y, fixed-point values of the reference and the to-be-predicted couplings, percent uncertainty at the fixed point, and percent uncertainty at the low scale for the models introduced in Sec. 5.3.2. The uncertainties are defined w.r.t. the 1-loop results of Sec. 5.3.2, cf. 5.158.

Conversely, if the predicted coupling is small, $r^*_{y,2} \ll r^*_{g,l(k)}$, the relative uncertainty can grow substantially and we lose control of the prediction,

$$\left|\frac{\delta r^*_{y,2}}{r^*_{y,2}}\right| \gg \left|\frac{\delta r^*_{g,l(k)}}{r^*_{g,l(k)}}\right| . \tag{5.161}$$

As a quantitative example, let us consider again the simple case of two Yukawa couplings, y_1^*, y_2^*, and one gauge coupling g_1^* (hypercharge), all irrelevant at the fixed point. Equation (5.159) becomes in this case

$$\frac{\delta r^*_{y,2}}{r^*_{y,2}} = \frac{r^{*2}_{g,1}}{r^{*2}_{y,2}} \cdot \frac{a'^{(1)}_{11} - a'^{(2)}_{11}}{a^{(1)}_2 - a^{(2)}_2} \cdot \frac{\delta r^*_{g,1}}{r^*_{g,1}} . \tag{5.162}$$

This is the case, *e.g.*, of the S_3 LQ model, whose 1-loop coefficients were given below 5.156. One can show numerically (1-loop RGEs will suffice) that an eventual shift in the value of the Planck scale will induce a variation in the fixed point values g_1^*, y_1^*, and, consequently, $r^*_{g,1} \equiv g_1^*/y_1^*$. For example, let us move the Planck scale to $M_{\rm Pl} = 10^{16}$ GeV in one case, and to $M_{\rm Pl} = 10^{20}$ GeV in another. This results in the changing of $g_1^* = g_Y^*$ from the value in 5.135 to 0.45 and 0.49, respectively. One finds $\delta r^*_{g,1}/r^*_{g,1}(10^{16}) \approx -10\%$ and $\delta r^*_{g,1}/r^*_{g,1}(10^{20}) \approx 4\%$. We can thus use 5.162 to predict $\delta r^*_{y,2}/r^*_{y,2} \approx -1.63 \times \delta r^*_{g,1}/r^*_{g,1}$, which agrees well with numerical derivations showing $\delta r^*_{y,2}/r^*_{y,2}(10^{16}) \approx 18.1\%$ and $\delta r^*_{y,2}/r^*_{y,2}(10^{20}) \approx -7.8\%$.

Numerical examples In Table 5.6 we summarize the findings of this subsection for our benchmark models. For two different values of the Planck scale, $M_{\rm Pl} = 10^{20}$ GeV and $M_{\rm Pl} = 10^{16}$ GeV, we show determinations of the gravity parameters f_g and f_y, the fixed-point values of the model couplings, their percent uncertainties at the fixed point and the uncertainties at the scale $\mu = M_t$. One can immediately see that all the fixed-point values of the gauge couplings are rescaled by the same amount, so the low-scale predictions are not altered.

The RG-invariance of the gauge-coupling ratios $r^*_{g,i}$ is made transparent in Fig. 5.9(a), where we show the difference in the flow of the gauge couplings of the $B-L$ model for different choices of the Planck scale. The shift in the flow of the Yukawa sector of the $B-L$ models is presented in Fig. 5.9(b), whereas the difference in the flow of the S_3 LQ model is shown in Fig. 5.9(c).

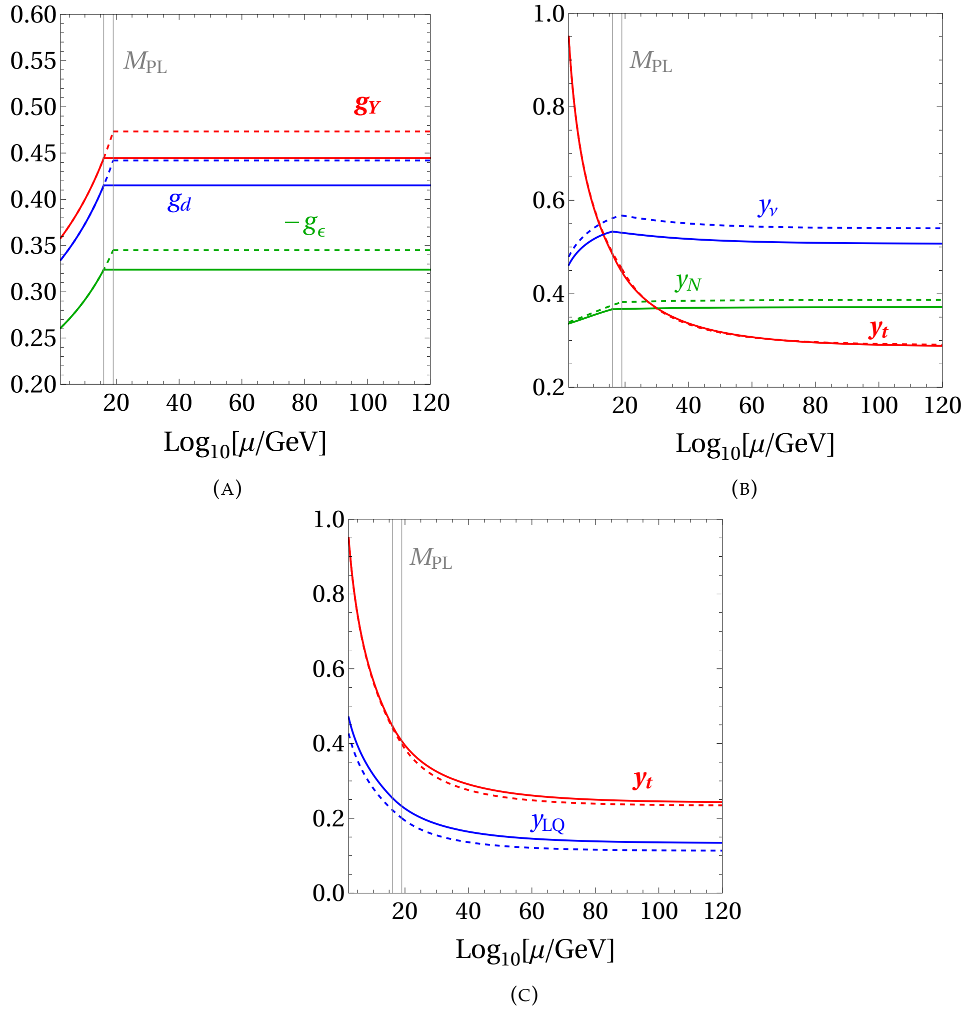

FIGURE 5.9: (a) 1-loop RG flow of the hypercharge (red), dark gauge (blue), and kinetic mixing (green) couplings of the $B-L$ model with the Planck scale set at 10^{19} GeV (solid) and 10^{16} GeV (dashed). The gray vertical line indicates the fixed positions of the Planck scale. (b) Same as in (a) for the top Yukawa (red), the Dirac neutrino Yukawa (blue) and sterile neutrino Yukawa coupling (green) of the $B-L$ model. (c) Same as in (a) for the top Yukawa (red) and LQ Yukawa coupling (blue) of the S_3 model.

As was discussed in Sec. 5.3.3.1, we observe focusing of the RG trajectories of the Yukawa couplings below the Planck scale. This indicates that the uncertainty calculated at the fixed point according to 5.159 is the maximal uncertainty that can be observed in a given NP model.

5.3.3.3 Scale-dependence of the gravitational correction

Finally, in this subsection we are going to drop the third of the approximations listed in Sec. 5.3.1, *i.e.*, we include in the analysis the scale dependence of the gravitational parameters. The actual functional form of f_g and f_y is subject to technical assumptions within the FRG framework. For example, in the Einstein-Hilbert truncation and in the Landau-gauge limit the relevant formulae can be found in Ref. [182]. In the following analysis we will avoid sticking to any particular form of $f_g(t)$ and $f_y(t)$ to be able to draw conclusions that remain as generic as possible.

Gauge couplings Consider 5.1, applied *e.g.* to the three (irrelevant) gauge couplings of the $B-L$ model, $i = Y, d, \epsilon$. Due to its universality, the explicit gravitational contribution to the matter beta function f_g entirely factors out of the running ratios:

$$\frac{d}{dt}\left(\frac{g_d}{g_Y}\right) = \frac{1}{g_Y}\left(\beta_d^{\text{matter}} - \frac{g_d}{g_Y}\beta_Y^{\text{matter}}\right)[t] \equiv F_d(g_Y(t), g_d(t), g_\epsilon(t), ...)\,, \quad (5.163)$$

$$\frac{d}{dt}\left(\frac{g_\epsilon}{g_Y}\right) = \frac{1}{g_Y}\left(\beta_\epsilon^{\text{matter}} - \frac{g_\epsilon}{g_Y}\beta_Y^{\text{matter}}\right)[t] \equiv F_\epsilon(g_Y(t), g_d(t), g_\epsilon(t), ...)\,, \quad (5.164)$$

where the matter beta functions β_i^{matter} are given in parametric form in Eqs. (5.141)–(5.143) and we have formally defined slope functions F_d and F_ϵ which do not depend on f_g. We are going to show that the 1-loop ratios g_d/g_Y and g_ϵ/g_Y are exact invariants of the RG flow, whereas, at order $n \geq 2$, RG invariance is respected up to a very good approximation.
To understand the underlying mechanism, let us apply the definition of total derivative to 5.163 and focus on a sequence of infinitesimal scale intervals, ... $t_2 < t_1 < t_0$, with the system lying at the fixed point at t_0. Moving backwards in t, one gets

$$\frac{g_d(t_1)}{g_Y(t_1)} = r^*_{g,d} + (t_1 - t_0)F_d(g_Y^*, g_d^*, g_\epsilon^*, ...) \quad (5.165)$$

$$\frac{g_d(t_2)}{g_Y(t_2)} = \frac{g_d(t_1)}{g_Y(t_1)} + (t_2 - t_1)F_d(g_Y(t_1), g_d(t_1), g_\epsilon(t_1), ...) \quad (5.166)$$

$$\frac{g_d(t_3)}{g_Y(t_3)} \quad ...$$

where $r^*_{g,d}$ was defined in 5.146 for REGs at arbitrary loop order. The same steps can be repeated for 5.164. One can check, by directly imposing boundary condition (5.146) into 5.163 at t_0, that F_d vanishes at the fixed point: $F_d(g_Y^*, ...) = 0$. Equivalently, one can show that $F_\epsilon(g_Y^*, ...) = 0$. Thus, $g_d(t_1)/g_Y(t_1) = r^*_{g,d}$ and $g_\epsilon(t_1)/g_Y(t_1) = r^*_{g,\epsilon}$. For the next time interval one can plug Eqs. (5.146), (5.147) in Eqs. (5.141)–(5.143) and express the slope functions in terms of fixed-point ratios:

$$F_d(g_Y(t_1), g_d(t_1), ...) = \frac{g_Y^2(t_1)}{16\pi^2}\left[\tilde{b}_Y(t_1) r^{*2}_{g,\epsilon} + \tilde{b}_d(t_1) r^{*2}_{g,d} + \tilde{b}_\epsilon(t_1) r^*_{g,\epsilon} r^*_{g,d} - \tilde{b}_Y(t_1)\right] r^*_{g,d}\,, \quad (5.167)$$

$$F_\epsilon(g_Y(t_1), g_d(t_1), ...) = \frac{g_Y^2(t_1)}{16\pi^2}\left[\left(\tilde{b}_Y(t_1) r^*_{g,\epsilon} + \tilde{b}_\epsilon(t_1) r^*_{g,d}\right)\left(1 + r^{*2}_{g,\epsilon}\right) + \tilde{b}_d(t_1)\, r^{*2}_{g,d}\, r^*_{g,\epsilon}\right], \quad (5.168)$$

where, in agreement with 5.148, we have defined

$$\tilde{b}_i(t) \equiv b_i + \Pi^{(i)}_{n\geq 2}(t) \quad (5.169)$$

away from the fixed point.
At order $n = 1$, $\tilde{b}_i(t) = b_i$. Boundary conditions (5.146) and (5.147) ensure that $F_d^{(n=1)}(t_1) = 0$ and $F_\epsilon^{(n=1)}(t_1) = 0$, independently of the actual values of the running gauge couplings. As an immediate consequence, $g_d(t)/g_Y(t) = r^*_{g,d}$ and $g_\epsilon(t)/g_Y(t) = r^*_{g,\epsilon}$ along the entire RG flow. Given that the ratios $r^*_{g,d}$ and $r^*_{g,\epsilon}$ are, at 1 loop, uniquely determined by the gauge quantum numbers, we can conclude that the predictions of AS for the gauge couplings do not depend on the particular functional form of the gravitational contribution $f_g(t)$.
On the other hand, the scale-invariance of the gauge coupling ratios is washed out by higher-order loop contributions, which introduce a t-dependent deviation from the 1-loop prediction due to appearance in 5.169 of couplings (relevant gauge couplings, Yukawa and quartic

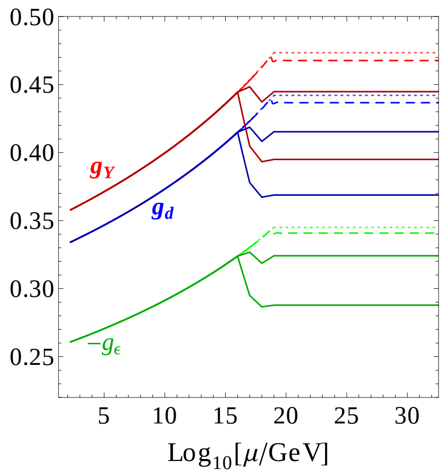

FIGURE 5.10: RG flow of the hypercharge (red), dark gauge (blue), and kinetic mixing (green) couplings of the $B-L$ model at 1 loop. Dotted lines correspond to the benchmark scenario with f_g constant above the Planck scale. Darker solid lines indicate two arbitrary parametrizations of $f_g(t)$. Dashed lines correspond to the FRG results of Ref. [182].

couplings) that lie outside of the system (5.141)–(5.143). While these deviations from scale-invariance could potentially build up over scales spanning many orders of magnitude, they remain in practice quite limited.

For illustration, we show in Fig. 5.10 the RG flow of the three gauge couplings of the $B-L$ model: g_Y (red), g_d (blue), and $-g_\epsilon$ (green). Dotted lines correspond to the benchmark scenario with f_g and f_y constant above the Planck scale ($M_{\text{Pl}} = 10^{19}$ GeV). Darker solid lines indicate two random parametrizations of the functional dependence $f_g(t)$, where the gravity parameter is allow to vary by a factor 10 in the range between 10^{16} GeV and 10^{20} GeV. One can see that, in spite of different fixed-point values in each case, the RG invariance of the coupling ratios leads to unchanged low-scale predictions. Finally, the dashed lines correspond to the $f_g(t)$ parametrization based on the FRG results of Ref. [182]. Note that in that framework it is reasonable to expect only very moderate changes in the gravity parameters.

Yukawa couplings In the case of the Yukawa coupling RGEs given in 5.2 one can consider the ratio of two irrelevant Yukawa couplings y_1 and y_2:

$$\frac{d}{dt}\left(\frac{y_2}{y_1}\right) = \frac{1}{y_1}\left(\beta_2^{\text{matter}} - \frac{y_2}{y_1}\beta_1^{\text{matter}}\right)[t] \equiv G(y_j(t), g_k(t), ...)\,, \tag{5.170}$$

where the parametric form of the matter beta functions is given in 5.150 and the slope function G does not depend explicitly on f_y. Unlike the gauge sector, which features scale-invariant ratios at 1 loop, for the Yukawa couplings the t-dependence of f_g and f_y can impact the running of the y_2/y_1 ratio even at 1 loop.

Repeating the infinitesimal-step analysis,

$$\frac{y_2(t_1)}{y_1(t_1)} = \frac{y_2^*}{y_1^*} + (t_1 - t_0)\, G(y_j^*, g_k^*, ...)\,, \tag{5.171}$$

$$\frac{y_2(t_2)}{y_1(t_2)} = \frac{y_2(t_1)}{y_1(t_1)} + (t_2 - t_1)\, G(y_j(t_1), g_k(t_1), ...)\,, \tag{5.172}$$

$$\cdots$$

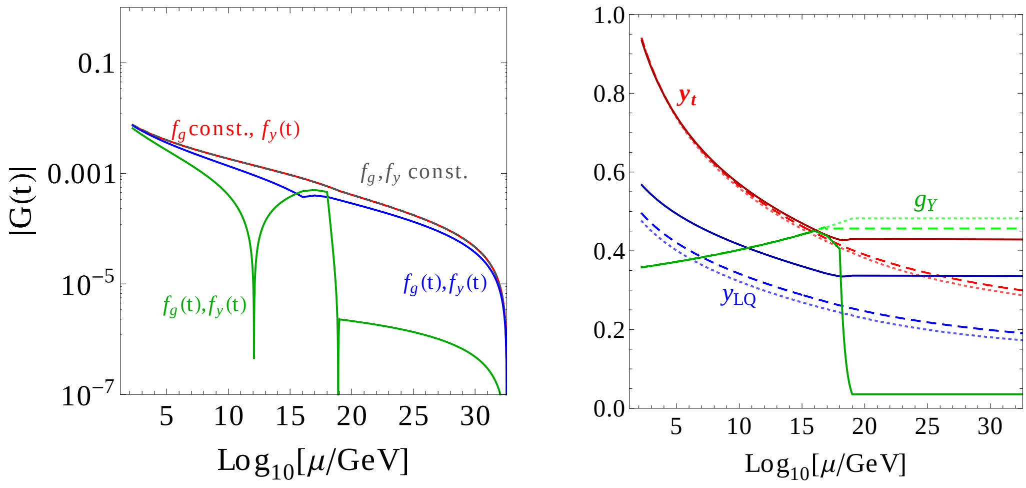

(A) (B)

FIGURE 5.11: (a) Function $|G(t)|$ in the S_3 LQ model for different parametrizations of $f_g(t)$ and $f_y(t)$. Gray dashed line indicates the benchmark scenario with both gravitational parameters constant above the Planck scale ($M_{\rm Pl} = 10^{19}$ GeV). Red solid line corresponds to f_g constant and f_y allowed to vary by a factor 10 in the range between 10^{16} GeV and 10^{20} GeV. Blue and green lines show two arbitrary parametrizations of $f_g(t)$ and $f_y(t)$. (b) 1-loop RG flow of the top Yukawa (red), LQ Yukawa (blue) and hypercharge gauge (green) couplings of the S_3 model for different parametrizations of $f_g(t)$ and $f_y(t)$. Dotted lines correspond to the benchmark 1-loop scenario with f_g constant above the Planck scale. Dashed lines indicate a parametrization based on the FRG results of Ref. [182]. Solid lines show a parametrization resulting in $f_g(t) \ll |f_y(t)|$ in the trans-Planckian regime.

one finds, again, that $G(y_j^*, g_k^*, ...) = 0$, so that $y_2(t_1)/y_1(t_1) = y_2^*/y_1^*$. However, even at 1 loop, $G(y_j(t_1), g_k(t_1), ...) \neq 0$.
In order to see this, let us neglect for simplicity the additive contribution to the Yukawa beta functions in 5.150. In analogy to the gauge coupling case, one can then express

$$G(y_j(t_1), g_k(t_1), ...) = \frac{y_1^2(t_1)\, r_{y,2}^*}{16\pi^2}\left[\sum_j \left(a_j^{(2)} - a_j^{(1)}\right)\frac{y_j^2(t_1)}{y_1^2(t_1)} - \sum_{l,k}\left(a_{lk}^{\prime(2)} - a_{lk}^{\prime(1)}\right)\frac{g_l(t_1) g_k(t_1)}{y_1^2(t_1)}\right] + \frac{r_{y,2}^*}{16\pi^2}\sum_{n\geq 2}\left[\widetilde{\Pi}_n^{(2)}(t_1) - \widetilde{\Pi}_n^{(1)}(t_1)\right]. \quad (5.173)$$

where $r_{y,2}^*$ was defined before 5.158. Note that the non-abelian gauge couplings and some of the Yukawa couplings contributing to the sums within square brackets in 5.173 correspond to relevant directions of the parameter space. Thus, even at 1 loop, if any of the couplings deviates from its fixed point (due to the change of the gravity parameters or the presence of relevant directions in the coupling space) the contribution from the first line of 5.173 does not vanish exactly at t_1 and the ratio $y_2(t)/y_1(t)$ starts to flow.
This effect is illustrated in Fig. 5.11(a), where we show the actual size of the function $|G(t)|$ for different parametrizations of $f_g(t)$ and $f_y(t)$ in the S_3 LQ model. Gray dashed line indicates our benchmark scenario with both gravitational parameters constant above the Planck scale ($M_{\rm Pl} = 10^{19}$ GeV). Red solid line corresponds to a situation in which f_g is kept constant, but f_y is allowed to vary by a factor 10 in the range between 10^{16} GeV and 10^{20} GeV. Once can see that there is no difference with the previous case, confirming the fact that the f_y dependence factors out from the RG running of the Yukawa-coupling ratio. Finally, in green

and blue we show two arbitrary parametrizations of $f_g(t)$, $f_y(t)$. Despite broad fluctuations, $|G(t)|$ remains small in size. We can conclude that the flow of the ratio $y_2(t)/y_1(t)$ remains fairly stable throughout.
As a matter of fact, the dominant source of uncertainty for the prediction of a Yukawa coupling is not given by the changing of $y_2(t)/y_1(t)$ along the RG flow, but rather by the fact that the fixed-point ratio $r^*_{y,2}$ itself becomes unknown once we factor in the t-dependence of f_g and f_y. As was shown in several papers [110, 195, 196], at 1 loop in the matter RGEs the fixed-point ratio of two Yukawa couplings takes the parametric form

$$r^*_{y,2} = \sqrt{\frac{A'\, f_g + B'\, f_y}{A\, f_g + B\, f_y}}\,. \tag{5.174}$$

Numerical coefficients A, A', B, B' are combinations of the 1-loop coefficients of the matter beta functions. They can be finite or zero. Referring, again, to the simple case of two irrelevant Yukawa couplings, y_1, y_2, and one gauge coupling, g_1, one can write

$$A = a_2^{(2)} a_{11}^{\prime(1)} - a_2^{(1)} a_{11}^{\prime(2)}, \qquad B = b_1\left(a_2^{(2)} - a_2^{(1)}\right), \tag{5.175}$$

$$A' = a_1^{(1)} a_{11}^{\prime(2)} - a_1^{(2)} a_{11}^{\prime(1)}, \qquad B' = b_1\left(a_1^{(1)} - a_1^{(2)}\right), \tag{5.176}$$

where $a_j^{(r)}$, $a_{lk}^{\prime(r)}$ are coefficients of the Yukawa-coupling beta functions, cf. 5.150, and b_1 is the 1-loop coefficient of the g_1 beta function.
In the limiting case of one of the two gravitational parameters being strongly dominant with respect to the other, the ratio becomes known, albeit possibly extreme (even zero or infinity). For example, in the S_3 LQ model one gets

$$\lim_{f_g\to\infty} r^*_{y,2} = \sqrt{\frac{A'}{A}} = 0.55, \qquad \text{or} \qquad \lim_{|f_y|\to\infty} r^*_{y,2} = \sqrt{\frac{B'}{B}} = 0.78\,, \tag{5.177}$$

which are not far from the prediction obtained from 5.135, $r^*_{y,2} \approx 0.48$. In general, however, cancellations in the numerator/denominator of 5.174 might take place, so that there is no real handle on the prediction.
This is illustrated in Fig. 5.11(b), where we show the RG flow of the top Yukawa (red), LQ Yukawa (blue) and hypercharge (green) gauge coupling of the S_3 model with different functional forms of $f_g(t)$ and $f_y(t)$. The color code is the same as in Fig. 5.10(a). While it was shown above that even extreme fluctuations do not modify the low-scale predictions for the gauge couplings, we can see in Fig. 5.11(b) that the trans-Planckian behavior of the running $y_{\rm LQ}$ (blue) and y_t (red) couplings is drastically different in the cases in solid vs. those in dotted/dashed.
An assessment from first principles of the uncertainties on the action was attempted in Ref. [189]. Several choices of the truncation, and different matter content, were shown to induce significant shifts in the fixed-point values of the cosmological and Newton constant. On the other hand, when those shifts are plugged into typical FRG computations of f_g and f_y – *e.g.*, those in Ref. [182] – the actual percent uncertainty on $f_g(t)$ and $f_y(t)$ rarely exceeds the $\mathcal{O}(1)$ level along the entire trans-Planckian flow. In Fig. 5.11(b), the parametrization based on the explicit FRG results of Ref. [182] is depicted in dashed lines. It introduces a small uncertainty on the prediction of $y_{\rm LQ}$, of around 5%.
Incidentally, in the sub-Planckian regime of Fig. 5.11(b) we observe focusing due to the presence of a large coupling g_3, in agreement with the discussion at the very end of Sec. 5.3.3.1. The resulting low-scale uncertainty on $y_{\rm LQ}$ reduces to 4% for the FRG-inspired functional

dependence of the gravitational parameters. For the case in solid, which corresponds to $f_g(t) \ll |f_y(t)|$, the low-scale uncertainty on y_{LQ} reads $\sim 19\%$.

5.3.4 Conclusions

In this section , we have investigated in detail the issue of the theoretical uncertainties associated with predictions for irrelevant Lagrangian couplings emerging from trans-Planckian AS. We have decided to bypass strictly gravitational aspects following a popular phenomenological approach which relies on a parametric description of quantum gravity with universal coefficients that are eventually obtained from low-energy observations. Our focus lies squarely on the uncertainties pertaining to the matter sector, which takes the form of a system of gauge- and Yukawa-coupling RGEs.

We have quantified the impact of relaxing several approximations commonly used in the literature to extract phenomenological predictions. In particular we have considered: the effect of including higher-order corrections in the matter RGEs of the gauge-Yukawa system; the impact of selecting a value different from 10^{19} GeV for the (somewhat arbitrary) position of the Planck scale; and the effects of using scale-dependent parametrizations of the gravitational UV completion in the matter RGEs, resulting in a non-instantaneous decoupling of gravity from matter around the Planck scale.

The main findings of our study are the following. First, in the gauge sector the uncertainty induced by relaxing any of the simplifying assumptions never exceeds the 1% level. We can conclude that fixed-point predictions for the irrelevant gauge couplings of the SM and/or NP models are extremely robust, even when they are obtained in a heuristic, simplified approach to AS that is based on some approximations.

A similar conclusion can be drawn for the Yukawa sector of the NP theory, if the predicted Yukawa couplings are of comparable size to the irrelevant gauge couplings. The uncertainties remain at bay, not exceeding $\sim 10\%$ at the fixed point if higher-order corrections are included, or if the Planck scale is moved to, *e.g.*, 10^{16} GeV. The situation is additionally helped by focusing of the RG trajectories in the sub-Planckian regime.

Potentially more dangerous uncertainties could stem from considering the non-trivial scale dependence of the gravitational contributions to the matter beta functions, parameterized by functions $f_g(t)$ and $f_y(t)$, as in this case we lose the ability of determining the actual value of the Yukawa couplings at the fixed point. However, we have argued, based on both an analytical and numerical discussion, that in the range of variability of the gravitation parameters that can be realistically expected in the framework of the FRG, the resulting uncertainty is moderate.

Finally, we have identified one situation in which the AS-based predictions cannot be trusted as any modification of the setup would lead to a drastic change on the predicted value of a NP coupling. This happens if the predicted Yukawa coupling is much smaller than the irrelevant gauge couplings, since in this case it is a result of an accidental, precise cancellation of two quantities of comparable size. This is a manifestation of fine tuning, exactly analogous to some of the cases described in, *e.g.*, Ref. [197], for which the fixed-point gravitational contribution f_y happens to be unnaturally close to a critical value $f_{Z,XY}^{\rm crit}$ which depends exclusively on the gauge quantum numbers of the matter sector. Since the prediction itself finds its origin on a fortuitous cancellation of unrelated quantities it is very subject to the approximations employed for its derivation.

Appendix 5.D: Renormalisation group equations

In this appendix we presents the DREG matter RGEs used in this work. They are listed order-by-order according to the following notation:

$$\beta(X) \equiv \mu \frac{dX}{d\mu} \equiv \frac{1}{(4\pi)^2}\beta^{(1)}(X) + \frac{1}{(4\pi)^4}\beta^{(2)}(X)\,.$$

We do not write explicitly the contributions from the down-type quark and charged-lepton Yukawa matrices which do not affect our numerical analysis.

Gauged U(1)$_{B-L}$

Gauge sector

$$\beta^{(1)}(g_Y) = \frac{41}{6}g_Y^3$$

$$\begin{aligned}\beta^{(2)}(g_Y) = &+\frac{199}{18}g_Y^5 + \frac{92}{9}g_Y^3 g_d^2 + \frac{199}{18}g_Y^3 g_\epsilon^2 + \frac{164}{9}g_Y^3 g_d g_\epsilon + \frac{9}{2}g_2^2 g_Y^3 + \frac{44}{3}g_3^2 g_Y^3\\ &-\frac{17}{6}g_Y^3 \mathrm{Tr}\left(Y_u^\dagger Y_u\right) - \frac{1}{2}g_Y^3\mathrm{Tr}\left(Y_\nu^\dagger Y_\nu\right)\end{aligned}$$

$$\beta^{(1)}(g_\epsilon) = +\frac{32}{3}g_Y^2 g_d + \frac{32}{3}g_d g_\epsilon^2 + \frac{41}{3}g_Y^2 g_\epsilon + 12 g_d^2 g_\epsilon + \frac{41}{6}g_\epsilon^3$$

$$\begin{aligned}\beta^{(2)}(g_\epsilon) = &+\frac{224}{9}g_Y^2 g_d^3 + \frac{199}{6}g_Y^2 g_\epsilon^3 + \frac{164}{9}g_Y^4 g_d + \frac{656}{9}g_Y^2 g_d g_\epsilon^2 + \frac{448}{9}g_d^3 g_\epsilon^2 + \frac{184}{3}g_d^2 g_\epsilon^3\\ &+\frac{328}{9}g_d g_\epsilon^4 + 12 g_2^2 g_Y^2 g_d + 12 g_2^2 g_d g_\epsilon^2 + \frac{32}{3}g_3^2 g_Y^2 g_d + \frac{32}{3}g_3^2 g_d g_\epsilon^2 + \frac{199}{9}g_Y^4 g_\epsilon\\ &+\frac{644}{9}g_Y^2 g_d^2 g_\epsilon + \frac{800}{9}g_d^4 g_\epsilon + \frac{199}{18}g_\epsilon^5 + 9 g_2^2 g_Y^2 g_\epsilon + 12 g_2^2 g_d^2 g_\epsilon + \frac{88}{3}g_3^2 g_Y^2 g_\epsilon\\ &+\frac{32}{3}g_3^2 g_d^2 g_\epsilon + \frac{9}{2}g_2^2 g_\epsilon^3 + \frac{44}{3}g_3^2 g_\epsilon^3 - \frac{10}{3}g_Y^2 g_d \mathrm{Tr}\left(Y_u^\dagger Y_u\right) - 2 g_Y^2 g_d \mathrm{Tr}\left(Y_\nu^\dagger Y_\nu\right)\\ &-\frac{10}{3}g_d g_\epsilon^2 \mathrm{Tr}\left(Y_u^\dagger Y_u\right) - 2 g_d g_\epsilon^2 \mathrm{Tr}\left(Y_\nu^\dagger Y_\nu\right) - \frac{17}{3}g_Y^2 g_\epsilon \mathrm{Tr}\left(Y_u^\dagger Y_u\right) - g_Y^2 g_\epsilon \mathrm{Tr}\left(Y_\nu^\dagger Y_\nu\right)\\ &-\frac{4}{3}g_d^2 g_\epsilon \mathrm{Tr}\left(Y_u^\dagger Y_u\right) - 4 g_d^2 g_\epsilon \mathrm{Tr}\left(Y_\nu^\dagger Y_\nu\right) - 4 g_d^2 g_\epsilon \mathrm{Tr}\left(Y_N^* Y_N\right) - \frac{17}{6}g_\epsilon^3 \mathrm{Tr}\left(Y_u^\dagger Y_u\right)\\ &-\frac{1}{2}g_\epsilon^3 \mathrm{Tr}\left(Y_\nu^\dagger Y_\nu\right)\end{aligned}$$

$$\beta^{(1)}(g_d) = +12 g_d^3 + \frac{41}{6}g_d g_\epsilon^2 + \frac{32}{3}g_d^2 g_\epsilon$$

$$\begin{aligned}\beta^{(2)}(g_d) = &+\frac{92}{9}g_Y^2 g_d^3+\frac{199}{18}g_Y^2 g_d g_\epsilon^2+\frac{800}{9}g_d^5+\frac{184}{3}g_d^3 g_\epsilon^2+\frac{328}{9}g_d^2 g_\epsilon^3+\frac{199}{18}g_d g_\epsilon^4+\frac{9}{2}g_2^2 g_d g_\epsilon^2\\&+\frac{44}{3}g_3^2 g_d g_\epsilon^2+\frac{164}{9}g_Y^2 g_d^2 g_\epsilon+\frac{448}{9}g_d^4 g_\epsilon+12 g_2^2 g_d^2 g_\epsilon+\frac{32}{3}g_3^2 g_d^2 g_\epsilon+12 g_2^2 g_d^3+\frac{32}{3}g_3^2 g_d^3\\&-\frac{4}{3}g_d^3\mathrm{Tr}\left(Y_u^\dagger Y_u\right)-4g_d^3\mathrm{Tr}\left(Y_\nu^\dagger Y_\nu\right)-4g_d^3\mathrm{Tr}\left(Y_N^* Y_N\right)-\frac{17}{6}g_d g_\epsilon^2\mathrm{Tr}\left(Y_u^\dagger Y_u\right)\\&-\frac{1}{2}g_d g_\epsilon^2\mathrm{Tr}\left(Y_\nu^\dagger Y_\nu\right)-\frac{10}{3}g_d^2 g_\epsilon\mathrm{Tr}\left(Y_u^\dagger Y_u\right)-2g_d^2 g_\epsilon\mathrm{Tr}\left(Y_\nu^\dagger Y_\nu\right)\end{aligned}$$

$$\beta^{(1)}(g_2) = -\frac{19}{6}g_2^3$$

$$\begin{aligned}\beta^{(2)}(g_2) = &+4g_2^3 g_d g_\epsilon+\frac{3}{2}g_2^3 g_Y^2+4g_2^3 g_d^2+\frac{3}{2}g_2^3 g_\epsilon^2+\frac{35}{6}g_2^5+12g_2^3 g_3^2-\frac{3}{2}g_2^3\mathrm{Tr}\left(Y_u^\dagger Y_u\right)\\&-\frac{1}{2}g_2^3\mathrm{Tr}\left(Y_\nu^\dagger Y_\nu\right)\end{aligned}$$

$$\beta^{(1)}(g_3) = -7g_3^3$$

$$\beta^{(2)}(g_3) = +\frac{4}{3}g_3^3 g_d g_\epsilon+\frac{9}{2}g_2^2 g_3^3+\frac{11}{6}g_3^3 g_Y^2+\frac{4}{3}g_3^3 g_d^2+\frac{11}{6}g_3^3 g_\epsilon^2-26g_3^5-2g_3^3\mathrm{Tr}\left(Y_u^\dagger Y_u\right)$$

Yukawa sector The Higgs potential couplings λ_1, λ_2, and λ_3 are defined according to Ref. [269].

$$\begin{aligned}\beta^{(1)}(Y_u) = &+\frac{3}{2}Y_u Y_u^\dagger Y_u+3\mathrm{Tr}\left(Y_u^\dagger Y_u\right)Y_u+\mathrm{Tr}\left(Y_\nu^\dagger Y_\nu\right)Y_u-\frac{17}{12}g_Y^2 Y_u-\frac{2}{3}g_d^2 Y_u-\frac{5}{3}g_d g_\epsilon Y_u\\&-\frac{17}{12}g_\epsilon^2 Y_u-\frac{9}{4}g_2^2 Y_u-8g_3^2 Y_u\end{aligned}$$

$$\begin{aligned}
\beta^{(2)}(Y_u) = &+\frac{3}{2}Y_uY_u^\dagger Y_uY_u^\dagger Y_u-\frac{27}{4}\mathrm{Tr}\left(Y_u^\dagger Y_uY_u^\dagger Y_u\right)Y_u-\frac{27}{4}\mathrm{Tr}\left(Y_u^\dagger Y_u\right)Y_uY_u^\dagger Y_u\\
&-\frac{9}{4}\mathrm{Tr}\left(Y_\nu^\dagger Y_\nu\right)Y_uY_u^\dagger Y_u-\frac{9}{4}\mathrm{Tr}\left(Y_\nu^\dagger Y_\nu Y_\nu^\dagger Y_\nu\right)Y_u-3\mathrm{Tr}\left(Y_\nu^\dagger Y_\nu Y_N^* Y_N\right)Y_u\\
&-12\lambda_1Y_uY_u^\dagger Y_u+6\lambda_1^2Y_u+\frac{1}{2}\lambda_3^2Y_u+\frac{223}{48}g_Y^2Y_uY_u^\dagger Y_u+\frac{4}{3}g_d^2Y_uY_u^\dagger Y_u\\
&+\frac{25}{12}g_dg_\epsilon Y_uY_u^\dagger Y_u+\frac{223}{48}g_\epsilon^2Y_uY_u^\dagger Y_u+\frac{135}{16}g_2^2Y_uY_u^\dagger Y_u+16g_3^2Y_uY_u^\dagger Y_u\\
&+\frac{85}{24}g_Y^2\mathrm{Tr}\left(Y_u^\dagger Y_u\right)Y_u+\frac{5}{3}g_d^2\mathrm{Tr}\left(Y_u^\dagger Y_u\right)Y_u+\frac{25}{6}g_dg_\epsilon\mathrm{Tr}\left(Y_u^\dagger Y_u\right)Y_u\\
&+\frac{85}{24}g_\epsilon^2\mathrm{Tr}\left(Y_u^\dagger Y_u\right)Y_u+\frac{45}{8}g_2^2\mathrm{Tr}\left(Y_u^\dagger Y_u\right)Y_u+20g_3^2\mathrm{Tr}\left(Y_u^\dagger Y_u\right)Y_u\\
&+\frac{5}{8}g_Y^2\mathrm{Tr}\left(Y_\nu^\dagger Y_\nu\right)Y_u+5g_d^2\mathrm{Tr}\left(Y_\nu^\dagger Y_\nu\right)Y_u+\frac{5}{2}g_dg_\epsilon\mathrm{Tr}\left(Y_\nu^\dagger Y_\nu\right)Y_u\\
&+\frac{5}{8}g_\epsilon^2\mathrm{Tr}\left(Y_\nu^\dagger Y_\nu\right)Y_u+\frac{15}{8}g_2^2\mathrm{Tr}\left(Y_\nu^\dagger Y_\nu\right)Y_u+\frac{1187}{216}g_Y^4Y_u+\frac{91}{12}g_Y^2g_d^2Y_u\\
&+\frac{1187}{108}g_Y^2g_\epsilon^2Y_u+\frac{203}{27}g_d^4Y_u+\frac{1085}{36}g_d^2g_\epsilon^2Y_u+\frac{502}{27}g_Y^2g_dg_\epsilon Y_u+\frac{502}{27}g_dg_\epsilon^3Y_u\\
&+\frac{9}{4}g_2^2g_dg_\epsilon Y_u-\frac{20}{9}g_3^2g_dg_\epsilon Y_u+\frac{665}{27}g_d^3g_\epsilon Y_u+\frac{1187}{216}g_\epsilon^4Y_u-\frac{3}{4}g_2^2g_Y^2Y_u+\frac{3}{4}g_2^2g_d^2Y_u\\
&-\frac{3}{4}g_2^2g_\epsilon^2Y_u-\frac{23}{4}g_2^4Y_u+9g_2^2g_3^2Y_u+\frac{19}{9}g_3^2g_Y^2Y_u-\frac{8}{9}g_3^2g_d^2Y_u+\frac{19}{9}g_3^2g_\epsilon^2Y_u-108g_3^4Y_u
\end{aligned}$$

$$\begin{aligned}
\beta^{(1)}(Y_\nu) = &+\frac{3}{2}Y_\nu Y_\nu^\dagger Y_\nu+2Y_\nu Y_N^*Y_N+3\mathrm{Tr}\left(Y_u^\dagger Y_u\right)Y_\nu+\mathrm{Tr}\left(Y_\nu^\dagger Y_\nu\right)Y_\nu-\frac{3}{4}g_Y^2Y_\nu-6g_d^2Y_\nu\\
&-3g_dg_\epsilon Y_\nu-\frac{3}{4}g_\epsilon^2Y_\nu-\frac{9}{4}g_2^2Y_\nu
\end{aligned}$$

$$\begin{aligned}
\beta^{(2)}(Y_\nu) = &+\frac{3}{2}Y_\nu Y_\nu^\dagger Y_\nu Y_\nu^\dagger Y_\nu+7Y_\nu Y_N^*Y_\nu^{\mathrm{T}}Y_\nu^*Y_N-\frac{1}{2}Y_\nu Y_N^*Y_NY_\nu^\dagger Y_\nu-2Y_\nu Y_N^*Y_NY_N^*Y_N\\
&-\frac{27}{4}\mathrm{Tr}\left(Y_u^\dagger Y_uY_u^\dagger Y_u\right)Y_\nu-\frac{27}{4}\mathrm{Tr}\left(Y_u^\dagger Y_u\right)Y_\nu Y_\nu^\dagger Y_\nu-\frac{9}{4}\mathrm{Tr}\left(Y_\nu^\dagger Y_\nu Y_\nu^\dagger Y_\nu\right)Y_\nu\\
&-\frac{9}{4}\mathrm{Tr}\left(Y_\nu^\dagger Y_\nu\right)Y_\nu Y_\nu^\dagger Y_\nu-3\mathrm{Tr}\left(Y_\nu^\dagger Y_\nu Y_N^*Y_N\right)Y_\nu-6\mathrm{Tr}\left(Y_N^*Y_N\right)Y_\nu Y_N^*Y_N\\
&-12\lambda_1Y_\nu Y_\nu^\dagger Y_\nu-8\lambda_3Y_\nu Y_N^*Y_N+6\lambda_1^2Y_\nu+\frac{1}{2}\lambda_3^2Y_\nu+\frac{93}{16}g_Y^2Y_\nu Y_\nu^\dagger Y_\nu+12g_d^2Y_\nu Y_\nu^\dagger Y_\nu\\
&+\frac{39}{4}g_dg_\epsilon Y_\nu Y_\nu^\dagger Y_\nu+\frac{93}{16}g_\epsilon^2Y_\nu Y_\nu^\dagger Y_\nu+\frac{135}{16}g_2^2Y_\nu Y_\nu^\dagger Y_\nu+40g_d^2Y_\nu Y_N^*Y_N\\
&-12g_dg_\epsilon Y_\nu Y_N^*Y_N+\frac{85}{24}g_Y^2\mathrm{Tr}\left(Y_u^\dagger Y_u\right)Y_\nu+\frac{5}{3}g_d^2\mathrm{Tr}\left(Y_u^\dagger Y_u\right)Y_\nu\\
&+\frac{25}{6}g_dg_\epsilon\mathrm{Tr}\left(Y_u^\dagger Y_u\right)Y_\nu+\frac{85}{24}g_\epsilon^2\mathrm{Tr}\left(Y_u^\dagger Y_u\right)Y_\nu+\frac{45}{8}g_2^2\mathrm{Tr}\left(Y_u^\dagger Y_u\right)Y_\nu\\
&+20g_3^2\mathrm{Tr}\left(Y_u^\dagger Y_u\right)Y_\nu+\frac{5}{8}g_Y^2\mathrm{Tr}\left(Y_\nu^\dagger Y_\nu\right)Y_\nu+5g_d^2\mathrm{Tr}\left(Y_\nu^\dagger Y_\nu\right)Y_\nu\\
&+\frac{5}{2}g_dg_\epsilon\mathrm{Tr}\left(Y_\nu^\dagger Y_\nu\right)Y_\nu+\frac{5}{8}g_\epsilon^2\mathrm{Tr}\left(Y_\nu^\dagger Y_\nu\right)Y_\nu+\frac{15}{8}g_2^2\mathrm{Tr}\left(Y_\nu^\dagger Y_\nu\right)Y_\nu+\frac{35}{24}g_Y^4Y_\nu\\
&+\frac{187}{12}g_Y^2g_d^2Y_\nu+\frac{35}{12}g_Y^2g_\epsilon^2Y_\nu+65g_d^4Y_\nu+\frac{799}{12}g_d^2g_\epsilon^2Y_\nu+21g_Y^2g_dg_\epsilon Y_\nu+21g_dg_\epsilon^3Y_\nu\\
&+\frac{9}{4}g_2^2g_dg_\epsilon Y_\nu+\frac{253}{3}g_d^3g_\epsilon Y_\nu+\frac{35}{24}g_\epsilon^4Y_\nu-\frac{9}{4}g_2^2g_Y^2Y_\nu+\frac{27}{4}g_2^2g_d^2Y_\nu-\frac{9}{4}g_2^2g_\epsilon^2Y_\nu\\
&-\frac{23}{4}g_2^4Y_\nu
\end{aligned}$$

$$\beta^{(1)}(Y_N) = +Y_\nu^{\mathrm{T}} Y_\nu^* Y_N + Y_N Y_\nu^\dagger Y_\nu + 4 Y_N Y_N^* Y_N + 2\mathrm{Tr}\left(Y_N^* Y_N\right) Y_N - 6 g_d^2 Y_N$$

$$\begin{aligned}\beta^{(2)}(Y_N) = & -\frac{1}{4} Y_\nu^{\mathrm{T}} Y_\nu^* Y_\nu^{\mathrm{T}} Y_\nu^* Y_N + 4 Y_\nu^{\mathrm{T}} Y_\nu^* Y_N Y_\nu^\dagger Y_\nu - \frac{1}{4} Y_N Y_\nu^\dagger Y_\nu Y_\nu^\dagger Y_\nu - Y_N Y_\nu^\dagger Y_\nu Y_N^* Y_N \\
& - Y_N Y_N^* Y_\nu^{\mathrm{T}} Y_\nu^* Y_N + 28 Y_N Y_N^* Y_N Y_N^* Y_N - \frac{9}{2}\mathrm{Tr}\left(Y_u^\dagger Y_u\right) Y_\nu^{\mathrm{T}} Y_\nu^* Y_N \\
& - \frac{9}{2}\mathrm{Tr}\left(Y_u^\dagger Y_u\right) Y_N Y_\nu^\dagger Y_\nu - \frac{3}{2}\mathrm{Tr}\left(Y_\nu^\dagger Y_\nu\right) Y_\nu^{\mathrm{T}} Y_\nu^* Y_N - \frac{3}{2}\mathrm{Tr}\left(Y_\nu^\dagger Y_\nu\right) Y_N Y_\nu^\dagger Y_\nu \\
& - 6\mathrm{Tr}\left(Y_\nu^\dagger Y_\nu Y_N^* Y_N\right) Y_N - 12\mathrm{Tr}\left(Y_N^* Y_N Y_N^* Y_N\right) Y_N - 12\mathrm{Tr}\left(Y_N^* Y_N\right) Y_N Y_N^* Y_N \\
& - 4\lambda_3 Y_\nu^{\mathrm{T}} Y_\nu^* Y_N - 4\lambda_3 Y_N Y_\nu^\dagger Y_\nu - 32\lambda_2 Y_N Y_N^* Y_N + 4\lambda_2^2 Y_N + \lambda_3^2 Y_N + \frac{17}{8} g_Y^2 Y_\nu^{\mathrm{T}} Y_\nu^* Y_N \\
& - 16 g_d^2 Y_\nu^{\mathrm{T}} Y_\nu^* Y_N - \frac{13}{2} g_d g_\epsilon Y_\nu^{\mathrm{T}} Y_\nu^* Y_N + \frac{17}{8} g_\epsilon^2 Y_\nu^{\mathrm{T}} Y_\nu^* Y_N + \frac{51}{8} g_2^2 Y_\nu^{\mathrm{T}} Y_\nu^* Y_N \\
& + \frac{17}{8} g_Y^2 Y_N Y_\nu^\dagger Y_\nu - 16 g_d^2 Y_N Y_\nu^\dagger Y_\nu - \frac{13}{2} g_d g_\epsilon Y_N Y_\nu^\dagger Y_\nu + \frac{17}{8} g_\epsilon^2 Y_N Y_\nu^\dagger Y_\nu \\
& + \frac{51}{8} g_2^2 Y_N Y_\nu^\dagger Y_\nu + 176 g_d^2 Y_N Y_N^* Y_N + 10 g_d^2 \mathrm{Tr}\left(Y_N^* Y_N\right) Y_N - 127 g_d^4 Y_N - \frac{35}{6} g_d^2 g_\epsilon^2 Y_N \\
& - \frac{32}{3} g_d^3 g_\epsilon Y_N\end{aligned}$$

Leptoquark S_3 In this model the 2-loop Yukawa RGEs depend also on the dimensionless BSM Higgs potential parameters λ_{S_3} and λ_{HS_3}, which we define as

$$\mathcal{V}|_{S_3} = \frac{1}{2} m_{S_3}^2 \mathrm{Tr}\left[S_3^\dagger S_3\right] + \frac{1}{8}\lambda_{S_3}\left(\mathrm{Tr}\left[S_3^\dagger S_3\right]\right)^2 + \frac{1}{2}\lambda_{HS} H^\dagger H\, \mathrm{Tr}\left[S_3^\dagger S_3\right]. \tag{5.178}$$

We have checked that these couplings do not influence predictions for the gauge and Yukawa sector in a significant manner. As such, they are set to 0 in our numerical analysis.
Note that there was an error in the normalization of Y_{LQ} in the RGEs given in Ref. [196]. Below we present the correct expressions.

Gauge sector

$$\beta^{(1)}(g_Y) = \frac{43}{6} g_Y^3$$

$$\beta^{(2)}(g_Y) = +\frac{23}{2} g_Y^5 + \frac{25}{2} g_2^2 g_Y^3 + 20 g_3^2 g_Y^3 - \frac{17}{6} g_Y^3 \mathrm{Tr}\left(Y_u^\dagger Y_u\right) - 5 g_Y^3 \mathrm{Tr}\left(Y_{\mathrm{LQ}}^\dagger Y_{\mathrm{LQ}}\right)$$

$$\beta^{(1)}(g_2) = -\frac{7}{6} g_2^3$$

$$\beta^{(2)}(g_2) = +\frac{25}{6} g_2^3 g_Y^2 + \frac{371}{6} g_2^5 + 44 g_2^3 g_3^2 - \frac{3}{2} g_2^3 \mathrm{Tr}\left(Y_u^\dagger Y_u\right) - 9 g_2^3 \mathrm{Tr}\left(Y_{\mathrm{LQ}}^\dagger Y_{\mathrm{LQ}}\right)$$

$$\beta^{(1)}(g_3) = -\frac{13}{2} g_3^3$$

$$\beta^{(2)}(g_3) = +\frac{33}{2} g_2^2 g_3^3 + \frac{5}{2} g_3^3 g_Y^2 - 15 g_3^5 - 2 g_3^3 \mathrm{Tr}\left(Y_u^\dagger Y_u\right) - 3 g_3^3 \mathrm{Tr}\left(Y_{\mathrm{LQ}}^\dagger Y_{\mathrm{LQ}}\right)$$

Yukawa sector

$$\beta^{(1)}(Y_u) = +\frac{3}{2} Y_u Y_u^\dagger Y_u + \frac{3}{2} Y_{\mathrm{LQ}}^\dagger Y_{\mathrm{LQ}} Y_u + 3\mathrm{Tr}\left(Y_u^\dagger Y_u\right) Y_u - \frac{17}{12} g_Y^2 Y_u - \frac{9}{4} g_2^2 Y_u - 8 g_3^2 Y_u$$

$$\begin{aligned}
\beta^{(2)}(Y_u) = &+\frac{3}{2} Y_u Y_u^\dagger Y_u Y_u^\dagger Y_u - \frac{3}{4} Y_u Y_u^\dagger Y_{\mathrm{LQ}}^\dagger Y_{\mathrm{LQ}} Y_u - \frac{27}{8} Y_{\mathrm{LQ}}^\dagger Y_{\mathrm{LQ}} Y_{\mathrm{LQ}}^\dagger Y_{\mathrm{LQ}} Y_u \\
&- \frac{27}{4}\mathrm{Tr}\left(Y_u^\dagger Y_u Y_u^\dagger Y_u\right) Y_u - \frac{27}{4}\mathrm{Tr}\left(Y_u^\dagger Y_u\right) Y_u Y_u^\dagger Y_u - \frac{27}{4}\mathrm{Tr}\left(Y_u^\dagger Y_{\mathrm{LQ}}^\dagger Y_{\mathrm{LQ}} Y_u\right) Y_u \\
&- \frac{9}{2}\mathrm{Tr}\left(Y_{\mathrm{LQ}}^\dagger Y_{\mathrm{LQ}}\right) Y_{\mathrm{LQ}}^\dagger Y_{\mathrm{LQ}} Y_u - 12\lambda Y_u Y_u^\dagger Y_u - 6\lambda_{HS_3} Y_{\mathrm{LQ}}^\dagger Y_{\mathrm{LQ}} Y_u + 6\lambda^2 Y_u \\
&+ \frac{9}{2}\lambda_{HS_3}^2 Y_u + \frac{223}{48} g_Y^2 Y_u Y_u^\dagger Y_u + \frac{135}{16} g_2^2 Y_u Y_u^\dagger Y_u + 16 g_3^2 Y_u Y_u^\dagger Y_u + \frac{43}{6} g_Y^2 Y_{\mathrm{LQ}}^\dagger Y_{\mathrm{LQ}} Y_u \\
&+ \frac{45}{2} g_2^2 Y_{\mathrm{LQ}}^\dagger Y_{\mathrm{LQ}} Y_u + 11 g_3^2 Y_{\mathrm{LQ}}^\dagger Y_{\mathrm{LQ}} Y_u + \frac{85}{24} g_Y^2 \mathrm{Tr}\left(Y_u^\dagger Y_u\right) Y_u + \frac{45}{8} g_2^2 \mathrm{Tr}\left(Y_u^\dagger Y_u\right) Y_u \\
&+ 20 g_3^2 \mathrm{Tr}\left(Y_u^\dagger Y_u\right) Y_u + \frac{449}{72} g_Y^4 Y_u - \frac{3}{4} g_2^2 g_Y^2 Y_u + \frac{1}{4} g_2^4 Y_u + 9 g_2^2 g_3^2 Y_u + \frac{19}{9} g_3^2 g_Y^2 Y_u \\
&- \frac{302}{3} g_3^4 Y_u
\end{aligned}$$

$$\begin{aligned}
\beta^{(1)}(Y_{\mathrm{LQ}}) = &+\frac{1}{2} Y_{\mathrm{LQ}} Y_u Y_u^\dagger + 6 Y_{\mathrm{LQ}} Y_{\mathrm{LQ}}^\dagger Y_{\mathrm{LQ}} + 2\mathrm{Tr}\left(Y_{\mathrm{LQ}}^\dagger Y_{\mathrm{LQ}}\right) Y_{\mathrm{LQ}} - \frac{5}{6} g_Y^2 Y_{\mathrm{LQ}} - \frac{9}{2} g_2^2 Y_{\mathrm{LQ}} \\
&- 4 g_3^2 Y_{\mathrm{LQ}}
\end{aligned}$$

$$\begin{aligned}
\beta^{(2)}(Y_{\mathrm{LQ}}) = &-\frac{1}{4} Y_{\mathrm{LQ}} Y_u Y_u^\dagger Y_u Y_u^\dagger - \frac{9}{8} Y_{\mathrm{LQ}} Y_u Y_u^\dagger Y_{\mathrm{LQ}}^\dagger Y_{\mathrm{LQ}} + \frac{13}{4} Y_{\mathrm{LQ}} Y_{\mathrm{LQ}}^\dagger Y_{\mathrm{LQ}} Y_{\mathrm{LQ}}^\dagger Y_{\mathrm{LQ}} \\
&- \frac{9}{4}\mathrm{Tr}\left(Y_u^\dagger Y_u\right) Y_{\mathrm{LQ}} Y_u Y_u^\dagger - \frac{3}{2}\mathrm{Tr}\left(Y_u^\dagger Y_{\mathrm{LQ}}^\dagger Y_{\mathrm{LQ}} Y_u\right) Y_{\mathrm{LQ}} \\
&- 18\mathrm{Tr}\left(Y_{\mathrm{LQ}}^\dagger Y_{\mathrm{LQ}} Y_{\mathrm{LQ}}^\dagger Y_{\mathrm{LQ}}\right) Y_{\mathrm{LQ}} - 18\mathrm{Tr}\left(Y_{\mathrm{LQ}}^\dagger Y_{\mathrm{LQ}}\right) Y_{\mathrm{LQ}} Y_{\mathrm{LQ}}^\dagger Y_{\mathrm{LQ}} - 2\lambda_{HS_3} Y_{\mathrm{LQ}} Y_u Y_u^\dagger \\
&- 24\lambda_{S_3} Y_{\mathrm{LQ}} Y_{\mathrm{LQ}}^\dagger Y_{\mathrm{LQ}} + 5\lambda_{S_3}^2 Y_{\mathrm{LQ}} + \lambda_{HS_3}^2 Y_{\mathrm{LQ}} + \frac{427}{144} g_Y^2 Y_{\mathrm{LQ}} Y_u Y_u^\dagger + \frac{33}{16} g_2^2 Y_{\mathrm{LQ}} Y_u Y_u^\dagger \\
&- \frac{8}{3} g_3^2 Y_{\mathrm{LQ}} Y_u Y_u^\dagger + \frac{23}{3} g_Y^2 Y_{\mathrm{LQ}} Y_{\mathrm{LQ}}^\dagger Y_{\mathrm{LQ}} + 96 g_2^2 Y_{\mathrm{LQ}} Y_{\mathrm{LQ}}^\dagger Y_{\mathrm{LQ}} + 62 g_3^2 Y_{\mathrm{LQ}} Y_{\mathrm{LQ}}^\dagger Y_{\mathrm{LQ}} \\
&+ \frac{25}{18} g_Y^2 \mathrm{Tr}\left(Y_{\mathrm{LQ}}^\dagger Y_{\mathrm{LQ}}\right) Y_{\mathrm{LQ}} + \frac{15}{2} g_2^2 \mathrm{Tr}\left(Y_{\mathrm{LQ}}^\dagger Y_{\mathrm{LQ}}\right) Y_{\mathrm{LQ}} + \frac{20}{3} g_3^2 \mathrm{Tr}\left(Y_{\mathrm{LQ}}^\dagger Y_{\mathrm{LQ}}\right) Y_{\mathrm{LQ}} \\
&+ \frac{599}{144} g_Y^4 Y_{\mathrm{LQ}} - \frac{23}{24} g_2^2 g_Y^2 Y_{\mathrm{LQ}} - \frac{173}{16} g_2^4 Y_{\mathrm{LQ}} - 31 g_2^2 g_3^2 Y_{\mathrm{LQ}} - \frac{1}{9} g_3^2 g_Y^2 Y_{\mathrm{LQ}} - \frac{55}{3} g_3^4 Y_{\mathrm{LQ}}
\end{aligned}$$

6

Conclusions

This thesis has presented a multifaceted investigation into VLFs as promising candidates for physics beyond the SM, exploring their phenomenological signatures, their theoretical embedding, and the constraints that UV consistency requirements may impose on them. The interplay between RG techniques, phenomenological analysis, and non-perturbative methods has provided a coherent framework through which to understand the potential role of VLFs in particle physics.

Chapter 2 laid the foundation by revisiting the structure of the SM, the mechanism of electroweak symmetry breaking, and the theoretical machinery of the RG. Key motivations for BSM physics – such as the hierarchy problem, vacuum stability, and lepton flavor anomalies – were introduced, and the EFT perspective was discussed as a guiding paradigm in modern model building. The need for non-perturbative tools was emphasized, especially in regimes where perturbation theory breaks down, setting the stage for the FRG methods developed in later chapters.

In Chapter 3 we introduced a minimal renormalisable extension of the SM with extra scalars and VLQs and VLLs. The main motivation for studying such model is that it represents an alternative to the Higgs mechanism for generating mass for the fermions of the SM. We scanned its parameter space under vacuum-stability, flavor observables and perturbativity constraints, and identified benchmark points that remain fully consistent with all current bounds. Specifically, the mass of the extra scalars is at around 300-600 GeV, while the VLFs masses are at 800-1200 GeV. One distinctive feature of these solutions is that the charged scalar/heavy neutrino loops provide dominant contributions to the observable Δa_μ. The main reason behind this feature is that the same coupling which generates the neutral scalar/charged lepton loops is also responsible for the correct tree-level mass of the muon and thus it is required to be small. Regarding future prospects for experimental verification of the model, the main result is that VLLs can not be tested in the current run of the LHC, while VLQs and some of the scalar states are already accessible.

In Chapter 4, the investigation moved from phenomenology to more formal territory. We studied the UV fixed point of a class of gauge-Yukawa theories in the limit where the number of colour and VLFs is taken to infinity, while keeping their ratio fixed. The theory at the UV fixed point switches on all possible beyond marginal operators, and so it is important to consider them in the action. While the perturbative regime of the theory is studied in very details in the literature, the corrections to the effective potential given by beyond marginal operators are computed for the first time within functional renormalisation in our work, at leading order in the Veneziano parameter. In our study, we include an infinite tower of beyond marginal operators in the model, compute their UV fixed point, and show how the effective potential at the fixed point can be written in a closed form.

In Chapter 5.2 we assumed that quantum gravity itself approaches a fixed point at the Planck scale $M_{\rm Pl}$ and introduced a universal contribution f into matter β-functions. We refer to this approach as "heuristic", since we do not make any assumption on the action of quantum gravity, and fix f in such a way to match the SM. We tested this idea on two simple and well-known Z' extensions of the SM providing a solution to the flavor anomalies in $b \to s\mu^+\mu^-$ transitions. Thanks to the trans-Planckian fixed-point we were able to derive a fairly precise determination of the abelian kinetic mixing ϵ, the NP Yukawa couplings, and the scalar quartic couplings. Bounds on the VL masses have been set using direct production of heavy VLQs and VLLs at the LHC.

Finally, in Chapter 5.3 we have studied the robustness of the predictions within the "heuristic" approach, by relaxing some of its main assumptions. In particular we have considered: the effect of including higher-order corrections; the impact of moving the Planck scale; and the effects of a non-instantaneous decoupling of gravity from matter around the Planck scale. The main results are that the gauge sector is extremely stable, with an uncertainty of less than 1% level. A similar conclusion can be drawn for the Yukawa sector if the predicted Yukawa couplings are of comparable size to the irrelevant gauge couplings. Conversely, if the predicted Yukawa coupling is much smaller than the irrelevant gauge couplings, then the uncertainty becomes much larger.

Taken together, these studies demonstrate that VLFs provide a rich arena for exploring NPs. Their unique properties and versatile phenomenological implications make them a natural focal point for investigating how BSM scenarios can reconcile theoretical challenges with experimental data. Moreover, by employing both traditional parameter space analyses and modern non-perturbative techniques, this work aims to bridge different methodological approaches and to present a coherent picture of the impact of VLFs on particle physics phenomenology.

Acknowledgements

I would like to express my gratitude to my supervisor, Kamila Kowalska, for giving me the opportunity to start the PhD journey, and for guiding me in my first steps in research and academia. Her insight and critical feedback have been fundamental in shaping this thesis and my development as a physicist. For the same reason, I am also very thankful to Enrico Sessolo, whose support and discussions were invaluable and whose presence added a welcome touch of Italian spirit that often made me feel more at home throughout this journey. This work was supported by the National Science Centre (Poland) under the research Grant No. 2017/26/E/ST2/00470, without which this research would not have been possible.

I am also grateful to all the people I have had the opportunity to collaborate with. Each of these interactions has contributed to my growth as a physicist, helping me learn not only technical skills but also what it means to engage in scientific research. Through conferences, seminars, and my long-term attachment, I was fortunate to meet researchers from a wide range of backgrounds and experiences. These encounters have enriched me both professionally and personally, broadening my perspective and deepening my appreciation for the international nature of the scientific community.

Bibliography

[1] A. E. Cárcamo Hernández et al. Global analysis and LHC study of a vectorlike extension of the standard model with extra scalars. *Phys. Rev. D* 109.3 (2024), p. 035010. DOI: 10.1103/PhysRevD.109.035010.

[2] Abhishek Chikkaballi et al. Constraints on Z′ solutions to the flavor anomalies with trans-Planckian asymptotic safety. *JHEP* 01 (2023), p. 164. DOI: 10.1007/JHEP01(2023)164.

[3] Wojciech Kotlarski et al. How robust are particle physics predictions in asymptotic safety? *Eur. Phys. J. C* 83.7 (2023), p. 644. DOI: 10.1140/epjc/s10052-023-11813-3.

[4] Michael Edward Peskin and Daniel V. Schroeder. *An Introduction to Quantum Field Theory*. Reading, USA: Addison-Wesley (1995) 842 p. Westview Press, 1995.

[5] Matthew D. Schwartz. *Quantum Field Theory and the Standard Model*. Cambridge University Press, 2014.

[6] François Englert and Robert Brout. Broken Symmetry and the Mass of Gauge Vector Mesons. *Phys. Rev. Lett.* 13 (1964), p. 321. DOI: 10.1103/PhysRevLett.13.321.

[7] Peter W. Higgs. Broken Symmetries and the Masses of Gauge Bosons. *Phys. Rev. Lett.* 13 (1964), p. 508. DOI: 10.1103/PhysRevLett.13.508.

[8] Gerald S. Guralnik, C. R. Hagen, and T. W. B. Kibble. Global Conservation Laws and Massless Particles. *Phys. Rev. Lett.* 13 (1964), p. 585. DOI: 10.1103/PhysRevLett.13.585.

[9] Steven Weinberg. Baryon and Lepton Nonconserving Processes. *Phys. Rev. Lett.* 43 (1979), p. 1566. DOI: 10.1103/PhysRevLett.43.1566.

[10] Steven D. Bass, Albert De Roeck, and Marumi Kado. The Higgs boson implications and prospects for future discoveries. *Nature Rev. Phys.* 3.9 (2021), pp. 608–624. DOI: 10.1038/s42254-021-00341-2.

[11] ATLAS Collaboration. A detailed map of Higgs boson interactions by the ATLAS experiment ten years after the discovery. *Nature* 607 (2022), pp. 52–59. DOI: 10.1038/s41586-022-04893-w.

[12] CMS Collaboration. A portrait of the Higgs boson by the CMS experiment ten years after the discovery. *Nature* 607 (2022), pp. 60–68. DOI: 10.1038/s41586-022-04892-x.

[13] Stephen L. Adler. Axial-Vector Vertex in Spinor Electrodynamics. *Phys. Rev.* 177 (1969), pp. 2426–2438. DOI: 10.1103/PhysRev.177.2426.

[14] John S. Bell and Roman Jackiw. A PCAC Puzzle: $\pi^0 \to \gamma\gamma$ in the Sigma Model. *Nuovo Cim. A* 60 (1969), pp. 47–61. DOI: 10.1007/BF02823296.

[15] R. Aaij et al. Test of lepton universality using $B^+ \to K^+\ell^+\ell^-$ decays. *Phys. Rev. Lett.* 113 (2014), p. 151601. DOI: 10.1103/PhysRevLett.113.151601.

[16] R. Aaij et al. Test of lepton universality with $B^0 \to K^{*0}\ell^+\ell^-$ decays. *JHEP* 08 (2017), p. 055. DOI: 10.1007/JHEP08(2017)055.

[17] R. Aaij et al. Test of lepton universality in $B^+ \to K^+\ell^+\ell^-$ decays. *Phys. Rev. Lett.* 128 (2022), p. 191802. DOI: 10.1103/PhysRevLett.128.191802.

[18] Li-Sheng Geng et al. Implications of new evidence for lepton-universality violation in b→sℓ+ℓ- decays. *Phys. Rev. D* 104.3 (2021), p. 035029. DOI: 10.1103/PhysRevD.104.035029.

[19] M. Algueró et al. Global fit to $b \to s\ell^+\ell^-$ anomalies after the 2022 LHCb update. *JHEP* 06 (2023), p. 069. DOI: 10.1007/JHEP06(2023)069.

[20] Wilfried Buchmuller and Dario Wyler. Effective Lagrangian Analysis of New Interactions and Flavor Conservation. *Nucl. Phys. B* 268 (1986), pp. 621–653. DOI: 10.1016/0550-3213(86)90262-2.

[21] B. Grzadkowski et al. Dimension-Six Terms in the Standard Model Lagrangian. *JHEP* 10 (2010), p. 085. DOI: 10.1007/JHEP10(2010)085.

[22] David J. Gross and Frank Wilczek. Ultraviolet behavior of non-Abelian gauge theories. *Phys. Rev. Lett.* 30 (1973), p. 1343. DOI: 10.1103/PhysRevLett.30.1343.

[23] H. David Politzer. Reliable Perturbative Results for Strong Interactions? *Phys. Rev. Lett.* 30 (1973), p. 1346. DOI: 10.1103/PhysRevLett.30.1346.

[24] H. Georgi and S. L. Glashow. Unity of All Elementary Particle Forces. *Phys. Rev. Lett.* 32 (1974), p. 438. DOI: 10.1103/PhysRevLett.32.438.

[25] H. Fritzsch and P. Minkowski. Unified Interactions of Leptons and Hadrons. *Annals Phys.* 93 (1975), p. 193. DOI: 10.1016/0003-4916(75)90211-0.

[26] F. Gürsey, P. Ramond, and P. Sikivie. A Universal Gauge Theory Model Based on E6. *Phys. Lett. B* 60 (1976), p. 177. DOI: 10.1016/0370-2693(76)90417-2.

[27] U. Amaldi, W. de Boer, and H. Furstenau. Comparison of grand unified theories with electroweak and strong coupling constants measured at LEP. *Phys. Lett. B* 260 (1991), p. 447. DOI: 10.1016/0370-2693(91)91641-8.

[28] P. Langacker and N. Polonsky. Uncertainties in coupling constant unification. *Phys. Rev. D* 47 (1993), p. 4028. DOI: 10.1103/PhysRevD.47.4028.

[29] Giuseppe Degrassi et al. Higgs mass and vacuum stability in the Standard Model at NNLO. *JHEP* 08 (2012), p. 098. DOI: 10.1007/JHEP08(2012)098.

[30] Dario Buttazzo et al. Investigating the near-criticality of the Higgs boson. *JHEP* 12 (2013), p. 089. DOI: 10.1007/JHEP12(2013)089.

[31] Georges Aad et al. Observation of a new particle in the search for the Standard Model Higgs boson with the ATLAS detector at the LHC. *Phys. Lett. B* 716 (2012), pp. 1–29. DOI: 10.1016/j.physletb.2012.08.020.

[32] Christof Wetterich. Exact evolution equation for the effective potential. *Physics Letters B* 301.1 (1993), pp. 90–94. ISSN: 0370-2693. DOI: https://doi.org/10.1016/0370-2693(93)90726-X.

[33] Alessandro Codello. A novel functional renormalization group framework for gauge theories and gravity. PhD thesis. Mainz U., Inst. Phys., 2010.

[34] Stephen P. Martin. A Supersymmetry Primer. *Adv. Ser. Direct. High Energy Phys.* 21 (2010), pp. 1–153. DOI: 10.1142/9789812839657_0001.

[35] Roberto Contino. The Higgs as a Composite Nambu-Goldstone Boson. *TASI 2009 lectures* (2011). arXiv: 1005.4269.

[36] Lisa Randall and Raman Sundrum. A Large Mass Hierarchy from a Small Extra Dimension. *Phys. Rev. Lett.* 83 (1999), p. 3370. DOI: 10.1103/PhysRevLett.83.3370.

[37] Gerard Jungman, Marc Kamionkowski, and Kim Griest. Supersymmetric Dark Matter. *Phys. Rept.* 267 (1996), pp. 195–373. DOI: 10.1016/0370-1573(95)00058-5.

[38] Roberto D. Peccei and Helen R. Quinn. CP Conservation in the Presence of Instantons. *Phys. Rev. Lett.* 38 (1977), p. 1440. DOI: 10.1103/PhysRevLett.38.1440.

[39] Steven Weinberg. A New Light Boson? *Phys. Rev. Lett.* 40 (1978), p. 223. DOI: 10.1103/PhysRevLett.40.223.

[40] Alexey Boyarsky et al. Sterile neutrino Dark Matter. *Prog. Part. Nucl. Phys.* 104 (2019), pp. 1–45. DOI: 10.1016/j.ppnp.2018.07.004.

[41] Steven Weinberg. The Cosmological Constant Problem. *Rev. Mod. Phys.* 61 (1989), p. 1. DOI: 10.1103/RevModPhys.61.1.

[42] Peter Minkowski. $\mu \to e\gamma$ at a Rate of One Out of 10^9 Muon Decays? *Phys. Lett. B* 67 (1977), pp. 421–428. DOI: 10.1016/0370-2693(77)90435-X.

[43] Rabindra N. Mohapatra and Goran Senjanovic. Neutrino Mass and Spontaneous Parity Nonconservation. *Phys. Rev. Lett.* 44 (1980), p. 912. DOI: 10.1103/PhysRevLett.44.912.

[44] Murray Gell-Mann, Pierre Ramond, and Richard Slansky. Complex Spinors and Unified Theories (1979). Ed. by P. van Nieuwenhuizen and D.Z. Freedman, pp. 315–321.

[45] Tsutomu T. Yanagida. Horizontal gauge symmetry and masses of neutrinos (1979). Ed. by O. Sawada and A. Sugamoto, p. 95.

[46] David E. Morrissey and Michael J. Ramsey-Musolf. Electroweak baryogenesis. *New J. Phys.* 14 (2012), p. 125003. DOI: 10.1088/1367-2630/14/12/125003.

[47] M. Fukugita and T. Yanagida. Baryogenesis Without Grand Unification. *Phys. Lett. B* 174 (1986), pp. 45–47. DOI: 10.1016/0370-2693(86)91126-3.

[48] C. D. Froggatt and Holger Bech Nielsen. Hierarchy of Quark Masses, Cabibbo Angles and CP Violation. *Nucl. Phys. B* 147 (1979), pp. 277–298. DOI: 10.1016/0550-3213(79)90316-X.

[49] Nima Arkani-Hamed and Martin Schmaltz. Hierarchies without symmetries from extra dimensions. *Phys. Rev. D* 61 (2000), p. 033005. DOI: 10.1103/PhysRevD.61.033005.

[50] Tony Gherghetta and Alex Pomarol. Bulk fields and supersymmetry in a slice of AdS. *Nucl. Phys. B* 586 (2000), pp. 141–162. DOI: 10.1016/S0550-3213(00)00392-8.

[51] Stephan J. Huber and Qaisar Shafi. Fermion masses, mixings and proton decay in a Randall-Sundrum model. *Phys. Lett. B* 498 (2001), pp. 256–262. DOI: 10.1016/S0370-2693(00)01399-X.

[52] Murray Gell-Mann, Pierre Ramond, and Richard Slansky. Complex Spinors and Unified Theories. *Conf. Proc. C* 790927 (1979), pp. 315–321. arXiv: 1306.4669 [hep-th].

[53] Tsutomu Yanagida. Horizontal gauge symmetry and masses of neutrinos. *Conf. Proc. C* 7902131 (1979). Ed. by Osamu Sawada and Akio Sugamoto, pp. 95–99.

[54] S. L. Glashow. The Future of Elementary Particle Physics. *NATO Sci. Ser. B* 61 (1980), p. 687. DOI: 10.1007/978-1-4684-7197-7_15.

[55] Rabindra N. Mohapatra and Goran Senjanovic. Neutrino Masses and Mixings in Gauge Models with Spontaneous Parity Violation. *Phys. Rev. D* 23 (1981), p. 165. DOI: 10.1103/PhysRevD.23.165.

[56] J. Schechter and J. W. F. Valle. Neutrino Decay and Spontaneous Violation of Lepton Number. *Phys. Rev. D* 25 (1982), p. 774. DOI: 10.1103/PhysRevD.25.774.

[57] J. Schechter and J. W. F. Valle. Neutrino Masses in SU(2) x U(1) Theories. *Phys. Rev. D* 22 (1980), p. 2227. DOI: 10.1103/PhysRevD.22.2227.

[58] Stephen F. King. $R_{K^{(*)}}$ and the origin of Yukawa couplings. *JHEP* 09 (2018), p. 069. DOI: 10.1007/JHEP09(2018)069.

[59] A. E. Cárcamo Hernández, S. F. King, and H. Lee. Z mediated flavor changing neutral currents with a fourth vectorlike family. *Phys. Rev. D* 105.1 (2022), p. 015021. DOI: 10.1103/PhysRevD.105.015021.

[60] A. E. Cárcamo Hernández, S. F. King, and H. Lee. Fermion mass hierarchies from vectorlike families with an extended 2HDM and a possible explanation for the electron and muon anomalous magnetic moments. *Phys. Rev. D* 103.11 (2021), p. 115024. DOI: 10.1103/PhysRevD.103.115024.

[61] H. Lee and A. E. Cárcamo Hernández. Can the muon anomalous magnetic moment and the B anomalies be simultaneously explained in a minimally extended Z' model? (July 2022). arXiv: 2207.01710 [hep-ph].

[62] Lincoln Wolfenstein. Parametrization of the Kobayashi-Maskawa Matrix. *Phys. Rev. Lett.* 51 (1983), p. 1945. DOI: 10.1103/PhysRevLett.51.1945.

[63] R. L. Workman et al. Review of Particle Physics. *PTEP* 2022 (2022), p. 083C01. DOI: 10.1093/ptep/ptac097.

[64] Margarete Muhlleitner et al. The N2HDM under Theoretical and Experimental Scrutiny. *JHEP* 03 (2017), p. 094. DOI: 10.1007/JHEP03(2017)094.

[65] J. E. Camargo-Molina and B. O'Leary. **VevaciousPlusPlus** (2014). DOI: Accessed: 2023-08.

[66] J. E. Camargo-Molina et al. **Vevacious**: A Tool For Finding The Global Minima Of One-Loop Effective Potentials With Many Scalars. *Eur. Phys. J. C* 73.10 (2013), p. 2588. DOI: 10.1140/epjc/s10052-013-2588-2.

[67] Andrzej Czarnecki, William J. Marciano, and Arkady Vainshtein. Refinements in electroweak contributions to the muon anomalous magnetic moment. *Phys. Rev. D* 67 (2003). [Erratum: Phys.Rev.D 73, 119901 (2006)], p. 073006. DOI: 10.1103/PhysRevD.67.073006.

[68] Kirill Melnikov and Arkady Vainshtein. Hadronic light-by-light scattering contribution to the muon anomalous magnetic moment revisited. *Phys. Rev. D* 70 (2004), p. 113006. DOI: 10.1103/PhysRevD.70.113006.

[69] Tatsumi Aoyama et al. Complete Tenth-Order QED Contribution to the Muon g-2. *Phys. Rev. Lett.* 109 (2012), p. 111808. DOI: 10.1103/PhysRevLett.109.111808.

[70] Alexander Kurz et al. Hadronic contribution to the muon anomalous magnetic moment to next-to-next-to-leading order. *Phys. Lett. B* 734 (2014), pp. 144–147. DOI: 10.1016/j.physletb.2014.05.043.

[71] Michel Davier et al. Reevaluation of the Hadronic Contributions to the Muon g-2 and to alpha(MZ). *Eur. Phys. J. C* 71 (2011). [Erratum: Eur.Phys.J.C 72, 1874 (2012)], p. 1515. DOI: 10.1140/epjc/s10052-012-1874-8.

[72] C. Gnendiger, D. Stöckinger, and H. Stöckinger-Kim. The electroweak contributions to $(g-2)_\mu$ after the Higgs boson mass measurement. *Phys. Rev. D* 88 (2013), p. 053005. DOI: 10.1103/PhysRevD.88.053005.

[73] Gilberto Colangelo et al. Remarks on higher-order hadronic corrections to the muon g−2. *Phys. Lett. B* 735 (2014), pp. 90–91. DOI: 10.1016/j.physletb.2014.06.012.

[74] Michel Davier et al. Reevaluation of the hadronic vacuum polarisation contributions to the Standard Model predictions of the muon $g-2$ and $\alpha(m_Z^2)$ using newest hadronic cross-section data. *Eur. Phys. J. C* 77.12 (2017), p. 827. DOI: 10.1140/epjc/s10052-017-5161-6.

[75] Pere Masjuan and Pablo Sanchez-Puertas. Pseudoscalar-pole contribution to the $(g_\mu - 2)$: a rational approach. *Phys. Rev. D* 95.5 (2017), p. 054026. DOI: 10.1103/PhysRevD.95.054026.

[76] Gilberto Colangelo et al. Dispersion relation for hadronic light-by-light scattering: two-pion contributions. *JHEP* 04 (2017), p. 161. DOI: 10.1007/JHEP04(2017)161.

[77] Martin Hoferichter et al. Dispersion relation for hadronic light-by-light scattering: pion pole. *JHEP* 10 (2018), p. 141. DOI: 10.1007/JHEP10(2018)141.

[78] Alexander Keshavarzi, Daisuke Nomura, and Thomas Teubner. Muon $g-2$ and $\alpha(M_Z^2)$: a new data-based analysis. *Phys. Rev. D* 97.11 (2018), p. 114025. DOI: 10.1103/PhysRevD.97.114025.

[79] Gilberto Colangelo, Martin Hoferichter, and Peter Stoffer. Two-pion contribution to hadronic vacuum polarization. *JHEP* 02 (2019), p. 006. DOI: 10.1007/JHEP02(2019)006.

[80] Martin Hoferichter, Bai-Long Hoid, and Bastian Kubis. Three-pion contribution to hadronic vacuum polarization. *JHEP* 08 (2019), p. 137. DOI: 10.1007/JHEP08(2019)137.

[81] Michel Davier et al. A new evaluation of the hadronic vacuum polarisation contributions to the muon anomalous magnetic moment and to $\alpha(m_Z^2)$. *Eur. Phys. J. C* 80.3 (2020), p. 241. DOI: 10.1140/epjc/s10052-020-7792-2.

[82] Alexander Keshavarzi, Daisuke Nomura, and Thomas Teubner. $g-2$ of charged leptons, $\alpha(M_Z^2)$, and the hyperfine splitting of muonium. *Phys. Rev. D* 101.1 (2020), p. 014029. DOI: 10.1103/PhysRevD.101.014029.

[83] Antoine Gérardin, Harvey B. Meyer, and Andreas Nyffeler. Lattice calculation of the pion transition form factor with $N_f = 2+1$ Wilson quarks. *Phys. Rev. D* 100.3 (2019), p. 034520. DOI: 10.1103/PhysRevD.100.034520.

[84] Johan Bijnens, Nils Hermansson-Truedsson, and Antonio Rodríguez-Sánchez. Short-distance constraints for the HLbL contribution to the muon anomalous magnetic moment. *Phys. Lett. B* 798 (2019), p. 134994. DOI: 10.1016/j.physletb.2019.134994.

[85] Gilberto Colangelo et al. Longitudinal short-distance constraints for the hadronic light-by-light contribution to $(g-2)_\mu$ with large-N_c Regge models. *JHEP* 03 (2020), p. 101. DOI: 10.1007/JHEP03(2020)101.

[86] Thomas Blum et al. Hadronic Light-by-Light Scattering Contribution to the Muon Anomalous Magnetic Moment from Lattice QCD. *Phys. Rev. Lett.* 124.13 (2020), p. 132002. DOI: 10.1103/PhysRevLett.124.132002.

[87] Tatsumi Aoyama, Toichiro Kinoshita, and Makiko Nio. Theory of the Anomalous Magnetic Moment of the Electron. *Atoms* 7.1 (2019), p. 28. DOI: 10.3390/atoms7010028.

[88] T. Aoyama et al. The anomalous magnetic moment of the muon in the Standard Model. *Phys. Rept.* 887 (2020), pp. 1–166. DOI: 10.1016/j.physrep.2020.07.006.

[89] G. W. Bennett et al. Final Report of the Muon E821 Anomalous Magnetic Moment Measurement at BNL. *Phys. Rev. D* 73 (2006), p. 072003. DOI: 10.1103/PhysRevD.73.072003.

[90] B. Abi et al. Measurement of the Positive Muon Anomalous Magnetic Moment to 0.46 ppm. *Phys. Rev. Lett.* 126.14 (2021), p. 141801. DOI: 10.1103/PhysRevLett.126.141801.

[91] D. P. Aguillard et al. Measurement of the Positive Muon Anomalous Magnetic Moment to 0.20 ppm (Aug. 2023). arXiv: 2308.06230 [hep-ex].

[92] Szabolcs Borsanyi et al. Leading hadronic contribution to the muon magnetic moment from lattice QCD. *Nature* 593 (2021), pp. 51–55. DOI: 10.1038/s41586-021-03418-1.

[93] Kamila Kowalska and Enrico Maria Sessolo. Expectations for the muon g-2 in simplified models with dark matter. *JHEP* 09 (2017), p. 112. DOI: 10.1007/JHEP09(2017)112.

[94] Peter Athron et al. New physics explanations of a in light of the FNAL muon $g - 2$ measurement. *JHEP* 09 (2021), p. 080. DOI: 10.1007/JHEP09(2021)080.

[95] Werner Porod. SPheno, a program for calculating supersymmetric spectra, SUSY particle decays and SUSY particle production at e+ e- colliders. *Comput. Phys. Commun.* 153 (2003), pp. 275–315. DOI: 10.1016/S0010-4655(03)00222-4.

[96] W. Porod and F. Staub. SPheno 3.1: Extensions including flavour, CP-phases and models beyond the MSSM. *Comput. Phys. Commun.* 183 (2012), pp. 2458–2469. DOI: 10.1016/j.cpc.2012.05.021.

[97] Rusa Mandal and Antonio Pich. Constraints on scalar leptoquarks from lepton and kaon physics. *JHEP* 12 (2019), p. 089. DOI: 10.1007/JHEP12(2019)089.

[98] A. Abdesselam et al. Search for lepton-flavor-violating tau-lepton decays to $\ell\gamma$ at Belle. *JHEP* 10 (2021), p. 19. DOI: 10.1007/JHEP10(2021)019.

[99] K. Hayasaka et al. Search for Lepton Flavor Violating Tau Decays into Three Leptons with 719 Million Produced Tau+Tau- Pairs. *Phys. Lett. B* 687 (2010), pp. 139–143. DOI: 10.1016/j.physletb.2010.03.037.

[100] Yuval Grossman, Emilie Passemar, and Stefan Schacht. On the Statistical Treatment of the Cabibbo Angle Anomaly. *JHEP* 07 (2020), p. 068. DOI: 10.1007/JHEP07(2020)068.

[101] Benedetta Belfatto and Sokratis Trifinopoulos. Cabibbo angle anomalies and oblique corrections: The remarkable role of the vectorlike quark doublet. *Phys. Rev. D* 108.3 (2023), p. 035022. DOI: 10.1103/PhysRevD.108.035022.

[102] Andreas Crivellin and Martin Hoferichter. β Decays as Sensitive Probes of Lepton Flavor Universality. *Phys. Rev. Lett.* 125.11 (2020), p. 111801. DOI: 10.1103/PhysRevLett.125.111801.

[103] Andrzej Czarnecki, William J. Marciano, and Alberto Sirlin. Pion beta decay and Cabibbo-Kobayashi-Maskawa unitarity. *Phys. Rev. D* 101.9 (2020), p. 091301. DOI: 10.1103/PhysRevD.101.091301.

[104] Kingman Cheung et al. Vector-like Quark Interpretation for the CKM Unitarity Violation, Excess in Higgs Signal Strength, and Bottom Quark Forward-Backward Asymmetry. *JHEP* 05 (2020), p. 117. DOI: 10.1007/JHEP05(2020)117.

[105] G. C. Branco et al. Addressing the CKM unitarity problem with a vector-like up quark. *JHEP* 07 (2021), p. 099. DOI: 10.1007/JHEP07(2021)099.

[106] Francisco Albergaria and Gustavo C. Branco. Unitarity Relations in the Presence of Vector-Like Quarks (July 2023). arXiv: 2307.13073 [hep-ph].

[107] Florian Staub. SARAH 4 : A tool for (not only SUSY) model builders. *Comput. Phys. Commun.* 185 (2014), pp. 1773–1790. DOI: 10.1016/j.cpc.2014.02.018.

[108] Florian Staub. Exploring new models in all detail with SARAH. *Adv. High Energy Phys.* 2015 (2015), p. 840780. DOI: 10.1155/2015/840780.

[109] Luc Darmé et al. Flavor anomalies and dark matter in SUSY with an extra U(1). *JHEP* 10 (2018), p. 052. DOI: 10.1007/JHEP10(2018)052.

[110] Kamila Kowalska and Enrico Maria Sessolo. Minimal models for g-2 and dark matter confront asymptotic safety. *Phys. Rev. D* 103.11 (2021), p. 115032. DOI: 10.1103/PhysRevD.103.115032.

[111] E Kou et al. The Belle II Physics Book. *Progress of Theoretical and Experimental Physics* 2019.12 (Dec. 2019), p. 123C01. ISSN: 2050-3911. DOI: 10.1093/ptep/ptz106. URL: https://doi.org/10.1093/ptep/ptz106.

[112] Latika Aggarwal et al. Snowmass White Paper: Belle II physics reach and plans for the next decade and beyond (July 2022). arXiv: 2207.06307 [hep-ex].

[113] Kamila Kowalska and Dinesh Kumar. Road map through the desert: unification with vector-like fermions. *JHEP* 12 (2019), p. 094. DOI: 10.1007/JHEP12(2019)094.

[114] Ubaldo Cavazos Olivas, Kamila Kowalska, and Dinesh Kumar. Road map through the desert with scalars. *JHEP* 03 (2022), p. 132. DOI: 10.1007/JHEP03(2022)132.

[115] G. Aad et al. Search for pair-produced vector-like top and bottom partners in events with large missing transverse momentum in pp collisions with the ATLAS detector. *Eur. Phys. J. C* 83.8 (2023), p. 719. DOI: 10.1140/epjc/s10052-023-11790-7.

[116] Armen Tumasyan et al. Search for pair production of vector-like quarks in leptonic final states in proton-proton collisions at $\sqrt{s}$ = 13 TeV. *JHEP* 07 (2023), p. 020. DOI: 10.1007/JHEP07(2023)020.

[117] Georges Aad et al. Search for pair-production of vector-like quarks in pp collision events at s=13 TeV with at least one leptonically decaying Z boson and a third-generation quark with the ATLAS detector. *Phys. Lett. B* 843 (2023), p. 138019. DOI: 10.1016/j.physletb.2023.138019.

[118] J. Alwall et al. The automated computation of tree-level and next-to-leading order differential cross sections, and their matching to parton shower simulations. *JHEP* 07 (2014), p. 079. DOI: 10.1007/JHEP07(2014)079.

[119] Georges Aad et al. Search for singly produced vector-like top partners in multilepton final states with 139 fb^{-1} of pp collision data at $\sqrt{s} = 13$ TeV with the ATLAS detector (July 2023). arXiv: 2307.07584 [hep-ex].

[120] Georges Aad et al. Search for single production of vector-like T quarks decaying into Ht or Zt in pp collisions at $\sqrt{s}$ = 13 TeV with the ATLAS detector. *JHEP* 08 (2023), p. 153. DOI: 10.1007/JHEP08(2023)153.

[121] Georges Aad et al. Search for single production of a vectorlike T quark decaying into a Higgs boson and top quark with fully hadronic final states using the ATLAS detector. *Phys. Rev. D* 105.9 (2022), p. 092012. DOI: 10.1103/PhysRevD.105.092012.

[122] Georges Aad et al. Search for single vector-like B quark production and decay via $B \to bH(b\bar{b})$ in pp collisions at $\sqrt{s} = 13$ TeV with the ATLAS detector (Aug. 2023). arXiv: 2308.02595 [hep-ex].

[123] Darius A. Faroughy, Admir Greljo, and Jernej F. Kamenik. Confronting lepton flavor universality violation in B decays with high-p_T tau lepton searches at LHC. *Phys. Lett. B* 764 (2017), pp. 126–134. DOI: 10.1016/j.physletb.2016.11.011.

[124] Kamila Kowalska, Enrico Maria Sessolo, and Yasuhiro Yamamoto. Constraints on charmphilic solutions to the muon g-2 with leptoquarks. *Phys. Rev. D* 99.5 (2019), p. 055007. DOI: 10.1103/PhysRevD.99.055007.

[125] G. Aad et al. Search for third-generation vector-like leptons in pp collisions at $\sqrt{s} =$ 13 TeV with the ATLAS detector. *JHEP* 07 (2023), p. 118. DOI: 10.1007/JHEP07(2023)118.

[126] A. M. Sirunyan et al. Search for vectorlike leptons in multilepton final states in proton-proton collisions at $\sqrt{s} = 13$ TeV. *Phys. Rev. D* 100 (5 Sept. 2019), p. 052003. DOI: 10.1103/PhysRevD.100.052003. URL: https://link.aps.org/doi/10.1103/PhysRevD.100.052003.

[127] Georges Aad et al. Search for direct production of winos and higgsinos in events with two same-charge leptons or three leptons in pp collision data at $\sqrt{s} = 13$ TeV with the ATLAS detector (May 2023). arXiv: 2305.09322 [hep-ex].

[128] Felix Kling, Shufang Su, and Wei Su. 2HDM Neutral Scalars under the LHC. *JHEP* 06 (2020), p. 163. DOI: 10.1007/JHEP06(2020)163.

[129] Henning Bahl et al. HiggsTools: BSM scalar phenomenology with new versions of HiggsBounds and HiggsSignals. *Comput. Phys. Commun.* 291 (2023), p. 108803. DOI: 10.1016/j.cpc.2023.108803.

[130] Georges Aad et al. Search for heavy Higgs bosons decaying into two tau leptons with the ATLAS detector using pp collisions at $\sqrt{s} = 13$ TeV. *Phys. Rev. Lett.* 125.5 (2020), p. 051801. DOI: 10.1103/PhysRevLett.125.051801.

[131] Albert M Sirunyan et al. Search for heavy Higgs bosons decaying to a top quark pair in proton-proton collisions at $\sqrt{s} = 13$ TeV. *JHEP* 04 (2020). [Erratum: JHEP 03, 187 (2022)], p. 171. DOI: 10.1007/JHEP04(2020)171.

[132] Albert M Sirunyan et al. Search for additional neutral MSSM Higgs bosons in the $\tau\tau$ final state in proton-proton collisions at $\sqrt{s} = 13$ TeV. *JHEP* 09 (2018), p. 007. DOI: 10.1007/JHEP09(2018)007.

[133] Albert M Sirunyan et al. Search for MSSM Higgs bosons decaying to $\mu + \mu -$ in proton-proton collisions at s=13TeV. *Phys. Lett. B* 798 (2019), p. 134992. DOI: 10.1016/j.physletb.2019.134992.

[134] M. Aaboud et al. Search for scalar resonances decaying into $\mu^+\mu^-$ in events with and without b-tagged jets produced in proton-proton collisions at $\sqrt{s} = 13$ TeV with the ATLAS detector. *JHEP* 07 (2019), p. 117. DOI: 10.1007/JHEP07(2019)117.

[135] Albert M Sirunyan et al. Search for beyond the standard model Higgs bosons decaying into a $\mathrm{b\bar{b}}$ pair in pp collisions at $\sqrt{s} = 13$ TeV. *JHEP* 08 (2018), p. 113. DOI: 10.1007/JHEP08(2018)113.

[136] Georges Aad et al. Search for heavy neutral Higgs bosons produced in association with b-quarks and decaying into b-quarks at $\sqrt{s} = 13$ TeV with the ATLAS detector. *Phys. Rev. D* 102.3 (2020), p. 032004. DOI: 10.1103/PhysRevD.102.032004.

[137] Albert M Sirunyan et al. Search for a charged Higgs boson decaying into top and bottom quarks in events with electrons or muons in proton-proton collisions at $\sqrt{\mathrm{s}} =$ 13 TeV. *JHEP* 01 (2020), p. 096. DOI: 10.1007/JHEP01(2020)096.

[138] Georges Aad et al. Search for charged Higgs bosons decaying into a top quark and a bottom quark at $\sqrt{\mathrm{s}} = 13$ TeV with the ATLAS detector. *JHEP* 06 (2021), p. 145. DOI: 10.1007/JHEP06(2021)145.

[139] Gautam Bhattacharyya and Dipankar Das. Scalar sector of two-Higgs-doublet models: A minireview. *Pramana* 87.3 (2016), p. 40. DOI: 10.1007/s12043-016-1252-4.

[140] Daniel F. Litim and Francesco Sannino. Asymptotic safety guaranteed. *JHEP* 12 (2014), p. 178. DOI: 10.1007/JHEP12(2014)178.

[141] Daniel F. Litim et al. Asymptotic safety guaranteed at four-loop order. *Phys. Rev. D* 108.7 (2023), p. 076006. DOI: 10.1103/PhysRevD.108.076006.

[142] Andrew D. Bond et al. UV conformal window for asymptotic safety. *Phys. Rev. D* 97.3 (2018), p. 036019. DOI: 10.1103/PhysRevD.97.036019.

[143] Daniel F. Litim. Optimized renormalization group flows. *Phys. Rev. D* 64 (2001), p. 105007. DOI: 10.1103/PhysRevD.64.105007.

[144] G. Fejs and A. Patkós. Field dependence of the Yukawa coupling in the three flavor quark-meson model. *Phys. Rev. D* 103.5 (2021), p. 056015. DOI: 10.1103/PhysRevD.103.056015.

[145] Tom Steudtner. Effective potential and vacuum stability in the Litim-Sannino model. *JHEP* 05 (2024), p. 149. DOI: 10.1007/JHEP05(2024)149.

[146] S. Weinberg. General Relativity. S.W.Hawking, W.Israel (Eds.), Cambridge Univ. Press, 1980, pp. 790–831.

[147] Tim R. Morris. The Exact renormalisation group and approximate solutions. *Int. J. Mod. Phys. A* 9 (1994), pp. 2411–2450. DOI: 10.1142/S0217751X94000972.

[148] M. Reuter. Nonperturbative evolution equation for quantum gravity. *Phys. Rev. D* 57 (1998), pp. 971–985. DOI: 10.1103/PhysRevD.57.971.

[149] O. Lauscher and M. Reuter. Ultraviolet fixed point and generalized flow equation of quantum gravity. *Phys. Rev. D* 65 (2002), p. 025013. DOI: 10.1103/PhysRevD.65.025013.

[150] M. Reuter and Frank Saueressig. Renormalization group flow of quantum gravity in the Einstein-Hilbert truncation. *Phys. Rev. D* 65 (2002), p. 065016. DOI: 10.1103/PhysRevD.65.065016.

[151] O. Lauscher and M. Reuter. Flow equation of quantum Einstein gravity in a higher derivative truncation. *Phys. Rev. D* 66 (2002), p. 025026. DOI: 10.1103/PhysRevD.66.025026.

[152] Daniel F. Litim. Fixed points of quantum gravity. *Phys. Rev. Lett.* 92 (2004), p. 201301. DOI: 10.1103/PhysRevLett.92.201301.

[153] Alessandro Codello and Roberto Percacci. Fixed points of higher derivative gravity. *Phys. Rev. Lett.* 97 (2006), p. 221301. DOI: 10.1103/PhysRevLett.97.221301.

[154] Pedro F. Machado and Frank Saueressig. On the renormalisation group flow of f(R)-gravity. *Phys. Rev. D* 77 (2008), p. 124045. DOI: 10.1103/PhysRevD.77.124045.

[155] Alessandro Codello, Roberto Percacci, and Christoph Rahmede. Investigating the Ultraviolet Properties of Gravity with a Wilsonian Renormalization Group Equation. *Annals Phys.* 324 (2009), pp. 414–469. DOI: 10.1016/j.aop.2008.08.008.

[156] Dario Benedetti, Pedro F. Machado, and Frank Saueressig. Asymptotic safety in higher-derivative gravity. *Mod. Phys. Lett. A* 24 (2009), pp. 2233–2241. DOI: 10.1142/S0217732309031521.

[157] Juergen A. Dietz and Tim R. Morris. Asymptotic safety in the f(R) approximation. *JHEP* 01 (2013), p. 108. DOI: 10.1007/JHEP01(2013)108.

[158] K. Falls et al. A bootstrap towards asymptotic safety (Jan. 2013). arXiv: 1301.4191 [hep-th].

[159] Kevin Falls et al. Further evidence for asymptotic safety of quantum gravity. *Phys. Rev. D* 93.10 (2016), p. 104022. DOI: 10.1103/PhysRevD.93.104022.

[160] Kin-ya Oda and Masatoshi Yamada. Non-minimal coupling in Higgs–Yukawa model with asymptotically safe gravity. *Class. Quant. Grav.* 33.12 (2016), p. 125011. DOI: 10.1088/0264-9381/33/12/125011.

[161] Yuta Hamada and Masatoshi Yamada. Asymptotic safety of higher derivative quantum gravity non-minimally coupled with a matter system. *JHEP* 08 (2017), p. 070. DOI: 10.1007/JHEP08(2017)070.

[162] Nicolai Christiansen et al. Asymptotic safety of gravity with matter. *Phys. Rev. D* 97.10 (2018), p. 106012. DOI: 10.1103/PhysRevD.97.106012.

[163] Sean P. Robinson and Frank Wilczek. Gravitational correction to running of gauge couplings. *Phys. Rev. Lett.* 96 (2006), p. 231601. DOI: 10.1103/PhysRevLett.96.231601.

[164] Artur R. Pietrykowski. Gauge dependence of gravitational correction to running of gauge couplings. *Phys. Rev. Lett.* 98 (2007), p. 061801. DOI: 10.1103/PhysRevLett.98.061801.

[165] David J. Toms. Quantum gravity and charge renormalisation. *Phys. Rev. D* 76 (2007), p. 045015. DOI: 10.1103/PhysRevD.76.045015.

[166] Yong Tang and Yue-Liang Wu. Gravitational Contributions to the Running of Gauge Couplings. *Commun. Theor. Phys.* 54 (2010), pp. 1040–1044. DOI: 10.1088/0253-6102/54/6/15.

[167] David J. Toms. Cosmological constant and quantum gravitational corrections to the running fine structure constant. *Phys. Rev. Lett.* 101 (2008), p. 131301. DOI: 10.1103/PhysRevLett.101.131301.

[168] Andreas Rodigast and Theodor Schuster. Gravitational Corrections to Yukawa and phi**4 Interactions. *Phys. Rev. Lett.* 104 (2010), p. 081301. DOI: 10.1103/PhysRevLett.104.081301.

[169] O. Zanusso et al. Gravitational corrections to Yukawa systems. *Phys. Lett. B* 689 (2010), pp. 90–94. DOI: 10.1016/j.physletb.2010.04.043.

[170] Jan-Eric Daum, Ulrich Harst, and Martin Reuter. Running Gauge Coupling in Asymptotically Safe Quantum Gravity. *JHEP* 01 (2010), p. 084. DOI: 10.1007/JHEP01(2010)084.

[171] J.-E. Daum, U. Harst, and M. Reuter. Non-perturbative QEG Corrections to the Yang-Mills Beta Function. *Gen. Rel. Grav.* 43 (2011). Ed. by Konstantinos Anagnostopoulos and George Zoupanos, p. 2393. DOI: 10.1007/s10714-010-1032-2.

[172] Sarah Folkerts, Daniel F. Litim, and Jan M. Pawlowski. Asymptotic freedom of Yang-Mills theory with gravity. *Phys. Lett. B* 709 (2012), pp. 234–241. DOI: 10.1016/j.physletb.2012.02.002.

[173] Astrid Eichhorn, Aaron Held, and Jan M. Pawlowski. Quantum-gravity effects on a Higgs-Yukawa model. *Phys. Rev. D* 94.10 (2016), p. 104027. DOI: 10.1103/PhysRevD.94.104027.

[174] Astrid Eichhorn and Aaron Held. Viability of quantum-gravity induced ultraviolet completions for matter. *Phys. Rev. D* 96.8 (2017), p. 086025. DOI: 10.1103/PhysRevD.96.086025.

[175] U. Harst and M. Reuter. QED coupled to QEG. *JHEP* 05 (2011), p. 119. DOI: 10.1007/JHEP05(2011)119.

[176] Nicolai Christiansen and Astrid Eichhorn. An asymptotically safe solution to the U(1) triviality problem. *Phys. Lett. B* 770 (2017), pp. 154–160. DOI: 10.1016/j.physletb.2017.04.047.

[177] Astrid Eichhorn and Fleur Versteegen. Upper bound on the Abelian gauge coupling from asymptotic safety. *JHEP* 01 (2018), p. 030. DOI: 10.1007/JHEP01(2018)030.

[178] Mikhail Shaposhnikov and Christof Wetterich. Asymptotic safety of gravity and the Higgs boson mass. *Phys. Lett. B* 683 (2010), pp. 196–200. DOI: 10.1016/j.physletb.2009.12.022.

[179] Astrid Eichhorn et al. Quantum gravity fluctuations flatten the Planck-scale Higgs potential. *Phys. Rev. D* 97.8 (2018), p. 086004. DOI: 10.1103/PhysRevD.97.086004.

[180] Jan H. Kwapisz. Asymptotic safety, the Higgs boson mass, and beyond the standard model physics. *Phys. Rev. D* 100.11 (2019), p. 115001. DOI: 10.1103/PhysRevD.100.115001.

[181] Astrid Eichhorn, Martin Pauly, and Shouryya Ray. Towards a Higgs mass determination in asymptotically safe gravity with a dark portal. *JHEP* 10 (2021), p. 100. DOI: 10.1007/JHEP10(2021)100.

[182] Astrid Eichhorn and Aaron Held. Top mass from asymptotic safety. *Phys. Lett. B* 777 (2018), pp. 217–221. DOI: 10.1016/j.physletb.2017.12.040.

[183] Alessandro Codello, Roberto Percacci, and Christoph Rahmede. Ultraviolet properties of f(R)-gravity. *Int. J. Mod. Phys. A* 23 (2008), pp. 143–150. DOI: 10.1142/S0217751X08038135.

[184] Kevin Falls et al. Asymptotic safety of quantum gravity beyond Ricci scalars. *Phys. Rev. D* 97.8 (2018), p. 086006. DOI: 10.1103/PhysRevD.97.086006.

[185] Kevin G. Falls, Daniel F. Litim, and Jan Schröder. Aspects of asymptotic safety for quantum gravity. *Phys. Rev. D* 99.12 (2019), p. 126015. DOI: 10.1103/PhysRevD.99.126015.

[186] Gaurav Narain and Roberto Percacci. On the scheme dependence of gravitational beta functions. *Acta Phys. Polon. B* 40 (2009). Ed. by Michal Praszalowicz, pp. 3439–3457. arXiv: 0910.5390 [hep-th].

[187] Roberto Percacci and Daniele Perini. Constraints on matter from asymptotic safety. *Phys. Rev. D* 67 (2003), p. 081503. DOI: 10.1103/PhysRevD.67.081503.

[188] Roberto Percacci and Daniele Perini. Asymptotic safety of gravity coupled to matter. *Phys. Rev. D* 68 (2003), p. 044018. DOI: 10.1103/PhysRevD.68.044018.

[189] Pietro Donà, Astrid Eichhorn, and Roberto Percacci. Matter matters in asymptotically safe quantum gravity. *Phys. Rev. D* 89.8 (2014), p. 084035. DOI: 10.1103/PhysRevD.89.084035.

[190] John F. Donoghue. A Critique of the Asymptotic Safety Program. *Front. in Phys.* 8 (2020), p. 56. DOI: 10.3389/fphy.2020.00056.

[191] Alfio Bonanno et al. Critical reflections on asymptotically safe gravity. *Front. in Phys.* 8 (2020), p. 269. DOI: 10.3389/fphy.2020.00269.

[192] Astrid Eichhorn and Aaron Held. Mass difference for charged quarks from asymptotically safe quantum gravity. *Phys. Rev. Lett.* 121.15 (2018), p. 151302. DOI: 10.1103/PhysRevLett.121.151302.

[193] Frederic Grabowski, Jan H. Kwapisz, and Krzysztof A. Meissner. Asymptotic safety and Conformal Standard Model. *Phys. Rev. D* 99.11 (2019), p. 115029. DOI: 10.1103/PhysRevD.99.115029.

[194] Manuel Reichert and Juri Smirnov. Dark Matter meets Quantum Gravity. *Phys. Rev. D* 101.6 (2020), p. 063015. DOI: 10.1103/PhysRevD.101.063015.

[195] Reinhard Alkofer et al. Quark masses and mixings in minimally parameterized UV completions of the Standard Model. *Annals Phys.* 421 (2020), p. 168282. DOI: 10.1016/j.aop.2020.168282.

[196] Kamila Kowalska, Enrico Maria Sessolo, and Yasuhiro Yamamoto. Flavor anomalies from asymptotically safe gravity. *Eur. Phys. J. C* 81.4 (2021), p. 272. DOI: 10.1140/epjc/s10052-021-09072-1.

[197] Kamila Kowalska, Soumita Pramanick, and Enrico Maria Sessolo. Naturally small Yukawa couplings from trans-Planckian asymptotic safety. *JHEP* 08 (2022), p. 262. DOI: 10.1007/JHEP08(2022)262.

[198] Jens Boos et al. Asymptotic safety and gauged baryon number. *Phys. Rev. D* 106.3 (2022), p. 035015. DOI: 10.1103/PhysRevD.106.035015.

[199] Jens Boos et al. Asymptotically safe dark matter with gauged baryon number. *Phys. Rev. D* 107.3 (2023), p. 035018. DOI: 10.1103/PhysRevD.107.035018.

[200] Astrid Eichhorn and Aaron Held. Dynamically vanishing Dirac neutrino mass from quantum scale symmetry (Apr. 2022). arXiv: 2204.09008 [hep-ph].

[201] Astrid Eichhorn and Martin Pauly. Safety in darkness: Higgs portal to simple Yukawa systems (May 2020). arXiv: 2005.03661 [hep-ph].

[202] Gustavo P. de Brito, Astrid Eichhorn, and Rafael R. Lino dos Santos. Are there ALPs in the asymptotically safe landscape? *JHEP* 06 (2022), p. 013. DOI: 10.1007/JHEP06(2022)013.

[203] Christof Wetterich and Masatoshi Yamada. Gauge hierarchy problem in asymptotically safe gravity–the resurgence mechanism. *Phys. Lett. B* 770 (2017), pp. 268–271. DOI: 10.1016/j.physletb.2017.04.049.

[204] Jan M. Pawlowski et al. Higgs scalar potential in asymptotically safe quantum gravity. *Phys. Rev. D* 99.8 (2019), p. 086010. DOI: 10.1103/PhysRevD.99.086010.

[205] C. Wetterich. Effective scalar potential in asymptotically safe quantum gravity. *Universe* 7.2 (2021), p. 45. DOI: 10.3390/universe7020045.

[206] Astrid Eichhorn and Martin Pauly. Constraining power of asymptotic safety for scalar fields. *Phys. Rev. D* 103.2 (2021), p. 026006. DOI: 10.1103/PhysRevD.103.026006.

[207] Roel Aaij et al. Test of lepton universality in beauty-quark decays. *Nature Phys.* 18.3 (2022), pp. 277–282. DOI: 10.1038/s41567-021-01478-8.

[208] A. Abdesselam et al. Test of Lepton-Flavor Universality in $B \to K^*\ell^+\ell^-$ Decays at Belle. *Phys. Rev. Lett.* 126.16 (2021), p. 161801. DOI: 10.1103/PhysRevLett.126.161801.

[209] Roel Aaij et al. Angular analysis of the $B^0 \to K^{*0}e^+e^-$ decay in the low$-\mathrm{q}^2$ region. *JHEP* 04 (2015), p. 064. DOI: 10.1007/JHEP04(2015)064.

[210] Roel Aaij et al. Angular analysis and differential branching fraction of the decay $B_s^0 \to \phi\mu^+\mu^-$. *JHEP* 09 (2015), p. 179. DOI: 10.1007/JHEP09(2015)179.

[211] Vardan Khachatryan et al. Angular analysis of the decay $B^0 \to K^{*0}\mu^+\mu^-$ from pp collisions at $\sqrt{s} = 8$ TeV. *Phys. Lett.* B753 (2016), pp. 424–448. DOI: 10.1016/j.physletb.2015.12.020.

[212] Roel Aaij et al. Angular analysis of the $B^0 \to K^{*0}\mu^+\mu^-$ decay using 3 fb^{-1} of integrated luminosity. *JHEP* 02 (2016), p. 104. DOI: 10.1007/JHEP02(2016)104.

[213] Roel Aaij et al. Measurements of the S-wave fraction in $B^0 \to K^+\pi^-\mu^+\mu^-$ decays and the $B^0 \to K^*(892)^0\mu^+\mu^-$ differential branching fraction. *JHEP* 11 (2016). [Erratum: JHEP 04, 142 (2017)], p. 047. DOI: 10.1007/JHEP11(2016)047.

[214] S. Wehle et al. Lepton-Flavor-Dependent Angular Analysis of $B \to K^*\ell^+\ell^-$. *Phys. Rev. Lett.* 118.11 (2017), p. 111801. DOI: 10.1103/PhysRevLett.118.111801.

[215] Albert M Sirunyan et al. Measurement of angular parameters from the decay $\mathrm{B}^0 \to \mathrm{K}^{*0}\mu^+\mu^-$ in proton-proton collisions at $\sqrt{s} = 8$ TeV. *Phys. Lett. B* 781 (2018), pp. 517–541. DOI: 10.1016/j.physletb.2018.04.030.

[216] Morad Aaboud et al. Angular analysis of $B_d^0 \to K^*\mu^+\mu^-$ decays in pp collisions at $\sqrt{s} = 8$ TeV with the ATLAS detector. *JHEP* 10 (2018), p. 047. DOI: 10.1007/JHEP10(2018)047.

[217] Roel Aaij et al. Measurement of CP-Averaged Observables in the $B^0 \to K^{*0}\mu^+\mu^-$ Decay. *Phys. Rev. Lett.* 125.1 (2020), p. 011802. DOI: 10.1103/PhysRevLett.125.011802.

[218] Roel Aaij et al. Angular Analysis of the $B^+ \to K^{*+}\mu^+\mu^-$ Decay. *Phys. Rev. Lett.* 126.16 (2021), p. 161802. DOI: 10.1103/PhysRevLett.126.161802.

[219] Guido D'Amico et al. Flavour anomalies after the R_{K^*} measurement. *JHEP* 09 (2017), p. 010. DOI: 10.1007/JHEP09(2017)010.

[220] Marco Ciuchini et al. New Physics in $b \to s\ell^+\ell^-$ confronts new data on Lepton Universality. *Eur. Phys. J. C* 79.8 (2019), p. 719. DOI: 10.1140/epjc/s10052-019-7210-9.

[221] Marcel Algueró et al. Emerging patterns of New Physics with and without Lepton Flavour Universal contributions. *Eur. Phys. J. C* 79.8 (2019). [Addendum: Eur.Phys.J.C 80, 511 (2020)], p. 714. DOI: 10.1140/epjc/s10052-019-7216-3.

[222] Ashutosh Kumar Alok et al. Continuing search for new physics in $b \to s\mu\mu$ decays: two operators at a time. *JHEP* 06 (2019), p. 089. DOI: 10.1007/JHEP06(2019)089.

[223] Alakabha Datta, Jacky Kumar, and David London. The B anomalies and new physics in $b \to se^+e^-$. *Phys. Lett. B* 797 (2019), p. 134858. DOI: 10.1016/j.physletb.2019.134858.

[224] Jason Aebischer et al. B-decay discrepancies after Moriond 2019. *Eur. Phys. J. C* 80.3 (2020), p. 252. DOI: 10.1140/epjc/s10052-020-7817-x.

[225] Kamila Kowalska, Dinesh Kumar, and Enrico Maria Sessolo. Implications for new physics in $b \to s\mu\mu$ transitions after recent measurements by Belle and LHCb. *Eur. Phys. J. C* 79.10 (2019), p. 840. DOI: 10.1140/epjc/s10052-019-7330-2.

[226] Marco Ciuchini et al. Lessons from the $B^{0,+} \to K^{*0,+}\mu^+\mu^-$ angular analyses. *Phys. Rev. D* 103.1 (2021), p. 015030. DOI: 10.1103/PhysRevD.103.015030.

[227] T. Hurth, F. Mahmoudi, and S. Neshatpour. Model independent analysis of the angular observables in $B^0 \to K^{*0}\mu^+\mu^-$ and $B^+ \to K^{*+}\mu^+\mu^-$. *Phys. Rev. D* 103 (2021), p. 095020. DOI: 10.1103/PhysRevD.103.095020.

[228] Jorge Alda, Jaume Guasch, and Siannah Penaranda. Anomalies in B mesons decays: a phenomenological approach. *Eur. Phys. J. Plus* 137.2 (2022), p. 217. DOI: 10.1140/epjp/s13360-022-02405-3.

[229] Wolfgang Altmannshofer and Peter Stangl. New physics in rare B decays after Moriond 2021. *Eur. Phys. J. C* 81.10 (2021), p. 952. DOI: 10.1140/epjc/s10052-021-09725-1.

[230] Marcel Algueró et al. $b \to s\ell^+\ell^-$ global fits after R_{K_S} and $R_{K^{*+}}$. *Eur. Phys. J. C* 82.4 (2022), p. 326. DOI: 10.1140/epjc/s10052-022-10231-1.

[231] David London and Joaquim Matias. *B* Flavour Anomalies: 2021 Theoretical Status Report (Oct. 2021). DOI: 10.1146/annurev-nucl-102020-090209.

[232] Andrzej J. Buras, Fulvia De Fazio, and Jennifer Girrbach. The Anatomy of Z′ and Z with Flavour Changing Neutral Currents in the Flavour Precision Era. *JHEP* 02 (2013), p. 116. DOI: 10.1007/JHEP02(2013)116.

[233] Rhorry Gauld, Florian Goertz, and Ulrich Haisch. An explicit Z′-boson explanation of the $B \to K^*\mu^+\mu^-$ anomaly. *JHEP* 01 (2014), p. 069. DOI: 10.1007/JHEP01(2014)069.

[234] Wolfgang Altmannshofer et al. Quark flavor transitions in $L_\mu - L_\tau$ models. *Phys. Rev.* D89 (2014), p. 095033. DOI: 10.1103/PhysRevD.89.095033.

[235] Andrzej J. Buras, Fulvia De Fazio, and Jennifer Girrbach. 331 models facing new $b \to s\mu^+\mu^-$ data. *JHEP* 02 (2014), p. 112. DOI: 10.1007/JHEP02(2014)112.

[236] Andreas Crivellin, Giancarlo D'Ambrosio, and Julian Heeck. Explaining $h \to \mu^\pm\tau^\mp$, $B \to K^*\mu^+\mu^-$ and $B \to K\mu^+\mu^-/B \to Ke^+e^-$ in a two-Higgs-doublet model with gauged $L_\mu - L_\tau$. *Phys. Rev. Lett.* 114 (2015), p. 151801. DOI: 10.1103/PhysRevLett.114.151801.

[237] D. Aristizabal Sierra, Florian Staub, and Avelino Vicente. Shedding light on the $b \to s$ anomalies with a dark sector. *Phys. Rev. D* 92.1 (2015), p. 015001. DOI: 10.1103/PhysRevD.92.015001.

[238] Ben Allanach et al. Z models for the LHCb and $g-2$ muon anomalies. *Phys. Rev. D* 93.5 (2016). [Erratum: Phys.Rev.D 95, 119902 (2017)], p. 055045. DOI: 10.1103/PhysRevD.93.055045.

[239] Cheng-Wei Chiang, Xiao-Gang He, and German Valencia. Z′ model for $b \to sl\bar{l}$ flavor anomalies. *Phys. Rev.* D93.7 (2016), p. 074003. DOI: 10.1103/PhysRevD.93.074003.

[240] Cesar Bonilla et al. $U(1)_{B_3-3L_\mu}$ gauge symmetry as a simple description of $b \to s$ anomalies. *Phys. Rev.* D98.9 (2018), p. 095002. DOI: 10.1103/PhysRevD.98.095002.

[241] Stefano Di Chiara et al. Minimal flavor-changing Z' models and muon $g-2$ after the R_{K^*} measurement. *Nucl. Phys.* B923 (2017), pp. 245–257. DOI: 10.1016/j.nuclphysb.2017.08.003.

[242] Rigo Bause et al. B-anomalies from flavorful U(1)$'$ extensions, safely. *Eur. Phys. J. C* 82.1 (2022), p. 42. DOI: 10.1140/epjc/s10052-021-09957-1.

[243] Robert Foot. New Physics From Electric Charge Quantization? *Mod. Phys. Lett. A* 6 (1991), pp. 527–530. DOI: 10.1142/S0217732391000543.

[244] X. G. He et al. NEW Z-prime PHENOMENOLOGY. *Phys. Rev. D* 43 (1991), pp. 22–24. DOI: 10.1103/PhysRevD.43.R22.

[245] Xiao-Gang He et al. Simplest Z-prime model. *Phys. Rev. D* 44 (1991), pp. 2118–2132. DOI: 10.1103/PhysRevD.44.2118.

[246] K. S. Babu. Renormalization Group Analysis of the Kobayashi-Maskawa Matrix. *Z. Phys. C* 35 (1987), p. 69. DOI: 10.1007/BF01561056.

[247] K. Sasaki. Renormalization Group Equations for the Kobayashi-Maskawa Matrix. *Z. Phys. C* 32 (1986), pp. 149–152. DOI: 10.1007/BF01441364.

[248] Vernon D. Barger, M. S. Berger, and P. Ohmann. Universal evolution of CKM matrix elements. *Phys. Rev. D* 47 (1993), pp. 2038–2045. DOI: 10.1103/PhysRevD.47.2038.

[249] P. Kielanowski, S. Rebeca Juarez Wysozka, and J. H. Montes de Oca Y. Renormalization Group Equations for the CKM matrix. *Phys. Rev. D* 78 (2008), p. 116010. DOI: 10.1103/PhysRevD.78.116010.

[250] T. Robens. Extended scalar sectors at current and future colliders. *55th Rencontres de Moriond on QCD and High Energy Interactions*. May 2021. arXiv: 2105.07719 [hep-ph].

[251] Joerg Jaeckel, Martin Jankowiak, and Michael Spannowsky. LHC probes the hidden sector. *Phys. Dark Univ.* 2 (2013), pp. 111–117. DOI: 10.1016/j.dark.2013.06.001.

[252] Georges Aad et al. Search for high-mass dilepton resonances using 139 fb^{-1} of pp collision data collected at $\sqrt{s}$ =13 TeV with the ATLAS detector. *Phys. Lett. B* 796 (2019), pp. 68–87. DOI: 10.1016/j.physletb.2019.07.016.

[253] Albert M Sirunyan et al. Search for resonant and nonresonant new phenomena in high-mass dilepton final states at $\sqrt{s}$ = 13 TeV. *JHEP* 07 (2021), p. 208. DOI: 10.1007/JHEP07(2021)208.

[254] P A. Zyla et al. Review of Particle Physics. *Prog. Theor. Exp. Phys.* (2020), p. 083C01. DOI: 10.1093/ptep/ptaa104.

[255] Wolfgang Altmannshofer and David M. Straub. New physics in $b \to s$ transitions after LHC run 1. *Eur. Phys. J. C* 75.8 (2015), p. 382. DOI: 10.1140/epjc/s10052-015-3602-7.

[256] Wolfgang Altmannshofer et al. Neutrino Trident Production: A Powerful Probe of New Physics with Neutrino Beams. *Phys. Rev. Lett.* 113 (2014), p. 091801. DOI: 10.1103/PhysRevLett.113.091801.

[257] S. R. Mishra et al. Neutrino tridents and W Z interference. *Phys. Rev. Lett.* 66 (1991), pp. 3117–3120. DOI: 10.1103/PhysRevLett.66.3117.

[258] D. Geiregat et al. First observation of neutrino trident production. *Phys. Lett. B* 245 (1990), pp. 271–275. DOI: 10.1016/0370-2693(90)90146-W.

[259] Georges Aad et al. Search for squarks and gluinos in final states with same-sign leptons and jets using 139 fb^{-1} of data collected with the ATLAS detector. *JHEP* 06 (2020), p. 046. DOI: 10.1007/JHEP06(2020)046.

[260] Georges Aad et al. Search for squarks and gluinos in final states with one isolated lepton, jets, and missing transverse momentum at $\sqrt{s} = 13$ with the ATLAS detector. *Eur. Phys. J. C* 81.7 (2021). [Erratum: Eur.Phys.J.C 81, 956 (2021)], p. 600. DOI: 10.1140/epjc/s10052-021-09748-8.

[261] A. M. Sirunyan et al. Search for electroweak production of charginos and neutralinos in multilepton final states in proton-proton collisions at $\sqrt{s} = 13$ TeV. *JHEP* 03 (2018), p. 166. DOI: 10.1007/JHEP03(2018)166.

[262] Jia Liu, Xiao-Ping Wang, and Felix Yu. A Tale of Two Portals: Testing Light, Hidden New Physics at Future e^+e^- Colliders. *JHEP* 06 (2017), p. 077. DOI: 10.1007/JHEP06(2017)077.

[263] Bob Holdom. Two U(1)'s and Epsilon Charge Shifts. *Phys. Lett. B* 166 (1986), pp. 196–198. DOI: 10.1016/0370-2693(86)91377-8.

[264] K. S. Babu, Christopher F. Kolda, and John March-Russell. Leptophobic U(1) s and the R(b) - R(c) crisis. *Phys. Rev. D* 54 (1996), pp. 4635–4647. DOI: 10.1103/PhysRevD.54.4635.

[265] Florian Staub. Automatic Calculation of supersymmetric Renormalization Group Equations and Self Energies. *Comput. Phys. Commun.* 182 (2011), pp. 808–833. DOI: 10.1016/j.cpc.2010.11.030.

[266] Anders Eller Thomsen. Introducing RGBeta: a Mathematica package for the evaluation of renormalisation group β-functions. *Eur. Phys. J. C* 81.5 (2021), p. 408. DOI: 10.1140/epjc/s10052-021-09142-4.

[267] Colin Poole and Anders Eller Thomsen. Constraints on 3- and 4-loop β-functions in a general four-dimensional Quantum Field Theory. *JHEP* 09 (2019), p. 055. DOI: 10.1007/JHEP09(2019)055.

[268] Lohan Sartore and Ingo Schienbein. PyR@TE 3. *Comput. Phys. Commun.* 261 (2021), p. 107819. DOI: 10.1016/j.cpc.2020.107819.

[269] Claudio Coriano, Luigi Delle Rose, and Carlo Marzo. Constraints on abelian extensions of the Standard Model from two-loop vacuum stability and $U(1)_{B-L}$. *JHEP* 02 (2016), p. 135. DOI: 10.1007/JHEP02(2016)135.

[270] Florian Lyonnet and Ingo Schienbein. PyR@TE 2: A Python tool for computing RGEs at two-loop. *Comput. Phys. Commun.* 213 (2017), pp. 181–196. DOI: 10.1016/j.cpc.2016.12.003.

[271] R. L. Workman et al. Review of Particle Physics. *PTEP* 2022 (2022), p. 083C01. DOI: 10.1093/ptep/ptac097.

[272] W. Buchmuller, R. Ruckl, and D. Wyler. Leptoquarks in Lepton - Quark Collisions. *Phys. Lett. B* 191 (1987). [Erratum: Phys.Lett.B 448, 320–320 (1999)], pp. 442–448. DOI: 10.1016/0370-2693(87)90637-X.

[273] A. J. Davies and Xiao-Gang He. Tree Level Scalar Fermion Interactions Consistent With the Symmetries of the Standard Model. *Phys. Rev. D* 43 (1991), pp. 225–235. DOI: 10.1103/PhysRevD.43.225.

[274] Peter Athron, Dominik Stockinger, and Alexander Voigt. Threshold Corrections in the Exceptional Supersymmetric Standard Model. *Phys. Rev. D* 86 (2012), p. 095012. DOI: 10.1103/PhysRevD.86.095012.

[275] Florian Staub. From Superpotential to Model Files for FeynArts and CalcHep/CompHep. *Comput. Phys. Commun.* 181 (2010), pp. 1077–1086. DOI: 10.1016/j.cpc.2010.01.011.

[276] Florian Staub. SARAH 3.2: Dirac Gauginos, UFO output, and more. *Comput. Phys. Commun.* 184 (2013), pp. 1792–1809. DOI: 10.1016/j.cpc.2013.02.019.

[277] B. C. Allanach. SOFTSUSY: a program for calculating supersymmetric spectra. *Comput. Phys. Commun.* 143 (2002), pp. 305–331. DOI: 10.1016/S0010-4655(01)00460-X.

[278] Peter Athron et al. FlexibleSUSYA spectrum generator generator for supersymmetric models. *Comput. Phys. Commun.* 190 (2015), pp. 139–172. DOI: 10.1016/j.cpc.2014.12.020.

[279] Peter Athron et al. FlexibleSUSY 2.0: Extensions to investigate the phenomenology of SUSY and non-SUSY models. *Comput. Phys. Commun.* 230 (2018), pp. 145–217. DOI: 10.1016/j.cpc.2018.04.016.